Fakultät für Mathematik, Informatik und Naturwissenschaften | RWTH AACHEN UNIVERSITY

# Investigation of new technologies to improve light collection from scintillating crystals for fast timing

Von der Fakultät für Mathematik, Informatik und Naturwissenschaften der RWTH Aachen University zur Erlangung des akademischen Grades einer Doktorin der Naturwissenschaften genehmigte Dissertation

vorgelegt von

*Rosalinde Hendrika Pots, MSc.*

aus

*Zeist, Niederlande*



Berichter*:*

Univ.-Prof. Dr. Dr. h.c. Nadim Jon Shah

Univ.-Prof. Dr. rer. nat. Achim Stahl

Prof. Dr. rer. nat. Karl Ziemons

Tag der mündlichen Prüfung*:* 22.04.2022

*In memory of my father*

*“ God, give us the grace to accept with serenity the things*
*that cannot be changed, courage to change the things*
*that should be changed, and the wisdom to distinguish*
*the one from the other.*

*Living one day at a time.*
*Enjoying one day at a time;*
*Accepting hardship as a*
*pathway to peace ”*

- Reinhold Niebuhr -

# Abstract

Inorganic scintillating crystals have been very successful in a variety of applications, such as high energy physics, medical physics, home land security and others. Next to the energy information these detectors deliver, also their potential to achieve precise timing information has become of increasing importance. Already today, recent developments in time-of-flight detectors based on scintillating crystals have reached coincidence time resolutions as high as ∼100 ps FWHM for 20 mm long crystals. The goal of this thesis is to pave the road towards the 10 ps regime, to make high energy physics cope with the future extreme luminosity and ultrashort bunch crossing intervals (as low as 500 ps) at the next generation of colliding beam accelerators. It may also serve to make medical physics benefit from simpler reconstruction algorithms, leading to higher image resolution and shorter imaging time in, e.g., PET. To reach this ambitious goal, an interdisciplinary approach in the domain of photodetection in general is needed. Therefore, this work must go hand in hand with advancements in the fields of scintillators, photodetectors and ultrafast electronics. Among these, this thesis focuses on the fields of scintillators and light transport.

One aspect investigated in this thesis, is light transport inside- and light extraction from the crystal, based on the knowledge of the photon propagation modes in the crystal. Owing to the fact that scintillation light is emitted isotropically, the high refractive index of the crystal makes light rays undergo multiple reflections at the crystal surfaces, preventing an efficient and fast light extraction. To overcome the time spread generated by this effect, which ultimately limits the time resolution, photonic crystals slabs applied at the scintillator readout face might be a promising method to improve light extraction at the crystal-photodetector interface.

The work in this thesis starts with with a study on improving imaging quality of an existing, breast-dedicated, scanner by introducing photonic crystals on the readout surfaces of the existing large monolithic LYSO crystals, of order 50x50 $mm^2$, already in use in the device. For that purpose, the author, in collaboration with partners of the TurboPET project, developed production methods for photonic crystals that were then applied and tested on the large LYSO crystals for the purpose of selecting the best method for a new prototype of this PET scanner. The best results were obtained with a sol-gel lithography process, that has produced a pattern of $TiO_2$ cones (RI=2.4) with a 1.17 times increase in light output and a 1.3 times increase in energy resolution (at the single-crystal level). In total 10 such large crystals were produced with this pattern, which then led to an average increase in light output by a factor of 1.16 and an average improvement in energy resolution by a factor of 1.3. Following their implementation in the existing PET scanner, phantom tests were run to evaluate the overall performance of the device. These tests showed that the modified PET scanner benefited from an increase in signal-to-noise ratio of only ∼6%, nonetheless a promising result taken the fact that this was a first attempt of improving an existing PET scanner.

The second part of the thesis entailed a dedicated investigation of photonic crystals, applied to smaller crystals, to search for an improvement in light output and in addition an improvement in the timing behavior in terms of coincidence time resolution (CTR). The focal point was a comparison between two photonic patterns, one with $TiO_2$ pillars (RI=2.4) and the other with polymer cones (RI=1.82), both in a square lattice and imprinted on 10 mm LYSO cubes. It turns out from this comparison that the polymer cone pattern is superior in both light output (x1.7 over unpatterned) and CTR (x1.5 over unpatterned) than the $TiO_2$ pillar pattern (x1.5 and 1.2, respectively).

Additional tests addressed the question how the classical methods of improving light output, i.e. wrapping and optical coupling of the crystals, would compare to the results obtained with the results derived from photonic patterning.

The third subject investigated in this thesis is related to exploring intrinsically fast scintillation mechanisms. The reason for this is that the determining factor for the time resolution of a scintillator is the initial photon density upon gamma conversion in the crystal. To first approximation, this initial photon density is given by the light output of the crystal divided by its decay time. As such, a high light output and a short decay time are crucial ingredients for fast timing. To break the CTR bench mark of 58 ps FWHM, obtained with *classical*, 3 mm long, LSO:Ce:0.4%Ca crystals, $BaF_2$ was chosen as a promising candidate owing to its sub-nanosecond scintillation process due to cross-luminescence in this crystal.

A true challenge coming from using cross-luminescence stems from the very short emission wavelengths, usually in the deep UV, like e.g. 210 nm and 195 nm in $BaF_2$. This imposes significant constraints on the use of photodetectors, as well as optical coupling agents and reflective wrapping materials, to cope with this short wavelength region. This limits the choice of fast UV-sensitive SiPMs, and in the long run only two producers were found to manufacture adequate SiPMs, i.e. Fondazione Bruno Kessler (FBK) and Hamamatsu, albeit with still relatively low photon detection efficiencies of around 20%. Comparing the two different producers it was found that, while both deliver adequate results, FBK clearly outperforms the Hamamatsu devices.

As to the $BaF_2$ crystals themselves, two different producers for their manufacture were chosen: Epic and Proteus. Among the two tested candidates, Epic and Proteus, the Epic crystal delivered consistently better results owing to its higher transparency at the cross-luminescence wavelengths.

In first instance, the CTR measurements were made with air-coupling only. As such, from the arguments above an Epic crystal in conjunction with a Hamamatsu device delivered a CTR of 98±5 ps FWHM. In the case of coupling the same crystal to an FBK device, a clearly superior CTR of 54±6 ps FWHM was reached.

Further to this, different optical coupling agents were tested in an attempt to see if the already very promising air-coupling results could still be improved. After initial selection tests, only glycerine and Viscasil remained as promising candidates for an eventual improvement in the CTR. While the behaviour of the two coupling agents, in particular glycerine, in terms of their potential improvement in CTR, is still debatable, the best result obtained with $BaF_2$ coupled to a FBK SiPM with glycerine sets a new record in CTR of 51±6 ps FWHM, despite the FBK's significantly inferior photon detection efficiency in the deep UV.

This thesis has shown that exploiting cross-luminescence in crystals like $BaF_2$ is a promising road to further research in the domain of ultra-high time resolution with photons.

# Abstrakt

Anorganische Kristallen finden Gebrauch als Szintillatoren in zahlreichen Gebieten wie z.B. in der Hochenergiephysik, im medizinischen Physik, sowie im alltäglichen Heimatschutz. Im Allgemeinen bauen diese Anwendungen auf die Energieinformation, die diese Detektoren beim Durchgang von geladenen Teilchen oder der Absorption von hochenergetischen Photonen, i.e. X-Rays und Gammas, in Form von Licht abgeben. Zunehmend gewinnt auch ihre Eigenschaft, zusätzlich zur Energie ebenso präzise Zeitinformationen der registrierten Ereignisse zu liefern, an Bedeutung. Eine bedeutende Rolle spielt dabei die Zeitauflösung coinzidenter Ereignisse (coincident time resolution) auch CTR genannt, die in solchen Kristallen von z.B. 20 mm Länge annähernd 100 ps FWHM (Halbwertsbreite) erreichen kann.
Ziel dieser Arbeit ist es, mit Fotodetektoren neue Wege in der Flugzeitmessung von hochenergetischen Teilchen und Lichtquanten zu betreten, um CTR-Auflösungen bis hinab zu 10 ps FWHM zu erreichen. Auflösungen dieser Größenordnung sind von größter Bedeutung für die Teilchenphysik an Beschleunigern der nächsten Generation ausgerüstet mit extremen Strahlintensitäten und ultra-kurzen Paket-Intervallen ($\leq$ 500 ps). Auch die Bildrekonstruktion in der Nuklearmedizin, insbesondere PET, profitiert von höchsten Zeitauflösungen, die dann durch Verwendung einfacherer Algorithmen schnellere und zugleich höherwertige (zuverlässigere) Diagnosen ermöglichen.
Ein solch ehrgeiziges Ziel ist nur mit einer interdisziplinären Vorgehensweise in der Photon Messung allgemein zu erreichen. Daher geht diese Arbeit Hand in Hand mit grundlegenden, neuen Entwicklungen im Bereich von Szintillatoren, Fotodetektoren, und superschneller Elektronik einher. Der Fokus dieser Doktorarbeit liegt dabei auf der Forschung an Szintillatoren und deren Lichttransport zum Fotodetektor.
Ein weiterer wichtiger Aspekt dieser Forschungsarbeit ist, unter Berücksichtigung der spezifischen Photonen-Ausbreitungsmoden im Kristall, den Lichttransports im Kristall und die Lichtextraktion vom Kristall zum Fotodetektor zu optimisieren. Unter der Vorgabe, dass Szintillationslicht isotropisch emittiert wird, bewirkt der hohe Brechungsindex (B.I.) des Kristalls Mehrfachreflexionen der Photonen an den Kristallwänden und unterbindet damit eine effiziente und schnelle Lichtentnahme vom Szintillator. Dieser Effekt verursacht eine Zeitverschmierung (time spread) des Signals, die damit auch letzten Endes die Zeitauflösung des Systems (bestimmt) limitiert. Eine vielversprechende Methode, diesen Effekt zu umgehen und die Lichtausbeute zu verstärken, sind sogenannte photonische Kristalle, die als Nanostrukturen auf der Lichtaustrittsseite des Kristalls aufgetragen werden.

Der erste Teil der Doktorarbeit befasst sich mit einer Studie zur Bildverbesserung eines existierenden Brust-PET-Scanners, durch die Auftragung einer photonischen Kristallschicht auf die vorhandenen monolithischen LYSO-Kristalle von 50x50 $mm^2$ Fläche. Die Aufgabe des Verfassers dieser Doktorarbeit bestand darin, in Kollaboration mit Partnern des TurboPET Projekts, neue Produktionsverfahren für photonische Kristalle zu entwickeln, um diese dann an den vorhandenen LYSO-Monolithen zu testen, mit dem Zweck

die besten herauszufiltern und, im Rahmen eines neuen PET-Prototyps, am existierenden PET-Scanner zu evaluieren. Beste Resultate wurden mit der "SolGel" Lithografie erzielt, bei der eine regelmäßige Struktur (Muster) aus TiO2-Kegeln (cones) mit B.I.=2.4 auf die Oberfläche der Originalkristalle aufgetragen wurde. Die Lichtausbeute verbesserte sich dadurch um 17%, und die Energieauflösung der einzelnen Kristalle um 30%. Nach der Fertigstellung zehn solcher Kristalle mit dieser Nanostruktur und Tests des Ensembles zeichnete sich im Durchschnitt eine Verbesserung des Lichtoutputs um 17% und der Energieauflösung um 30% ab. Nach der Implementierung der modifizierten Kristalle im Prototyp-Scanner wurden Testreihen mit Phantomen im Scanner unternommen, um den Benefiz dieser Methode unter realen Bedingungen zu demonstrieren. Es zeigte sich jedoch nur eine Verbesserung von 6% im Signal-zu-Untergrund Verhältnis (S/N), was für einen ersten Versuch am realen Apparat des TurboPET als durchaus positiv zu bewerten ist.

Der zweite Zeitabschnitt der Doktorarbeit beschäftigt sich mit einer dedizierten Studie der photonischen Kristallstrukturen, die im Gegensatz zu den Arbeiten an den oben beschriebenen monolithischen Szintillatoren hier auf kleinere Szintillatoren (10x10 $mm^2$) angebracht werden. Ziel dieser Studie war einerseits eine Verbesserung der Lichtausbeute und andererseits der Einfluss der Methode auf die Zeitauflösung der Detektoren mit Blick auf die Koinzidenz-Zeitauflösung (CTR). Im Vordergrund stand dabei ein Vergleich zwischen zwei konkurrierenden photonischen Kristallstrukturen: auf der einen Seite ein quadratisches Gitter aus TiO2-"Säulen" mit einem B.I. von 2.4, und auf der anderen ein ähnliches Muster jedoch aus polymeren "Kegeln" mit B.I.=1.82. Beide Schichten wurden auf 10 mm LYSO "Würfel" (Kubus) aufgetragen und das Ensemble auf Lichtoutput und CTR getestet. Dabei zeigte sich, dass die polymere Kegelstruktur in beiden Kategorien bessere Resultate als die Titan-Dioxyd Säulen lieferte: nämlich 70% vs. 50% mehr Lichtausbeute, und eine um 50% vs. 20% höhere Koinzidenz-Zeitauflösung (CTR); diese signifikanten Verbesserungen beziehen sich auf Werte, die am nackten Kristall, d.h. ohne photonische Schichten, vorab gemessen wurden.
Ein Seitenaspekt dieser Studie war, wie sich die bekannten "klassischen" Methoden zur Verbesserung der Lichtausbeute, d.h. die Verwendung von sogenannten "optischen Kopplungssubstanzen" (coupling greases) zwischen Kristall und Fotodetektor sowie die Umwicklung des Szintillators mit reflektierendem Material (wrapping), mit denen der photonischen Kristalle vergleichen würden.

Der dritte Teil dieser Arbeit beinhaltet eine Erkundung von inhärent schnellen Szintillations-Mechanismen, die von Natur aus sehr viel schneller sind als die herkömmliche Lichtemission. Dies resultiert aus der Tatsache, dass die intrinsische Zeitauflösung eines Kristalls von der initialen Photondichte, entstanden aus der Gammakonvertierung im Kristall, bestimmt wird. In erster Näherung lässt sich die Photondichte aus dem Lichtoutput des Kristalls, dividiert durch ihre Abfallszeit, herleiten. Das bedeutet, dass, zur Erreichung einer möglichst hohen Zeitauflösung, hoher Lichtoutput und kurze Licht-Abfallzeiten vom Kristall verlangt werden. Die gegenwärtige Referenzmarke in koinzidenter Zeitauflösung, gemessen mit "klassischen", 3 mm langen, LSO:Ce:0.4%Ca Kristallen liegt bei 58 ps FWHM. Um diese Marke übertreffen zu können, wurde $BaF_2$ als vielversprechender Kandidat ob seiner typischen "Cross"-Lumineszenz, die zu sub-nano-Sekunden-Szintillationsprozessen führt, gewählt.
Diese hat jedoch zum Nachteil, dass die Emissionswellenlängen im tief-ultravioletten Bereich liegen, d.h. in $BaF_2$ bei 195nm und 210nm. Das hat beträchtliche Einschränkungen bei der Wahl von geeigneten Fotodetektoren, optischen Koppelsubstanzen (greases), sowie

von Reflektoren (wrapping), zur Folge. Betroffen davon sind in erster Linie schnelle, UV-empfindliche Silizium-Fotodetektoren (SiPMs), unter denen nur zwei Hersteller adäquate Detektoren liefern konnten: Fondazione Bruno Kessler (FBK) und Hamamatsu, allerdings beide mit geringer Photonen-Nachweis-Effizienz (photon detection efficiency / PDE) von nur 20%. Im direkten Vergleich beider Hersteller zeigte sich jedoch eine deutlich höhere Leistungsfähigkeit der FBK SiPM Komponenten als bei Hamamatsu.
Bei der Wahl der $BaF_2$ Kristalle standen zwei Hersteller zur Verfügung: Epic und Proteus. Auch hier zeichnete sich im direkten Vergleich beider Hersteller ein klarer Vorteil zugunsten eines von ihnen ab, d.h. hier von Epic, deren Kristall durchgehend bessere Resultate lieferte als der Proteus-Kristall. Erklärbar ist dieses Ergebnis durch die deutlich höhere Transparenz des Epic-Kristalls im Cross-Lumineszenz Wellenlängenbereich. So erreichte dieser Kristall in *direkter* Kopplung (in Luft) mit dem Hamamatsu SiPM eine Koinzidenz-Zeitauflösung (CTR) von 98±5 ps FWHM. Im Verbund mit dem FBK-SiPM erzielte der Epic-Kristall sogar eine CTR von 54±6 ps FWHM.
Obwohl schon mit dieser Konfiguration (=Luftkopplung) beste Resultate erreicht wurden, wurde die Testreihe mit verschiedenen Kopplungssubstanzen fortgesetzt, um eventuell noch höhere Zeitauflösungen mit $BaF_2$ zu entdecken. Von den verschiedenen Kopplungssubstanzen, die vorab auf Transparenz im UV-Bereich getestet wurden, blieben nur Glyzerin und Viscasil als mögliche Probanden übrig. Während die Verwendung von Glyzerin, insbesondere dessen Einfluss auf die CTR, nicht schlüssig ist, brach die Kombination aus Viscasil-Kopplung von BaF2 mit dem FBK SiPM die alte "konventionelle" CTR-Richtgröße von 58 ps und erzielte einen neuen Rekord in KoinzidenzZeitauflösung von 51±6 ps FWHM. Dieses Resultat ist umso spektakulärer angesichts einer PhotonNachweis-Effizienz (PDE) des SiPM im DUV von nur ∼20%.
Diese Arbeit demonstriert, dass die Exploration anderer, superschneller Szintillationsmechanismen, wie der Cross-Lumineszenz in $BaF_2$, ein vielversprechender Weg zu ultraschnellen und höchst-zeitauflösenden Anwendungen ist.

# Acknowledgements

During my PhD I have met so many amazing, intelligent and kind people that have helped me with my work or with whom I simply had a really good time, or both. I have also received a lot of support from friends that I had already met before beginning this special adventure and of course from my family. It is probably impossible to acknowledge everyone who has helped me over the last four years or made in some way a positive contribution to my happiness and well-being. Still I will make an attempt, knowing that I will most definitely forget to mention some incredible individuals.
I first of all want to thank my supervisors of the RWTH Aachen, Prof. Jon Shah and Prof. Achim Stahl, for supporting my research and coming to my help when it was needed. I also am indebted to my supervisor from the FH Aachen, Prof. Karl Ziemons, who believed in me and supported me from the very beginning until the very end of my doctoral thesis. I am also very much thankful to Etiennette Auffray. Not only was she my supervisor at CERN, she was the one who originally invited me to apply to the CERN doctoral program after having finished an internship of a year in her group and she introduced me to Prof. Karl Ziemons. I also want to thank the people that have made it possible for me to follow my path towards this position at CERN. Ugo Amaldi probably does not know that he played a key role in this story. During my original stay at CERN as a summer student, I asked him whether he had a 1-year project for me to do an intern on detector R&D in medical applications, for my master thesis at the time. He could not offer me one, but brought me into contact with Paul Lecoq. That brings me to thanking Paul Lecoq, for originally bringing me into the group to work on the European TurboPET project, his input in my research work, but also for the many interesting and inspiring discussions we had, also about research that he was not involved in himself.
I want to thank everyone from the Crystal Clear Group at CERN, current and former members, for all their support and for the good times we had, during work as well as outside. I would like to thank a few people in particular. First of all, I want to thank Stefan Gundacker, who has taught me everything I know about coincidence time resolution (CTR) and silicon photomultipliers (SiPMs). Stefan is one of the brightest scientists I have ever met and has helped me throughout my thesis. Specifically, he has taught me how to perform CTR measurements and without him probably none of the measurements in this thesis would have been possible. He is the person who designed the readout electronics for timing measurements and who established contact with the Fundazione Bruno Keller (FBK), as such making it possible to use their devices. He is also the person who made me interested into researching $BaF_2$, he helped with the measurements whenever needed and taught me how to perform the time correlated single photon counting measurements. Apart from his immense support at work we have also enjoyed many good moments outside of work, often together with our colleague Rosana Martínez Turtos, who has also been a great support during work, as well as a very good friend throughout the major part of my thesis. I would also like to specifically thank Matteo Salomoni, with whom I worked together during research activities on photonic crystals. Matteo and I shared the workload from the TurboPET project, part of which is presented in chapter

5. He furthermore provided the Geant4 simulations needed as input for my simulations of photonic crystals, he also made some specific simulations (from section 6.2.2) and light output measurements (section 6.2.4.1 and table 6.8). I am also very thankful to Thomas Meyer, who was always ready to help me whenever I needed it and helped me enormously with editing and rewriting the text of my first-author articles and especially this thesis. Furthermore, I want to specifically thank him for translating the abstract of this thesis into German. I want to thank the people from FBK for providing their SiPMs for the $BaF_2$ measurements and also about the interesting conversations on measuring deep UV light. I would furthermore like to thank Dominique Deyrail, who has performed a lot of work for me as our group's technician and always had time for a nice conversation. Dominique, merci pour tout ton support technique durant ma thèse, ainsi que pour ton amitié. I want to thank Nicolaus Kratochwil for his company during the many discussions and drinks, and for your support during the last year of my thesis. I also want to thank Loris Martinazzoli for the nice times together while sharing an office. I furthermore want to thank everyone that I have met during my work visits to Prague, to Valencia and to the conferences I have been, for all the interesting conversations and the nice time together. I want to make a special mention to the personnel of CERN that helps us perform our job in a proper way on a daily basis, especially the people that make sure that the offices and toilets in our building were always cleaned and the different people that worked in the cafeteria of building 13, where we always had our coffee breaks, and in restaurants R1 and R2.
This brings me to my friends and family, who I want to thank for supporting me throughout my PhD. I first want to specifically thank my boyfriend, Victor Batista Tiburcio, who has been there for me, supporting me and believing in me, almost from the very moment that we met. Victor, tu m'as toujours supporté et t'étais toujours là pour moi quand j'avais besoin du support. Tu m'as soigné pendant un période où j'avais des problemes de la santé, mais tu m'as surtout donné des supper belles moments. I also want to thank his daughter, Ayanna, for not making me forget that life continues even when I was having the feeling that my PhD was breaking me up. Chère Ayanna, tu m'as appris que la vie continue toujours, aussi quand on est dans une période difficile. Je te remercie pour cette leçon de vie. I also want to thank my mother, Franca Haas, and my sister, Jacintha Pots, for their support and many calls when I needed advice or blow off steam. I very much want to thank Alba Zuidema and Aletta van der Wal, who are very dear friends to me since a long time and did not fail to continue to be so during this exciting but challenging adventure and living 1000 km apart, especially for their uninterrupted support and many good times together. I also want to thank Maria Bader, who already was a good friend to me during my master studies in Utrecht, but during our PhDs our friendship has grown closer and especially towards the end she has been a real anchor. I want to thank Rebecca Muller, Natalie Au-Yeung and Kalliopi Lazari for being great friends to me and for all the nice moments we have shared together. I also want to thank Tim Mulder and Edwar de la Cruz Alejandro for their friendship and the nice outdoor activities.
I would like to also make a special mention to my father, who passed away in 2013 and to whom I dedicated this thesis. While I for sure had many inspirations in my life and reasons to follow my path into physics the way I did, my father is beyond any doubt among them. It is painful for me that my father could not be here to see me accomplish such a milestone in my scientific education and career. I know that he would have been so proud, mainly because he was *always* proud of both me and my sister! As long as we would follow our own paths, no matter what they would be. I want to thank my father for everything that he brought to my life, he helped shaping me during his life and beyond.

# Contents

# Chapter 1

# Preface

Inorganic scintillating crystals have been very successful in a variety of applications, such as high energy physics, medical physics, home land security and others. Next to the energy information these detectors deliver, also their potential to achieve precise timing information has become of increasing importance. Already today, recent developments in time-of-flight detectors based on scintillating crystals have reached coincidence time resolutions as low as ∼100 ps FWHM for 20 mm long crystals. The goal of this thesis is to pave the road towards the 10 ps regime, to make high energy physics cope with the future extreme luminosities and ultrashort bunch crossing intervals (as low as 500 ps) at the next generation of colliding beam accelerators, and to make medical physics benefit from simpler reconstruction algorithms, leading to higher image resolution and shorter imaging time in, e.g., PET. Also, very high timing precision has the additional potential of hadron therapy benefiting from fast online monitoring of the dose delivered by fast reconstruction of spontaneous $\beta^+$ emitting isotopes produced by target spallation during particle therapy. To reach this ultimate goal, an interdisciplinary approach in the domain of photodetection in general is needed. Therefore, this work must go hand in hand with advancements in the fields of scintillators, photodetectors and ultrafast electronics. Among these, this thesis focuses on the field of scintillators and light transport.

A determining factor for the time resolution of a scintillator is the initial photon density upon gamma conversion in the crystal. In first approximation, this initial photon density is given by the light output of the crystal divided by its decay time. As such, a high light output and a short decay time are key requirements for fast timing. However, even evaluating the timing potential with short (3 mm) crystals of a relatively fast and bright scintillator such as LSO:Ce co-doped with 0.4% calcium (light yield of 32 kph/MeV, decay time of ∼28 ns), using the best photodetectors and fastest readout electronics, leads to a coincidence time resolution of 58 ps FWHM. In order to break this timing record and make a significant step towards 10 ps, different, sub-nanosecond, scintillation processes need to be investigated, such as quantum confinement as observed in quantum dots and nanoparticles and the exploitation of cross-luminescence in suitable scintillators, e.g. $BaF_2$. Also Cherenkov radiation, i.e. prompt photons generated by particles traveling faster than the speed of light in the medium of the crystal bulk, would be an option for the investigation of ultrafast timing. This work focuses on the phenomenon of cross-luminescence in $BaF_2$, potentially leading to a break through towards the 10 ps time time domain.

Another important aspect, investigated in this thesis, is light transport inside- and light extraction from the crystal, based on the knowledge of the photon propagation modes in the crystal. Owing to the fact that scintillation light is emitted isotropically, the high refractive index of the crystal makes light rays undergo multiple reflections in the crystal,

preventing an efficient light extraction. To overcome the time spread generated by this effect, which ultimately limits the time resolution, photonic crystal slabs applied at the scintillator readout face could be a suitable method to improve the light extraction at the crystal-photodetector interface. Photonic crystals are nano-structures that enable the matching of light propagation modes inside the crystal to those outside. More standard methods to improve light extraction, like coupling greases, are also investigated in this context.

# Chapter 2

# Inorganic scintillators for gamma detection

Scintillators are materials that absorb the energy of ionizing radiation and transfer this energy into an amount of light proportional to this energy [1]. While there are several types of scintillators, this thesis restricts itself to inorganic scintillators, also called scintillating crystals.

Several steps are involved in the detection of ionizing radiation, from the moment that radiation traverses a scintillating crystal up to the moment that the produced scintillation photons are detected by a photodetector:

1. **Ionizing radiation deposits energy in the scintillator**: this occurs via specific different physical interactions with the inorganic crystal.
2. **Creation and thermalization of electron-hole pairs.**
3. **Recombination of electron-hole pairs**, leading to the emission of scintillation light inside the crystal.
4. **Transportation of the scintillation light to the photodetector.**
5. **Production of a signal by a photodetector** upon detection of the scintillation light.

This chapter gives a comprehensive overview of the important aspects involved in the different steps. It also shortly describes some applications for which scintillators are used, like e.g. positron emission tomography (PET) and gamma- and particle detection in high energy physics (HEP).

## 2.1 Interaction of photons with inorganic scintillators

While inorganic scintillators are often used for the detection of photons, electrons (and positrons) and, depending on the scintillator material, neutrons, this work only focuses on the detection of photons. Note, photons in this work is the general term used for visible photons, X-rays and gamma-rays. The interactions of X- and gamma-rays in scintillators are described in the following section and follow the explanation from [2]. For the interaction of particles with scintillating crystals, the reader is referred to [2], [3] and [4].

As written above, the first step of radiation detection with scintillators is the loss of energy in the scintillator material. This energy loss is caused by the photons interacting with the electrons of the scintillating crystal. How well the photons interact with these electrons is described by the cross section of their interaction $\sigma_e$. The photon can interact in four different ways with the material, i.e. photoelectric effect, Compton scattering, pair production and Rayleigh scattering. Since the latter of the four is an elastic scattering process where the incoming photon merely changes direction and does not lose any of its energy to the material [5], it will not be further discussed in this thesis. Therefore, $\sigma_e$ can be written as follows:

$$\sigma_e = \sigma_{ph} + \sigma_{compt} + \sigma_{pair} \tag{2.1}$$

### 2.1.1 Photoelectric effect

Described as the photoelectric effect, an incoming photon is completely absorbed by a bound electron, consequently liberating it from its shell and ionizing the atom. After the electron's ejection, the energy $E_e$ of this so-called photoelectron is given by:

$$E_e = E_\gamma - E_b \tag{2.2}$$

where $E_\gamma$ is the energy of the photon and $E_b$ the original binding energy of the electron in the atom, usually several tens of keVs. Therefore, the energy of the electron freed by the photoelectric effect is directly related to the energy of the original photon. After its liberation, it is quickly replaced by reconfiguration of the electron cloud of the atom via emission of X-rays or Auger electrons [4]. Thereafter the freed electron loses its energy by ionizing the surrounding scintillating material for as long as its energy is above the ionization threshold.
The cross section $\sigma_{ph}$ increases with effective atomic number $Z_{eff}$ of the scintillator material, but decreases with the energy of the photon:

$$\sigma_{ph} \propto \frac{Z_{eff}^5}{E_\gamma^{7/2}} \tag{2.3}$$

### 2.1.2 Compton scattering

Compton scattering is inelastic scattering of a photon with a nearly "free" electron from an atom in the scintillating material. As such, the photon transfers part of its energy to the electron, while being scattered over an angle $\theta$. The photon energy after scattering $E'_\gamma$ is determined by conservation of energy and momentum. As such, it depends on its original energy $E_\gamma$ and its scattered angle:

$$E'_\gamma = \frac{E_\gamma}{1 + \frac{E_\gamma}{m_0 c^2}(1 - cos\theta)} \tag{2.4}$$

where $m_0$ is the rest mass of the electron and $c$ the speed of light. The hit electron, on the other hand, has received an energy of $E_e = E_\gamma - E'_\gamma$, which it will lose by ionizing the scintillating material until its energy also falls below the ionization threshold.
The scattered photon can also lose its remaining energy by interacting again for instance via the photoelectric effect, therefore losing in total all its energy to the scintillator. It may, however, also escape the scintillator, as such its remaining energy is not deposited in the scintillating material. Therefore, the total amount of energy deposited into the scintillator due to Compton scattering can range from practically 0 to the maximum

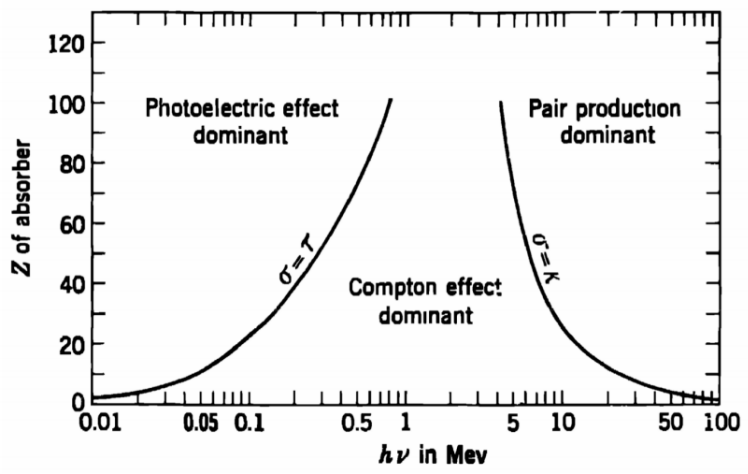


Figure 2.1: Relative importance of the three major types of $\gamma$-ray interaction. The continuous lines $\sigma = \tau$ and $\sigma = \kappa$ denote the boundaries between two adjacent zones, along these lines the neighboring effects are equally dominant. [6]

energy (at $\theta \approx 180°$) depending on $E_\gamma$. As a result, Compton scattering shows up in an energy spectrum over a range of energies, all the way up to the so-called Compton edge, where the maximum energy is transferred.
The cross section of a photon to interact with one of the electrons in the scintillator is:

$$\sigma_{compt} \propto \frac{Z_{eff}}{E_\gamma} \tag{2.5}$$

meaning that the interaction probability increases with atomic number of the scintillating material, however less pronounced as that of the photoelectric effect, see equation 2.3. On the other hand, its dependence on the photon energy is significantly less than that of the interaction through photoelectric effect.

### 2.1.3 Pair production

When the $\gamma$-particle has an energy of at least $2m_0c^2 = 1.02$ MeV, it has sufficient energy to create an electron-positron pair; this process is called pair production. Since it is not possible to fulfill both conservation of energy *and* conservation of momentum *in free space*, pair-production can only take place in the presence of an external field. While the process is possible both in the Coulomb field of the nuclei and the electron fields of the atoms of the scintillating material, the pair production in the electron fields only starts at $E_\gamma > 4m_0c^2$ and is approximately a thousand times weaker than pair production in the nuclear field. Therefore, the process is dominated by pair production in the nuclear fields.
The cross section of pair production is given by the following expression:

$$\sigma_{pair} \propto Z_{eff}^2 \; ln\,(2E_\gamma) \tag{2.6}$$

It increases rapidly with the square of the effective atomic number, but rather moderately with increasing photon energy.
For applications in medical imaging, such as PET, SPECT and gamma cameras, the energy of the detected photons is far below 1.02 MeV, usually around 511 keV (in the case of PET) or lower. Therefore, in this domain pair productions does not play a role in the energy loss mechanisms in the scintillator.

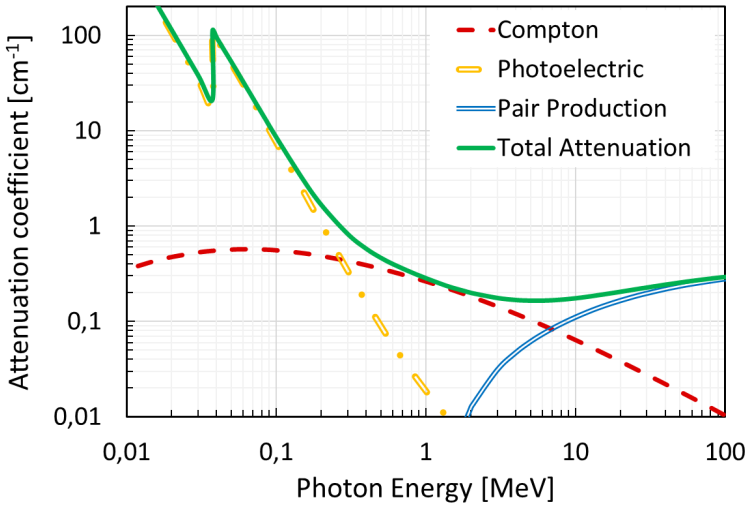


Figure 2.2: Attenuation coefficient of $BaF_2$ for different photon energies (green) and contributions of photoelectric effect (yellow), Compton scattering (red) and pair production (blue). Data from [7], using 4.89 $g/cm^3$ as $BaF_2$ density.

### 2.1.4 Interaction domains and attenuation in the scintillator

When $\gamma$-radiation with an initial intensity $I_0$ is traversing a scintillator, it loses intensity following an exponential distribution:

$$I(x) = I_0 \; exp(-\mu x) \tag{2.7}$$

where $I(x)$ is the intensity of the radiation after traversing a distance $x$ in the scintillator with a material-specific attenuation coefficient $\mu$. Therefore, this attenuation coefficient determines how fast the material absorbs the $\gamma$-radiation and hence plays an important role as to the sensitivity of the final detector in which it is used. It is linked to the cross section $\sigma_e$ as follows:

$$\mu = \frac{n_e \sigma_e}{Z_{eff}} \tag{2.8}$$

where $n_e$ is the electron density of the material. While $\mu$ depends on the *total* gamma-electron interaction cross section in the material, the contribution of the photoelectric effect to this cross section plays an important role, for it carries directly the original photon energy information. This property is particularly important in e.g. PET imaging, where only photopeak events are selected for image reconstruction. This property is represented by the photofraction dependent on the scintillator material, i.e. $\sigma_{ph}/(\sigma_{ph}+\sigma_{compton}+\sigma_{pair})$ (note $\sigma_{pair}$ in most cases can be neglected since the incoming gamma energy is far below the pair production threshold). Figure 2.1 illustrates the three interaction domains, i.e. photoelectric, Compton and pair production, as a function of $Z_{eff}$ and the gamma-ray energy. Figure 2.2 shows the attenuation coefficient as a function of energy for the three different interaction types, with the example of $BaF_2$ having a density of 4.89 g/cm$^3$. The cross section of gammas interacting through the photoelectric effect always peaks around energies comparable to the binding energy of an electron on its atomic shell [4]. This manifests itself as a peak in the corresponding attenuation plot of figure 2.2 (yellow line), which in the case of barium corresponds to a K-shell electron of 37 keV.

The attenuation length corresponding to equation 2.8 is given by $L = 1/\mu$. In the case of $BaF_2$ and gammas with an energy of 511 keV, as is common e.g. in PET applications,

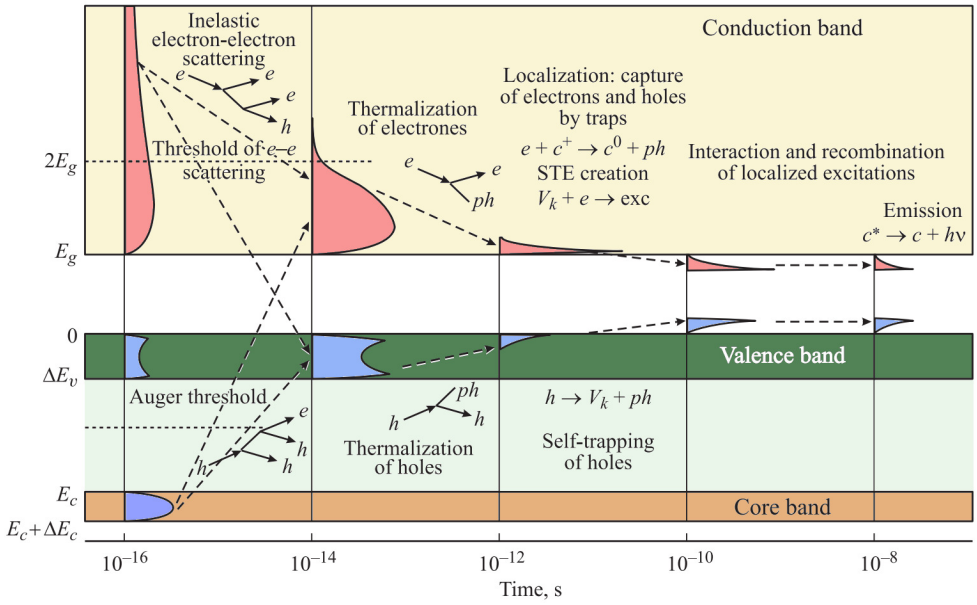


Figure 2.3: Relaxation and thermalization of electrons and holes in a crystal. Modified from [9]

this leads to an attenuation length of:

$$L = \frac{1}{\mu} \approx \frac{1}{0.467\ cm^{-1}} \approx 2.14\ cm \tag{2.9}$$

where the value for $\mu$ has been taken from figure 2.2. In the case of LSO, a heavier and commonly used scintillator, this attenuation length is intrinsically smaller, i.e. ∼1.18 cm [8].

## 2.2 Scintillation mechanism: creation and recombination of electron-hole pairs

In the previous section, the different interactions of $\gamma$-particles with the scintillator material were explained. Following these interactions, atoms in the material are ionized, i.e. electrons are freed from their bound state. These electrons are generally called “hot” electrons as they still have substantial kinetic energy. They generally lose their energy by creating electron-hole pairs in the material, a process called “cool down”. Since this leaves the electrons in an excited state, the electrons and holes will eventually recombine and a fraction of it thereby produces the scintillation light.
These two steps, creation and thermalization, and recombination of electron-hole pairs leading to the emission of scintillation light, will be explained in detail in this section, based on theoretical work in [2], [10] and [11].
The ability of scintillating crystals to produce light stems from the band-structure with only certain energy levels being allowed in the crystal. Due to its crystalline structure, the scintillator has a core band, a valence band and a conduction band, each with corresponding sub-bands. Between the conduction- and valence band there is a bandgap with energy $E_g$, the so-called forbidden gap. Recombination of an electron above and a hole below this bandgap can result in the emission of scintillation light. The previously mentioned hot electrons are created in the conduction band, the “holes” that they leave behind are

created in the core- and the valence band. Figure 2.3 gives a schematic overview of the scintillation process in a simple ionic crystal scintillator. The hot electrons in the scintillator first lose their energy inside the material by inelastic scattering with other electrons. As such, a new electron-hole pair is created at every scattering event, thus multiplying the amount of electric excitations in the scintillator. This process continues until the energy of the electrons falls below the threshold of inelastic electron-electron scattering, which is generally about twice to three times the bandgap energy, after which the electron cannot create new electron-hole pairs. The holes in the core band will move towards the valence band through, e.g., Auger processes, until the energy of the hole passes the Auger threshold.

In the next stage, both the electrons and holes thermalize via interactions with phonons (ph), being effectively lattice vibrations. The energy that they lose in this process does not contribute to the final production of scintillation light in the crystal and is in that sense lost. The thermalization process continues until the electrons and holes are at the bottom of the conduction band and the top of the valence band, respectively. Then, localization of electrons and holes takes place by interactions with defects and impurities in the crystal. As a result, electrons and holes are trapped by different types of traps or by self-trapping. An example is the creation of a self-trapped exciton that is formed by an electron in the conduction band and a hole in the valence band or a deep hole in the core band ($V_k$ center). Depending on the trap, the excitations can stay "trapped" for a relatively long time, i.e. of order hundreds of nanoseconds or even long, before recombination takes place. However, in the end the electrons and holes will recombine, either non-radiatively or radiatively. The latter leads to the emission of scintillation light of which the wavelength then corresponds to the bandgap of the crystal. Non-radiative recombination also occurs in the crystal and consequently leads to losses.

This simple scenario describes the scintillation process in an ionic crystal. However, there are two different important groups of scintillators, one that contains rare earths, such as LSO and LYSO being doped with Cerium, and the other that exhibits the so-called core-valence luminescence, such as $BaF_2$. The corresponding scintillation processes for the two cases are shown in appendix B.

In the first case, e.g., $Ce^{3+}$ ions present in LSO introduce an extra set of bands within the bandgap of the crystal: the 5d level just below the conduction band and the 4f level just above the valence band. The effect of cerium ions is twofold. First, they make it possible for the hot electrons not only to scatter with electrons of the crystal but also with electrons of the cerium until the energy of the electrons is below the corresponding scattering threshold. Since this threshold generally lies below the electron-electron scattering threshold, the multiplication process in these types of scintillators continues longer, to the extend that more excitations take place and more scintillation photons *can* be produced. A second effect is that the electrons and holes thermalize into the 5d and 4f bands, respectively, which facilitates their fast recombination.

In the case of cross-luminescence, the crystal has an energy difference between the top core band and the bottom of the valence band that is less than the forbidden bandgap. In this case, Auger processes in the core band are energetically forbidden for the holes. As such, core holes can relax towards the top of the core band instead and recombine with electrons from the valence band, leading to the emission of scintillation light called cross-luminescence. Since the valence band is full of electrons, holes easily localize near an electron. As such, cross-luminescence is a very fast, sub-nanosecond, scintillation process. One should note that every recombination of a core hole and valence electron leads to a new valence hole. This hole can again take part in the "normal" scintillation process

between the conduction- and valence band.

## 2.3 Characteristics of scintillating crystals

During the scintillation process, as discussed in the previous section, light is produced inside the crystal. This process determines its intrinsic light yield (LY), one of the fundamental characteristics of a scintillator, as well as the rise- and decay time of the light pulse. The produced scintillation light subsequently travels inside the crystal until it leaves the crystal or gets absorbed at some point. The amount of light that is transferred to the outside of the crystal via its readout face can then be detected by a photodetector with certain efficiency and time resolution. All processes involved from the moment that the scintillation light is produced until the return of a signal from the photodetector determine the overall light output (LO) and coincidence time resolution (CTR). This section explains light output of the crystal (subsection 2.3.1), its timing properties (subsection 2.3.2) and light transport in the crystal (subsection 2.3.3).

### 2.3.1 Light yield and energy resolution

The total amount of electron-hole pairs $N_{eh}$ that participate in the recombination process depends not only on the deposited energy, but also on the characteristics of scintillation material:

$$N_{eh} = \frac{E_{dep}}{E_{eh}} = \frac{E_{dep}}{\beta E_g} \tag{2.10}$$

where $E_{dep}$ is the energy deposited in the crystal, $E_{eh}$ denotes the average energy to produce an electron-hole pair in the material and $E_g$ is the bandgap of the material. The factor $\beta$ in the equation is typically between 1 and 4 for most cases, but can also be much larger for specific cases, e.g., for cross-luminescence. The intrinsic light yield (LY) is a material property that determines the amount of photons produced $N_{ph}$ when a certain amount of energy $E_{dep}$ is deposited in the crystal and is only limited by the scintillation efficiency $\eta_{scint}$ of the material:

$$LY = N_{ph} = N_{eh} \cdot S \cdot Q = \frac{E_{dep}}{\beta E_g}\ S \cdot Q = \eta_{scint} \frac{E_{dep}}{E_g} \tag{2.11}$$

where $S$ is the transfer efficiency of the electron-hole pairs to the recombination point and $Q$ the luminescence quantum yield [11]. $S$ and $Q$ are generally assumed to be close to 1, making $\beta$ the most determining factor in the scintillation balance [11]; this includes all the losses discussed in section 2.2. The scintillation efficiency of a relatively bright scintillator, like LSO, for which the emission wavelength is 420 nm (corresponding to 2.95 eV) and the LY is $\sim 40,000$ph/MeV, can be calculated easily from equation 2.11:

$$\eta_{scint} = \frac{LY\ E_g}{E_{dep}} = \frac{40 \cdot 10^3 \times 2.95\ eV}{10^6\ eV} = 11.7\% \tag{2.12}$$

Therefore, even in one of the brighter crystals, only $\sim 12\%$ of the deposited energy in the scintillator is actually converted into light. Still, the net amount of photons that is extracted from the scintillator, i.e. the light output LO, is lower:

$$LO = LTE \times LY \tag{2.13}$$

where the LTE is the light transfer efficiency, being further explained in section 2.3.3.
As outlined in section 2.1, only the electron-hole pairs created through the photoelectric

effect carry the information of the energy of the original particle. As such, the resulting photopeak, see section 3.2, is to be used for the determination of the energy of that particle. While the energy deposited in the crystal through the photoelectric effect should be delta-shaped, i.e. at the original energy of the incoming photon, the produced scintillation light signal is broadened by several processes, resulting in a peak with a (almost) Gaussian shape. The full width at half maximum (FWHM) of the peak is the energy resolution $E_{res}$ of the system. The system's energy resolution is the quadratic sum of the individual contributions [12]:

- from non-proportionality between deposited energy and number of produced visible photons in the crystal ($E_{non-prop}$);
- from light transport effects owing to e.g. inhomogeneities inside the crystal and crystal surface imperfections ($E_{transport}$);
- from photoelectron statistics ($E_{stat}$);
- from noise in the photodetector ($E_{det}$);

In other words:

$$E_{res}^2 = E_{non-prop}^2 + E_{transport}^2 + E_{stat}^2 + E_{det}^2 \tag{2.14}$$

$E_{non-prop}$ and $E_{transport}$ are often taken together as the intrinsic energy resolution of the crystal $E_{intr}$. It should be noted that $E_{non-prop}$ can give a non-Gaussian broadening, as it can induce a tail on the left side of the photopeak due to a lower light production in some crystals when the photopeak event was cause by one or multiple Compton events, depositing a lower energy each, before full absorption of the gamma-particle [13] [14]. The statistical component takes only into account the statistics of the measured photoelectrons and as such follows Poisson statistics [13]:

$$E_{stat} \propto \frac{1}{\sqrt{N_{phe}}} \tag{2.15}$$

with $N_{phe}$ the number of photoelectrons created in the detector, assuming a perfect detector. The energy resolution is an important characteristic in e.g. PET detectors, as explained in section 2.6.1.

### 2.3.2 Timing properties

The intrinsic timing properties of the scintillator are of great importance as they effectively limit the overall time resolution of the final detector. The dominant intrinsic characteristics of scintillating crystals are the rise time ($\tau_r$) and the decay time ($\tau_d$) of the light production inside the crystal, also called kinematics of the scintillator. The rise time is determined by the thermalization and localization of the electron-hole pairs (see figure 2.3) and is typically small (order of tens of picoseconds) [8]. The decay time(s), on the other hand, describes the recombination process from the luminescent centers [8], and is of the order of tens to hundreds of nanoseconds, if not longer. If, in general, one assumes only one rise time and several $N$ decay times $\tau_{d,i}$ , the total pulse shape is described by a sum of exponential functions in the following way [15]:

$$f(t) = \sum_{i=1}^{N} \frac{A_i}{\tau_{d,i} - \tau_r} \left( exp\left(\frac{\Theta - t}{\tau_{d,i}}\right) - exp\left(\frac{\Theta - t}{\tau_r}\right)\right) \tag{2.16}$$

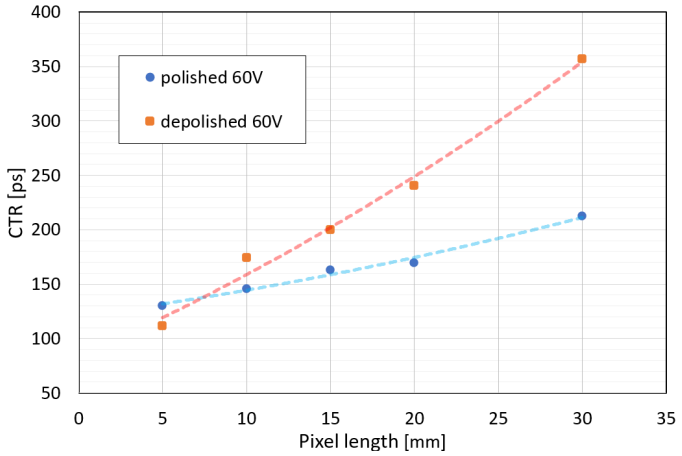


Figure 2.4: CTR measured of both polished and a depolished (all sides accept for the readout surface) crystals of different lengths, with a readout surface of 3.1x3.1 $mm^2$.

with $A_i$ the amount of photons emitted during the scintillation process with decay time $\tau_{d,i}$. $\Theta$ is the origin of the gamma conversion.

The rise- and decay time also contribute to the coincident time resolution (CTR), a measurable quantity that is one of the most important features of scintillating crystals when used in time-of-flight applications. A third contribution to this CTR [16] is the *amount* of scintillation photons i.e. the light output (LO):

$$CTR \propto \sqrt{\frac{\tau_d \ \tau_r}{LO}} \tag{2.17}$$

In case of multiple decay times that are of the same order of magnitude, $\tau_d$ in equation 2.17 is the *effective* decay time. However, in case of large differences between decay times, the shorter ones dominate since the photon density at the beginning of the scintillation pulse is determinant for the CTR. The CTR is furthermore dependent on the light transport in the crystal, for it contributes to the light travel time spread in the crystal. As such, it introduces an extra time-jitter which is shown in figure 2.4. A final contribution to the timing is given by the photodetector as discussed in section 2.4.2.

Apart from its contribution to the CTR, a short decay time is also an important requirement for detectors used in high-rate applications. To avoid pile-up effects inside the crystal, the total scintillation pulse must be sufficiently fast. Therefore, if there are multiple decay times of different orders of magnitudes, then also the larger ones become significant in those applications.

For further reading on timing properties of inorganic scintillators, the reader is referred to [8] and [15].

### 2.3.3 Light transport in the crystal

The scintillation light that is produced in the crystal is emitted isotropically. Even considering a perfect crystal, only part of the generated light will reach the readout surface of the crystal. This light can only be extracted if it is in the so-called *extraction cone*, as illustrated in the left hand part of figure 2.5. To facilitate the extraction of light usually an optical coupling between the readout surface and the photodetector is applied, such that it reduces the difference of the indices of refraction between the scintillator (high RI) and its ambient environment, e.g. air (low RI). The right-hand side of figure 2.5 shows

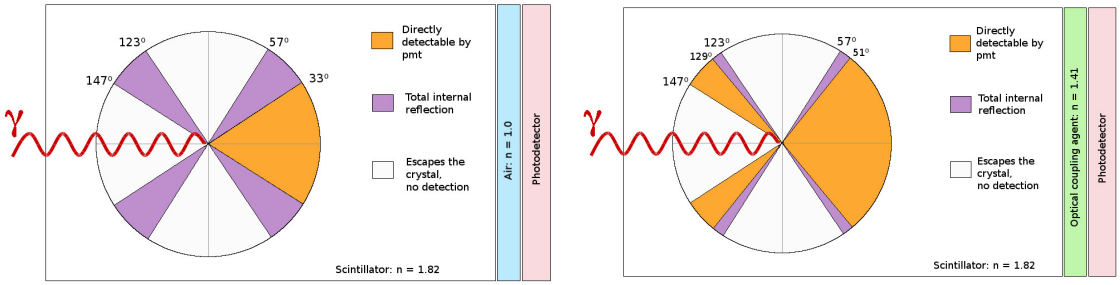


Figure 2.5: The extraction of light from a crystal with index of refraction of $n = 1.82$, coupled to air. The extraction angles can be calculated from Snell's law. Left: crystal is *not* wrapped and *no* optical coupling is used. Right: crystal is *not* wrapped, an optical coupling with n=1.41 has been applied to the readout surfaces. Both figures are reproductions of [8].

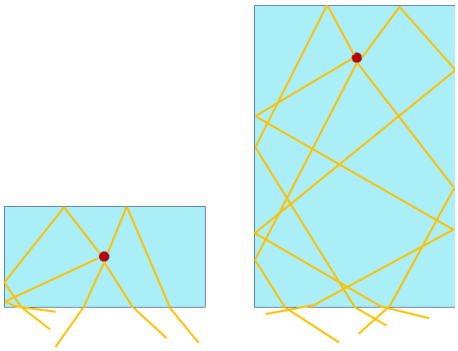

Figure 2.6: Two scintillating crystals with different lengths, in both cases scintillation light is produced in the center (red spot) of the crystal. The left crystal is a short crystal, comparable to a geometry of for instance 3x3x2 $mm^3$, the right is a slightly longer crystal, comparable to a geometry of for instance 3x3x5 $mm^3$.

the effect of such coupling. To further increase the light output, a reflector can be used on all faces of the crystal but the readout face. A perfect specular reflector ensures that the light emitted opposite to the readout face is reflected and ultimately read out from the readout face. On the other hand, light emitted towards the side walls of the crystal stays outside the extraction cone and will therefore be trapped in the crystal. When using a (partially) Lambertian reflector, i.e. one that also *diffuses* the reflected light, part of this light can be reflected into the extraction cone and will thereby be extracted at the readout face as well.

Unfortunately, in reality the scintillating crystal is not a perfect crystal. Even if not substantial, absorption processes occur inside the crystal due to imperfections at its surface and its edges. Also imperfections in the crystal lattice, such as color centers, can play a certain part in the absorption of light. Depending on the crystal geometry, a small amount of the generated light travels directly towards the readout face and into the photodetector, whereas the majority of light actually travels a much longer path before it reaches the readout face. Taking the extreme example of a crystal being a plate, i.e. its length << crystal cross section, most of the produced light directly hits both the readout- and

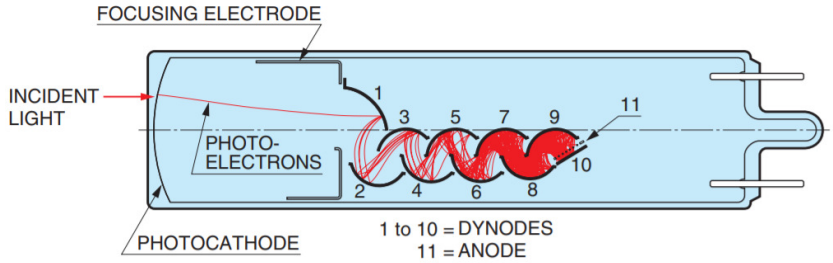


Figure 2.7: Schematic drawing of a photomultiplier tube, with its principle components. [17]

the back face of the plate, and light coming back form the opposite face will subsequently reach the readout face. In this scenario very little light will be reflected by the side faces before it reaches the readout surface, too. In other words, the longer the crystal the more reflections on the side faces will take place before the light reaches the readout face. This effect is shown in figure 2.6 for an almost flat crystal and a short pixel.
The more reflections in the crystal take place the more one increases the chance of light absorption due to the previously mentioned edge- and surface imperfections, but also owing to some absorption effects in the crystal bulk. A way to quantify this effect on the net light output (LO) is to define the light transfer efficiency (LTE) as:

$$LY = LTE \times LO, \tag{2.18}$$

where LY is the intrinsic light yield of the crystal. Therefore, the LTE takes into account all the possible light losses during the transport of light. As mentioned before, the LTE can be enhanced by e.g. the use of reflective wrapping around the crystal and an optical coupling grease on the readout surface. Furthermore, the light output, and as such also the LTE, influence the coincidence time resolution of the crystal (see section 2.3.2). The light transport in the crystal also *directly* influences the time resolution because of the photon travel time spread in the crystal. Therefore, multiple reflections are also responsible for a deterioration in time resolution as they increase the photon travel time spread, as shown in figure 2.4.

## 2.4 Photodetectors

The photodetector is the other important component in this detection system as it converts light into an electric signal. In this section two types of photodetectors are discussed, i.e. the classical photomultiplier tube (PMT), a type of vacuum photodetector, and the silicon photomultiplier (SiPM), also called a multi-pixel photon counter (MPPC), a solid state photodetector.

### 2.4.1 Photomultiplier tube

Photomultiplier tubes (PMTs) are the original photodetectors for high sensitivity, high speed and high amplification applications. They have been in use since the thirties of last century [17] and have become the work horse for many types of experiments in many branches of physics. Figure 2.7 shows the drawing of a typical PMT. It consists of a vacuum tube with an entry window covered with a photosensitive layer on the inside called the photocathode and focusing electrodes, dynodes and an anode as the final stage. A high

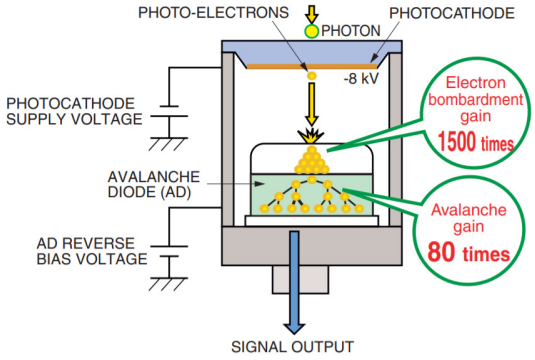


Figure 2.8: Schematic drawing of a hybrid-photomultiplier tube, with its principle components. [17]

voltage between the photocathode and the anode, and intermediately subdivided by the dynodes, acts as an accelerating field for electrons being liberated from each of the stages. When light illuminates the photocathode, it frees primary electrons into the vacuum of the tube via the photoelectric effect. Each of the freed electrons, called photoelectrons, is focused and accelerated towards the first dynode via the applied electric field in the PMT. By hitting the first dynode, each electron liberates other secondary electrons from that dynode stage. This process repeats itself for each of the subsequent dynodes, freeing and multiplying more and more electrons in a cascade until they reach the anode, collecting the final amount of electrons, large enough to produce an electrical signal. At the end of the multiplication chain, the total gain can be of the order of $10^6 - 10^7$ [17]. The detection efficiency of the PMT depends mainly on the quantum efficiency (QE) of the photocathode, i.e. the probability of one incoming photon to free a photoelectron from the photocathode. The QE of a PMT at peak sensitivity generally ranges between 15 and 40% [17]. Furthermore, the QE is strongly dependent on the wavelength of the incoming light. The great advantage of PMTs is their excellent linearity from low to high light levels. They generally maintain this linearity from a single photon all the way up to a light signal of thousands of photons. As such, they serve as perfect devices for making energy histograms over a wide dynamic range. Originally PMTs were the fastest photodetectors on the market and are still relatively fast today with a time jitter of 1-5 ns FWHM or even exceeding 500 ps FWHM for dedicated fast timing applications. A well known disadvantage is that PMTs are rather bulky owing to their numerous multiplication stages to achieve sufficient pulse height.

A special type of PMT is the hybrid-PMT or H-PMT, as illustrated in figure 2.8. Instead of a chain of dynodes, the primary photoelectrons are only accelerated in one stage towards a so-called avalanche photodiode, a medium-gain semiconductor photodetector and a precursor to the high-gain silicon photomultiplier, to be discussed in the next section. The device is operated at a rather high voltage (compared to the classical PMT) of around 10 kV [17]. On the other hand, it has an excellent time resolution and also provides higher energy resolution making it possible to distinguish between single- and multiple photoelectron peaks.

### 2.4.2 Silicon photomultiplier

This subsection is based on the comprehensive work by S. Gundacker [18]. The silicon photomultiplier (SiPM) is a solid state photodetector, the photosensitive surface of which

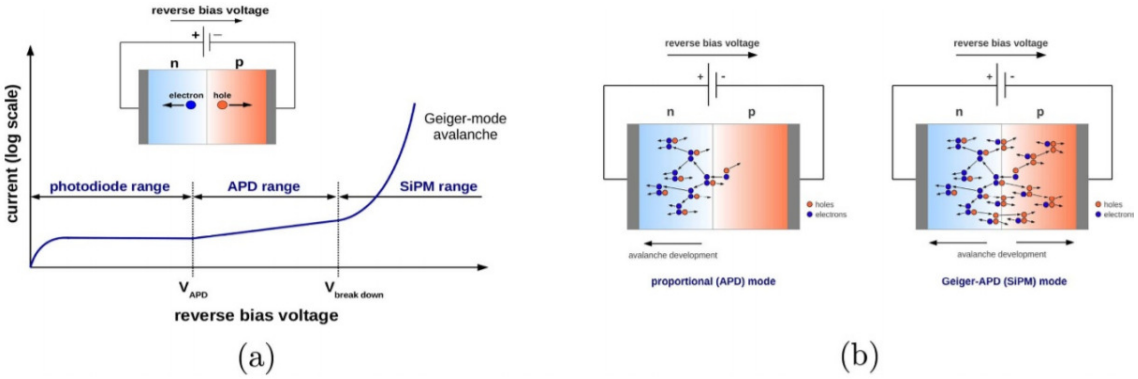


Figure 2.9: (a) An electron-hole pare produced in the p-n junction is separated by the applied field, the graph shows the different operation regimes. (b) In the APD regime only the electrons multiply, i.e. create new electron-hole pairs, in the SiPM regime both electrons and holes can multiply. [18]

is subdivided into a large number of single cells, the so-called single-photon avalanche diodes (SPADs). As the name says, the SPAD is a diode, or p-n junction, across which a bias voltage is applied. As such, an incoming photon can create an electron-hole pair in the junction, which is then separated by the applied electric field, as shown in figure 2.9. If the voltage applied is below a certain threshold, no multiplication of the signal takes place. If the field is increased such that the electron is sufficiently accelerated to produce new electron-hole pairs in the material, one reaches the regime of the avalanche photodiode (APD), where the original signal is amplified. Since the mobility of the holes is much lower than that of the electrons, they do not gain enough energy in this regime to create new electron-hole pairs and therefore do not contribute to the signal gain of the device. This is shown on the left hand side of figure 2.9b. Therefore, the the so-called electron avalanche merely flows in one direction and does not need an external circuit to be stopped. When the applied voltage is increased even further, i.e. above the so-called breakdown voltage, the device is then operated in the so-called SiPM regime. In this case, also the holes gain enough energy to create new electron-hole pairs themselves, as shown on the right hand of figure 2.9b. This makes it possible that already one photon can create a self-sustained avalanche that, however, needs to be quenched by an external current-limiting circuit. Since the created signal from this avalanche rises very fast, the SiPM currently is the perfect device to determine the arrival time of each photon impacting on a SPAD.
The SiPM is an array of SPADs, all coupled in parallel, where each SPAD fires individually when hit by a photon. The pulse height of the SiPM is then proportional to the number of SPADs fired, as such counting the amount of detected photons. The SPAD only detects one photon at a time, being limited only by the number of consecutive photons due to its intrinsic dead time. Therefore, it cannot respond linearly to high light intensity. This deficiency, though, can be calibrated and corrected for to a certain extent. Today, the SiPM, by nature, is so fast that it is an excellent detector for highest time resolution, even outperforming the best PMTs. This is also due to the fact that today's SiPMs have a single photon time resolution (SPTR) of the order of 100 ps FWHM. Another reason to use SiPMs is their relatively high photon detection efficiency (PDE), being as large as $\sim$50-60% when operated at the optimum voltage.

## 2.5 State-of-the-art coincident time resolution and how to improve it

From a timing point of view, the currently best performing inorganic scintillator is LSO:Ce, co-doped with calcium. Despite slight absorption of light inside this crystal type, the co-doping with calcium effectively reduces the scintillation decay time, thereby improving the timing performance of this crystal. The best coincidence time resolution (CTR), measured with a 2x2x3 $mm^3$ LSO:Ce:0.4%Ca crystal coupled with Meltmount to a Fondazione Bruno Kessler (FBK) NUV-HD 4x4 $mm^2$ SiPM with 40 $\mu$m SPAD-size, resulted in a state-of-the-art value of 58±2 ps FWHM [16]. Note, a distinctive feature of this SiPM is that its entrance window is free of a protective resin that could give cause to UV-light absorption. If a longer crystal, of 2x2x20 $mm^3$ crystal, is used, the content of calcium was reduced to 0.2 % in order to reduce the light absorption effects. Notwithstanding the longer crystal, this configuration led to a sub-100 ps CTR of 98±2 ps FWHM [16].
At this time, LSO:Ce:Ca crystals are not commercially available and therefore not used in full scintillation detector systems. Also the new cutting-edge FBK SiPMs of the type described above are not on the market yet either. Therefore, to put the above-mentioned results into context with commercially available products, like LYSO:Ce crystals and Hamamatsu HPK S13360-3050PE SiPMs of 3x3 $mm^2$ and 50 $\mu$m SPAD-size, the best achievable results in CTR are 86±2 ps and 135±2 ps FWHM for 2x2x3 $mm^3$ and 2x2x20 $mm^3$ crystals, respectively [18].

The above-mentioned performances are already very impressive and raise the question if and how one could further improve this CTR. An obvious way to go is to make improvements in the entire detector chain, from light emission to light detection, all the way up to light detection, including ultrafast signal processing.
As to light generation, one could develop different scintillators, that are both faster and brighter. A good example of an intrinsically fast scintillator is $BaF_2$, which benefits from its fast cross-luminescence. An comprehensive investigation of this promising crystal is presented in chapter 7.
Another goal is to preserve light that has been generated in the crystal, which requires an understanding and improvement of the transportation of the scintillation light in the crystal up to the photodetector. Common procedures in this direction are, e.g., changing the crystal geometry, wrapping the crystal and using optical coupling between the scintillator and the photodetector (see chapter 7.5). Another promising method to facilitate light extraction is the use of photonic crystal slabs on the readout face of the scintillator. This technology is investigated and discussed in depth in chapters 4-6.
The third objective in this context is to see whether photodetectors, the development of which is usually in the hands of commercial producers, can be further advanced in particular in terms of their photodetection efficiency (for short wavelengths) and single photon time resolution (see chapter 7).

## 2.6 Applications of scintillators

Scintillation-based detectors for ionizing radiation are used in many fields, such as high energy physics, medical physics, homeland security, material research and thermal neutron detection. The different fields of application also have their specific detector demands.
In this thesis, the focus is on applications in medical physics, especially for positron emission tomography (PET). The principle of PET is explained in the next section. The

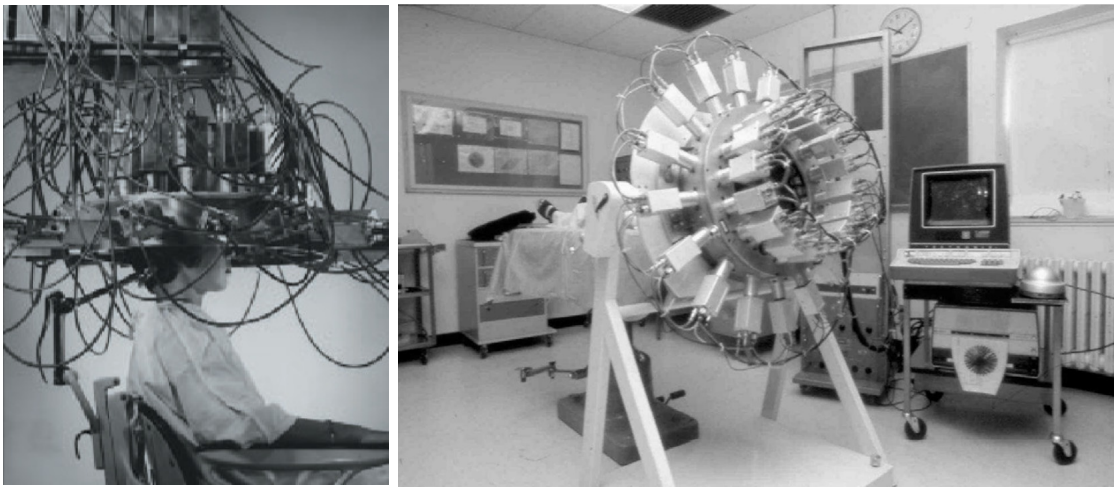

(a) The "Headshrinker" [19] (b) The "Positome" [20]

Figure 2.10: Two of the first PET scanners in history, from the seventies of the last century.

second field of interest in the application of scintillators is particle and photon detection in high energy physics, an application that is also being investigated by the Crystal Clear group at CERN. The specific crystal demands with an example of a high energy physics scintillation-based detector are discussed in section 2.6.2.

### 2.6.1 Scintillation-based detection in PET

Research on positron emission tomography started immediately after the discovery of the positron in 1932 [21]. The experimental basis for the first PET scanners registering photons in coincidence originating from electron-positron annihilation, was laid down in the fifties with the development of a scanner called the "Head Shrinker" (figure 2.10a). An improved version of this device was developed in the sixties of the last century at the Brookhaven National Laboratoy (BNL) [22], with further improvements made at the Montreal Neurological Institute (MNI) [20] [23]. The new device was renamed "Positome" and is illustrated in figure 2.10b.

As the name says, PET makes use of spontaneous positron emission by a radioactive tracer in the patients body. This tracer, the most common of which is $^{18}$F-fluorodeoxyglucose (FDG), is effectively a sugar molecule doped with a radioactive $^{18}$F isotope, which is a $\beta^+$ emitter. The positrons emitted by the fluorine, within a millimeter range (on average 0.6 mm in this case [24]), will recombine with an electron in the surrounding tissue, the result of which are two photons emitted back-to-back (neglecting the momentum of the emitted $\beta^+$), each with an energy of 511 keV, corresponding to the mass of an electron. FDG, being effectively a sugar, is preferentially absorbed in cells with a high glucose consumption, such as tumor cells. As such, the highest photon activity will necessarily originate from such cells in the human body. If a patient is positioned inside a ring, or rather a sequence of rings, of scintillation-based detectors one can detect the two co-linear photons, originating from the tumor cells, in coincidence, as illustrated in figure 2.11 left. Upon response by the respective detector, a line can be drawn between the two impacts. This is called a line of response (LOR). The intersection of all LORs determine the point from which the photons are emitted. In reality, one does not want to identify one single point of positron emission in the body, but rather create a functional image of it, as

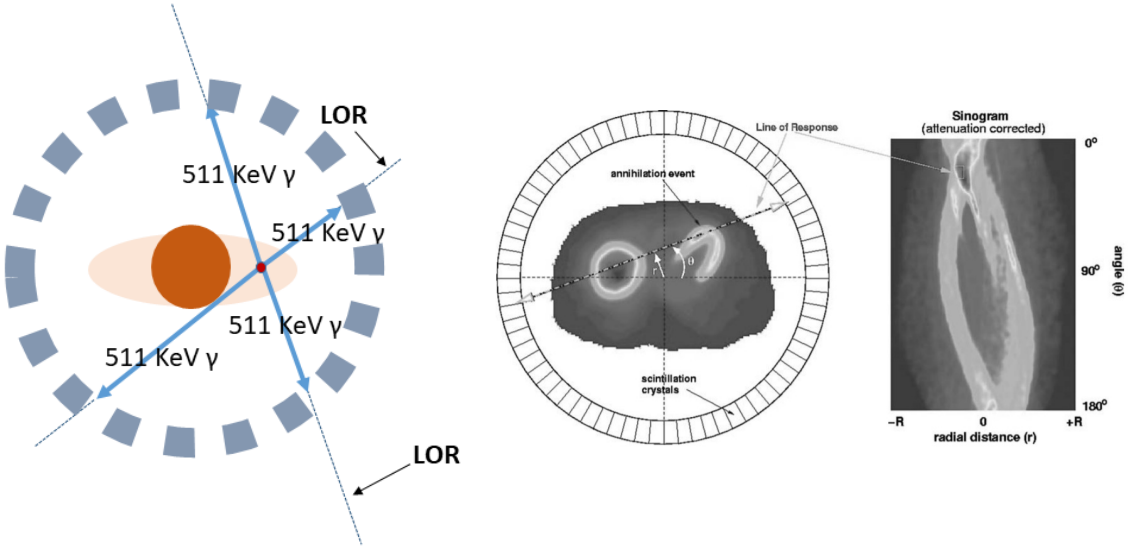


Figure 2.11: Left: positrons emitted from the patients tumor recombine with an electron in the body emitting two photons back-to-back, each with an energy of $511keV$. When the detector ring detects the two photons, a line, a so-called LOR, can be drawn between them. The intersection of all the LORs, give the point from which they are emitted. Right: The actual image coming directly from the PET scanner is called a sinogram and has to be reconstructed with specific algorithms in order to obtain the final image. Image from [21].

illustrated on the right hand side of figure 2.11. The obtained intermediate image is the so-called sinogram, as depicted in figure 2.11, necessitating further reconstruction algorithms to obtain the actual image. Note, in order to physically attach the PET "hot spots", in other words the tumors with their increased positron activity, to the morphology of the body, the PET scan is usually overlaid with either a CT scan or an MRI session.
Among the registered events, there are also contributions that correspond to false lines of response (a) caused by scattered coincident photons, (b) random noise hits or (c) where two gammas from two different true conversions are measured in coincidence but belonging to two different events. This is illustrated in figure 2.12 left and right. In the case where a scattered photon leads to a (false) LOR, its energy will not be the same as that of the other photon with its full energy of 511 keV. Therefore, in order to filter out these events, next to the position of the photons, it is necessary to register also the energy of the detected gammas. Likewise, events due to random incidences, i.e. two non-correlated photons, can be substantially suppressed by selecting only events resulting from photons with an energy of 511 keV. This illustrates the importance of high energy resolution in PET.

In view of the high-speed- and high-time-resolution-photodetectors on the market, time-of-flight (TOF) PET has become a point of particular interest in PET. The principle of TOF imaging is illustrated in figure 2.13. In conventional PET the constraints for reconstruction of the image are only the co-linearity and the energy of the photons; in other words, along the entire line of response the probability of gamma emission is taken the same. Knowing the flight time of the two co-linear photons in addition, allows one to narrow down the emission point along the LOR and thereby to define a weighted probability distribution for the location of this point in the reconstruction. This is shown

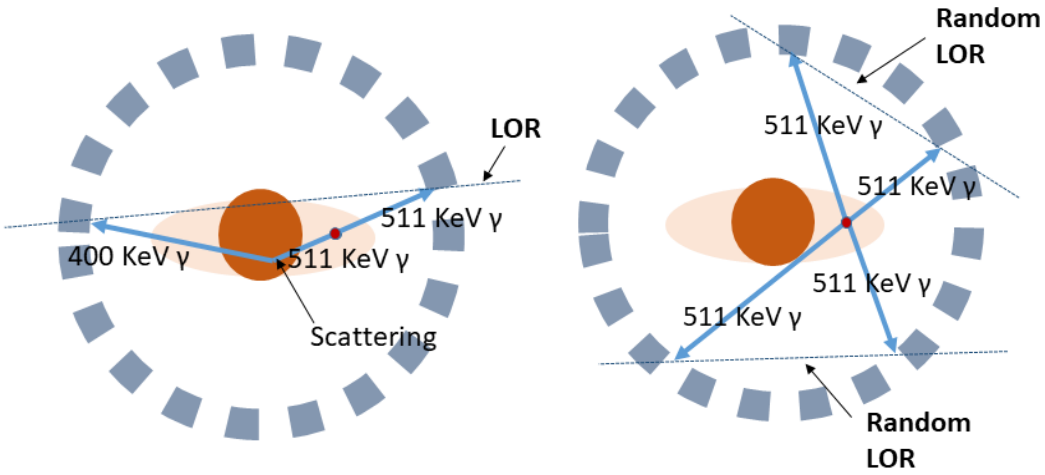


Figure 2.12: Scattered- and random events can introduce noise in the PET image. Left: one of the two back-to-back emitted photons is scattered in the body and therefore changed direction. As such, the registered position is not the same as the projected one from the moment of emission, therefore creating a false LOR. The energy of this scattered photon is then less than the original 511 keV. Right: A random incidence, where two non-correlated photons are detected at the same time "by chance", creates a random LOR.

in figure 2.13. As such, time-of-flight information of the arrival time of the photons can significantly improve the signal-to-noise (SNR) ratio [25]:

$$\frac{SNR_{tof}}{SNR_{non-tof}} = \sqrt{\frac{2D}{c \cdot CTR}} \tag{2.19}$$

where $D$ is the diameter of the imaged object and $c$ the speed of light. We are currently in the position to produce, under laboratory conditions, coincidence time resolutions in the sub-100ps regime with conventional crystals and photodetectors, leading, according to equation 2.19, to a substantial improvement in image contrast owing to time-of-flight. On the commercial side, the current state-of-the-art PET scanner, the Siemens Biograph Vision [28], runs at a CTR of 210 ps FWHM [29]. The improvement in image quality from this device, owing to its TOF information, is shown in figure 2.14. This underlines the importance of the continuous advancements in time resolution, for all possible parts of a scintillation-based detector. It is conceivable that in the near future, research will lead us to a coincidence time resolution of the order of 10-30 ps, in which case the reconstruction algorithms could be reduced to the simple determination of pure space points along the LOR.

Apart from the importance of the energy resolution and the coincidence time resolution, also the density of the crystal and its photofraction are important characteristics for PET and imaging in general. These features are a determinant factor for the *sensitivity* of the scanners.

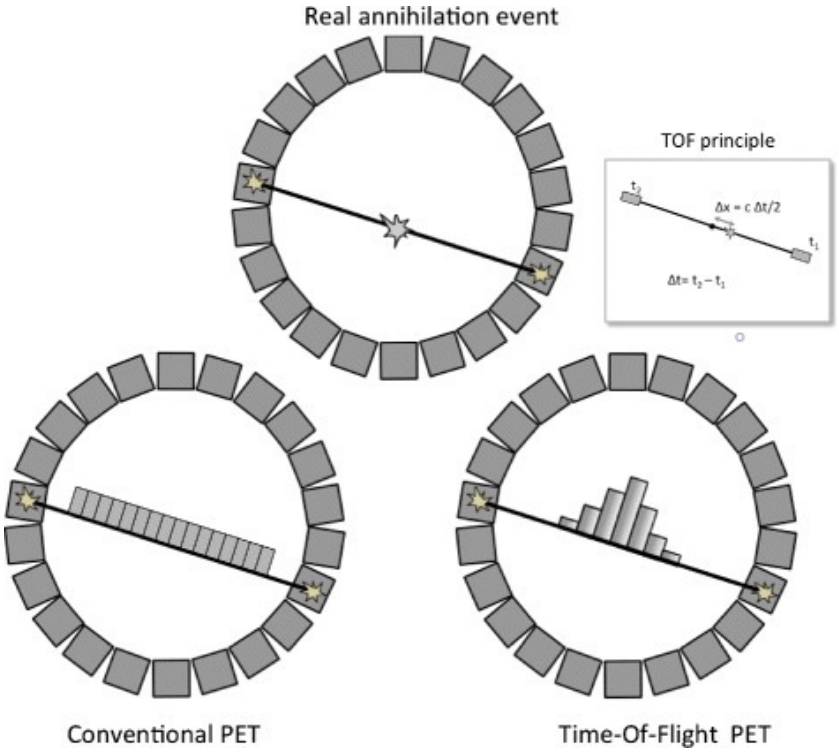


Figure 2.13: While in conventional PET the probability of the location of the annihilation point is constant over the LOR, in TOF-PET the timing information enables to make a probability distribution along the LOR. [26]

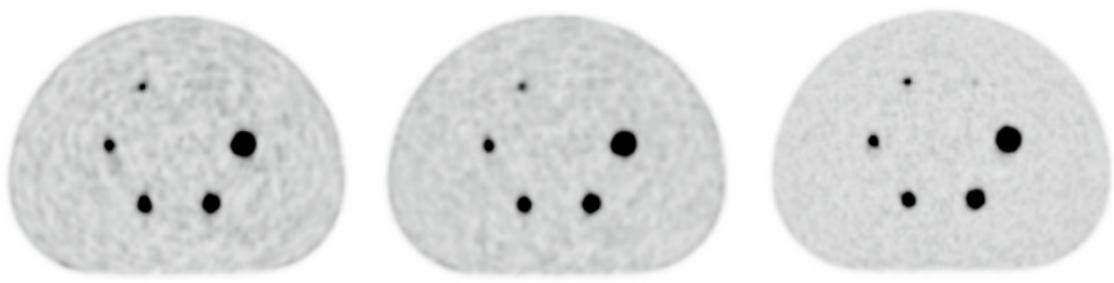


Figure 2.14: " Transaxial slices of an image quality phantom, reconstructed with high-resolution iterative reconstruction with resolution recovery. The scans were performed on a Siemens Biograph mCT PET/CT scanner (527 ps coincidence time resolution) and the new Siemens Biograph Vision (210 ps coincidence time resolution). From left to right: (**a**) non TOF image from mCT, (**b**) TOF image from Biograph mCT, and (**c**) TOF image from Biograph Vision. The phantom had six hot spheres (5, 8, 10, 13, 17, 22 mm diameter) with a contrast of about 4:1, and a total activity in the background of about 50 MBq of $^{18}$F." [27]

### 2.6.2 Scintillation-based detection in High Energy Physics

While in PET applications energies are typically of the order of half an MeV, energies generated in high energy physics events are typically more than a thousand times higher. Therefore, the demands on crystals and photodetectors used in electromagnetic calorimetry in high energy physics are not the same as those in medical applications. First of all, the density of these crystals needs to be even higher than in medical physics. A density of $> 5$ g/cm$^3$ [1] is deemed essential in order to contain the high energy showers produced by high energetic electrons (and positrons) and gammas. Another distinctive feature is the demand for these crystals to be radiation hard as they are exposed to very high levels of radiation, predominantly from high energetic hadrons. Particularly in view of experiments running at very high luminosity, e.g. the Large Hadron Collider (LHC) at CERN, crystals are prone to coloring, an effect that gradually decreases the light output of the crystal and thereby crucially affects the linearity of the calorimeter. On the other hand, the overall light output of the crystal is less crucial than in medical applications, since sufficient amounts of light are produced by the large energies deposited in the crystal.

#### 2.6.2.1 The CMS electromagnetic calorimeter

The Compact Muon Solenoid (CMS) is one of the main experiments at the Large Hadron Collider (LHC) at CERN [30]. The LHC accelerates protons up to an energy of about two times 7 TeV at a luminosity of $\mathscr{L} \sim 10^{34}\text{cm}^{-2}\text{s}^{-1}$, as such producing large amounts of particles in every collision occurring at an interval of 25 ns. This easily leads to pileup effects in detectors running in such harsh environments.
The electromagnetic calorimeter (called ECAL) is the detector part of CMS that measures the energy of the electromagnetic particles produced in the p-p collisions. A schematic drawing of ECAL is shown in figure 2.15; it is the largest crystal calorimeter ever built, made entirely of more than 75.000 scintillating crystals. It measures 3.2 m in diameter and 6 m in length and weighs 92 t.
The crystals of ECAL are made of lead-tungstate ($PbWO_4$), which has a density of 8.28 g/cm$^3$, resulting in a radiation length of only 0.85 cm [1]. This property allowed one to build the calorimeter very compact and with high granularity. The crystals in the barrel part of the detector measure $22 \times 22 \times 230$ mm$^3$ and those of the endcap $29 \times 29 \times 220$ mm$^3$.
Compared to the light yield found in the previously discussed medical-type crystals, $PbWO_4$ produces only 0.25% of the light yield of those crystals, i.e. $\sim$100 photons/MeV [31]. However, given the very high energies of the particles converting in the $PbWO_4$, sufficient light is produced within the required dynamic range. Furthermore, $PbWO_4$ has a comparatively short decay time of only 6 ns (40 ns for LSO), an important requirement to cope with the high-rate environment when running at high luminosity and short bunch crossing interval of the LHC.
The main objective of this calorimeter was to detect the $\gamma$-$\gamma$ decay channel of the Higgs Boson, this being about the cleanest signature among the other Higgs' decay channels. Especially in view of this decay channel, crystal calorimetry was deemed to be the best choice over conventional sampling calorimeters, for it offers the highest energy resolution among all other calorimeter types. It is widely known that the discovery of the Higgs Boson, both by CMS [33] and ATLAS [34], was a success.

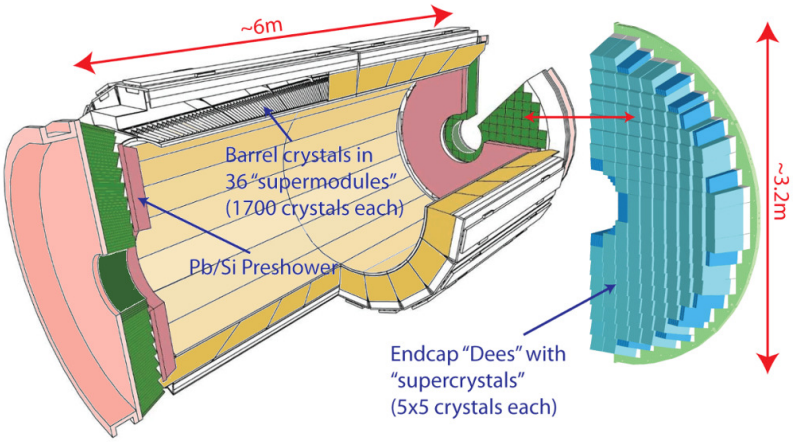


Figure 2.15: Schematic overview of the Electromagnetic Calorimeter (ECAL) of CMS. Modified from [32].

## Bibliography

[1] P. Lecoq, A. Gektin, and M. Korzhik, *Scintillation and Inorganic Scintillators*, pp. 1–42. Particle Acceleration and Detection, 2017.

[2] P. A. Rodnyi, *Physical Processes in Inorganic Scintillators*. CRC Press LLC, 1997. Chapter 1.

[3] H. Bichsel and H. Schindler, *The Interaction of Radiation with Matter*, pp. 5–44. Cham: Springer International Publishing, 2020.

[4] P. Lecoq, *Scintillation Detectors for Charged Particles and Photons*, pp. 45–89. Gewerbestrasse 11, 6330 Cham, Switzerland: Springer International Publishing, 2020.

[5] G. F. Knoll, *Radiation Detectibn and Measurement*. John Wiley Sons, Inc., 2000. Chapter 2.

[6] R. Evans, *The Atomic Nucleus*. Tata McGraw-Hill publishing company LTD., 1955.

[7] M. Berger, J. Hubbell, S. Seltzer, J. Chang, J. Coursey, R. Sukumar, D. Zucker, and K. Olsen, *XCOM: Photon Cross Sections Database, NIST Standard Reference Database 8 (XGAM)*. National Institute of Standards and Technology, Gaithersburg, MD, November 2010.

[8] S. Gundacker, *Time resolution in scintillator based detectors for positron emission tomography*. PhD thesis, Technische Universität Wien, 2014.

[9] A. Vasile'ev, "Relaxation of hot electronic excitations in scintillators: account for scattering, track effects, complicated electronic structure," *Proceedings of the fifth conference on Inorganic Scintillators and Their Applications*, pp. 43–52, August 1999.

[10] C. Pedrini, "Scintillation mechanisms and limiting factors on each step of relaxation of electronic excitations," *Fizika Tverdogo Tela*, vol. 47, Aug 2005.

[11] P. Lecoq, A. Gektin, and M. Korzhik, *Scintillation mechanisms in Inorganic Scintillators*, pp. 125–174. Particle Acceleration and Detection, 2017.

[12] M. Moszyński, J. Zalipska, M. Balcerzyk, M. Kapusta, W. Mengesha, and J. Valentine, "Intrinsic energy resolution of nai(tl)," *Nuclear Instruments and Methods in Physics Research Section A: Accelerators, Spectrometers, Detectors and Associated Equipment*, vol. 484, no. 1, pp. 259 – 269, 2002.

[13] P. Lecoq, A. Gektin, and M. Korzhik, *Energy Resolution and Non-proportionality of Scintillators*, pp. 175–196. Particle Acceleration and Detection, 2017.

[14] M. Moszyński, A. Syntfeld-Każuch, L. Swiderski, M. Grodzicka, J. Iwanowska, P. Sibczyński, and T. Szcześniak, "Energy resolution of scintillation detectors," *Nuclear Instruments and Methods in Physics Research Section A: Accelerators, Spectrometers, Detectors and Associated Equipment*, vol. 805, pp. 25–35, 2016. Special Issue in memory of Glenn F. Knoll.

[15] R. Martìnez Turtos, *Prompt photon emission - A novel approach towards highest time resolution with scintillators*. PhD thesis, Università degli studi Milano Bicocca, 2017.

[16] S. Gundacker, R. M. Turtos, E. Auffray, M. Paganoni, and P. Lecoq, "High-frequency SiPM readout advances measured coincidence time resolution limits in TOF-PET," *Physics in Medicine & Biology*, vol. 64, p. 055012, feb 2019.

[17] *Photomultiplier tubes: Basics and Applications*. Hamamatsu K. K., 4 ed., 2017.

[18] S. Gundacker and A. Heering, "The silicon-photomultiplier: fundamentals and applications of a modern solid-state photon detector," *Physics in Medicine & Biology*, 2020.

[19] J. S. Robertson, R. B. Marr, M. Rosenblum, V. Radeka, and Y. L. Yamamoto, "32-crystal positron transverse section detector.," 1 1972.

[20] C. J., "30 years ago: First pet scanner in canada," *Canadian Medical Physics Newsletter*, vol. 51, pp. 48–49, April 2005.

[21] R. Wells, R. deKemp, and R. Beanlands, *Addressing the increased demand for fast timing*, pp. 25–45. Am J Physiol Imaging, 1988.

[22] S. Rankowitz, J. S. Robertson, W. A. Higinbotham, and M. J. Rosenblum, "Positron scanner for locating brain tumors," 3 1961.

[23] C. J., Thompson, Y. L. Yamamoto, and E. Meyer, "Positron imaging system for the measurement of regional cerebral blood flow," *Proceedings of SPIE - The International Society for Optical Engineering*, vol. 96, p. 263, December 1975.

[24] M. Conti and L. Eriksson, "Physics of pure and non-pure positron emitters for pet: a review and a discussion," *EJNMMI Physics*, vol. 3, 2016.

[25] P. Lecoq, C. Morel, J. Prior, D. Visvikis, S. Gundacker, E. Auffray, P. Krizan, R. M. Turtos, D. Thers, E. Charbon, J. Varela, C. de La Taille, A. Rivetti, D. Breton, J.-F. Pratte, J. Nuyts, S. Surti, S. Vandenberghe, P. K. Marsden, K. Parodi, J. M. Benlloch, and M. Benoit, "Roadmap toward the 10 ps time-of-flight pet challenge," *Physics in Medicine & Biology*, 2020.

[26] S. Vandenberghe, "Recent developments in time-of-flight pet," *Physica Medica*, vol. 52, p. 69, 2018. Abstracts from the 2nd European Congress of Medical Physics.

[27] M. Conti and B. Bendriem, "The new opportunities for high time resolution clinical tof pet," *Clinical and Translational Imaging*, vol. 7, pp. 139–147, 2019.

[28] "Siemens biograph product information webpage." `https://www.siemens-healthineers.com/molecular-imaging/pet-ct/biograph-vision`. Accessed: 2021-01-19.

[29] J. van Sluis, J. de Jong, J. Schaar, W. Noordzij, P. van Snick, R. Dierckx, R. Borra, A. Willemsen, and R. Boellaard, "Performance characteristics of the digital biograph vision pet/ct system," *Journal of Nuclear Medicine*, vol. 60, no. 7, pp. 1031–1036, 2019.

[30] "Homepage of the cms collaboration at cern." `https://cms.cern/collaboration`. Accessed: 2021-01-18.

[31] P. Lecoq, A. Gektin, and M. Korzhik, *Addressing the increased demand for fast timing*, pp. 103–124. Particle Acceleration and Detection, 2017.

[32] C. D. Barney, "The cms electromagnetic calorimeter its performance and role in the discovery of the higgs boson and perspectives for the future," *CMS Conference Report*, CMS CR -2013/410.

[33] C. Collaboration, "Observation of a new boson at a mass of 125 gev with the cms experiment at the lhc," *Physics Letters B*, vol. 716, no. 1, pp. 30–61, 2012.

[34] A. Collaboration, "Observation of a new particle in the search for the standard model higgs boson with the atlas detector at the lhc," *Physics Letters B*, vol. 716, no. 1, pp. 1–29, 2012.

# Chapter 3

# Instrumentation and methods for the characterization of scintillators

In study various techniques are used to characterize either the scintillator itself or the treatment applied to the scintillator to improve its performance. Furthermore scanning electron microscopy (SEM) imaging was used to verify the photonic structure produced on scintillator surfaces. Chapter 3 gives an overview of the different apparatus and techniques used in the course of this study.

## 3.1 Transmission Setup

The transmission of samples is measured with a Perkin Elmer LAMBDA 650 UV/VIS spectrophotometer [1], shown in figure 3.1. Appendix G shows the schematics of the device. The setup allows to measure the transmission of light over a wavelength range of 190-900 nm, with 1 nm steps. It has a tungsten-halogen and a deuterium light source the light of which passes through optical gratings to select the desired wavelength for the transmission measurement. Then the light beam is split into two, where one beam, the reference beam, goes directly to the photodetector and the second through the sample and then to the photodetector. The ratio of the reference and sample beam, having taken into account the calibration of the beams at the used wavelength, determines the transmission of the sample for that particular wavelength. Doing this measurement over the entire wavelength range, produces the transmission spectrum. It is important to understand that only light that passes straight through the sample can be measured by the photodetector. Therefore, if part of the light is only slightly refracted, for instance by imperfections on the surface of the sample (e.g. due to depolishing of the sample) or by imperfections inside the sample (e.g. due to small bubbles in the material), this amount of light is interpreted as a loss in transmission. Also effects from misaligning the sample, with its surface not perfectly perpendicular to the beam, can lead to a loss in measured transmission. This implies that the sample's surface needs to be flat, necessitating a proper holder when doing measurements with liquids or greases.
When samples with a refractive index different from that of air are measured, Fresnel reflection occurs at the air/sample-interfaces. This also leads to losses in light, appearing as a constant absorption in the transmission spectrum. The Fresnel effect is explained in detail in appendix E.
Although the cross section of the light beam can be reduced to $\sim$1 mm, it is nonetheless preferable to use samples with a minimum diameter of 2 mm or a square surface of

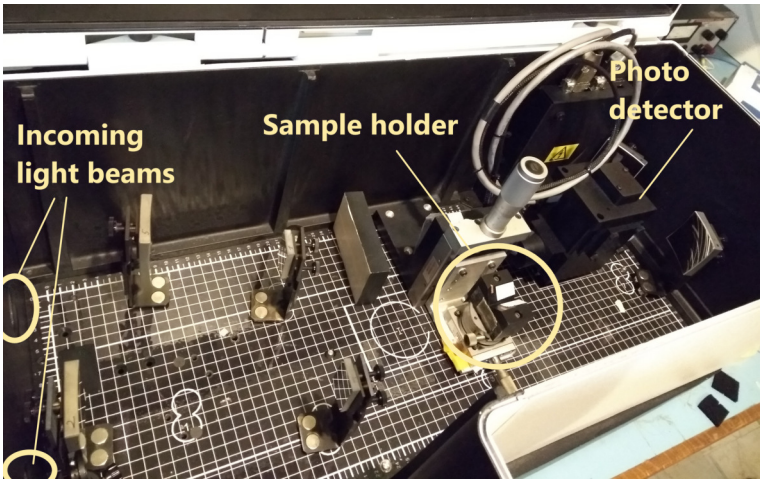


Figure 3.1: Picture of the Perkin Elmer LAMBDA 650 UV/VIS used for transmission measurements. The position of the incoming light beams, the sample holder and photodetector are indicated. Part of the optical mirrors are visible.

2x2$mm^2$, to prevent losses from light passing outside the sample.

## 3.2 Light Output (LO) Setup

One of the standard characterization methods for scintillating crystals is the light output (LO) measurement made to determine the extracted amount of light from the scintillator. This information is used to compare the performance of different types of scintillators or to analyze the effects of, e.g. the crystal geometry, its surface treatment and wrapping, and optical greases (if applied), on the scintillator performance. The LO can further be taken to calculate the crystal's intrinsic light yield (discussed in chapter 2.3.1) for which the light transport efficiency (LTE) of the specific crystal should be known as well. After all, the intrinsic light yield is a material property.

To measure the LO of a scintillating crystal, one has to excite it with a radioactive source. This excitation causes the crystal to produce its characteristic scintillation light, which is consequently detected by a photomultiplier tube (PMT) and converted to an electric signal. The functioning of the PMT is described in more detail in section 2.4.1. The electric output is then digitized for computational processing and analyzed by producing an energy spectrum.

The setup used in this thesis is placed in a light-tight and temperature-controlled box at a constant temperature of 18±0.5 °C.
For each measurement, the crystal is placed vertically on the entry window of the PMT, with a black, non-reflective, cover over it to prevent scattered scintillation light from entering the PMT. The radioactive source is then mounted on top of the crystal. This setup is shown in figure 3.2a.
To prevent unwanted afterglow of the crystal during the measurement and avoid excitation of the PMT photo-cathode, the light tight box was illuminated with red light during the necessary handling and manipulations of the apparatus prior to the actual measurement. The anode signal of the PMT is amplified and digitized by a DT5720A Caen digitizer

(a)

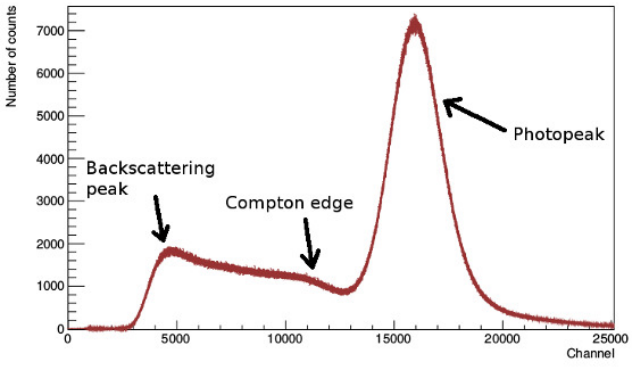


(b)

Figure 3.2: (a) A PMT in a light yield characterization setup. On top of the PMT a large trapezoidal crystal is placed, of which the central positioning is ensured by a holder. The small cylinder on top of the crystal is the Cs radioactive source used in the experiment. The red light is to ensure lighting without exciting the photo-cathode. (b) A typical light yield spectrum measured with an LYSO crystal excited by a Cs-137 radioactive source. In the figure the photo-peak and the compton-edge are shown, as well as the backscatter peak.

located outside the box. The computer allows to set a threshold and an integration gate, individually optimized for the various measurements. Software also determines the pedestal of the signal and subtracts it from the produced energy histogram, which is then analyzed offline.
Figure 3.2b shows an example of such a histogram, from a light output measurement with an LYSO crystal.

Among the multiple radioactive sources used for light output measurements, this thesis worked only with a $^{137}$Cs gamma source for the light output measurements. As the decay diagram in figure 3.3 shows, the gamma is actually emitted by the excited barium nucleus, following the $\beta$-decay of cesium. The electrons resulting from the $\beta$-decay of cesium are absorbed by the metal casing of the source and are not detected by the scintillator. Radioactive sources are chosen and mounted in such a way so as to avoid pile-up, predominately observed in measurements with larger crystals.

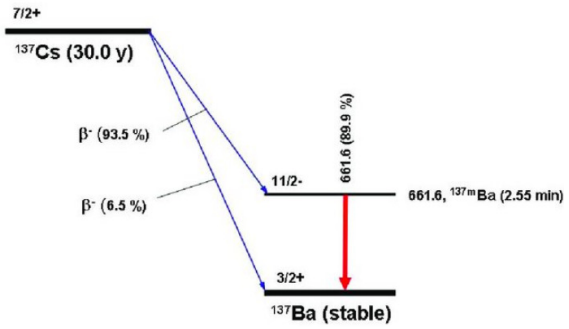


Figure 3.3: Decay diagram of the Cs-137 isotope.

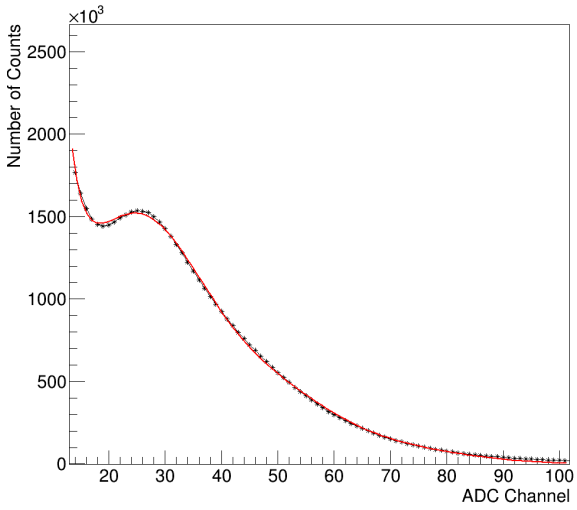


Figure 3.4: Measurement (black) and fit (red) of a single photo-electron measurement of a Hamamatsu R10755 PMT. The single photo-electron peak is assumed to be Gaussian, on top of an exponential decay from electronic noise. Also the two photo-electron and three photo-electron peaks are taken into account in the fit.

To get a true account of the light output from a scintillator, it is important that photodetectors with good linearity are used. This is the reason why typically PMTs are used for these types of measurements (unlike silicon photomultipliers, known to suffer from saturation effects). In order to be sure that one eliminates temperature-induced effects, these measurements are always performed in a temperature controlled environment.

The prominent peak in the histogram shown in figure 3.2b is the so-called photopeak, characteristic for the mono-energetic gamma emitted by the source. Hence, the center of the photopeak corresponds to the emitted gamma energy deposited in the crystal. To convert the number of ADC channels corresponding to the position of the photopeak into numbers of photons collected, the spectrum needs to be normalized to photons per ADC channel. There are two approaches to perform this calibration. One way is to use a reference crystal with its known light output and the second is to determine the single photoelectron signal, both of which will be discussed below.

The single photoelectron signal is the PMT's response to one electron that is thermally liberated from the photocathode and then detected by the anode of the PMT. This method requires to protect the PMT against any stray light and to use a very low threshold. Figure 3.4 shows an example of such a single photoelectron measurement. Thereafter, the light output per energy deposited in the scintillator is calculated by [2][3]:

$$LO = \frac{N_{pe}}{QE \cdot E_\gamma} = \frac{CH}{CH_{spe} \cdot QE \cdot E_\gamma} \tag{3.1}$$

where $N_{pe}$ is the number of photoelectrons, $QE$ is the effective quantum efficiency of the PMT for the produced scintillation light and $E_\gamma$ the energy of the emitted gamma (662 keV in the case of $^{137}$Cs). $CH$ is the ADC channel of the photopeak position, $CH_{spe}$ is the ADC channel of the single photoelectron peak position.

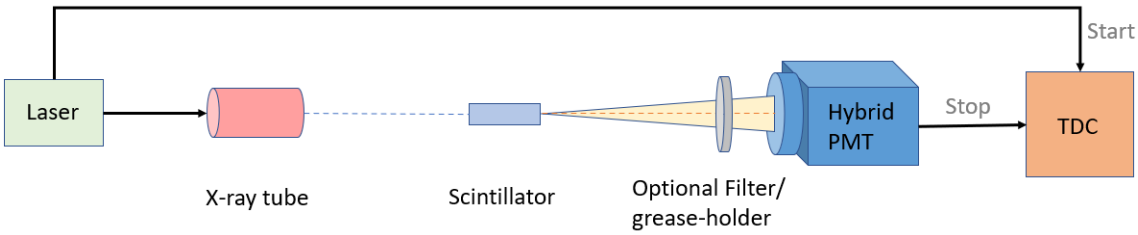


Figure 3.5: Drawing of the time correlated single photon counting (TCSPC) setup, using an X-ray tube excited by a picosecond laser, hybrid-PMT and a fast TDC. Filters can be placed in front of the hybrid-PMT.

If, on the other hand, a reference crystal with its known light output is used, first the photopeak position of the reference crystal and then that of the sample crystal are measured. In that case, the light output is calculated from:

$$LO = LO_{ref} \cdot \frac{CH \cdot QE_{ref} \cdot E^{\gamma}_{ref}}{CH_{ref} \cdot QE \cdot E_{\gamma}} \tag{3.2}$$

where $LO_{ref}$ is the light output of the reference crystal, $QE_{ref}$ is the effective quantum efficiency of the PMT for the scintillation light produced by the reference crystal and $E^{\gamma}_{ref}$ the energy of the source used for the reference measurement.

When one wants to determine the *intrinsic* light yield ($LY_{intr}$) of a scintillator, one also has to know the light transfer efficiency (LTE) [3], where:

$$LO = LTE \cdot LY_{intr} \tag{3.3}$$

There are various ways to determine the LTE, one is by simulating the photon transport in the crystals. The other method, stemming from the work by Turtos et al. [3], uses electrons for excitation of the crystal. In this case, the energy deposition of the electrons is well determined at the entry point of the crystal, contrary to the photons converting within a certain range inside the crystal.

The light output measurements also allow to determine the energy resolution of the crystal from the full width at half maximum (FWHM) of the photopeak. It is usually reported as the percentage of the photopeak position (CH):

$$E_{res} = \frac{FWHM}{CH} \cdot 100 \tag{3.4}$$

## 3.3 Time-correlated single photon counting (TCSPC) setup with X-ray excitation

The time-correlated single photon counting (TCSPC) measurements are used to determine the kinetics of the scintillation emission. They show the different decay components and their abundances in the emission and also provide the rise time of the scintillation signal. The setup for the TCSPC measurements in this work is shown in figure 3.5. A pulsed laser excites a Hamamatsu N5085 X-ray tube and simultaneously produces a "start" signal for a fast 8-ps time resolution time-to-digital converter (TDC), a Cronologic xTDC4. The resulting X-ray pulses, with an energy of up to 40 keV and a pulse width of ∼50 ps, then

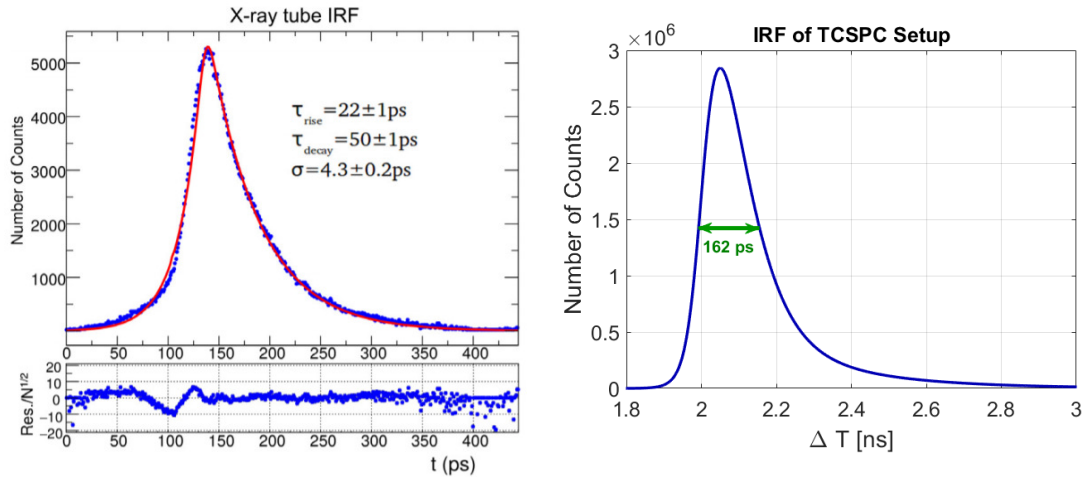


Figure 3.6: Left: IRF of the Hamamatsu N5084 pulsed x-ray measured with a streak camera [4]. Right: IRF of the entire TCSPC setup, a convolution of the IRF of the Hamamatsu N5084 pulsed x-ray and the IRF of the hybrid-PMT measured with a laser. The IRF of the total system has a FWHM of 162 ps.

excite the scintillator. The produced scintillation light is then detected by a Becker&Hickl HPK-100-07 hybrid PMT, which serves as the "stop" signal for the TDC. Therefore, every time a pulse is generated in the X-ray tube, a time measurement starts and the time delays of the detected single photon signals in the hybrid PMT are recorded. In this way the scintillation pulse produced by the scintillator is basically sampled one photon at a time (see figure A.1 of appendix A). At the end, the measurements produce a time delay spectrum, resulting from the differences between the laser start signal and the detection of the first photon by the Hybrid PMT (stop signal). To ensure that only individual photons are counted, the crystal should be placed sufficiently far away from the hybrid-PMT.

The overall impulse response function (IRF) of the setup, i.e. the intrinsic time response of the used apparatus, is then a convolution of the measured IRF of both the X-ray tube and the hybrid-PMT. The IRF of the X-ray tube was measured beforehand with a streak camera [4], the measurement of which is shown in figure 3.6 left. The IRF of the hybrid-PMT was measured with the pulsed laser from the TCSPC setup. Both together lead to a total impulse response function of 162 ps, as shown in figure 3.6 right.

An example of the delay spectrum obtained with this setup was fitted with an exponential decay function and is shown in figure 3.7. Depending on the sample under investigation, one determines whether one or more rise- and decay time components need to be used for the fit.

Since the setup cannot resolve wavelengths of the measured light, the different kinetic components can only be distinguished by the different decay times. The emission within certain spectral ranges can however be measured by introducing filters between the scintillator and the hybrid-PMT. The quantum efficiency of the hybrid-PMT HPM-100-07 is shown by the red curve in figure 3.8. The figure clearly shows that the quantum efficiency is not constant over the hybrid-PMT's sensitive wavelength range. Since there is no wavelength information for the different decay components contributing to the emission kinetics, the abundances of the different components cannot be corrected for their respective quantum efficiencies. Therefore, when different decay components result from different wavelength emissions, their abundances could be grossly under- or overestimated.

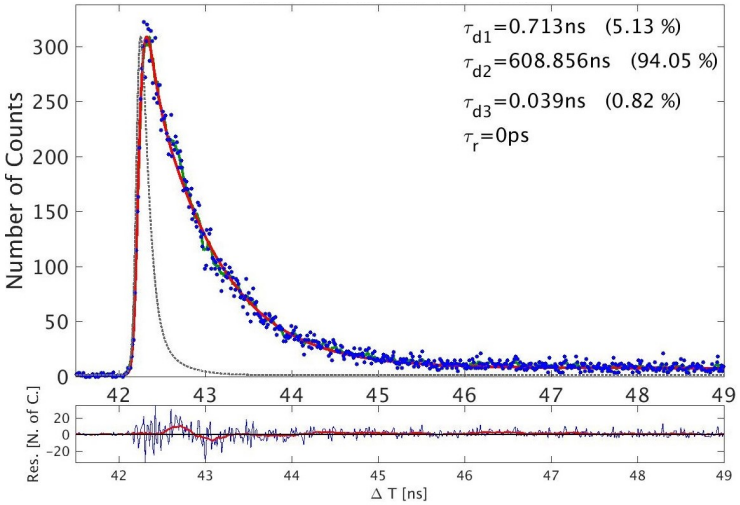


Figure 3.7: Example of a TCSPC measurement (blue) of a $BaF_2$ crystal, fitted with triple exponential decay function (red). The IRF is shown in black and is the same as shown in figure 3.6 right. The plot on the bottom shows the residual signal after subtraction of the fit.

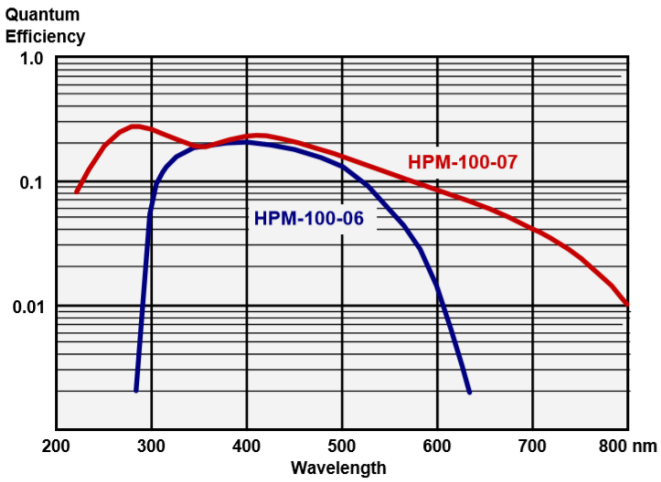


Figure 3.8: Quantum efficiency of the Becker&Hickl HPK-100-06 and HPK-100-07 hybrid PMTs, of which the latter was used for the TCSPC measurements.

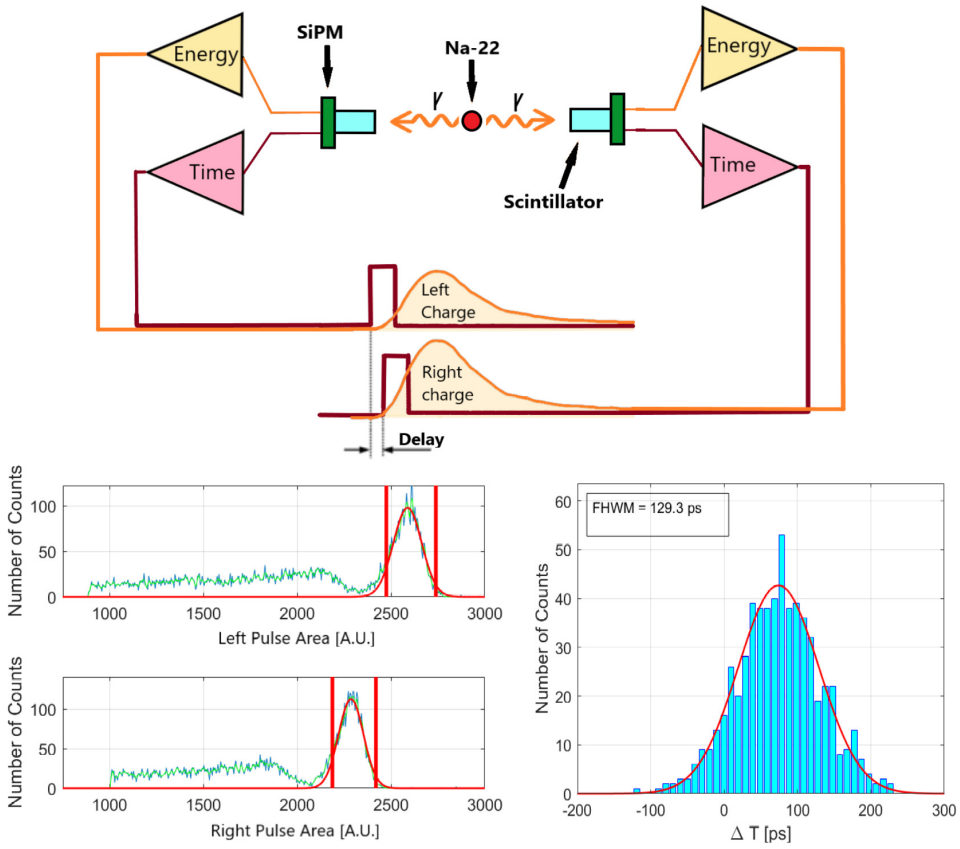


Figure 3.9: Top: General schematics of a CTR setup, based on [6]. Bottom left: Photopeak selection of the measured events, for both arms of the setup. Bottom right: Gaussian fit to the delays spectrum, where its full width at half maximum (FWHM) gives the CTR.

## 3.4 Coincident Time Resolution (CTR) Setup

For timing applications, the coincidence time resolution (CTR) is one of the most important characteristics of a crystal. Not only is it intrinsic to the scintillating material itself, but also influenced by other factors such as crystal geometry and crystal wrapping.
As the name suggests, the CTR is measured with two crystals in coincidence, i.e. opposite to each other, with the radioactive source between them. To measure coincident back-to-back mono-energetic photons, typically a $^{22}$Na source is used. Owing to their high timing performance, SiPMs are used to measure the scintillation light for these CTR evaluations. For best results in terms of both energy resolution and timing, the SiPM output signal is split into two parts. The first is amplified by an analog operational amplifier to obtain the energy with high precision, as shown in the top part of figure 3.9. The other is converted to a time stamp of very high precision, read out by the NINO chip [5] or by a High-Frequency (HF) readout circuit [6]. Both methods are explained in sections 3.4.1 and 3.4.2, respectively. The difference between the time stamps of the two crystals in coincidence produces a time delay spectrum from which the coincidence time resolution of the crystals can be derived.

The energies and time delays are analyzed offline. The energies are used to create an energy spectrum and then select only events from the photopeak for both detector arms. To do that, the photopeak is fitted with a Gaussian function, as shown in figure 3.9

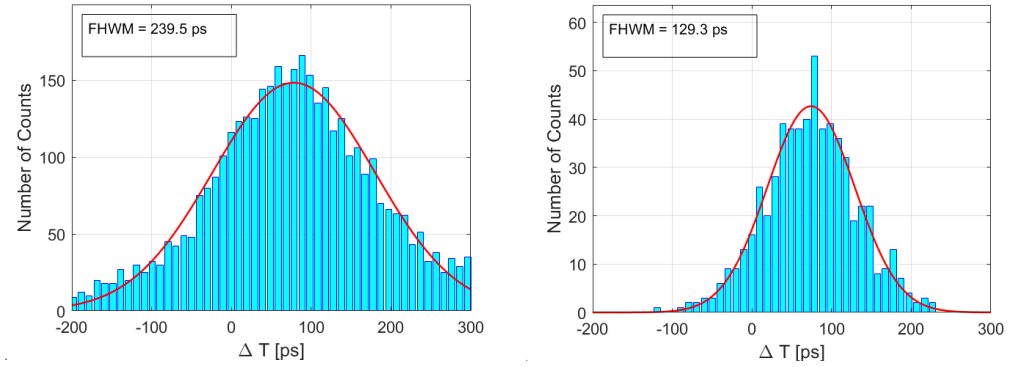


Figure 3.10: A histogram with the delays of a CTR measurement of a 2x2x3 $mm^3$ LYSO:Ce pixel air-coupled to a HPK S13360 SiPM (left) using all the measured events yielding 240 ps FWHM; and (right) using only photopeak events (between $-1.5\sigma$ and $+2.0\sigma$ around the median of the Gaussian fit to the photopeak) yielding 129 ps FWHM.

bottom left, and the appropriate cuts are applied. The resulting delay spectrum is also fitted with a Gaussian, as shown in figure 3.9 bottom right, where the full width at half maximum (FWHM) is commonly defined as the coincidence time resolution (CTR), unlike the terminology in high energy physics, where the CTR is usually reported in terms of $\sigma$. To convert from FWHM to $\sigma$, the expression $2\sqrt{2ln(2)} \cdot \sigma \approx 2.355\sigma$ is used. Constraining events to the photopeak region has the advantage of selecting events with most of the energy deposited inside the crystal and therefore producing the optimum amount of light, which in turn leads to higher photon statistics and less noise, both being beneficial to high time resolution. Furthermore, the difference in produced light has an effect on the skew of the time signal [7] and as such the introduces a jitter in the time stamp determination, the so-called time walk. This effect can be partly corrected for. The effect of photopeak selection on the CTR is demonstrated in figure 3.10 for the two cases, both time walk corrected, where one either takes all the measured events into account (left), leading in that case to a CTR of 240 ps FWHM, or if one only selects photopeak events (right), then significantly improving the CTR to less than 130 ps FWHM. Photopeak selection is particularly important in PET, since the selection of genuine photo-electric events reduces noise from random and scattered gamma incidences, and as such improves the image quality.

Typically CTR measurements are done at the lowest possible threshold to be sensitive to the first arriving photons from the gamma conversion. To asses the optimum threshold, the CTR is measured within a range of threshold values and plotted as shown in figure 3.11. As the figure shows, the CTR reaches a minimum towards low thresholds until it deteriorates due to noise. Although the increased CTR value towards higher thresholds is minimal for measurements with high photostatistics, as is the case in figure 3.11, this increase can be much steeper in cases where the photostatistics is so low that it has a significant influence on the CTR. To finally obtain the optimum CTR, the CTR spectrum is fitted with the following function:

$$CTR_{fit}(x) = \sqrt{p_1 x^{p_4} + \frac{p_2}{x^{p_5}} + p_3} \tag{3.5}$$

where x is the threshold and $p_n$ are the fitting parameters. The minimum of this fit gives the (optimum) CTR. Equation 3.5 is a modification, and as such a refinement, of the

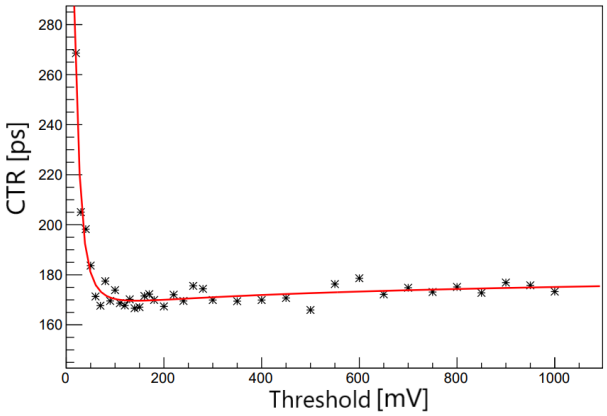


Figure 3.11: CTR measurement of a 3x3x20 $mm^3$ crystal glycerine coupled to a HPK S13360-3050 SiPM read out with NINO.

original function 3.6, as it shows better agreement with the data.

$$CTR(x) = \sqrt{p_1 x + \frac{p_2}{x^2} + p_3} \tag{3.6}$$

In both cases the first term represents the jitter in arrival time as a function of threshold, the second term describes the sensitivity of the CTR to the electronic- and dark noise when reaching very low threshold values, while $p_3$ is a global offset of the function.

The CTR also improves with a higher bias voltage applied to the SiPM, or rather overvoltage, i.e. the difference between the nominal bias and the breakdown voltage. The effect stems from an increase in both the PDE and signal-to-noise ratio of the SiPM in that regime. The best CTR values are therefore obtained slightly below the regime where the dark current begins to diverge due to spontaneous breakdowns in the avalanche region of the SiPMs.
To maintain an acceptable dark count rate in the SiPMs, the CTR is measured in a light-tight and temperature-controlled box held at a constant temperature of 18 °C±0.5 °C.

### 3.4.1 NINO Readout

The NINO chip [8] is an ultrafast amplifier-discriminator developed for the ALICE [9] experiment at CERN. Feeding the analog SiPM signal into the chip, the amplifying stages saturate and create a square wave when the signal exceeds a threshold determined by the user; owing to the time-over-threshold method the pulse width then contains information on the amplitude (and energy) of the signal. However, due to the non-linearity of the NINO chip, this method of encoding both the energy- and timing information in the same signal leads to an unwanted degradation of energy resolution at large input signals [5]. This results in a poor photopeak measurement and thereby deteriorates the CTR. To overcome this drawback, a special readout board was developed by Gundacker [5]. This board splits the signal from the SiPM into two parts: first, a *linear* part to be read out by a high speed operational amplifier to obtain the energy information of the event, and second the digital path where the signal is fed into the NINO chip to extract the time stamp. A LeCroy DDA735Zi oscilloscope serves as the data acquisition bench for both signals. The delay spectrum is derived from the two time stamps after prior selection of

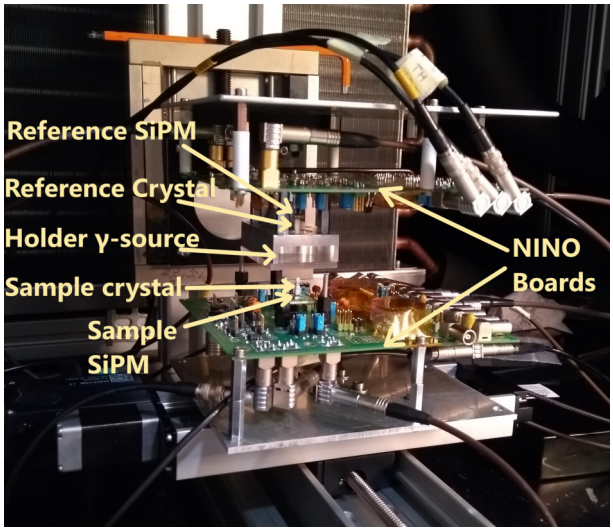


Figure 3.12: A picture of a CTR setup using NINO boards to read out the SiPMs.

the photoelectric events derived from the analog part.

### 3.4.2 High-Frequency Readout

The High-frequency (HF) readout was developed by Cates et al. [10] and refined by Gundacker [6] in our group. The high bandwidth of 1.5 GHz of this apparatus allows for higher signal slew rates [6], being particularly useful for the accurate measurement of the leading edge position of the pulse and thus the time stamp of the signal.
Like in the NINO readout, the HF-approach also splits the SiPM signal into two parts. One to serve as the linear analog signal for energy information and the other to deliver the time stamp.

## 3.5 Scanning Electron Microscopy (SEM)

Scanning electron microscopy (SEM) is an imaging technique that uses electrons for the visualization of the sample. The benefit of using electrons, compared to photons, is that one can go to much shorter wavelengths and therefore resolve smaller structures in the sample, even down to the nanometer scale. SEM uses a focused electron beam, scanning the surface of the sample, as shown in figure 3.13 [11]. The electrons of the beam can interact in two different ways with the atoms of the sample, i.e. either elastically or inelastically [12]. If the electrons scatter elastically in the sample, they will eventually exit from the samples' surface, in which case they are so-called back-scattered. On the other hand, if the scattering happens inelastically, it causes the electrons to slowly lose their energy and thus free secondary electrons and X-rays from the sample [12]. Also these electrons are used as a source for SEM imaging.
The electron beam scans the entire surface and dedicated detectors register the electrons, either back-scattered or otherwise, at every point of the beam position. This then develops the final image. It should be noted, that SEM can only image the surface of samples. Figure 3.14 shows an electron beam creating back-scattered and secondary electrons, together

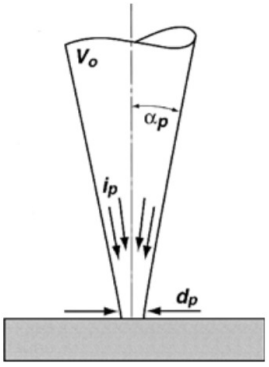


Figure 3.13: "Four major electron beam parameters are defined where the electron probe impinges on the specimen: electron probe diameter $d_p$, electron probe current $i_p$, electron probe convergence $\alpha_p$, and electron beam accelerating voltage $V_0$." [11]

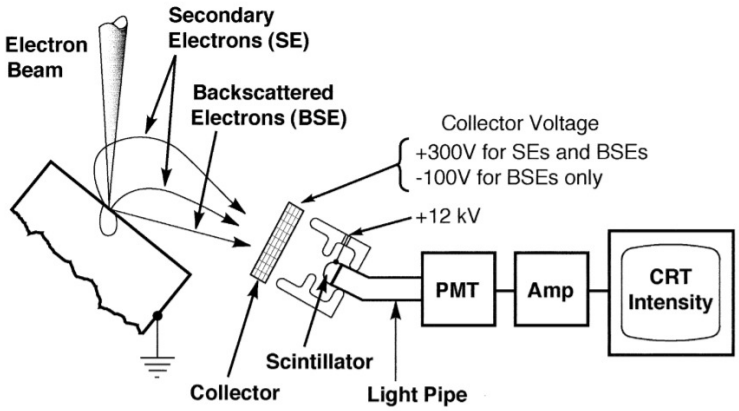


Figure 3.14: "Diagram showing backscattered and secondary electron collection of these signals by the Everhart–Thornley (E–T) detector." [11]

with a so-called Everhart-Thornley detector collecting their signal [11].

Since the electron beam delivers more electrons than actually being back-scattered or leaving as secondary electrons, there is a risk that the excess electrons would eventually charge up the sample [13]. However, if the sample is of conductive material, this charge can be drained to ground potential. For insulating materials, the accumulation of charge can go as high as that of the impacting electron beam, giving rise to electrostatic deflection of the beam itself [13]. These so-called charging effects lead to, among others, distortion of the image, bright spots and dark halos in the image [13]. To mitigate these image defects, one commonly deposits a thin conductive layer on the surface of the sample [13].

In this thesis, SEM is used to image the photonic crystal slabs produced on top of a scintillator surface (chapter 5 and 6). The difficulty of using an electron beam is that the scintillators, not being conductive, gradually collect charges on their surface, as discussed above, with the effect of distorting the image. What makes it worse, one cannot deposit a conductive layer on top of the photonic crystal slab, as this would render the crystal non-transparent and hence useless for further investigations. To overcome this effect, conductive tape was applied on all sides of the scintillator, not reaching into the zone of the photonic crystals. Nonetheless, SEM image quality turned out to be relatively

poor, but still allowed sufficient inspection of the photonic crystal pattern. The images produced in this work were taken with several different types of SEMs. All the SEM images produced at CERN were made with a Carl Zeiss LEO 430 microscope operated by the EN-MME-MM group of CERN [14]. Most of the images were taken with secondary electrons detected by an Everhart-Thornley Secondary Electron detector or in some cases with an InLens detector.

# Bibliography


[1] "Product description of the perkin elmer lambda 650 uv/vis spectrometer." `https://www.perkinelmer.com/lab-solutions/resources/docs/BRO_Lambda950850650Americas.pdf`. Accessed: 2020-05-26.

[2] M. Moszynski, M. Kapusta, M. Mayhugh, D. Wolski, and S. Flyckt, "Absolute light output of scintillators," *IEEE Transactions on Nuclear Science*, vol. 44, no. 3, pp. 1052–1061, 1997.

[3] R. Martinez Turtos, S. Gundacker, M. Pizzichemi, A. Ghezzi, K. Pauwels, E. Auffray, P. Lecoq, and M. Paganoni, "Measurement of lyso intrinsic light yield using electron excitation," *IEEE Transactions on Nuclear Science*, vol. 63, no. 2, pp. 475–479, 2016.

[4] S. Gundacker, R. Turtos, E. Auffray, and P. Lecoq, "Precise rise and decay time measurements of inorganic scintillators by means of x-ray and 511 kev excitation," *Nuclear Instruments and Methods in Physics Research Section A: Accelerators, Spectrometers, Detectors and Associated Equipment*, vol. 891, pp. 42 – 52, 2018.

[5] S. Gundacker, E. Auffray, B. Frisch, P. Jarron, A. Knapitsch, T. Meyer, M. Pizzichemi, and P. Lecoq, "Time of flight positron emission tomography towards 100ps resolution with l(y)SO: an experimental and theoretical analysis," *Journal of Instrumentation*, vol. 8, pp. P07014–P07014, jul 2013.

[6] S. Gundacker, R. M. Turtos, E. Auffray, M. Paganoni, and P. Lecoq, "High-frequency SiPM readout advances measured coincidence time resolution limits in TOF-PET," *Physics in Medicine & Biology*, vol. 64, p. 055012, feb 2019.

[7] A. Benaglia, S. Gundacker, P. Lecoq, M. Lucchini, A. Para, K. Pauwels, and E. Auffray, "Detection of high energy muons with sub-20ps timing resolution using l(y)so crystals and sipm readout," *Nuclear Instruments and Methods in Physics Research Section A: Accelerators, Spectrometers, Detectors and Associated Equipment*, vol. 830, pp. 30–35, 2016.

[8] F. Anghinolfi, P. Jarron, F. Krummenacher, E. Usenko, and M. C. S. Williams, "Nino: an ultrafast low-power front-end amplifier discriminator for the time-of-flight detector in the alice experiment," *IEEE Transactions on Nuclear Science*, vol. 51, no. 5, pp. 1974–1978, 2004.

[9] "Homepage of the alice collaboration at cern." `https://alice-collaboration.web.cern.ch/`. Accessed: 2021-01-13.

[10] J. W. Cates, S. Gundacker, E. Auffray, P. Lecoq, and C. S. Levin, "Improved single photon time resolution for analog SiPMs with front end readout that reduces influence of electronic noise," *Physics in Medicine & Biology*, vol. 63, p. 185022, sep 2018.

[11] J. I. Goldstein *et al.*, *Scanning Electron Microscopy and X-Ray Microanalysis, Chapter 2: The SEM and Its Modes of Operation.* New York: Kluwer Academic Plenum Publishers, 3 ed., 2003.

[12] J. I. Goldstein *et al.*, *Scanning Electron Microscopy and X-Ray Microanalysis, Chapter 3: Electron Beam–Specimen Interactions.* New York: Kluwer Academic Plenum Publishers, 3 ed., 2003.

[13] J. I. Goldstein *et al.*, *Scanning Electron Microscopy and X-Ray Microanalysis, Chapter 15: Procedures for Elimination of Charging in Nonconducting Specimens.* New York: Kluwer Academic Plenum Publishers, 3 ed., 2003.

[14] "Webpage of the cern en-mme group, of which the cern en-mme-mm is responsible for the material science and non-desctructive testing." `https://en.web.cern.ch/group/mme`. Accessed: 2021-01-13.

# Chapter 4

# Photonic Crystals

*Note, sections 4.2.4, 4.3 and 4.5 are based on the publication, "Photonic crystals applied to inorganic scintillators" by Salomoni and the author of this thesis et al. [1].*
As explained in chapter 2, the extraction of the scintillation light is intrinsically limited by the generally high refractive index of the scintillating crystals. This limitation can partly be overcome by the use of an optical coupling, e.g. optical grease or glue, attempting to match, as best as possible, the refractive index of the scintillator with that of the detector material. However, as explained in chapter 2.3, there still remains a mismatch in refractive index even when using optical grease. Furthermore, there are situations where it might not be possible to use a coupling agent at all. In such a scenario photonic crystals can play an important role, as they have the potential to increase the light extraction efficiency of inorganic crystals.
This chapter gives an introduction to the principle of photonic crystals (section 4.1) and a basic understanding of the theoretical background, and finally how they are applied to scintillators (section 4.2). An important aspect is to review production methods for photonic crystals (section 4.3) and to give a detailed explanation of the patterning methods for the produced prototypes (section 4.4). Finally, this chapter (section 4.5) discusses the simulation algorithms used in this thesis to asses the light extraction potential for different photonic crystal structures.

## 4.1 Introducing photonic crystals

Photonic crystals are periodic structures of two or more materials with different dielectric constants for which the scale of the periodicity is of the order of the wavelength of visible light. This creates a periodic electromagnetic field in the material that can interact with light inside the photonic structure. The periodicity of such structures can be one-, two- or three-dimensional, as illustrated in figure 4.1.

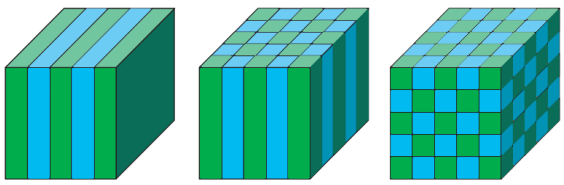

Figure 4.1: From left to right: examples of one-, two- and three dimensional photonic crystals. Different colors are materials with different refractive indices. Modified from [2].

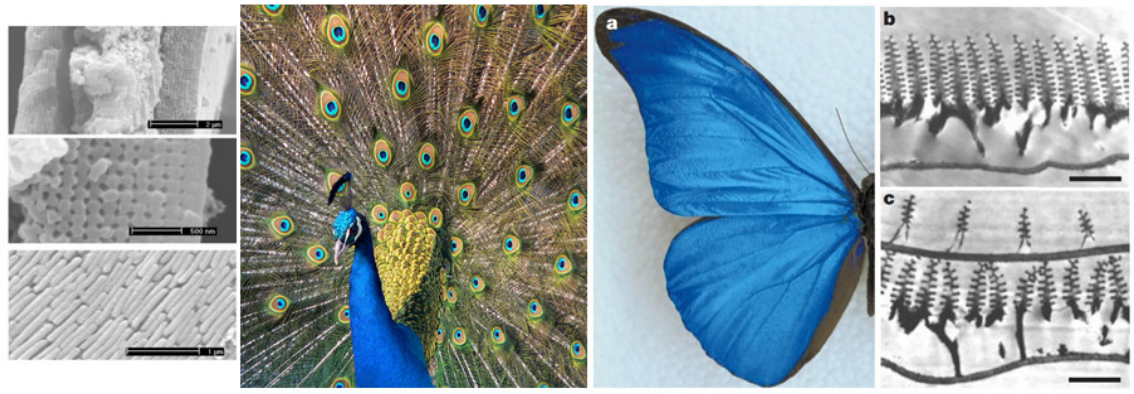


Figure 4.2: Left: Peacock feathers show iridescent coloring due to photonc crystal structures, SEM images taken from Zi et al. [3]. Peackock photo (cut) taken by BS Thurner Hof (GNU FDL). Right: The morpho butterfly has blue iridescent coloring on the wings due to tree-shaped photonic crystal structures, clearly visible on TEM images [4].

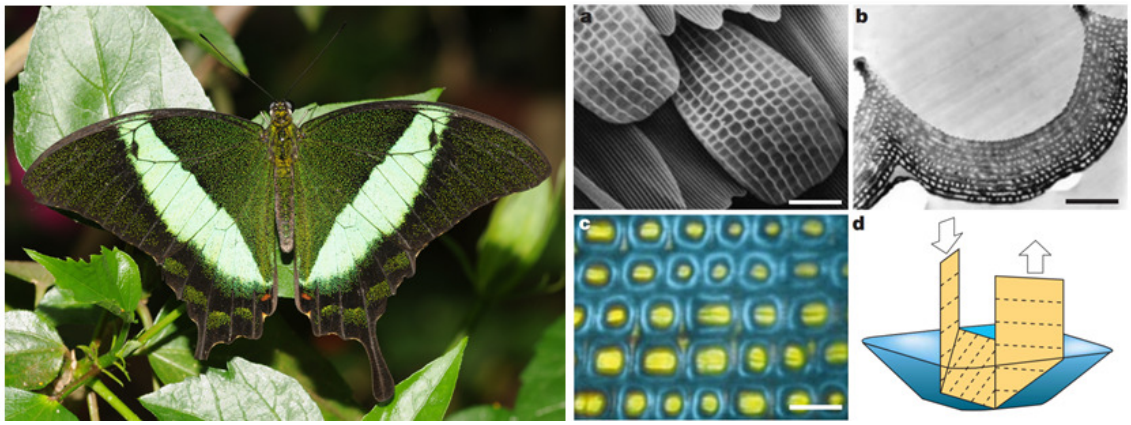


Figure 4.3: The Emerald Swallowtail is a butterfly with green iridescent colors, that are produced by photonic crystal structures allowing yellow light to be reflected from the center and blue light from the sides of the nano-structures [4]. Photo taken by Thomas Bresson (CC BY 2.0).

Photonic crystal structures are widely found in nature in the form of animal skins and plant surfaces, known for their iridescent coloring. Peacock feathers are an example of this effect and, seen under an SEM, show a typical periodic structure which is a photonic crystal structure (left hand side figure 4.2). Other examples are the wings of Morpho butterflies (right hand side figure 4.2), showing an even more spectacular, tree-shaped structure, producing its bright blue iridescent color. Figure 4.3 is a good example of wings of the Emerald Swallowtail with its microscopic, cup-like structure reflecting yellow light from the center of the cup and blue light from its sides, adding up to green. Photonic structures in nature are not only for the purpose of raising attention in wildlife, but also serve as tools to increase night vision of nocturnal animals where they act as anti-reflective layers in the case of e.g. moths (left hand side of figure 4.4), or as micro-lenses to focus light on photosensitive tissue of animals living in dark environments (right hand side of figure 4.4).

Artificial photonic crystals were first described in 1987 by Yablonovitch [6]. He sug-

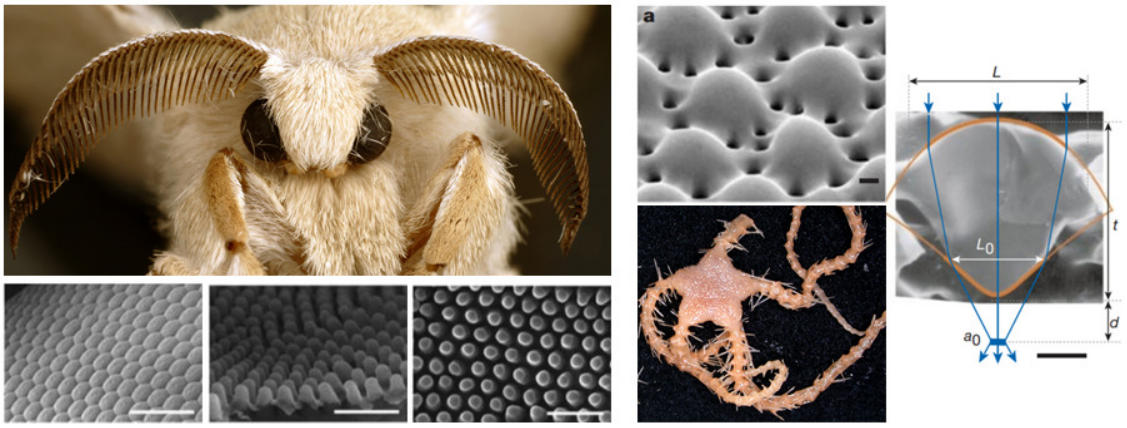


Figure 4.4: Left: Moths have a photonic crystal structures on their eyes, which function as an anti-reflective layer to help them see at night. SEM images taken from [5]. Photo (cut) from CSIRO (CC BY 3.0). Right: SEM images of a dorsal arm plate from the brittlestar Ophiocoma wendtii showing the microlenses. The SEM of an individual lens also shows the light paths in blue [4]. Photo (cut) from CSIRO (CC BY 3.0).

gested the use of three-dimensional photonic crystals as a means to limit spontaneous emission in semiconductor lasers, in hetero-junction bipolar transistors and solar cells, thus improving their performance. The same year, Sajeev published an article on using three-dimensional photonic crystals to restrict photons from escaping from certain parts of the photonic structure [7]. Both authors, already then, realized the connection between the bandgap structures for electrons in semiconductors and for photons in photonic crystals, which will also be discussed in the following sections.

## 4.2 Photonic crystals: a theoretical approach

### 4.2.1 The Maxwell equations

To understand the behavior of light, i.e. electromagnetic waves in photonic crystals one must start with the general description of electromagnetic dynamics. They are described by the Maxwell equations:

$$\nabla \times \mathbf{E} + \frac{\partial \mathbf{B}}{\partial t} = 0 \qquad (4.1) \qquad\qquad \nabla \cdot \mathbf{B} = 0 \qquad (4.3)$$

$$\nabla \times \mathbf{H} - \frac{\partial \mathbf{D}}{\partial t} = \mathbf{J} \qquad (4.2) \qquad\qquad \nabla \cdot \mathbf{D} = \rho \qquad (4.4)$$

where $\mathbf{E}$ and $\mathbf{D}$ are the electric and the displacement field, respectively, $\mathbf{H}$ and $\mathbf{B}$ the magnetic- and magnetic induction field, $\rho$ the free charge density and $\mathbf{J}$ the free current density. These four equations form the base of electrodynamics and are applicable in almost any situation.
Making specific assumptions about the system, these equations can be rewritten into equation 4.5, the derivation of which can be found in appendix C.

$$\nabla \times \left( \frac{1}{\epsilon(\mathbf{r})} \nabla \times \mathbf{H}(\mathbf{r}) \right) = - \left( \frac{\omega}{c} \right)^2 \mathbf{H}(\mathbf{r}) \qquad (4.5)$$

where $\omega$ is the frequency of the electromagnetic wave. This equation is called the Helmholtz equation, useful for the description of the system as an eigenvalue problem to be solved

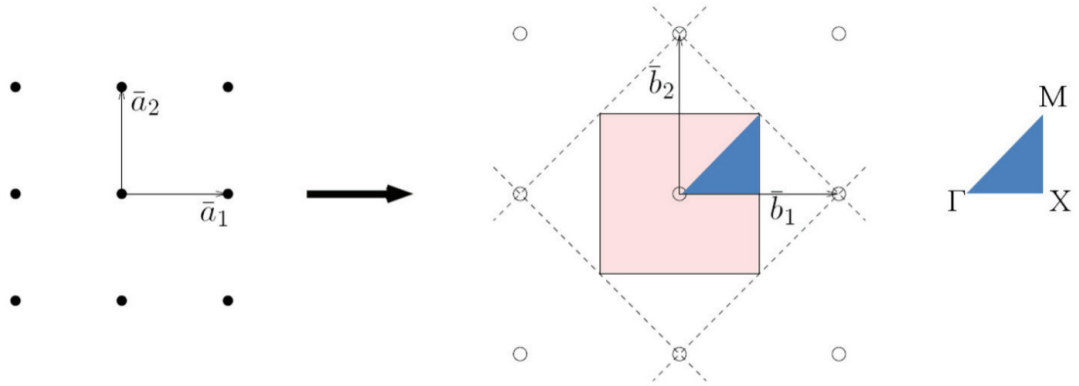


Figure 4.5: Square lattice in real space (left ), the corresponding lattice in reciprocal space (center) and its irreducible Brillouin zone with corners M, K and X (right). The Brillouin zone in the reciprocal lattice is colored pink, $\mathbf{a}_1$ and $\mathbf{a}_2$ are the lattice vectors and $\mathbf{b}_1$ and $\mathbf{b}_2$ the corresponding reciprocal lattice vectors. Image taken from [8].

for a given dielectric constant $\epsilon(\mathbf{r})$:

$$\hat{\Theta}\mathbf{H}(\mathbf{r}) = -\left(\frac{\omega}{c}\right)^2 \mathbf{H}(\mathbf{r}) \tag{4.6}$$

With $\hat{\Theta}F = \nabla \times \left(\frac{1}{\epsilon(\mathbf{r})}\nabla \times F\right)$, where F is an arbitrary function and $\hat{\Theta}$ a Hermitian operator. The solutions to this eigenvalue problem are the eigenmodes of the system that describe all the possible waves in the photonic crystal structure.

A similar expression can be derived for $\mathbf{E}(\mathbf{r})$, however $\mathbf{E}(\mathbf{r})$ can easily be reconstructed by inserting the solution for $\mathbf{H}(\mathbf{r})$ into the following equation:

$$\mathbf{E}\left(\mathbf{r}\right) = \frac{\imath}{\omega\epsilon_0\epsilon\left(\mathbf{r}\right)}\nabla \times \mathbf{H}\left(\mathbf{r}\right) \tag{4.7}$$

### 4.2.2 Introducing periodicity: Bloch modes and band diagrams

As stated in section 4.1, photonic crystals are periodic structures of two or more materials with different dielectric constants for which the scale of the periodicity is of the order of the wavelength of visible light. This periodicity can be in 1, 2 or 3 dimensions.
Let's assume a 2-dimensional photonic crystal, with pillars in a square lattice, as shown in figure 4.5 (left). The periodicity of the structure is described by two primitive lattice vectors, $\mathbf{a}_1 = a\hat{x}$ and $\mathbf{a}_2 = a\hat{y}$, with which the entire lattice can be described. The system is invariant over translation of any linear combination of these two lattice vectors.
The equivalent of this square lattice in *k-space* is depicted in figure 4.5 (center) and is called the reciprocal lattice. As its counterpart in real space, also the reciprocal lattice has two reciprocal lattice vectors; $\mathbf{b}_1 = \frac{2\pi}{a}\hat{x}$ and $\mathbf{b}_2 = \frac{2\pi}{a}\hat{y}$, with $\mathbf{a}_i \cdot \mathbf{b}_j = 2\pi\delta_{i,j}$ where $\delta_{i,j}$ is the Kronecker delta. Again, the system is invariant under translation of any linear combination of these two reciprocal lattice vectors. This also indicates that the entire lattice can be constructed by taking only a small part of the lattice and translating it over linear combinations of the reciprocal lattice vectors only. The smallest piece of the lattice with which it is possible to reconstruct the entire lattice, is called the Brillouin zone and is indicated in figure 4.5 (center) in pink. Still, there is a smaller part of the lattice that

already contains all the information of the entire lattice, which then can reconstruct the entire lattice by mirroring it and/or translating it over linear combinations of the reciprocal lattice vectors. This part of the lattice is called the irreducible Brillouin zone and is indicated in blue in figure 4.5 center and right.

In the previous section a differential equation for a general system has been derived without any specification for the dielectric constant $\epsilon(\mathbf{r})$ of the material. However, photonic crystals introduce the following constraint:

$$\epsilon(\mathbf{r}) = \epsilon(\mathbf{r} + \mathbf{R}) \tag{4.8}$$

where $\mathbf{R}$ is a linear combination of primitive lattice vectors:

$$\mathbf{R} = C_1\mathbf{a}_1 + C_2\mathbf{a}_2 \tag{4.9}$$

with $C_1, C_2 \in \mathbb{Z}$. Bloch's theorem states that in this case, the solutions to the differential equation 4.5 have the following shape:

$$\mathbf{H}_\mathbf{k} = \mathbf{u}_\mathbf{k}(\mathbf{r})e^{-\imath\mathbf{k}\cdot\mathbf{r}} \tag{4.10}$$

where $\mathbf{u}_\mathbf{k}(\mathbf{r})$ is a function with the same periodicity as the dielectric constant:

$$\mathbf{u}_\mathbf{k}(\mathbf{r} + \mathbf{R}) = \mathbf{u}_\mathbf{k}(\mathbf{r}) \tag{4.11}$$

for any linear combination $\mathbf{R} = C_1\mathbf{a}_1 + C_2\mathbf{a}_2$. The solutions of equation 4.10 are called Bloch states, showing the same periodicity as the medium in which they exist. Inserting equation 4.10 into the Helmholtz equation 4.5 makes the eigenvalue problem change slightly, in the following way [9]:

$$\nabla \times \frac{1}{\epsilon(\mathbf{r})}\nabla \times e^{\imath\mathbf{k}\cdot\mathbf{r}}\mathbf{u}_\mathbf{k}(\mathbf{r}) = \left(\frac{\omega(\mathbf{k})}{c}\right)^2 e^{\imath\mathbf{k}\cdot\mathbf{r}}\mathbf{u}_\mathbf{k}(\mathbf{r}) \tag{4.12}$$

$$(\imath\mathbf{k} + \nabla) \times \frac{1}{\epsilon(\mathbf{r})}(\imath\mathbf{k} + \nabla) \times \mathbf{u}_\mathbf{k}(\mathbf{r}) = \left(\frac{\omega(\mathbf{k})}{c}\right)^2 \mathbf{u}_\mathbf{k}(\mathbf{r}) \tag{4.13}$$

$$\hat{\Theta}_\mathbf{k}\mathbf{u}_\mathbf{k}(\mathbf{r}) = \left(\frac{\omega(\mathbf{k})}{c}\right)^2 \mathbf{u}_\mathbf{k}(\mathbf{r}) \tag{4.14}$$

with $\hat{\Theta}_\mathbf{k}F = (\imath\mathbf{k} + \nabla) \times \frac{1}{\epsilon(\mathbf{r})}(\imath\mathbf{k} + \nabla) \times F$. Now, the eigenvalue problem has been converted into one for $\mathbf{u}_\mathbf{k}$. Since $\mathbf{u}_\mathbf{k}$ is a periodic function where the Brillouin zone contains the information of the entire function, solving the eigenvalue problem can be restricted to this Brillouin zone. As a consequence, the solution to the problem leads to a discrete spectrum of degenerate eigenvalues [9] yielding an infinite set of modes with discretely spaced frequencies [9], for which each mode gives a continuous dispersion function dependent on $\mathbf{k}$ and which can be labeled by $m \in \mathbb{Z}$ indicating its mode. For further reading on solving the Helmholtz equation and examples, the reader is referred to [9], [10] and [11].

The ensemble of the modes for all the eigenvalues of the system defines the band structure of a photonic crystal. It can be plotted as a function of $\mathbf{k}_{//}$, with $\mathbf{k}_{//}$ being the wave vector in the two-dimensional plane that contains the periodicity. This plot then creates the band gap diagram. The most efficient way of containing all the information in the plot is to follow $\mathbf{k}_{//}$ over the three points, Γ, M and X, of the irreducible Brillouin zone as shown on the right hand side of figure 4.5. The left plot in figure 4.6 shows an example with a two dimensional photonic crystal consisting of pillars in a square lattice.

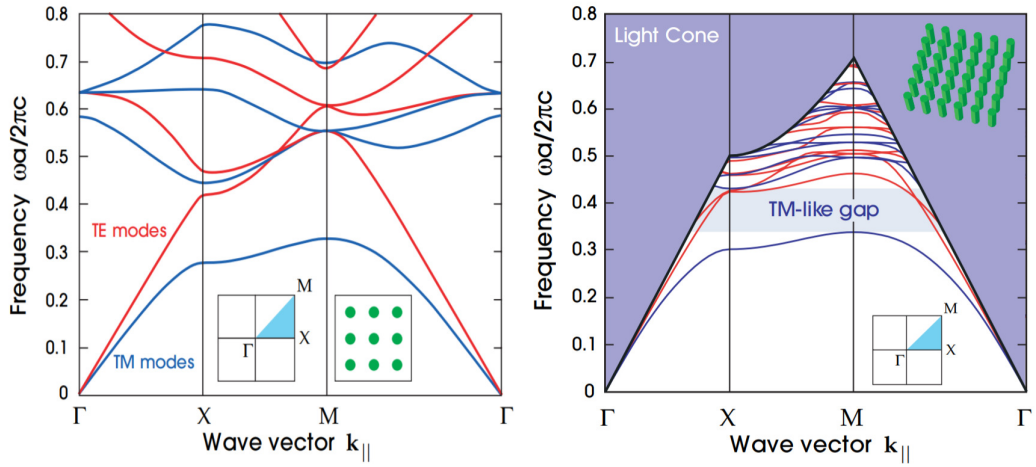


Figure 4.6: Left: Band diagram of a 2D photonic crystal of pillars in a square lattice (lower right, in green) in air. $\mathbf{k}_{//}$ lies in the plane in which the periodicity of the photonic crystal is contained. Image taken from [9]. Right: Band diagram for a photonic crystal slab with pillars in a square lattice (upper right corner, in green) suspended in air. The purple shaded area represents the light cone, i.e. modes in this region propagate into the air. Below the light cone are the modes localized in the slab. Image taken from [9].

### 4.2.3 Photonic crystal slabs: towards light extraction

To improve the extraction of light from inorganic scintillating crystals, this thesis investigates the potential of so-called photonic crystal slabs. These slabs are similar to two-dimensional photonic crystal structures, however, instead of having a constant value of the dielectric constant in the third dimension, i.e. $\epsilon(x, y)\ \hat{z} = constant$ for any $z \in \mathbb{R}$, their periodic structure extends only over a limited region into the z-direction, i.e. $\epsilon(x, y, z)\ \hat{z} = constant$ but only for $0 < z < l$, with $l$ being the physical thickness of the slab.
Because of this additional restriction to the eigenvalue problem in equation 4.14, the solutions and thus the band structure of the system are different. The resulting band structure, assuming the entire slab suspended in air, is visualized in the right plot of figure 4.6. Since the slab has a limited thickness there is a light cone indicating the modes that can propagate into air, also called "leaky" modes. It is through these modes, that light extraction from a scintillator can be enhanced.
Now consider an inorganic scintillator with a photonic crystal slab on the readout face. The $\mathbf{k}_{//}$ component of the electromagnetic waves (light) inside the scintillator, reaching the slab interface from outside the extraction cone, will couple to the degenerate modes $\mathbf{k}_{m,//} = \mathbf{k}_{//} + \mathbf{mG}$, with $\mathbf{mG}$ any linear combination of reciprocal lattice vectors. From these modes, the leaky ones still radiate into the ambient medium.

To explain the effect of a photonic crystal slab on light extraction from high refractive index (RI) material in a more comprehensive way, first let's consider the situation of an inorganic scintillator, with RI=$n_{sc}$, surrounded by a (ambient) material with RI=$n_{am}$. In the scintillator, an electromagnetic wave (light) with the wave vector $\mathbf{k}$ reaches the scintillator readout face. When the electromagnetic wave passes the scintillator-ambient interface, the component of its wave vector parallel to the interface, $\mathbf{k}_{in,//}$, is conserved. Therefore:

$$\mathbf{k}_{out,//} = \mathbf{k}_{in,//} = \mathbf{k}_{//} \tag{4.15}$$

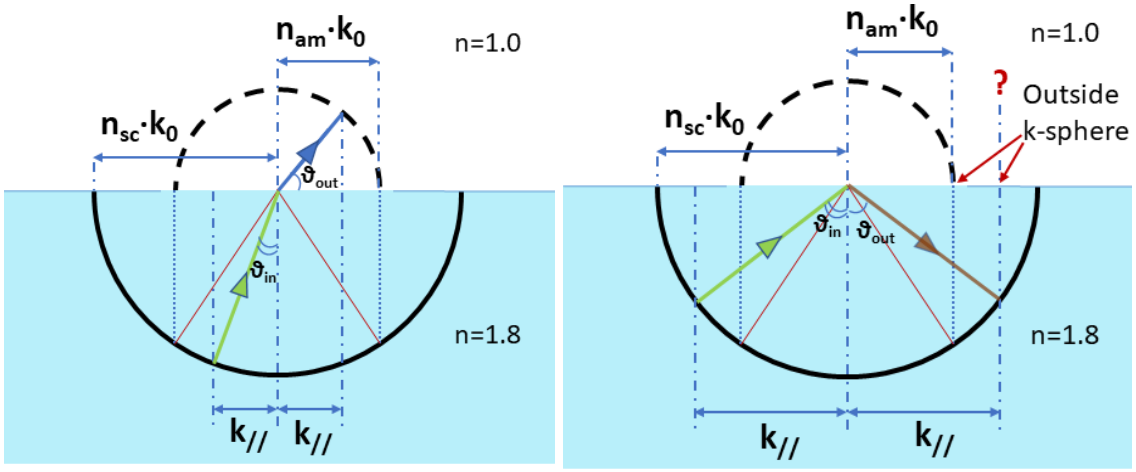


Figure 4.7: K-space diagrams of electromagnetic waves travelling inside a scintillator (n=1.8) entering a scintillator/air interface, from *inside* (left) and from *outside* (right) the extraction cone. The radius of the k-space half-sphere of the incoming wave is given by its wave number $|\mathbf{k}| = n_{sc}|\mathbf{k}_0|$ and the one of the outgoing wave is determined by conservation of energy to be $|\mathbf{k}| = n_{am}|\mathbf{k}_0|$. The position of the outgoing wave on the corresponding half-sphere is determined by the condition that $\mathbf{k}_{//}$ is conserved, in the right diagram there is no position following this condition on the outgoing k-space half-sphere. The red lines show the limits of the extraction cone.

The conservation of $k_{//}$ and the conservation of energy, expressed by:

$$E = \hbar\omega = \hbar\ c\ k_0 = \hbar\ c\ \frac{|\mathbf{k}|}{n} = \hbar\ c\ \frac{\sqrt{(k_\perp)^2 + |\mathbf{k}_{//}|}}{n} \tag{4.16}$$

with $k_0$ the wave number in vacuum, lead to an expression for the transverse component $\mathrm{k}_{out,\perp}$ of the wave vector:

$$k_{out,\perp} = \sqrt{\frac{n_{amb}^2\omega^2}{c^2} - |\mathbf{k}_{//}|} \tag{4.17}$$

Therefore, $|\mathbf{k}_{//}| > n_{amb}^2\omega^2/c^2$ leads to an imaginary value for $k_{out,\perp}$, meaning that the electromagnetic wave is evanescent as it decays exponentially into the ambient medium, i.e. it does not effectively travel outside the crystal, but rather is reflected into the scintillator; it is outside the extraction cone.
The effect of equations 4.15-4.17 is shown in figure 4.7, containing 2 two-dimensional k-vector diagrams illustrating the available states in k-space for light from inside- (left) and outside (right) the extraction cone. It shows the situation at the scintillator-ambient interface with the two half-spheres of the available states in k-space corresponding to the incoming and outgoing electromagnetic wave. The radius of the half-sphere of the incoming wave (solid circle) is given by its wave number $|\mathbf{k}| = n_{sc}|\mathbf{k}_0|$ and the one of the outgoing wave (dashed circle) is determined by conservation of energy to be $|\mathbf{k}| = n_{am}|\mathbf{k}_0|$.
For the case of light being inside the extraction cone, and under the condition that $\mathbf{k}_{//}$ is conserved, one can easily determine the position of the k-vector on the outgoing half-sphere, as well as its outgoing angle $\theta_{out}$ (see figure 4.7 left). On the other hand, the right diagram in figure 4.7 shows that, for light from outside the extraction cone, there is no state for the k-vector on the outgoing k-sphere that satisfies the above condition of $\mathbf{k}_{//}$ being conserved.

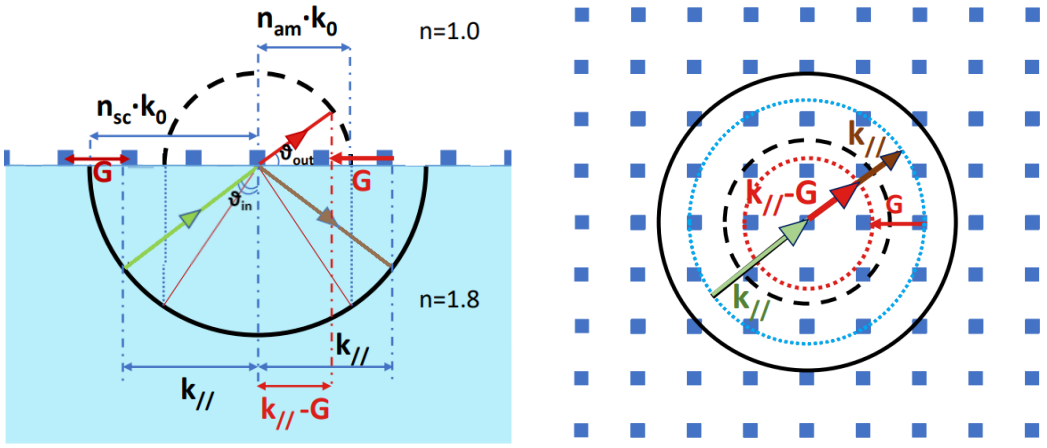


Figure 4.8: k-space diagram of an electromagnetic wave travelling inside a scintillator (n=1.8) and entering a scintillator-air interface with a photonic crystal structure. Left: the transverse view of the crystal geometry, with its corresponding k-space vectors; right: projection of the same geometry.

Figure 4.8 left shows the same situation for light outside the extraction cone, however, this time where a photonic crystal slab, with reciprocal lattice vectors $|G_x| = |G_y| = G$, is present at the interface. Without the photonic crystal layer all light from outside the extraction cone would be back reflected into the scintillator, as illustrated in figure 4.7 right. In this case, however, the photonic crystal slab enables part of the wave with $\mathbf{k}_{//}$, although outside the extraction cone, to couple to degenerate modes with a parallel component of the wave vector $\mathbf{k}_{//} + \mathbf{mG}$ in the slab. Some of these modes correspond to a state on the outgoing k-sphere and as such propagate into the ambient medium. Figure 4.8 right shows the same space-diagram from the top. The black solid circle represents the k-space half-sphere of the incoming electromagnetic wave from the scintillator and the green arrow is its $\mathbf{k}_{//}$. The dashed black circle corresponds to the available states in air for the outgoing wave. The brown vector is the $\mathbf{k}_{//}$ of the outgoing wave prior to coupling to any of the degenerate modes. Since it lies outside the dashed black sphere, it is consequently back reflected into the scintillator. As shown in figure 4.8 right, part of this outgoing wave couples to the degenerate modes with $\mathbf{k}_{//} + \mathbf{mG}$, some of which lie inside the dashed black circle, i.e. they escape from the crystal.

One should be aware that, while electromagnetic waves from outside the extraction cone can couple with harmonics from the photonic crystal slab of which some can still propagate into air, the opposite can also happen. Waves from inside the extraction cone that would normally be extracted completely can also couple to harmonics in the photonic crystal slab placing them, now, outside the extraction cone. This effect decreases the light extraction from the scintillator. Therefore, a proper balance has to be found between an increase in mode-extraction from outside the extraction cone and a decrease of light extraction from inside the extraction cone.

### 4.2.4 Conical structures: a different approach

While the photonic crystals can be used to diffract light, both inside and outside the extraction cone, there is also another approach: the anti-reflective coating. The anti-reflective coating does not increase extraction of light from outside the extraction cone,

but it eliminates Fresnel reflection (appendix E) for light from inside the extraction cone, improving the net light extraction. This anti-reflective behavior of the so called moth-eye structures, inspired by nature, is achieved by their conical shape, with a high aspect ratio and a sub-wavelength periodicity, creating a gradient in refractive index between the high- and low RI medium [12]. This effectively matches the RI of both media.
Though the refractive index of scintillators is much larger than that of air, e.g. in the case of LYSO the RI=1.8, the gain in extracted light that can be obtained by defying Fresnel reflection is limited. When using conical structures with a periodicity larger than the wavelength of the scintillation light, the structure will both exhibit index matching behavior of the anti-reflective coating and diffraction behavior as described before.

### 4.2.5 Improved light extraction from inorganic scintillators: the importance of the refractive index

One approach to increase light extraction is to engineer the photonic structure of high refractive index, to benefit most from its diffracting behavior [13]. In the case of index matching, the optimum is to design an effective refractive index at the scintillator surface that matches that of the scintillator bulk material itself. For a photonic crystal slab of cones with a period equal to their base diameter imprinted on a LYSO scintillator with RI=1.8, that optimal refractive index would be 2.0, see appendix D for details. In the case that the cones' diameter is smaller than their pitch, this leads to an increase of the optimal refractive index.
It is also important to consider absorption in the photonic crystal material, which is expressed by the imaginary part of the refractive index. One could wonder whether the absorption in a material whose thickness is of the scale of the wavelength of the light itself is still important. The answer to this is found in the wave functions of the electromagnetic waves themselves. Consider a Bloch state in a photonic crystal with complex refractive index $n' = n + \imath n''$:

$$\mathbf{H_k} \propto A_0\ e^{\imath \mathbf{k}\cdot\mathbf{r}} = A_0\ e^{\imath n' \mathbf{k}_0\cdot\mathbf{r}} = A_0\ e^{-\imath(n+\imath n'')\mathbf{k}_0\cdot\mathbf{r}} = A_0\ e^{-n''\mathbf{k}_0\cdot\mathbf{r}} e^{\imath n \mathbf{k}_0\cdot\mathbf{r}} \tag{4.18}$$

This leads to an expression where one factorizes out the real and imaginary part of the field $\mathbf{H_k}$. Or, in other words, with a real amplitude:

$$A(\mathbf{r}) = A_0\ e^{-n''\mathbf{k}_0\cdot\mathbf{r}} \tag{4.19}$$

leading to the following expression for the amplitude of the electromagnetic wave after traveling over a distance d:

$$A(d) = A_0\ e^{-n'' k_0 d} = A_0 e^{-2n''\pi d/\lambda} \tag{4.20}$$

with $\lambda$ the wavelength of the electromagnetic wave. This expression shows that the imaginary part of the refractive index introduces a damping factor reducing the amplitude of the electromagnetic wave exponentially over distance. As such, the absorption of the photonic crystal slab is significant despite its small thickness being only of the order of the wavelength of light.

## 4.3 Production methods for photonic crystals

In the beginning of the sixties of the last century, the first integrated circuits were produced using contact- or imprint lithography. A so-called mask was produced by cutting a

piece of blue-light-blocking plastic sheet to the desired shape, which was then repeatedly exposed to a photosensitive polymer on top of a layer of chromium on a large quartz plate [14]. Afterwards, the plate would be developed and the chromium etched away to obtain what is called the mask. After making usable copies of these masks, they were directly placed on top of a resist film to stamp the desired pattern. Patterns that were produced at that time only had a resolution of the order of 10 $\mu$m [14]. Ever since, the micro- and nano-electronics industry has been pushing the limits of these techniques, mainly investing in optical lithography for its high throughput, and electron- and laser lithography to develop the high resolution masks needed for optical lithography. Quickly, this high-tech industry was able to develop and improve new techniques, leading to structures at the scale of 20 nm with high throughput.

Even though nano-patterning techniques are well established today in nano-electronics industry, these processes generally need adjustments and further improvements to be applicable to the patterning on inorganic scintillators. The most common issues encountered when transferring these techniques to inorganic scintillators are either intrinsic to the scintillator material itself or simply due to technical issues linked to the handling of the equipment. An example of such an intrinsic issue is that inorganic scintillator surfaces easily charge up by the electron beam during the lithography process as they are highly non-conductive in contrast to silicon wafers. This effect leads to defects and a notable reduction in feature resolution. As described in [15], a thin conductive layer on the surface of the scintillator could alleviate this problem by sufficiently reducing the charging effect. Another common problem, though more on the technical side, is that scintillators of half a centimeter or more in size simply do not fit into the patterning equipment usually designed for thin silicon wafers.
There are methods that allow direct imprint of the photonic layer onto the scintillator. On the other hand, other imprint methods use an intermediate production step, where the material needed for the photonic structure production is deposited on top of the final layer to be imprinted. Therefore, the intermediate pattern needs to be transferred to the final material, usually achieved through etching techniques. Skills in transferring the pattern are equally important as the patterning itself. The resistance of the material chosen for the first imprinting step to the etching process *and* the resistance of the material where the pattern will be transferred to, both largely decide how high the nano-structures can be made and to what feature resolution, in all dimensions. Furthermore, if the pattern is to be produced on thick, non-conductive, scintillating crystal material, this causes extra challenges in terms of electrostatic distortion in the development of the etching process. For further explanations on etching techniques the reader is referred to [16].

### 4.3.1 Optical Lithography

As mentioned before, optical lithography has received its main focus in the micron- and deep submicron-electronics industry, particularly for high-density chip manufacture. This is because of its facility to pattern large surfaces in one go and the ease of producing a large number of surfaces using masks that can be re-used many times in this contactless patterning method. Sometimes a mask is not even required. As a result, this is a highly developed technology in terms of high resolution and high throughput.
There are multiple optical lithography techniques, such as optical projection lithography and light interference lithography, all being discussed below.

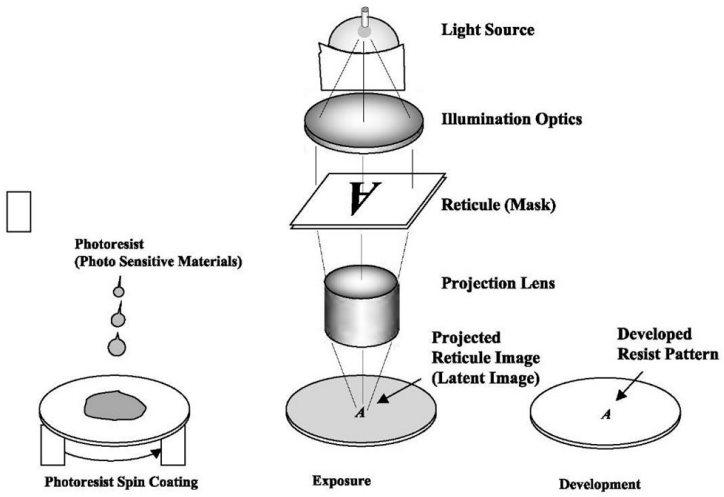


Figure 4.9: Schematic overview optical projection lithography [17].

#### 4.3.1.1 Optical Projection Lithography

In optical projection lithography, a mask with a copy of the final pattern is used to project light on a photosensitive resist, thus developing it. After the resist is sufficiently developed, the pattern can be transferred to another layer, whether the final or intermediate layer, through reactive ion etching. Figure 4.9 illustrates this process. A large surface is illuminated with the required pattern in one step, which makes this technique intrinsically fast and attractive. The production time is mainly limited by the exposure time needed for the resists [14]. On the other hand, the needed masks are expensive to fabricate, and also the optical system needed for the lithography process is rather costly, therefore this method has its merits only if large quantities of patterns are required [18].
The resolution of the pattern is mainly limited by the wavelength of the used light [14], but also by the numerical aperture [2]. To increase the resolution, a shorter wavelength and larger aperture can be used, while the depth of focus has to be maintained. For this purpose, deep UV patterning techniques have already been developed in the early '90s, where wavelengths down to 193 nm could be used. The development of *immersion* lithography permitted even further increases in numerical aperture, with a maximum of 1.35 [19][18]. This led to a maximum patterning resolution of $\sim$36 nm [19]. More recent developments, using extreme UV light at 13.5 nm, enabled the production of structures with a state-of-the-art feature resolution of $<$20 nm [19].

#### 4.3.1.2 Light Interference Lithography

In light interference lithography the final pattern is created by an interference pattern of multiple coherent light beams. Depending on the desired pattern, the light beams create the interference pattern either without the need of a mask or by passing through simple masks, as illustrated by figure 4.10.
The masks used in this technology, if ever needed, are much simpler to fabricate than the type of masks needed in optical projection lithography. This makes the production of the masks much less expensive, therefore rendering this patterning technique generally more cost effective than optical projection lithography (section 4.3.1.1), while still benefiting from re-using the mask and illuminating large surfaces in one go. Note also that the optics used in *interference* lithography systems are usually less expensive than those for

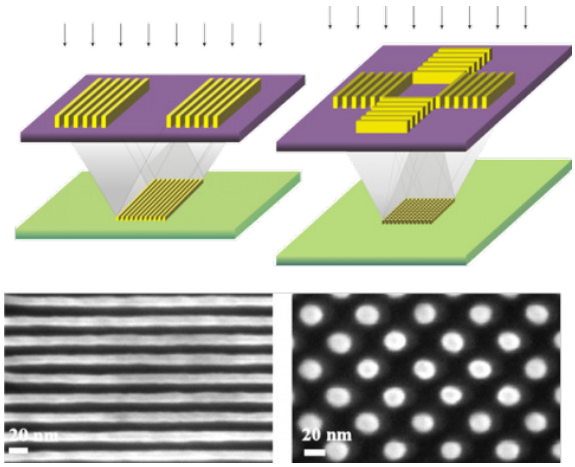


Figure 4.10: Schematic overview optical projection lithography [20].

*projection* lithography.
A principal drawback of this technique, however, is that patterns are limited to periodical structures of lines or dots [18]. Since photonic crystal patterns are effectively such periodic structures, this patterning method could still open up cost effective solutions for producing photonic crystal slabs, even at large quantities.

### 4.3.2 Scanning beam lithography

#### 4.3.2.1 Electron-beam lithography

Electron beam (e-beam) lithography was first developed in 1960 [21] and based on the same principle as scanning electron microscopy (SEM) (section 3.5), but using higher energies. A focused electron beam is used to expose a resist to be developed after using chemical methods. Depending on the used tone of the resist, positive or negative, the chemical development either washes away the areas that are exposed by the e-beam, or those that have not been exposed, respectively. Usually reactive ion etching is used at a third step to transfer the pattern to the final layer (note: there are also other techniques for the transfer of the pattern, see reference [21]).
Since this lithography method uses electrons instead of light, the resolution of the patterning is not limited by the wavelength of the light. Therefore, this method can produce patterns with much higher structure resolution compared to the different types of light lithography discussed above. Electron beam lithography provides the highest resolution of all lithography methods, limited mainly by electron scattering in the resist layer, but still resulting in a maximum resolution of a few nanometers [21].
Since the pattern is directly engraved into the resist by the focused e-beam, one does not need a (expensive) mask in this process. This also gives the freedom to produce patterns of any desired shape.
On the other hand, this patterning technique is intrinsically slow, for only one single electron beam is able to scan the entire surface to be imprinted. Even if the surface is of the order of only 1 $mm^2$ this process may take the order of days, depending on the desired feature size of the pattern. Another limitation to the writing speed is Coulomb scattering of the electrons in the resist, which effectively defocuses the e-beam and thus prohibits an increase in applied beam currents. Also, the resists made for higher resolution and higher aspect ratios in the final pattern, require a longer beam exposure time. In summary,

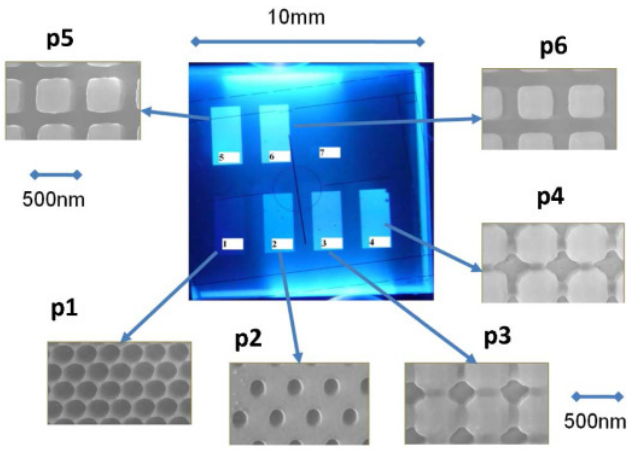


Figure 4.11: PhCs produced with e-beam lithography in ($Si_3N_4$) on a scintillator [15].

this patterning technique is very time consuming and hence very expensive. Attempts to circumvent some of these intrinsic limitations, such as implementing multiple e-beams, turned out to be rather unsuccessful until now [14]. Nonetheless, e-beam lithography remains an interesting technology for prototyping samples with highest required resolution. In view of the high costs and long production times, this technique is not scalable to large surfaces and/or large amounts of samples. It has, however, been used for the production of the first photonic crystal slabs tested by the Crystal Clear group at CERN and in collaboration with the Lyon Institute of Nanotechnology (INL) [22]. Figure 4.11 shows a UV-excited photo of the various photonic slabs produced on a scintillator, denoted as P1-P6, with their corresponding SEM images showing the details of the pattern.

#### 4.3.2.2 Focused ion-beam lithography

The focused ion-beam (FIB) lithograph in fact can be used either as a microscope operating at low energy and as a milling machine when it operates at higher energies, as illustrated on the left hand side of figure 4.12.
Ions do not exhibit space charge effects as strongly as electrons do and therefore in principle ion-beam lithography is capable of patterning with even higher resolution and in a shorter time. One very significant advantage of ion-beam lithography, as compared to e-beam lithography, is that the ion-beam can be used as a direct imprinting tool, meaning that it can carve the pattern directly into the final photonic crystal layer. This one-step process, called milling, makes it substantially faster and less prone to defects compared to e-beam lithography. One should bare in mind, however, that although faster than e-beam lithography, ion-beam lithography is still limited by low speeds and high costs, and should therefore be reserved to prototyping at highest precision.
First samples with this production method were produced on thin LYSO slices by Modrzynski et al. [23]. This thesis investigated the method after having produced a photonic crystal slab of holes in a layer of $TiO_2$ on the readout surface of a small LYSO pixel of 3x3x15 $mm^3$. A first visual inspection of the crystal and the subsequent transmission- and light yield measurements, however, revealed an unexpected loss in transparency of the crystal with its photonic layer. Upon further investigation made with energy-dispersive X-ray analysis during SEM, it was found that gallium ions from the ion-beam were implanted involuntarily in the $TiO_2$ layer causing the high absorption of light (see right

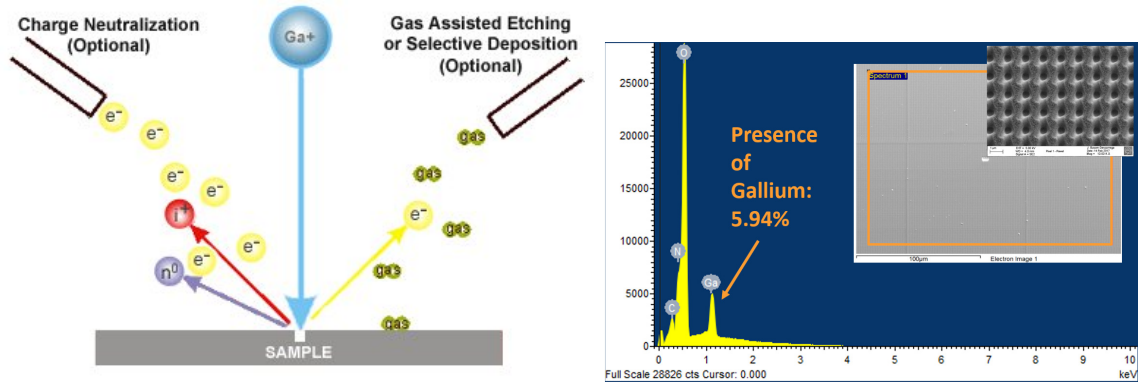


Figure 4.12: Left: Focused beam of gallium ions milling a small hole in the sample. The material of the sample leaves the hole in the form of secondary ions (i+ or i-) or neutral atoms [23]. Right: Energy-dispersive X-ray spectrum of part of the with FIB imprinted $TiO_2$ slab on a 3x3x15 $mm^3$ LYSO cube, showing 5.94% presence of gallium atoms. The top right corner shows the studied surface (two different zooms).

hand of figure 4.12). Therefore, it was concluded that, at first hand, gallium-based FIB is not suitable for the production of photonic slabs for applications on scintillating crystals. Instead Xenon-based FIB was suggested, however, still not guaranteeing the absence of implantation of these ions into the substrate. More research is therefore needed to mitigate the implantation of beam ions while maintaining an efficient milling process for optical applications.

### 4.3.3 Nano-imprint lithography

Contrary to the patterning techniques discussed before, nano-imprint lithography does not rely on radiation to imprint a pattern, but rather makes use of mechanical deformation by pressing a stamp into a resist material. Therefore, in nano-imprint lithography a high-resolution stamp or mask needs to be produced beforehand. The resist can be a thermoplastic, photo- or thermally curable layer [14].
In case of a thermoplastic resist, the resist is deposited as a solid layer on the surface of the substrate. Then the stamp is placed on this layer, with heat and high pressure applied [14] [24]. The heat makes the resist melt, while the pressure of the stamp ensures it to penetrate completely into the structure of the mold, which then engraves the pattern into the resist. Thereafter, the sample is cooled to solidify the resist. In the case of a curable resist, the layer applied to the substrate is a liquid, therefore only low pressure is needed to imprint the pattern with the stamp. After placing the stamp in contact with the resist, the layer is cured by heat or UV light or a combination of the two. This reduces the mechanical stress on the stamp and also avoids high temperatures that could cause damage to the sample.
Since the success of the nano-imprint lithography is completely dependent on the quality of the stamp, the main limitation for the resolution of the obtained structure is the resolution of that stamp. This is an advantage over the imprinting techniques based on radiation. Another advantage is the possibility to fairly easily produce 3D structures like pyramids or cones. Furthermore, the technique is very fast since it can imprint the entire surface of several square centimeters in one step. Unlike the previous techniques using beams, this process is scalable, in other words it is capable of imprinting large amounts of scintillator

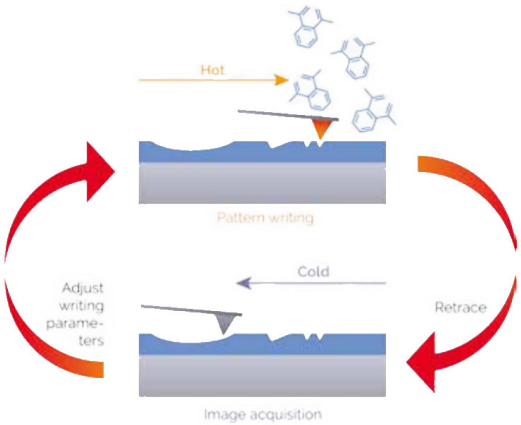


Figure 4.13: Illustration of the patterning process with the NanoFrazor [25], which implements thermal scanning probe lithography. It can image the produced patter during the patterning process and as such can compensate for upcoming patterning defects.

surfaces with a single stamp without resorting to time consuming alignment processes [14][18][24]. This type of imprinting can be used in two different ways. One possibility is to imprint an intermediate layer to be used as a mask for etching and then to transfer the pattern to the final material. The other possibility is to directly stamp the pattern into the final layer [14].
Although being scalable, the production of the stamp itself is still a time consuming and costly process, this being most likely the main drawback of this technique. Also, the mask will eventually wear out and get damaged because of its repeated contact with the substrates, and at some point, will have to be replaced [14] [18]. There are, however, means to produce inexpensive replicas of a master stamp. This partly compensates the production costs.

### 4.3.4 Scanning probe lithography

Scanning probe lithography is a technique where a mechanical probe is used to scan the surface and either add or carve away material on the surface. In this way a nanopattern can be created with high resolution. Yet, like scanning beam lithography techniques, scanning probe lithography faces the challenge of throughput. The technique is limited by the time the probe needs to interact with the material to be patterned. As a result, the patterning speed is comparable to that of e.g. an ion-beam. It is possible however to produce 3D structures with this technique. This would make it interesting for prototyping and also research on more complex photonic crystal structures.
An example of a commercially available scanning probe lithography device is the NanoFrazor, developed by SwissLitho and now in possession of Heidelberg Instruments [26]. This is a thermal scanning probe. It uses an atomic force microscope (AFM) cantilever to scan the surface to be patterned. Thereby, the cantilever is heated and thus melts away the resist where desired. While moving forward and being hot, the cantilever patterns the resist and, by moving backwards without being heated, it images and verifies via its AFM capabilities the pattern it had just engraved. This twofold functionality of the NanoFrazor is illustrated in figure 4.13. The system is rather simple, at least compared to e-beam lithography, for it does not need high beam currents or a vacuum environment. Another advantage over e-beam lithography is that patterns with smoother edges can be produced [27], however in only one available resist, i.e. polyphthalaldehyde (PPA). This constraint

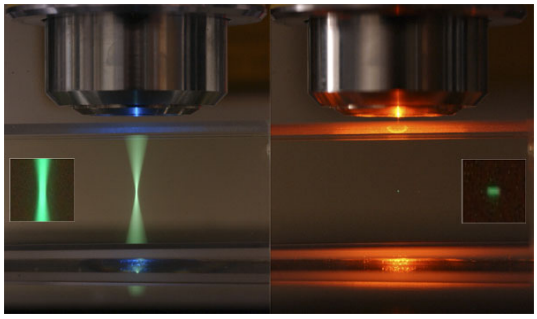

Figure 4.14: "The image was taken on a Zeiss LSM NLO system using a Nikon D1X digital camera. The sample is a dilute fluorescine solution in a quartz cuvette. No image manipulation was performed (except for creating the magnified insert)." Left: "The scanning blue (488nm) laser excites an entire column of sample." Right: "The scanning IR pulse laser (Zeiss NLO system) excites only a small spot of sample. " [29]

is the main limitation of this patterning device as far as our applications are concerned, because the pattern would have to be transferred to another layer, e.g. $TiO_2$ or $Si_3N_4$, the latter of which being commonly used. However, since the etching selectivity between PPA and $Si_3N_4$ is limited, only allow structures of up to ∼300 nm height can be built [28]. On the other hand, what makes this lithography method stand out positively compared to the others is its ability to produce more complex photonic structures that e.g. take into account the internal light distribution in the scintillator across the readout surface. This optimizes light extraction, particularly at the edges of the scintillator.

### 4.3.5 Two-photon lithography

Two-photon lithography is a method where two laser beams are used to directly imprint a photosensitive layer. Since this method works with overlapping beams and since the development of the photosensitive material only occurs at the crossing of the two beams, one can produce complex 3D structures with high resolution. This is the same principle which two-photon microscopy relies on, as illustrated in figure 4.14. A single-photon beam makes an exposure all the way along the beam, strongest at the focal spot if there is one, whereas the two-photon method provides exposure only at the spot where the two beams overlap. This, by principle, gives the highest resolution in all three dimensions from the exposure to the photons.
An example of an industrially available device is the Nanoscribe, produced by the company of the same name, a spin-off of Karlsruhe Institute of Technology [30]. It is principally a 3D-printer using two photon beams with a wavelength of 780 nm (NIR) [31] allowing, by the principle of 2-photon absorption, the polymerization of UV sensitive resins (780/2 = 390 nm) [32]. The parts of the resin that are exposed to the laser spot where the two-photon absorption takes place, polymerize and thus become solid. After washing away the unexposed resin the designed nano- (or micro-) structure is left. The size of the photonic structures needed for enhanced light extraction from the crystals is probably at the limits of the device's capabilities.
After the production of a structure other materials can be deposited on the resin, using e.g. atomic layer deposition, chemical- or physical vapor deposition, galvanization or electroplating [33]. This is specifically interesting when structures with high refractive indices are required, since in general the resins are limited to materials with a refractive index of

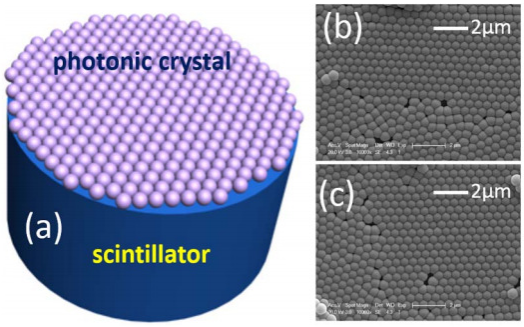


Figure 4.15: Photonic crystals produced with self-assembly of polystyrene nanospheres and a deposited conformal layer of $TiO_2$.(a) Schematic illustration of the photonic crystal structures covered on the surface of scintillator. (b), (c) SEM images of photonic crystal structures on the surface of LYSO scintillators A and B, respectively [36].

below 1.8 [34]. An example would be to deposit a $TiO_2$ layer on the resin structure [34]. Unfortunately, the resins used in the Nanoscribe machine absorb light emitted from L(Y)SO scintillation. To avoid this absorption in or near the emission of L(Y)SO, not only a different polymerization resin must be used, but also the entire NIR laser system with its wavelength of 780 nm must be replaced. Another way to circumvent this issue is to deposit another material on top of the resin structure and thereafter burn away the resin via oxygen plasma etching [35]. What still needs to be investigated is how small these structures can be made with this capability, as well as the scalability of the production method.

### 4.3.6 Self-Assembly

Self-assembly is an interesting field of research that investigates the spontaneous organization of nano-elements, either guided or non-guided. This is attractive as it gives rise to a relatively simple and cost-effective way to produce nanostructures, incomparably cheaper than to conventional lithography methods [18]. The real challenge with this structuring technique is to controlling the self-assembly process as the technique is relatively prone to defects such as voids and clusters in the pattern. Control of the self-assembly, i.e. ensuring that the process preferably starts from only one nucleation center and progresses homogeneously over the entire sample, is the key to sample quality.
One example is colloidal lithography with polystyrene nano-spheres, where first a monolayer of nanospheres is deposited on a surface to be patterned, usually via the Langmuir-Bodgett process [37]. This is a relatively simple method to obtain a monolayer of nanospheres that will arrange themselves in a hexagonal lattice. Thereafter, the layer is treated with a plasma in order to shrink the nanospheres to the desired dimension [13] [38]. If this is to be used as a mask for etching, one can then deposit a mask-specific material layer on top of these nanospheres. Then, the nanospheres are removed via lift-off leaving behind a hard mask with hexagonally arranged holes, an example of which is given in [13]. Another approach is to use the nano-spheres directly as an etching mask, resulting in a final structure of pillars in a hexagonal lattice. However, since polystyrene nanospheres are not very resistant to reactive ion etching, only structures with very low aspect ratios can be produced. To overcome this problem, either the produced structures need to be treated for further grow (as explained in [38]) or nanospheres made from a different material, being more resistant to the etching process, need to be used.

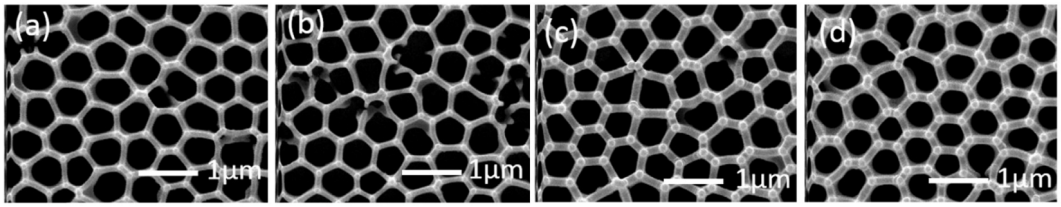


Figure 4.16: SEM images of (a) an AAO layer, (b) an AAO + 10 nm $Al_2O_3$, (c) an AAO + 20 nm Al2O3 and (d) an AAO + 20 nm $TiO_2$ [39].

Another application variant of self-assembly is to use the deposited nanospheres directly as photonic structures. For this option to work, the nanospheres need to be made of high refractive index, such as $TiO_2$. Alternatively, one can deposit a high refractive index layer, again of e.g. $TiO_2$, on top of the nano-spheres. An example of this is given in [36] and is shown in figure 4.15.

A completely different approach to self-assembly is to produce via anodization a layer of nanoporous material on a scintillator. This is a purely electro-chemical process. The original material is kept in an acidic solution while applying an electrical bias, resulting in self-ordered, nanometer-scale pores in the material. The work of [39] [40] describe such a process for the anodization of aluminum oxide and [41] [42] that of titanium oxide. The challenge of this process is to produce a homogeneous distribution of pores with diameters of equal size. The clear advantages of this method are its high speed and low cost, making it very attractive for large surface patterning [39]. An example of a photonic crystal slab of nanoporous aluminum oxide produced with this method is shown in figure 4.16.

### 4.3.7 Summary production methods

Table 4.1 gives an overview of the before-discussed production methods for photonic crystals.

Table 4.1: Summary of production methods for photonic crystal production on inorganic scintillators.

| Method | Positive features | Negative features |
|---|---|---|
| Optical Projection Lithography | High feature resolution<br>Large choice of patterns<br>Relatively fast | Very expensive |
| Light Interference Lithography | High feature resolution<br>Relatively fast<br>Relatively cheap | Limited choice of patterns |
| Electron-Beam lithography | High feature resolution<br>Large choice of patterns | Very expensive<br>Very slow |
| Focused Ion-Beam Lithography | High feature resolution<br>Large choice of patterns<br>Possibility of one-step patterning | Expensive<br>Slow<br>Implantation/light absorption issues |
| Nano-Imprint Lithography | Relatively fast<br>Relatively cheap<br>Choice of patterns<br>Possibility of one-step patterning | "Master stamp" is expensive |
| Scanning Probe Lithography | Large choice of (complex) patterns<br>Quality control during patterning<br>Liberty to change pattern across surface | Slow<br>Limited in pattern height |
| Two-Photon Lithography | Large choice of (3D) patterns | Limited feature resolution<br>Much process development needed/<br>too experimental |
| Self-Assembly | Extremely cheap<br>Extremely fast | Little choice patterns<br>Defect-sensitive |

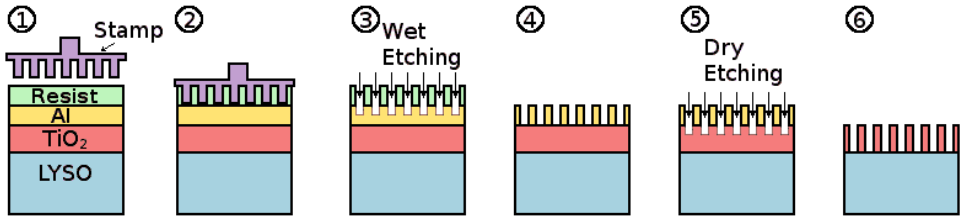


Figure 4.17: Processing steps in nano-imprint lithography: (1) LYSO scintillator with subsequent layers of $TiO_2$, aluminum, and a resist deposited on its surface. (2) A stamp imprints the pattern into the resist. (3) The pattern in the resist is transferred to the aluminum through wet-etching. (4) The imprinted aluminum layer is used as hard mask for the dry-etching process. (5) Dry-etching of the $TiO_2$ transfers the Al-pattern to the $TiO_2$. (6) The hard mask is removed and the $TiO_2$ is imprinted with its final pattern.

## 4.4 Detailed description of production methods used for prototypes in this thesis

The next two chapters of this thesis present prototypes of photonic crystal slabs produced on scintillators. The photonic nanopatterns discussed there were produced from three different lithography methods, specifically developed for nano-imprinting on full-sized inorganic scintillating crystals:

- nano-imprint lithography
- sol-gel lithography
- UV-cured nano-imprint lithography

It is these three methods that are explained in detail in the following three subsections.

### 4.4.1 Detailed description of nano-imprint lithography

This production method is described as a sequence of the following six steps (see also figure 4.17):

1. i. First, a 300 nm layer of $TiO_2$ is sputtered on the readout surface of the scintillating crystal;
   ii. thereafter a layer of aluminum (Al) is deposited on the $TiO_2$ coating;
   iii. and then a resist applied on top of these.

   This is the combined layer into which the desired pattern will be imprinted via the nano-imprint lithographic process. This is shown in step 1 of figure 4.17.

2. A stamp, which is replicated from a master mold, is then used to imprint its pattern into the resist layer (step 2 of figure 4.17). The master mold itself is produced beforehand via e-beam lithography.

3. After having imprinted the resist, the pattern is transferred to the aluminum layer via wet-etching (step 3 of figure 4.17), the results of which...

4. is the pattern left in the aluminum (step 4 of figure 4.17).

5. This patterned aluminum layer then serves as a hard mask for the dry-etching of the $TiO_2$ layer (step 5 of figure 4.17).

6. In this way, the final patterned layer is produced on the scintillator (step 6 of figure 4.17).

The stamp can be as large as to imprint in one step an entire crystal surface as large as 5x5 $cm^2$.
An important aspect if not a challenge with this method is to ensure a homogeneous layer of $TiO_2$ on the crystal surface, but moreover uniform etching over the entire surface of the bulk scintillator without distortions.

### 4.4.2 Detailed description of sol-gel lithography

The second lithography method discussed in detail in here, is the so-called sol-gel lithography, which is a type of soft nano-imprint lithography. The strong benefit of this production method is that the pattern be directly stamped into the final layer. This being a soft layer, a liquid solution or so-called sol, is cured to transform it to gel, which in the end after second stage curing becomes a solid.
The sol-gel method discussed here is based on the formation of inorganic polymers from a "precursor" [43]. To produce e.g. a layer of $TiO_2$, such a precursor would be $Ti(OC_3H_7)_4$ called tetraisopropyl orthotitanate (TIPT), see figure 4.18 (a), an alkoxide precursor. The different steps of the sol-gel process are summarized in figure 4.18 (b).

The above mentioned precursor is added to a solution of alcohol (or another organic solvent), water and a catalyst. In a sequence of hydrolysis and condensation reactions, polymer chains start to form in the solution. These reactions take place at room temperature. Then, longer polymer chains are form while the sol is transforming into a dry so-called xerogel, either at room temperature or in an accelerated fashion at higher temperatures. While changing from solution to xerogel, the volume of the layer reduces by a factor 5 to 10. This xerogel is still a relatively porous substance and has to be cured either by heat or by UV light to form a final stable layer. If a $TiO_2$ sol-gel is used, the last step can be obtained by heating the layer to 450° or higher, which makes the xerogel to become denser and to crystallize into the desired $TiO_2$ layer. After the stamp was applied to the sol-gel layer, while still being soft, the final layer will be nano-structured. During the sol-gel processing steps the layer does not only become denser, but also its refractive index increases and, at the same time, the structure shrinks. While the obtained increase in refractive index is beneficial for our applications, excessive shrinkage of the structure has the opposite effect, therefore necessitating a proper balance between the two by controlling the duration of the heating process.

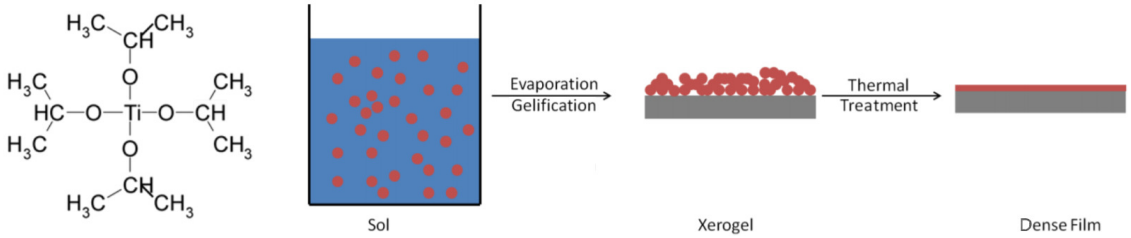


(a) (b)

Figure 4.18: (a) "Topological formula of TIPT" (tetraisopropyl orthotitanate) [43], sol-gel precursor of $TiO_2$. (b) "Sol-gel steps from a sol to a dense oxide-film." [43]

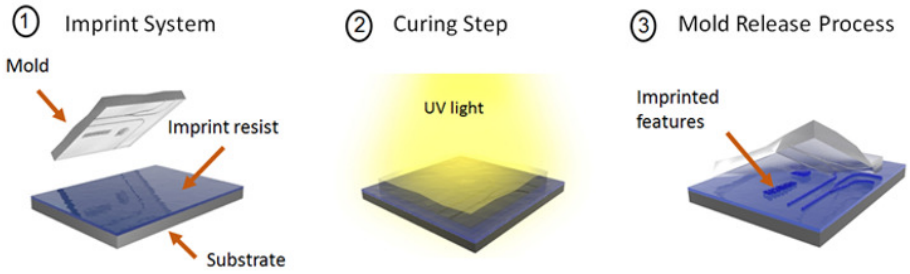


Figure 4.19: The different steps in UV nano-imprint lithography (UV-NIL) [46].

### 4.4.3 Detailed description of UV-cured nano-imprint lithography

In the framework of this thesis, this technology was selected for reasons of low production costs and the ease of handling soft polymers with the additional feature of being UV-curable. This production method was developed in the frame-work of a cooperation between the CERN-based Crystal Clear Laboratory, the US-based Radiation Monitoring Devices, Inc. (RMD) [44] and A-Beam Technologies [45].
Since polymers with sufficiently high refractive index are not commercially available [46], A-beam Technologies was able to develop one polymer with a relatively high refractive index of 1.82 that is curable with UV-light and transparent to the emission spectrum of LYSO. This polymer, prior to UV-curing, was imprinted by a patterned stamp pressed into it. This stamp is a reproduction, or replica, of a "master" stamp that is produced via interference lithography on silicon, whose production is rather expensive. Multiple replicas can then be made from the master stamp into quartz. The benefit of this method is that (1) several replicated stamps can be produced from the master and (2) that they are transparent to UV-light, a feature allowing to cure the polymer while the stamp is still in place. Furthermore, in this way the expensive master stamp will be subject to less wear, prolonging its lifetime.
Figure 4.19 illustrates the three production steps:

1. The UV-transparent stamp is pressed into the polymer layer, transferring the opted pattern into the polymer.

2. UV-light is used to cure the polymer, while the stamp is still embedded in the polymer layer.

3. After the polymer layer has turned solid, the stamp is removed.

## 4.5 Simulation framework

The parameters of a photonic crystal slab need to be chosen appropriately in order to enhance the light extraction from the scintillator. If chosen poorly, it might even result in a significant decrease in the extracted light. To understand the right values of the parameters, such as the period, diameter, and height of nanostructures, that are usually also strongly limited by production capabilities, one needs to perform simulations to assess the corresponding photonic behavior.
Several simulation tools are available for the simulation of photonic crystals like, one of which is CAMFR (CAvity Modelling FRamework) [47]. However, there is no one tool that can simulate the photonic crystal slab and the scintillation behavior within one single

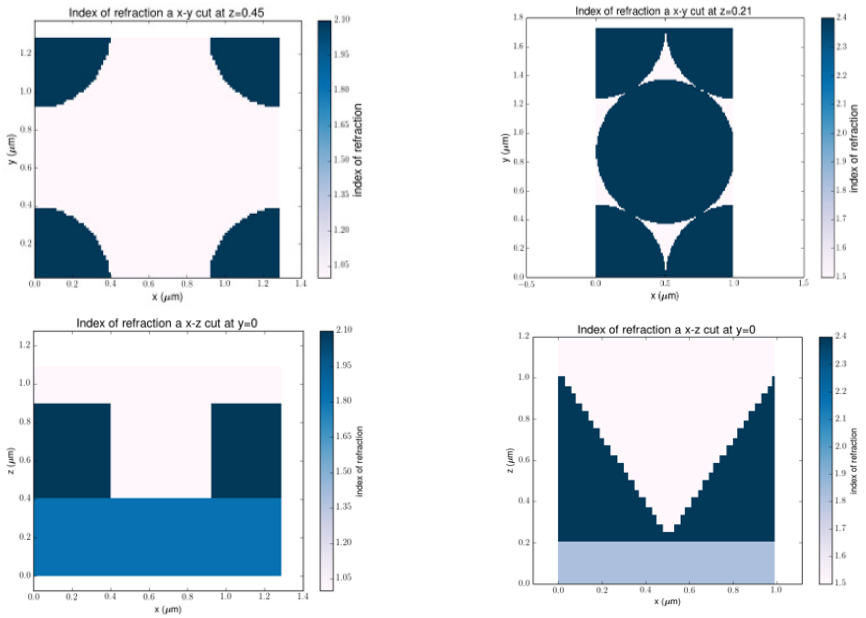


Figure 4.20: Two structures defined in CAMFR: pillars in a square lattice (left), cones in a hexagonal lattice (right), shown from the top (top) and from the side (bottom).

code [1][48]. Therefore, a combination of two simulation tools has been chosen. Therefore, in this thesis, CAMFR [47] was used for the calculation of the photon transmission by the photonic crystal slabs, whereas Geant4 [49] was teh tool to calculate the interaction of the incoming gammas with the scintillator material, as well for the production and transport of the scintillation photons in the crystal.

### 4.5.1 Simulating photonic crystals: CAvity Modelling FRamework (CAMFR)

The cavity modelling framework (CAMFR) [47] was developed in the Photonics Research Group at the University of Ghent, with P. Bienstmann as the main investigator. It is freely available under the *GNU general public license*, but at this moment not maintained any longer. CAMFR is a Maxwell solver using eigenvalue expansion methods in the frequency domain. As such, this simulation tool can calculate the behavior of photonic crystal slabs much faster than tools relying on e.g. finite-difference time-domain (FDTD) methods. Nonetheless, CAMFR was proven to be consistent with FDTD methods [50]. It is specially designed for the simulation of optical devices, although in principle it could solve any electromagnetic system. CAMFR implements C, C++ and Fortran libraries to calculate electromagnetic (EM) field expansion, which, relying on Python 'wrap' functions, are still accessible while having a convenient and user friendly Python interface. To define the structure of a slab, CAMFR gives the freedom to describe only a part of the total structure, which then, by infinite repetition, models the entire structure. CAMFR also needs, as input, the scintillator material on which the slab is located and from where the scintillation light is impinging on the slab, plus the ambient environment into which part of the light is extracted by the slab. Part of the work in this context was to to define sample structures as e.g. shown in figure 4.20. To calculate the behavior of a photonic crystal slab, this thesis descretized the volume of the structure under investigation into

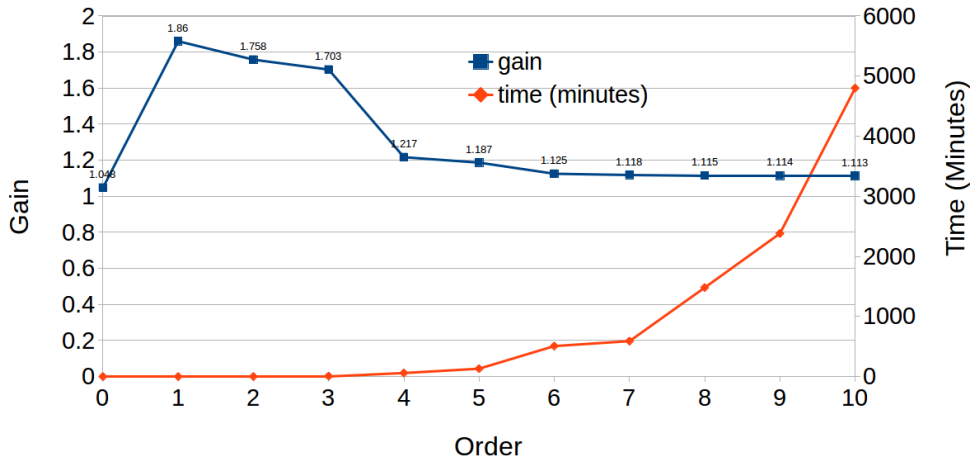


Figure 4.21: Simulated gain in light extraction from a scintillator with a nanostructured readout face, including different amounts of orders (blue squares) and corresponding simulation times (orange rhombus).

layered stacks, where inside each layer the scattering matrix method was applied for a given frequency using the mode matching principle [51]. The behavior of the slab is only calculated for one wavelength and k-vector, to be set by the author. The thesis also has to specify the order of the calculations; the higher the order, the more eigenmodes are to be calculated leading to a more precise result. However, the computing time also increases rapidly with the amount of modes, as depicted in figure 4.21. Figure 4.22 gives an example of the calculated transmission of a photonic pattern compared to a flat surface. One significant limitation of CAMFR is that, up until now, it was not possible to extract the information on the reflected and diffracted angles of the outgoing electromagnetic waves. Functions in the software that are made to access this information are not implemented. As such it is only possible to extract information on the *amount* of light that is either transmitted or reflected back into the crystal by the photonic crystal slab. The result of the CAMFR simulation gives a list of transmission factors for every impinging angle on the photonic crystal slab. While the simulation tool can in principle be used for the simulation of any kind of periodic, even 3D, pattern, for the application of scintillating crystals and considering the limitations of the production methods the main geometries to be simulated are pillars, holes or cones in a square- or triangular lattice.

### 4.5.2 Simulating photon generation and transport in scintillators: Geant4

Geant4, which stands for geometry and tracking, is a Monte Carlo simulator toolkit developed by the RD44 collaboration at CERN and is now maintained by the Geant4 Collaboration at CERN [49]. This kit was developed in a C++ object-oriented environment and is freely available under the *Geant4 software license* [52]. Originally developed for high energy physics, as well as for nuclear- and accelerator physics, the Geant4 toolkit can also be used for applications in medical physics, radiation science, space science or in fact in any situation where ionising particles interact with matter. It has been widely expanded over the years and today constitutes one of the most comprehensive simulation codes of its kind. The toolkit comes with an extensive library of material properties ready to be used in the simulations. Users can also define their own materials or material properties. For the modelling of scintillating crystals, Geant4 can be used for the simulation of gamma interactions in the scintillator and the creation and transport of optical (scintillation)

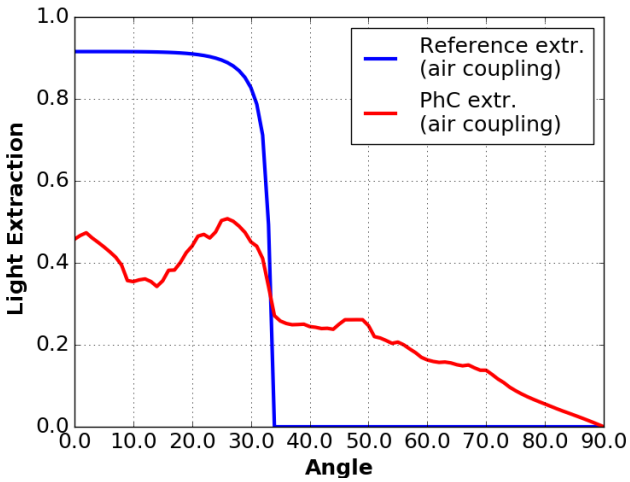


Figure 4.22: Example of a simulated transmission of a nanopattern from a medium with RI=1.82 to air, compared to a flat surface.

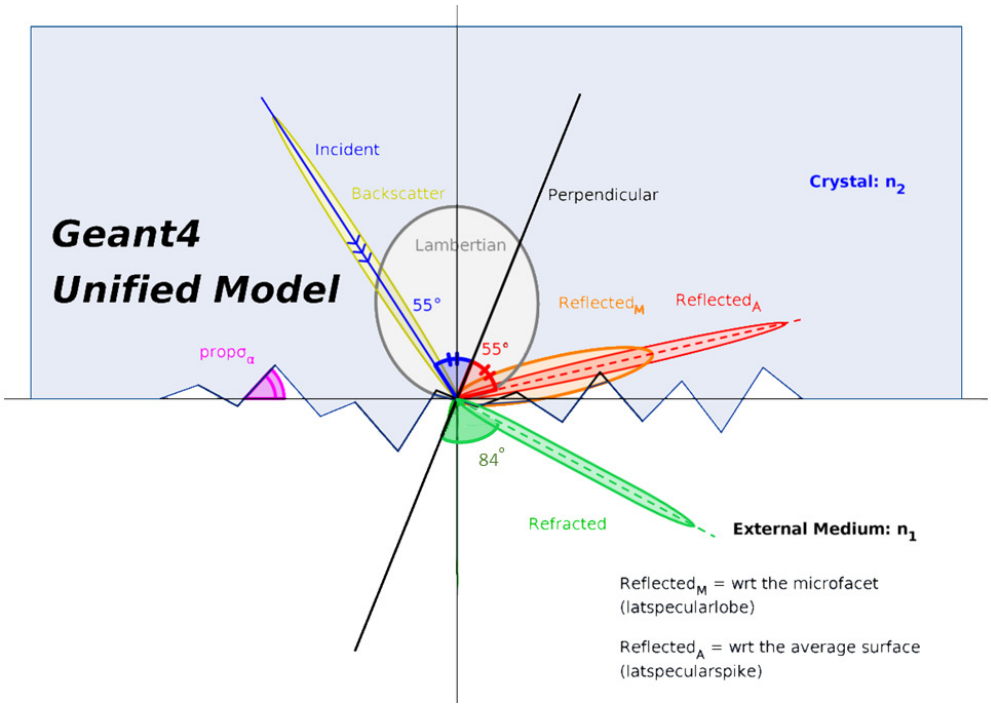


Figure 4.23: Representation of the UNIFIED model of Geant4, describing optical interfaces between different media. [1]

photons up to the point where they reach the readout interface with the PhC slab. The important parameters that were implemented for the simulation of the system are:

- the refractive index of all the materials involved, i.e. crystal bulk, surrounding medium, wrapping, optical coupling, and everything else that could interact with the optical photons as a function of the wavelength;
- the crystal emission wavelength and absorption spectrum;
- the surface state of the crystal, i.e. $\sigma_\alpha$ parameter and different types of reflections;
- energy and direction of the incoming gamma rays, as well as the density of the scintillator defining the stopping power;
- reflectivity of the surrounding materials.

As shown in figure 4.23, the surface roughness of a crystal is described by the parameter $\sigma_\alpha$ (pink angle), that defines a Gaussian distribution with $\sigma_\alpha$ as its sigma. For each impinging photon Geant4 chooses a random angle within the $\sigma_\alpha$ distribution, thus defining the corresponding microfacet tilted with the chosen angle from which the photon is either reflected or refracted. Large $\sigma_\alpha$s produce large fluctuations of microfacets. As seen in the figure, there are several types of lobes, the width of each represents the probability range of their particular reflection or refraction:

- orange lobe: reflection from the microfacet
- red lobe: reflection from the original flat surface
- grey lobe: Lambertian diffusion
- yellow lobe: back scattering
- green lobe: refraction by the microfacet

Geant4 allows for an easy implementation of all these parameters. As mentioned before, a principle drawback of Geant4 is that it treats optical photons as particles and as such does not take into account the wave behavior of the photons interacting with the nano-patterned slab on the scintillator's readout face. However, there is the possibility to measure optical properties of a surface separately and include them into the Geant4 simulation through the means of look-up tables [53][54].

### 4.5.3 Combining scintillator and photonic crystals: the full simulation

To simulate the full system of gamma radiation exciting a scintillator and to model the production and transport of scintillation light in the scintillator and consequently the light interaction with the photonic crystal layer, this thesis has made use of both Geant4 and CAMFR. To approaches to address the full system simulation were made: (1) let CAMFR simulate and provide the transmission and reflection features of the photonic crystal slab and save this information in a look-up table that will be used as an additional library in Geant4 or, (2) to simulate first the scintillator properties with Geant4, so as to create the angular distribution of the scintillation light when it arrives at the readout surface. It is this information then, that is used as input for the CAMFR simulation, which in turn resumes the calculation for the portions of light that are extracted or reflected back into the scintillator due to the presence of the photonic structure. In this thesis, the latter

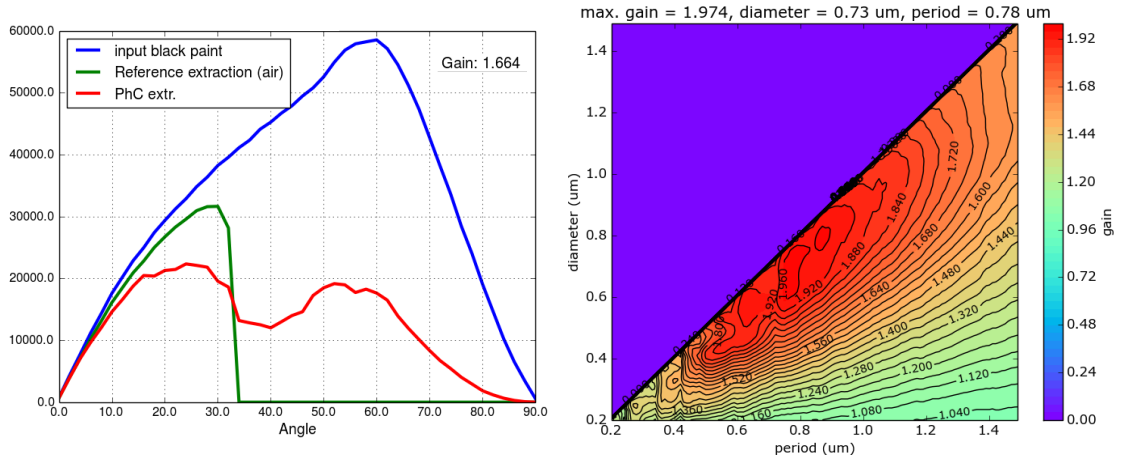


Figure 4.24: Simulation of the combined CAMFR and Geant4 tool, of a 600 nm high structure of cones in a hexagonal lattice. Left: Transmission plot with internal angular distribution of light at the readout face of the scintillator (blue), the extracted part *without* (green) and *with* photonic crystal slab (red). Right: Contour plot with gain in light extraction for different base diameters and the pitches of the structure.

approach was chosen.
As discussed before, Geant4 simulates the internal angular light distribution only for those photons that reach the readout face of the scintillator for the first time. This scenario and the amount of photons transmitted by the photonic crystal slab, as calculated by CAMFR, are then used to make a comparison of light extraction with and without a photonic crystal structure. In other words, photons that have undergone multiple reflections inside the scintillator and reach again the readout face, are not taken into account for this comparison. This was deemed a fair representation of a situation where e.g. black paint is applied to all scintillator walls except for the readout face. It can also be seen as an acceptable approximation for the case where no wrapping is used (a naked crystal). In general, the wavelength for both the Geant4 and the CAMFR simulation is chosen to be the maximum of the emission spectrum of the simulated scintillator. Every CAMFR simulation is done for a cycle of different k-vectors and then averaged to create the final transmission per incident angle, in order to best simulate the isotropically emitted light from the scintillator. An example of a result from a combined Geant4-CAMFR simulation is shown in the left hand plot of figure 4.24. Note, however, that when the crystal is wrapped with a reflector, e.g. Teflon, the combined simulation package of Geant4 and CAMFR reaches its limits to correctly model the behavior of the system.

The advantage of this dual approach is that the author could independently optimize CAMFR parameters, such as slab height, structure diameter and periodicity, while using each time the same Geant4 results as input. Figure 4.24, right, gives an example of an optimization of the periodicity and diameter of cones in a hexagonal photonic lattice, shown as a contour plot of achievable light gain.

# Bibliography

[1] M. Salomoni, R. Pots, E. Auffray, and P. Lecoq, "Enhancing light extraction of inorganic scintillators using photonic crystals," *Crystals*, vol. 8, p. 78, Feb 2018.

[2] B. Smith, "1 - optical projection lithography," in *Nanolithography* (M. Feldman, ed.), pp. 1 – 41, Woodhead Publishing, 2014.

[3] J. Zi, X. Yu, Y. Li, X. Hu, C. Xu, X. Wang, X. Liu, and R. Fu, "Coloration strategies in peacock feathers," *Proceedings of the National Academy of Sciences*, vol. 100, no. 22, pp. 12576–12578, 2003.

[4] P. Vukusic and R. Sambles, "Photonic structures in biology," *Nature*, vol. 424, pp. 852 – 855, 2003.

[5] P. Garg, P. Ghatmale, K. Tarwadi, and S. Chavan, "Influence of nanotechnology and the role of nanostructures in biomimetic studies and their potential applications," *Biomimetics*, vol. 2, p. 7, May 2017.

[6] E. Yablonovitch, "Inhibited spontaneous emission in solid-state physics and electronics," *Phys. Rev. Lett.*, vol. 58, pp. 2059–2062, May 1987.

[7] S. John, "Strong localization of photons in certain disordered dielectric superlattices," *Phys. Rev. Lett.*, vol. 58, pp. 2486–2489, Jun 1987.

[8] A. Knapitsch and P. Lecoq, "Review on photonic crystal coatings for scintillators," *International Journal of Modern Physics A*, vol. 29, no. 30, p. 1430070, 2014.

[9] J. Joannopoulos, S. Johnson, J. Winn, and R. Meade, *Photonic Crystals: Molding the Flow of Light - Second Edition*. Princeton University Press, 2011.

[10] K. Sakoda, *Optical Properties of Photonic Crystals*. Springer Series in Optical Sciences, Springer Berlin Heidelberg, 2004.

[11] S. G. Tikhodeev, A. L. Yablonskii, E. A. Muljarov, N. A. Gippius, and T. Ishihara, "Quasiguided modes and optical properties of photonic crystal slabs," *Phys. Rev. B*, vol. 66, p. 045102, Jul 2002.

[12] S. A. Boden and D. M. Bagnall, *Moth-Eye Antireflective Structures*, pp. 1467–1477. Dordrecht: Springer Netherlands, 2012.

[13] A. Knapitsch, E. Auffray, G. Barbastathis, C. Chevalier, C. H. Hsieh, J. G. Kim, S. Li, M. S. J. Marshall, R. Mazurczyk, P. Modrzynski, V. Nagarkar, I. Papakonstantinou, B. Singh, A. Taylor, and P. Lecoq, "Large scale production of photonic crystals on scintillators.," *IEEE Transactions on Nuclear Science*, vol. 63, pp. 639–643, 2016.

[14] R. F. Pease and S. Y. Chou, "Lithography and other patterning techniques for future electronics," *Proceedings of the IEEE*, vol. 96, pp. 248–270, Feb 2008.

[15] A. Knapitsch, E. Auffray, C. W. Fabjan, J. Leclercq, X. Letartre, R. Mazurczyk, and P. Lecoq, "Results of photonic crystal enhanced light extraction on heavy inorganic scintillators," *IEEE Transaction on Nuclear Science*, vol. 59, no. issue 5, pp. 2334–2339, 2012.

[16] A. Novembre and S. Liu, "7 - chemistry and processing of resists for nanolithography," in *Nanolithography* (M. Feldman, ed.), pp. 194 – 286, Woodhead Publishing, 2014.

[17] "Online tutorial on nanolithography." `http://what-when-how.com/nanoscience-and-nanotechnology/nanolithography-length-scale\-limitations-part-1-nanotechnology/`. Accessed: 30-11-2017.

[18] B. D. Gates, Q. Xu, M. Stewart, D. Ryan, G. C. Willson, and G. M. Whitesides, "New approaches to nanofabrication: molding, printing, and other techniques," Chemical Reviews, vol. 105, no. 4, pp. 1171–1196, 2005.

[19] B. Rice, "2 - extreme ultraviolet (euv) lithography," in *Nanolithography* (M. Feldman, ed.), pp. 42 – 79, Woodhead Publishing, 2014.

[20] "Webpage from the paul scherer institute (psi) on euv interference lithography." https://www.psi.ch/lmn/euv-interference-lithography.

[21] T. Groves, "3 - electron beam lithography," in *Nanolithography* (M. Feldman, ed.), pp. 80 – 115, Woodhead Publishing, 2014.

[22] "Homepage of the lyon institute of nanotechnology or institut des nanotechnologies de lyon (inl)." `https://inl.cnrs.fr/`. Accessed: 2021-01-27.

[23] P. J. Modrzynski, T. Gotszalk, A. Knapitsch, P. Kunicki, M. Lecoq, P.; Moczala, I. Papakonstantinou, and E. Auffray, "Light extraction from scintillating crystals enhanced by photonic crystal structures patterned by focused ion beam," *IEEE Transactions on Nuclear Science*, vol. 63, no. 2, pp. 644–648, 2016.

[24] D. Resnick, "9 - nanoimprint lithography," in *Nanolithography* (M. Feldman, ed.), pp. 315 – 347, Woodhead Publishing, 2014.

[25] "Brochure of the nanofrazor." `https://heidelberg-instruments.com/files/downloads/fact-sheets/fact-sheet-nanofrazor-explore.pdf`, Accessed: 20-08-2020.

[26] "Heidelberg instruments, producer of the nanofrazor." `https://heidelberg-instruments.com/en/products/nanofrazor-explore.html`, Accessed: 20-08-2020.

[27] X. Zheng, A. Calò, E. Albisetti, *et al.*, "Patterning metal contacts on monolayer mos2 with vanishing schottky barriers using thermal nanolithography," *Nature Electronics*, vol. 217.

[28] "Private communication with s. zimmermann and j. brugger from epfl."

[29] S. Ruzin and H. Aaron, "1p vs 2p fluorescence imaging." http://microscopy.berkeley.edu/courses/tlm/2P/index.html, Accessed: 21-08-2020.

[30] "Nanoscribe gmbh." `https://www.nanoscribe.com/en/`, Accessed: 20-08-2020.

[31] "Nanoscribe professional gt brochure." `http://www.nanoscribe-japan.com/wp-content/uploads/2015/01/DataSheet_Photonic_Professional_GT.pdf`, Accessed: 25-08-2020.

[32] "Nanoscribe professional gt2 brochure." `https://www.nanoscribe.com/fileadmin/Nanoscribe/Solutions/Photonic_Professional_GT2/Folder_PPGT2_A4.pdf`, Accessed: 21-08-2020.

[33] "Nanoscribe uv resins webpage." `https://www.nanoscribe.com/en/solutions/materials#tab-880`, Accessed: 21-08-2020.

[34] A. Vyatskikh, R. C. Ng, B. Edwards, R. M. Briggs, and J. R. Greer, "Additive manufacturing of high-refractive-index, nanoarchitected titanium dioxide for 3d dielectric photonic crystals," *Nano Letters*, vol. 20, no. 5, pp. 3513–3520, 2020. PMID: 32338926.

[35] L. R. Meza, S. Das, and J. R. Greer, "Strong, lightweight, and recoverable three-dimensional ceramic nanolattices," *Science*, vol. 345, no. 6202, pp. 1322–1326, 2014.

[36] J. Liu, B. Liu, Z. Zhu, L. Chen, J. Hu, M. Xu, C. Cheng, X. Ouyang, Z. Zhang, J. Ruan, S. He, L. Liu, M. Gu, and H. Chen, "Modified timing characteristic of a scintillation detection system with photonic crystal structures.," *Optics letter*, vol. 42, 2017.

[37] K. Blodgett, "Films built by depositing successive monomolecular layers on a solid surface.," *Journal of the American Chemical Society*, vol. 57, no. 107-1022, 1935.

[38] M. Domonkos, T. Izak, S. L., J. Proska, and A. Kromka, "Fabrication of periodically ordered diamond nanostructures by microsphere lithography.," *Physica status solidi*, vol. 251, pp. 2587–2592, 2014.

[39] J. Zhang, B. Liu, Z. Zhu, Q. Wu, C. Cheng, J. Liu, L. Chen, X. Ouyang, M. Gu, J. Xu, and H. Chen, "Enhanced light extraction of lyso scintillator by photonic crystal structures from a modified porous anodized aluminum oxide layer.,"

[40] Z. Zhu, B. Bo Liu, C. Cheng, H. Zhang, S. Wu, M. Gu, H. Chen, L. Chen, J. Liu, and X. Ouyang, "Improved light extraction of lyso scintillator by the photonic structure from a layer of anodized aluminum oxide.," *Nucl. Instrum. MethodsPhys. Res. Sect. A*, vol. 786, pp. 1–4, 2015.

[41] "Yu, x. and li, y and wlodarski, w and kandasamy, s. and kalantar-zadeh, k.," *Sensors and Actuators B: Chemical*, vol. 130, pp. 25–31, 2008.

[42] X. Yu, Y. Li, W. Ge, Q. Yang, N. Zhu, and K. Kalantar-zadeh, "Formation of nanoporous titanium oxide films on silicon substrates using an anodization process.," *Nanotechnology*, vol. 17, p. 808–814, 2006.

[43] V. Gâté, *Ecriture de motifs périodiques submicrométriques sur films TiO2 sol-gel par lithographie interférométrique dynamique sur de grandes surfaces.* PhD thesis, Université Jean MONNET de Saint-Etienne, Université de Lyon, Dec. 2013.

[44] "Rmd homepage." `https://www.dynasil.com/company/radiation-monitoring-devices/`. Accessed: 2020-09-25.

[45] "abeam homepage." `http://www.abeamtech.com/`. Accessed: 2020-09-25.

[46] B. Singh, M. S. J. Marshall, S. Waterman, C. Pina-Hernandez, A. Koshelev, K. Munechika, A. Knapitsch, M. Salomoni, R. Pots, P. Lecoq, and V. V. Nagarkar, "Enhanced scintillation light extraction using nanoimprinted photonic crystals," *IEEE Transactions on Nuclear Science*, vol. 65, pp. 1059–1065, April 2018.

[47] "Camfr homepage." `http://camfr.sourceforge.net/`. Accessed: 2020-12-04.

[48] R. H. Pots, M. Salomoni, S. Gundacker, S. Zanettini, V. Gâté, E. Usureau, D. Turover, P. Lecoq, and E. Auffray, "Improving light output and coincidence time resolution of scintillating crystals using nanoimprinted photonic crystal slabs," *Nuclear*

*Instruments and Methods in Physics Research Section A: Accelerators, Spectrometers, Detectors and Associated Equipment*, vol. 940, pp. 254 – 261, 2019.

[49] "Geant4 homepage." `https://geant4.web.cern.ch/`. Accessed: 2020-12-04.

[50] J.-G. Kim, C.-H. Hsieh, H. J. Choi, J. Gardener, B. Singh, A. Knapitsch, P. Lecoq, and G. Barbastathis, "Conical photonic crystals for enhancing light extraction efficiency from high refractive index materials," *Opt. Express*, vol. 23, pp. 22730–22739, Aug 2015.

[51] P. Bientsmann, *Rigorous and efficient modelling of wavelength scale photonic components*. PhD thesis, Ghent University, 2001.

[52] G. Collaboration, "Introduction to geant4, version: geant4 10.2," December 2015.

[53] E. Roncali, M. Stockhoff, and S. R. Cherry, "An integrated model of scintillator-reflector properties for advanced simulations of optical transport," *Physics in Medicine and Biology*, vol. 62, pp. 4811–4830, may 2017.

[54] M. Stockhoff, S. Jan, A. Dubois, S. R. Cherry, and E. Roncali, "Advanced optical simulation of scintillation detectors in GATE v8.0: first implementation of a reflectance model based on measured data," *Physics in Medicine and Biology*, vol. 62, pp. L1–L8, may 2017.

# Chapter 5

# Photonic Crystal Slabs for TurboPET: Improving a PET Scanner

Part of the research discussed in this chapter has been presented in a poster titled "Improved Light Extraction Efficiency on two-inch LYSO with Nanopatterned $TiO_2$ Photonic Crystals" by Zanettini et al., presented at the 2016 IEEE conference in Strasbourg, France [1].

As discussed in chapter 4 of this thesis, photonic crystals can be used to enhance the light extraction from inorganic scintillating crystals. This could improve the performance of the detector in which these crystals are used as active medium [1][2][3].
This chapter discusses the production of photonic crystals on large monolithic scintillators. As discussed before, the goal was to increase the light output, as well as to measure its influence on the energy resolution of the scintillator. At the end, the aim was to produce 12 scintillating crystals to be deployed in a complete PET system dedicated to breast imaging and to assess its performance. The photonic crystals have been produced in the framework of the European Eurostars Project TurboPET, which is explained in section 5.1. The photonic crystals were produced with two different production methods: nanoimprint lithography, as detailed in section 4.4.1, and sol-gel lithography, as explained in section 4.4.2. The work presented here was a joint effort of members of the CERN-based crystal clear group in particular with M. Salomoni [4].

## 5.1 The TurboPET project

TurboPET was Eurostars project N° E8974, co-funded by the European's Union Horizon 2020 Framework Program and the Eureka Member States. The execution of the project was in collaboration with CERN, the University of Troyes, Napa-technologies [5] (for the production of photonic crystals) and Oncovision [6] (a commercial producer of PET scanners) and the Centre Hôpitalier Universitair Vaudois (CHUV) in Lausanne. The project started in December 2014 and ended in April 2018.
The objective of TurboPET was to create a new generation of PET scanners targeting breast cancer, with very high sensitivity and resolution. The idea behind was to improve on an existing device produced by Oncovision, called MAMMI PET [7]. The improvement entailed the addition of a photonic crystal slab on the readout face of the existing

scintillating crystals of the scanner. This method was chosen to enhance light extraction and therefore increase the overall performance of the scanner.
Therefore, the project focused on the following tasks:

- Develop a nanolithography method to imprint *large* surfaces.
- Advance this technology such that it can be applied to inorganic scintillating crystals, with the ultimate goal of imprinting large and thick crystals.
- Design a suitable nanopattern that facilitates light extraction from the imprinted crystals to be used in the MAMMI PET.
- Produce 12 such scintillating crystals to be used in the scanner.
- Assemble the PET scanner with these new crystals and assess its performance with phantoms.
- The ultimate goal being a clinical trial with this new PET device and the evaluation of its performance under clinical conditions.

Therefore, the project was divided into the following work packages:

WP1: Feasibility and specifications;

WP2: Simulation of photonic solutions;

WP3: Nanopatterning of crystals;

WP4: Functional characterization;

WP5: Implementation in a prototype TurboPET;

WP6: Tests and validation of a pilot TurboPET;

WP7 Project management.

CERN's contribution in this work comprised WP1, WP2 and WP4.
This chapter focuses on WP2 and WP4, where the author of this thesis was predominantly involved, but also reports on the results from her participation in the phantom measurements performed at the Oncovision manufacturing plant.

### 5.1.1 MAMMI PET and TurboPET

Today, X-ray imaging is still the standard anatomical method for the detection and screening of breast cancer, with MRI being reserved for specific patient groups. The advantage of PET in tumor imaging stems from the metabolic information resulting from the uptake of the radioactive tracer in the region of interest, leading to a significant increase in detection sensitivity with respect to the former methods.
The Oncovision MAMMI PET [7] is a breast-dedicated PET scanner, shown in figure 5.1. The patient is in prone position on a bed with a hole, allowing the breast under investigation to be examined underneath, as shown in figure 5.1(a). The actual imaging PET ring is then placed around the breast, as illustrated in figure 5.1(b). The original Oncovision scanner has a spatial resolution of as high as 1.6 mm [8], an acquisition time of 5-16 minutes [8] and delivers a comparatively low patient dose of ∼4mCi [10]. As figure 5.2(a) shows, the PET scanner significantly reduces the false positives produced by the


(a) (b)

Figure 5.1: The MAMMI PET scanner produced by Oncovision. (a) The patient is placed on a bed with her breast positioned in a hollow cylinder underneath a hole in the bed [8]. (b) The ring of the actual PET scanner is placed around the cylinder underneath the bed [9].

MRI, thus clearly identifying the cancerous region in the breast tissue. On the other hand figure 5.2(b) demonstrates the shortcomings of traditional X-ray imaging delivering false negatives, to be resolved only by a PET scan.

The scanner consists of two coplanar rings, both of them equipped with 12 equidistantly placed crystals. This is shown in figure 5.3 for MAMMI PET, here without its protective casing.
The scintillators used for this scanner are large trapezoidal LYSO crystals with its larger face of 50x50 $mm^2$, its smaller face of 40x40 $mm^2$ and a thickness of 15 mm. This means that the scanner uses large *monolithic* crystals, contrary to the commonly implemented smaller pixel-type crystal arrays. The crystals are then arranged such that dead space is minimized and sensitivity optimized [11]. The larger crystal face is used as the readout face, and is polished and air-coupled to a Hamamatsu position-sensitive PMT (PSPMT) H8500 having 8 x 8(= 64) anodes. The other faces are depolished and black-painted so as to reduce reflections inside the crystal, allowing the calculation of the gamma interaction point inside the crystal [11]. This is done in the following way:
Each time an event is detected by the PSPMT, the position of the interaction in the crystal can be determined in two ways [11].

1. The x- and y-position of the gamma impact is calculated from the centroid of the light beam as measured by the segmented anode of the PSPMT.

2. The z-position, the in-depth of the impact, is a function of the radius of the light spot on the readout face, as detected by the PSPMT; in other words, a large spot indicates an impact remote from the PMT and a smaller spot an impact nearer to the PMT.

The MAMMI PET is a perfect test bench for the TurboPET project, for the following reasons:

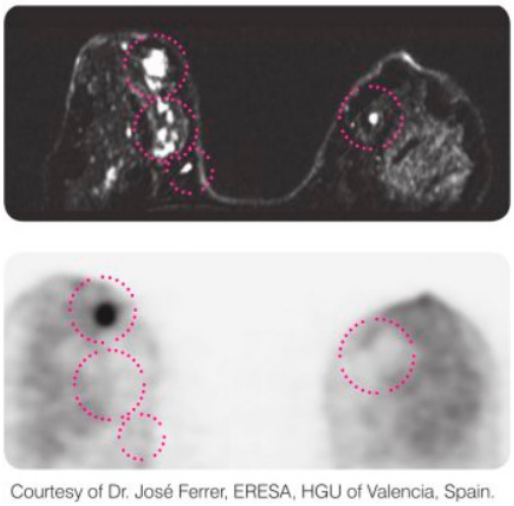


(a)

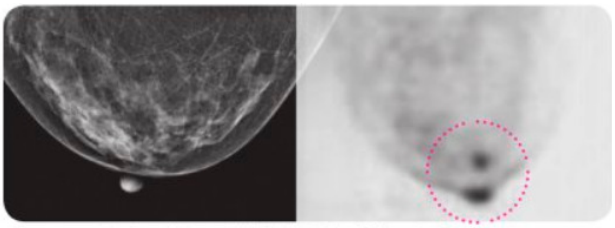


(b)

Figure 5.2: Comparing breast images obtained with a MAMMI PET scanner to other imaging techniques. (a) An MRI image and a MAMMI PET image of the same breast are compared. The MRI image shows multiple suspicious regions, while the MAMMI PET image shows that only one of them is a tumor [8]. (b) An X-ray image and a MAMMI PET image of the same breast are compared. The X-ray image does not show specific suspicious regions, while the MAMMI PET image clearly shows a tumor [8].

- It is a clinically available PET scanner.
- It has two identical rings, where, for the sake of comparison, one could be replaced with enhanced scintillator crystals without changing anything else. The fact that the MAMMI PET scanner is an approved clinical device enables to validate the new configuration directly in a clinical environment.
- Furthermore, since the scintillator surface is relatively large, edge effects in the deposition of the $TiO_2$ layer and during the patterning process are less significant.
- In order to benefit from the same algorithms that determine the gamma interaction point, the nanopatterned crystals, replacing the standard crystals, would also be painted black and read out without optical coupling grease. Such a configuration would produce the ideal scenario for the testing of photonic crystals.

## 5.2 Introduction to the patterning of photonic crystals for TurboPET

To understand and produce the optimal photonic patterns, simulations are an important tool to predict their possible performance before engaging in the production process. Thereafter, prototypes and selective samples were characterized in terms of light output.

According to what was explained in terms of the simulation tools in section 4.5.1, such calculations were also made for the TurboPET project. As such, Geant4 was used for

Figure 5.3: The PET ring in the MAMMI PET, without its plastic casing, consisting of two ring on top of each other, each with 12 scintillating crystals.

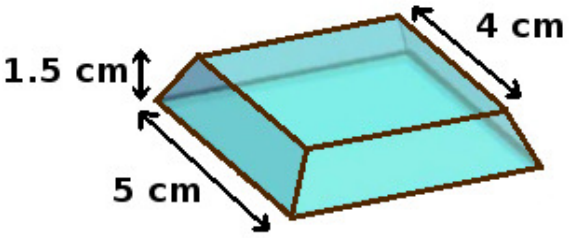


Figure 5.4: The MAMMI crystal, a trapezoidal LYSO crystal, with a 50x50 $mm^2$ and a 40x40 $mm^2$ face and a thickness of 15 mm.

the simulation of the internal light distribution in the trapezoidal LYSO crystal (figure 5.4), and CAMFR to calculate the effect of the photonic crystal layers for the final light extraction. From these simulations one can derive the net effect of the nanopattern on the readout efficiency as compared to a non-patterned crystal surface. Since the emphasis is on the first light incidence at the readout surface of the crystal, these simulations can be directly compared with the MAMMI crystals, offering the same scenario for the light extraction as they are depolished and black-painted.

Photonic crystal slabs have been produced both on the 15 mm thick MAMMI crystals and on thinner, 12 mm thick, crystals used in the so-called Albira PET scanner from the same manufacturer. Note, the geometrical difference between the MAMMI and Albira crystals was found to be negligible for the type of light output measurements that have been performed in this work. The simulation work provided the input to the manufacture of four different prototypes with four different patterns, from which the best pattern was selected to become the optimum pattern for the production of the 12 new crystals for TurboPET. All patterned crystals have been evaluated in the following way:

- **Visual inspection**; that is to spot gross defects on the patterned crystal surface.
- **SEM imaging**; this is to determine at the nanoscale (a) the shape of the produced nanostructure and (b) to identify defects.
- **Light output measurement**, with air-coupling, using the Hamamatsu R10755 PMT setup (datasheet in appendix H), with its advantage of being able to accommodate large crystals of a 50x50 $mm^2$ readout face.

## 5.3 Prototypes produced with nano-imprint lithography

At the beginning of the TurboPET project the nano-imprint lithography (NIL) method, as explained in section 4.4.1, was still under development. This method allows one to produce a photonic crystal pattern of pillars arranged in a square lattice, as shown in figure 5.5a. The pillars are produced from $TiO_2$, with a refractive index of 2.4.

### 5.3.1 Simulations for optimization of lattice parameters

The first set of simulations was used to predict the best possible pattern for the nano-imprint lithography method, aiming for a pillar height of 300 nm. This height is constrained by the thickness of the $TiO_2$ layer that needs to be deposited on the scintillator before the patterning can start. Given the fixed pillar height, simulations then focus on finding the best diameter and periodicity of the pattern. The results of these simulations are shown in figure 5.5b. The outcome of this is that the optimum gain in light yield is obtained when a pillar diameter of 450 nm and a pitch of 670 nm are used. The gain in light extraction is then a factor of 1.7.

### 5.3.2 Characterization of prototypes

These parameters, derived from the simulations, have then been taken as input for the production of the stamps needed for the actual lithography process. Photonic prototypes produced by this imprint lithography process were manufactures on two Albira crystals, 34LYSO85-3 and 34LYSO85-4. Note, although the same stamp with the given physical parameters of the pattern has been use, the variables controlling the etching process leave room for optimizing each pattern on a given crystal. This can result in patterns that are not necessarily the ones prescribed by the simulation
From the photos in figures 5.6a and 5.6b, and judging from the iridescence emanating from the surface, one can deduce two things. First, the patterning does not extend over the entire surface of the crystal, i.e. all the way up to the edges, and second that the pattern itself is not perfectly homogeneous over the entire patterned region. To investigate this further, SEM images were made of the two crystals the results of which are shown in figures 5.7a and 5.7b. Although the same stamp is used for the two crystals, the resulting final patterns are clearly not the same. For crystal number 34LYSO85-3, the SEM images show a pillar diameter of 600 nm, not being the prescribed diameter of 450 nm, albeit with a correct periodicity of 670 nm.
In case of the 34LYSO85-4 crystal, the etching parameters were different from those of the other crystal, leading to a pattern of excessively thick pillars, being so large that they effectively touch each other and thus make the pattern appear as holes, as seen in figure 5.7b. The SEM images prove our previous observations that the patterns are not homogeneous.

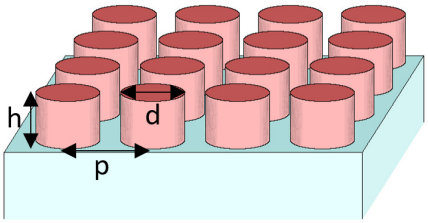


(a)

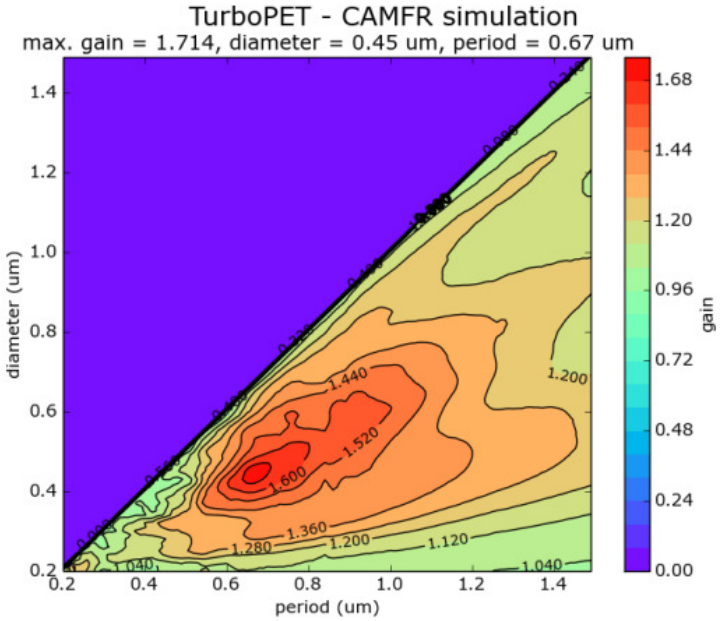


(b)

Figure 5.5: (a) Schematics of a nano-pattern with pillars in a square lattice. The diameter (d), period (p) and height (h) of the pattern have been indicated. (b) Optimization of period (p) and diameter (d) of a $TiO_2$ (RI=2.4) nano-pattern of pillars in a square lattice, with a height of 300 nm, on a MAMMI crystal.

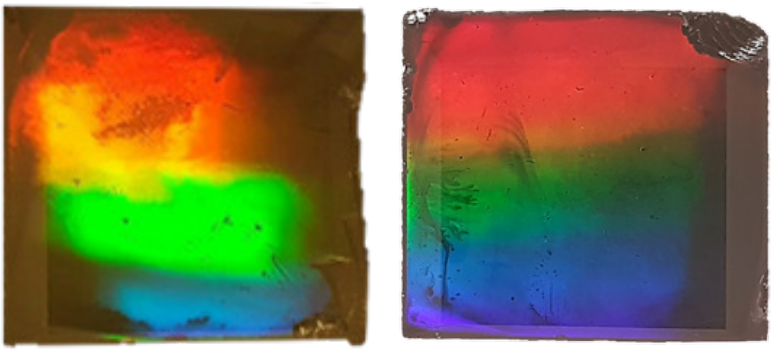

(a) (b)

Figure 5.6: (a) Surface of the 34LYSO85-3 Albira crystal after undergoing nano-imprinting with nano-imprint lithography. (b) Surface of the 34LYSO85-4 Albira crystal after undergoing nano-imprinting with nano-imprint lithography.

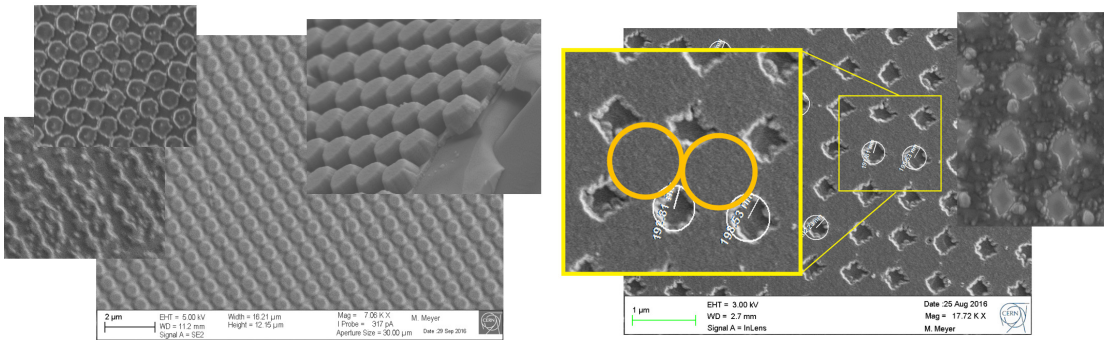

(a) (b)

Figure 5.7: (a) SEM image of the 34LYSO85-3 Albira crystal after undergoing nano-imprinting with nano-imprint lithography. The tilted image on the top right corner was taken from a piece that was broken of the the crystal. (b) SEM image of the 34LYSO85-4 Albira crystal after undergoing nano-imprinting with nano-imprint lithography.

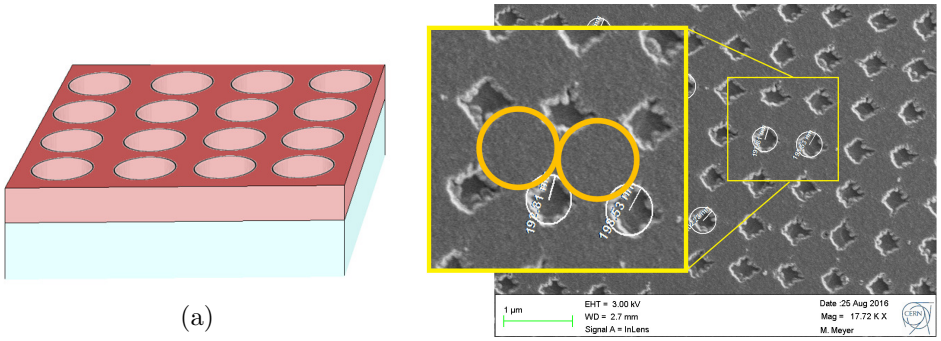

(a) (b)

Figure 5.8: (a) Schematics of a nano-pattern with holes in a square lattice. (b) SEM image of the 34LYSO85-3 crystal. It was attempted to imprint pillars in a square lattice, since the diameter of the pillars is large, the pattern resembles a pattern of holes in a square lattice.

#### 5.3.2.1 Readjustment of parameters in the simulations in view of the produced patterns

As stated before, crystal 34LYSO85-3, has pillars of 600 nm diameter instead of 450 nm, the difference of which needs to be taken into account in the calculations for the expected gain in light output. As in figure 5.5b, the simulations with this new geometry predict a light gain of 1.4 instead of 1.7 found previously for optimum performance.

For crystal 34LYSO85-4 the apparent pattern as shown by the SEM is so different from that of the other crystal that rather a new set of simulations with more than just a single adjustment as above is needed in order to understand whatever light gain could be expected from such a structure. The result of this turned out as a gain being close to 1.1, as marked by a read circle in the contour plot of figure 5.9. Nonetheless, with the new set of simulations in hand, the author was curious to see what a pattern of "holes" with yet the correct periodicity and diameter might yield in terms of light output. For such a pattern of "holes", the contour plot in figure 5.9 indicates a light gain of $\sim 1.4$, demonstrating that also a pattern of holes can be an option for a photonic crystal.

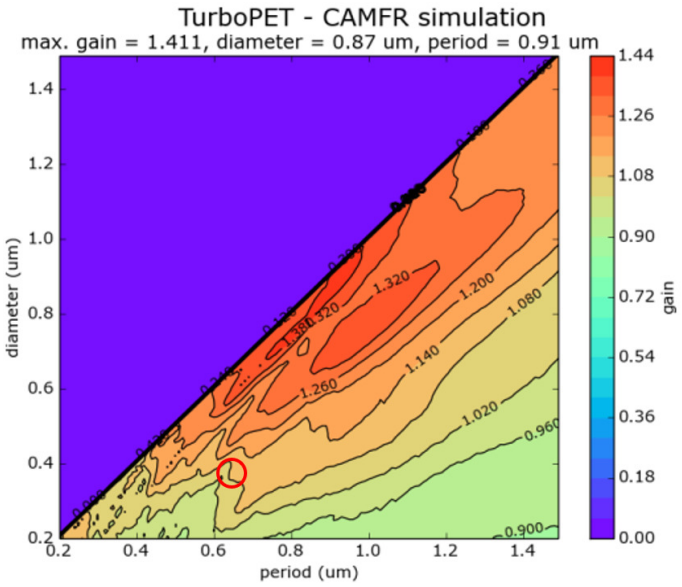


Figure 5.9: Optimization of period (p) and diameter (d) of holes in a square lattice, in a 300 nm thick $TiO_2$ (RI=2.4) layer, on a MAMMI crystal. The red circle shows the parameters for the pattern on the sample in figure 5.8 (b).

#### 5.3.2.2 Measurement of light output and energy resolution

The two crystals, 34LYSO85-3 and 34LYSO85-4, have undergone light output measurements with the setup described in section 3.2. Figure 5.10 shows an example of a light output measurement with crystal 34LYSO85-3, before and after nanostructuring.
The first crystal, 34LYSO85-3, has an effective gain in light output of 1.34, compared to a simulated gain of 1.4. The measured gain of 1.34 should have led to an *improvement* in energy resolution by a factor of $\sqrt{1.34} = 1.16$, whereas in fact the measured energy resolution showed a *deterioration* by a factor of 1.28. This is attributed to the inhomogeneities of the pattern itself.
Despite its anomalies, the other crystal produced a light gain of 1.19. This is not completely in line with the simulated gain, owing to the fact that the simulation was based on round shaped holes rather than the irregularly shaped holes as seen in the actual pattern. Also the fact that the energy resolution *degraded* by a factor of 1.33, despite this small light gain, is seen as a result from the inhomogeneities of the pattern.

## 5.4 Prototypes produced with sol-gel lithography

Relatively late into the project, the sol-gel production method, still under development, was added to the program. With its few production steps, as explained in 4.4.2, this method is fast and intrinsically safer. This process produces cones made of $TiO_2$ in a hexagonal lattice, as shown in figure 5.11a.

### 5.4.1 Simulated optimization of lattice parameters

Since the engraved patterns on the available stamps for this process have a periodicity of 1000 nm, the simulations have taken this as a fixed value. As explained before, a change in cone diameter and height goes hand in hand with a change in refractive index. The producers estimated a linear correlation between structure size and refractive index.

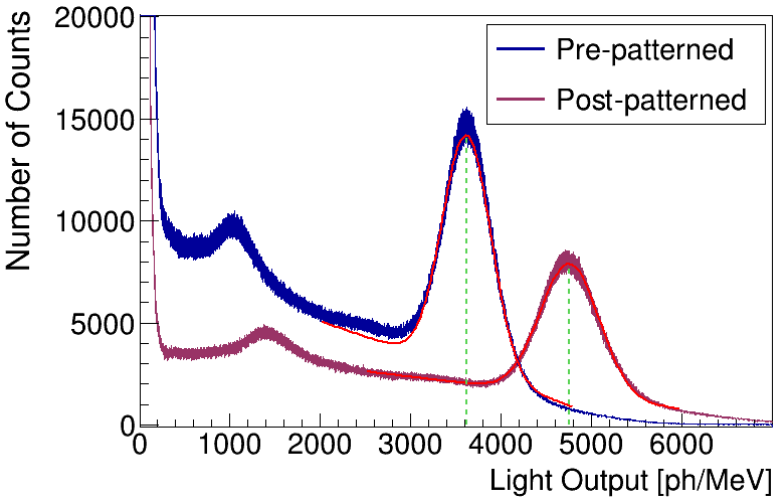


Figure 5.10: Examples of a light output measurement with crystal 34LYSO85-3, before and after nanostructuring.

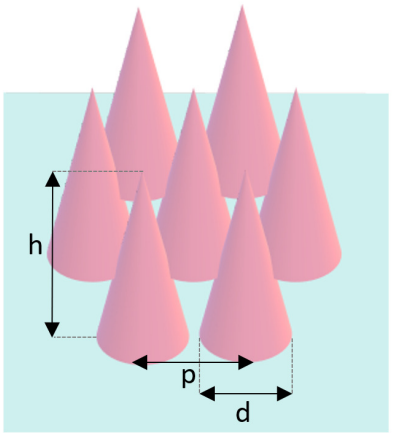


(a)

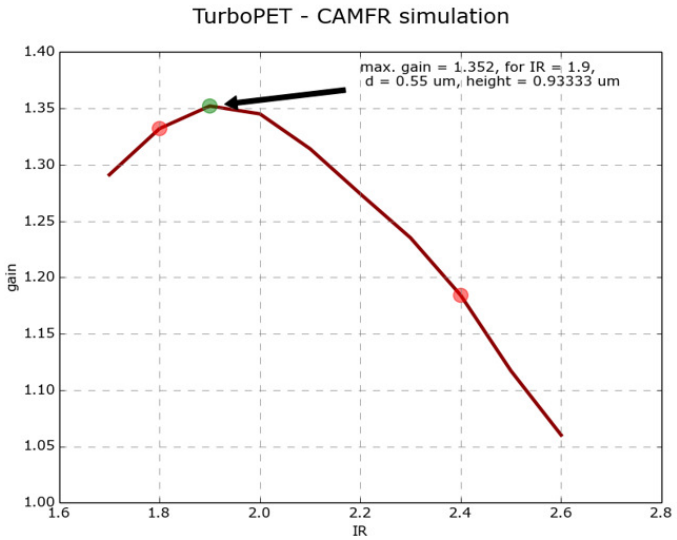


(b)

Figure 5.11: (a) Cones in a hexagonal lattice, as can be produced with the sol-gel production method. Periodicity (p), height (h) and diameter (d) are indicated in the image. (b) Optimization of the refractive index of the with sol-gel produced $TiO_2$ nano-structure.

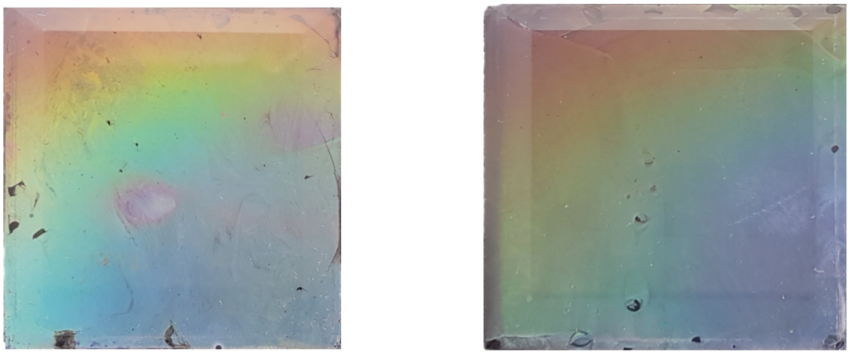

(a) 31LYSO-10 (b) 31LYSO-11

Figure 5.12: Surface of the two MAMMI crystals after undergoing nano-imprinting with sol-gel lithography.

Table 5.1 shows the relationship between the measured refractive index (RI) and the

Table 5.1: Produced $TiO_2$ sol-gel patterns and their measured parameters.

| Refractive Index | Period (nm) | Height (nm) | Diameter (nm) |
|---|---|---|---|
| 1.8 | 1000 | 1000 | 600 |
| 2.4 | 1000 | 600 | 300 |

corresponding structures of two test patterns. From this information one can derive the height and diameter as a function of RI in the following way:

$$height = 0.67 \cdot (1.8 - RI) + 1.00 = 2.2 - 0.67RI \tag{5.1}$$

$$diameter = 0.50 \cdot (1.8 - RI) + 0.60 = 1.5 - 0.5RI \tag{5.2}$$

This is used as input for the simulations where only the RI has been taken as variable parameter in the optimization. The results of these are illustrated in figure 5.11b. As indicated by the green dot in the graph, the maximum expected gain in light output under the given constraints is 1.35, where the refractive index of 1.9 gives a cone diameter of 550 nm and a cone height of 933 nm. It is clear that a higher refractive index, which is usually desired for the studied application, does not always guarantee a higher light extraction. While a higher refractive index is commonly favored for better light extraction, the simulations for *this* structure show an optimum in light output at cone sizes where the refractive index is not the highest. As a conclusion, larger cone sizes lead to higher light extraction from a scintillator despite a lower refractive index.

### 5.4.2 Characterization of prototypes

Two prototype MAMMI crystals, named crystal 31LYSO-10 and crystal 31LYSO-11, were imprinted from two different stamps, both produced via self-assembly (with its inherent deficiency to provide a perfect periodic pattern to begin with). Unfortunately, this produces only a *locally* regular periodicity, whereas *global* periodicity is not maintained, appearing as multiple clusters of locally regular structures grown together. Still, it is expected that this does not significantly affect the light output as long as the local periodicity is preserved over several wavelengths.

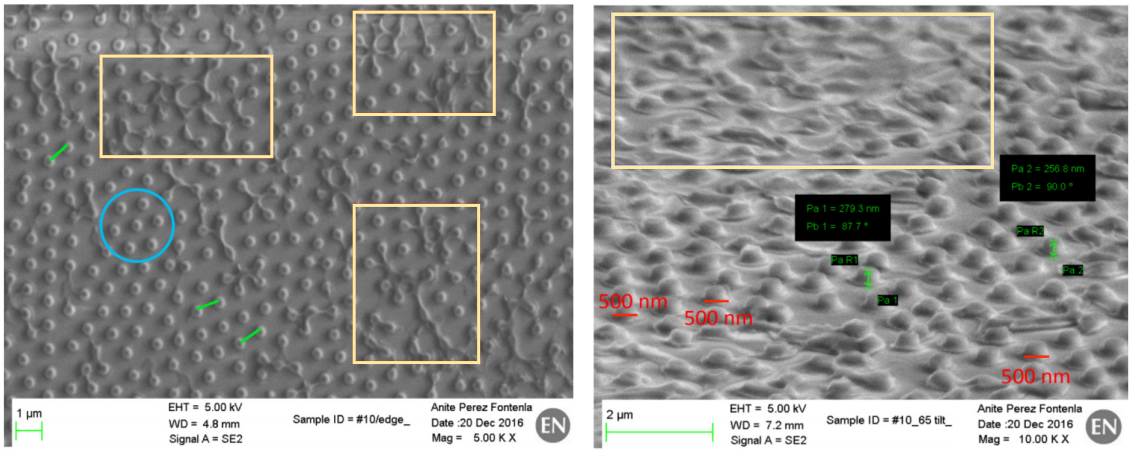


(a) 31LYSO-10

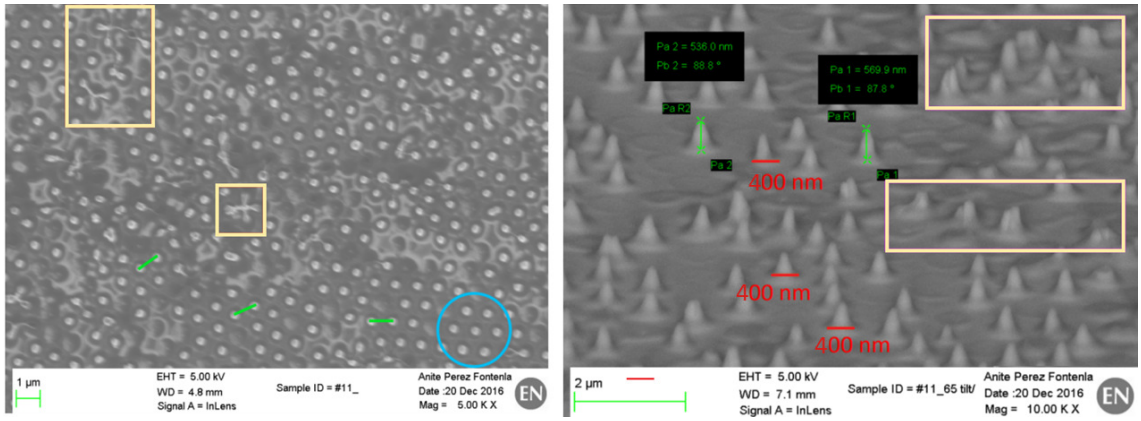


(b) 31LYSO-11

Figure 5.13: SEM images of the nano-pattern on the two MAMMI crystals, 31LYSO-10 (left) and 31LYSO-11 (right), after undergoing nano-imprinting with sol-gel lithography.

Figures 5.12a and 5.12b show images of the surfaces of the two MAMMI crystals after their imprint. The surface of both crystals shows iridescent coloring over the entire surface, all the way up to the crystal edges. This indicates a very homogeneous nanopattern across the entire surface. Both crystals, nonetheless, exhibit a few minor defects shown as dark spots and, besides that, a stain can be seen in the center of crystal 31LYSO-10 (figure 5.12a).

Figure 5.13a is an SEM image of the patterned 31LYSO-10 crystal. The tilted image on the right hand side of figure 5.13a shows cones with a bumpy, non-pointed structure. There is good local periodicity as shown by the light blue circle in figure 5.13a. Thus periodicity extends over a large region, nonetheless with a few visible defects to be seen inside the yellow squares of the image. In that case, the pronounced bumps of the otherwise intact structure seem to be deflated. The pitch of the bumps was measured to be 1000 nm, their base diameter to 450 nm and their average height to 300 nm.

Figure 5.13b is an SEM image of the other patterned crystal (crystal 31LYSO-11). In its tilted view on the right hand side one can see that in this case the cones are longer and more pointed, sitting on a pedestal-like base above the crystal surface, becoming more

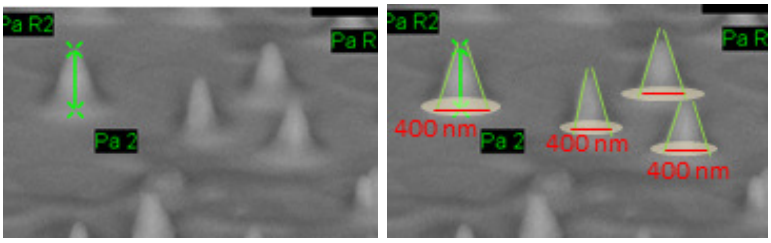


Figure 5.14: Twice the same zoom of SEM images of the nano-pattern on crystal 31LYSO-11, after undergoing nano-imprinting with sol-gel lithography. Right image indicates pedestal-like base of the cones.

visible in a zoomed section of the surface shown in figure 5.14. Again, the blue circle indicates a section of good local periodicity, however extending over shorter distances as compared to the 31LYSO-10 crystal. The right-hand image shows many cone-vacancies in the nanolattice, which as mentioned before are attributed to the imperfect mask originating from the self-assembly process. The periodicity in this crystal is again found to be 1000 nm, while the base diameter was 300 nm and the average height 600 nm. Details are given in figure 5.14.

#### 5.4.2.1 Simulations of produced patterns

The cones produced on the surface of crystal 31LYSO-10 have a refractive index measured by the producer of 2.4, however, their corresponding measured height is much smaller than initially predicted and used as input for the simulations in section 5.4.1. New simulation parameters were consequently applied for the cones, i.e. with a base diameter of 450 nm and a cone height of 300 nm. With these parameters, the expected gain in light extraction is 1.16. It should be noted that this simulation does not take into account the actual *bumpy* shape of the structure, thus leaving room for a possible error in the simulated value.
In the case of crystal 31LYSO-11, the produced structure, i.e. with an average cone diameter of 300 nm, and a height of 600 nm with a corresponding refractive index of 2.4, is in agreement with one of the previously simulated nanostructures, resulting in an expected gain of 1.18.

#### 5.4.2.2 Evaluation of light output and energy resolution

As explained in section 5.1.1, black-painting of the crystal was used as a means to facilitate the reconstruction of the $\gamma$-interaction point inside the crystal, an important feature for the final PET scanner. Therefore, table 5.2 shows only the results of light output measurements with black-painted crystals, specifically with crystals 31LYSO-10 and 31LYSO-11. As the table shows, crystal 31LYSO-10 has a gain in light output of 1.15 and 31LYSO-11 a gain of 1.17. Both values are in good agreement with the corresponding simulated expectations. Figure 5.15 shows an example of one light output measurement of crystal 31LYSO-11, before and after nanostructuring.
It should be noted that the measured improvement in energy resolution, i.e. by a factor of 1.3, seems to be inconsistent with the measured improvement in light gain, at least from a statistical point of view. This observation will be addressed in section 5.7.

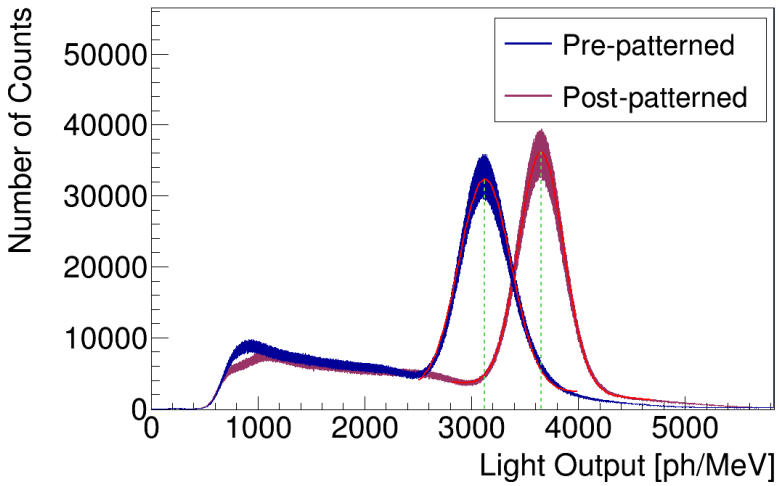


Figure 5.15: Examples of a light output measurement with crystal 31LYSO-11, before and after nanostructuring.

Table 5.2: Light output (LO) and energy resolution ($E_{res}$) measurements of two MAMMI crystals, 31LYSO-10 and 31LYSO-11, before and after nano-imprinting with sol-gel lithography, with and without black paint.

| Crystal | black-painted | **Pre-patterning** LO (kph/MeV) | $E_{res}$ (%) | **Post-patterning** LO (kph/MeV) | $E_{res}$ (%) | Gain LO | Gain $E_{res}$ | Simulated Gain LO |
|---|---|---|---|---|---|---|---|---|
| 31LYSO-10 | yes | 3.27 | 23 | 3.75 | 18 | 1.15 | 1.3 | 1.16 |
| 31LYSO-11 | yes | 3.13 | 24 | 3.67 | 19 | 1.17 | 1.3 | 1.18 |

Table 5.3: Average heights of the cones from the photonic crystal structures produced on the 7 imaged MAMMI crystals after nano-imprinting with sol-gel lithography.

| Crystal | Average cone height (nm) |
|---|---|
| 31LYSO-B1 | 570 |
| 31LYSO-B2 | 640 |
| 31LYSO-5 | 660 |
| 31LYSO-6 | 640 |
| 31LYSO-7 | 680 |
| 31LYSO-11 | 600 |
| 31LYSO-12 | 460 |
| average | 607 |

## 5.5 Crystal set produced for the TurboPET ring

Among the various patterns that were investigated, the pattern fabricated via sol-gel on crystal 31LYSO-11 (section 5.4) was chosen for the final TurboPET ring for of its higher reproducibility, although the crystal had a slightly lower light output as compared to the one imprinted via nano-imprint lithography, as discussed in section 5.3. Therefore, ten untreated MAMMI crystals (two had been damaged during transport and had to be eliminated) were fully characterized prior to sending them to the manufacturer for the patterning. Upon return from the manufacturer, some samples underwent scanning electron microscopy and all of them were tested for light output and energy resolution. For completeness, appendix F.1 shows nine crystals of the set after imprinting. From the observed homogeneity of the iridescence one can deduce the high quality of the produced nanostructured layer. Similarly, in appendix F.2, the respective SEM images of the imprinted crystals are shown. Unlike the figures given in appendix F.1 the SEM images show larger differences in quality between the crystals, such as void spaces in the nano-pattern and regions with broken cones. In general the structure parameters correspond to the features that were specified for the imprinting. To give an impression of the reproducibility of the structure, table 5.3 shows the fluctuations in cone height for 7 MAMMI crystals.

The light output and energy resolution of the 10 black-painted MAMMI crystals, including the 31LYSO-11 crystal from the previous section, were measured before and after patterning. To complete the set of 12 MAMMI crystals for the TurboPET ring, two additional crystals, called set1_1 and set2_1, were added to the characterization procedure, however only after their patterning. It should be noted that in view of a slightly different pattern structure, the performance of these crystals cannot be directly compared with that of the other 10. They principally serve as reserve crystals to complete the ring to be made out of 12 crystals. In order to get an estimate of their improvement in light output, the average pre-imprint light output of the other 10 MAMMI crystals was taken as reference. The results of the measurements for these 12 crystals are summarized in table 5.4. As seen from the table, the average gain in light output is a factor of 1.16, being in good agreement with the predicted gain for this stamp, and the average gain in energy resolution is 1.3, not to be expected on statistical grounds only. In line with the arguments above, it is not surprising that crystals set1_1 and set2_1 do not match the measured light output gains of the other 10 crystals. In fact, they do not show any improvement in light extraction whatsoever. On the other hand, their pattern does improve the energy resolution similar to the other 10 crystals. This reinforces the notion that not only by photostatistics, the energy resolution is influenced by the photonic structure.

Table 5.4: Light output (LO) and energy resolution ($E_{res}$) measurements of the MAMMI crystals for the TurboPET ring, before and after nano-imprinting with sol-gel lithography. The gains marked with an asterisk are LO or $E_{res}$ measurements compared to the corresponding average of the 10 MAMMI crystals before patterning.

| Crystal | **Pre-patterning** LO (kph/MeV) | $E_{res}$ (%) | **Post-patterning** LO (kph/MeV) | $E_{res}$ (%) | Gain LO | Gain $E_{res}$ |
|---|---|---|---|---|---|---|
| 31LYSO-B1 | 3.48 | 22 | 3.81 | 17 | 1.10 | 1.3 |
| 31LYSO-B2 | 3.39 | 21 | 3.88 | 17 | 1.14 | 1.2 |
| 31LYSO-B3 | 3.41 | 22 | 3.86 | 17 | 1.13 | 1.3 |
| 31LYSO-5 | 3.04 | 25 | 3.56 | 20 | 1.17 | 1.3 |
| 31LYSO-6 | 2.86 | 23 | 3.54 | 20 | 1.24 | 1.2 |
| 31LYSO-7 | 3.30 | 22 | 3.54 | 19 | 1.07 | 1.2 |
| 31LYSO-8 | 3.28 | 22 | 3.62 | 19 | 1.10 | 1.2 |
| 31LYSO-9 | 2.93 | 23 | 3.65 | 18 | 1.24 | 1.3 |
| 31LYSO-11 | 3.13 | 24 | 3.67 | 19 | 1.17 | 1.3 |
| 31LYSO-12 | 2.84 | 23 | 3.61 | 18 | 1.23 | 1.3 |
| Average | 3.16 | 23 | 3.67 | 18 | 1.16 | 1.3 |
| set1_1 | - | - | 3.04 | 16 | 0.96* | 1.4* |
| set2_1 | - | - | 3.03 | 16 | 0.96* | 1.4* |
| **Simulation** h=600, d=300 | | | | | 1.18 | |

## 5.6 Implementation in the TurboPET scanner

As mentioned before, in order to improve the detection capability of one of the two detector rings of the existing PET scanner MAMMI PET, one of the two rings was equipped with 12 MAMMI crystals with their imprinted nano-pattern. This modified PET scanner is called TurboPET. TurboPET was assembled and calibrated at Oncovision in Valencia. A number of phantom measurements were made in order to calibrate the modified scanner and also to assess its performance. Both Derenzo and Nema phantoms, standard tools in scanner evaluation, were used to test the new scanner for an improvement in image quality and in particular to evaluate its spatial resolution and lesion-to-noise ratio.

A Derenzo phantom, like the one illustrated in figure 5.16a, filled with FDG was used to determine the spatial resolution of the scanner. The produced images are shown in figure 5.17a,b. Both images display the intensity of the radioactive dots together with an intensity profile across a line of dots. Both TurboPET rings show that holes with 4.8 mm, 4.0 mm and 3.2 mm diameter can be clearly separated. On the other hand, differences show up for smaller sizes, e.g. with 2.4 mm holes, where the unpatterned ring (figure 5.17aa) is still capable to distinguish between most of the 2.4 mm holes, whereas the patterned ring (figure 5.17bb) falls short of differentiating between the inner ones. Based on this observation alone the patterned ring seems to exhibit a slightly worse spatial resolution than the unpatterned ring.

Figure 5.18a,b shows measurements with the Nema phantom, used to simulate lesions in the breast. As the pictures show, the general breast tissue shows normal background activity while the hot spots, i.e. areas of increased activity above the noise floor, represent lesions. Measuring the signal strength corresponding to the lesion activity and that outside the lesion provides an estimate of the lesion-to-noise ratio as expected in real

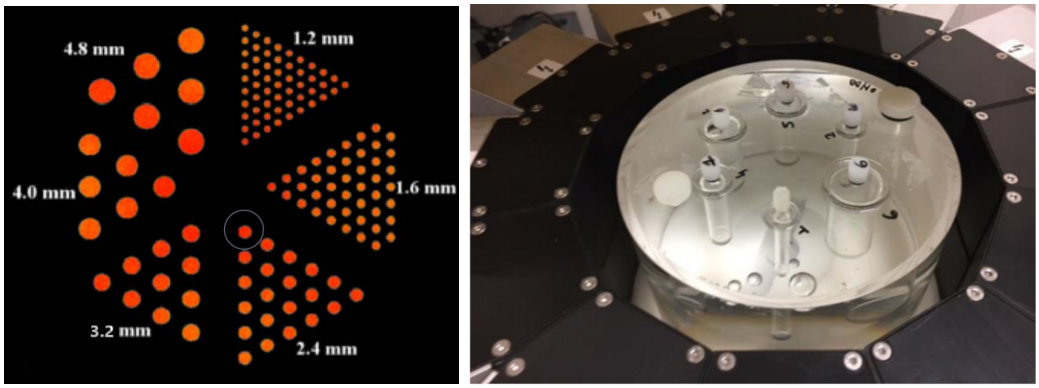


(a) (b)

Figure 5.16: (a) Schematics of a Derenzo Phantom [12], as used with the TurboPET scanner to assess spatial resolution. (b) A picture of the Nema phantom placed in the TurboPET rings for imaging.

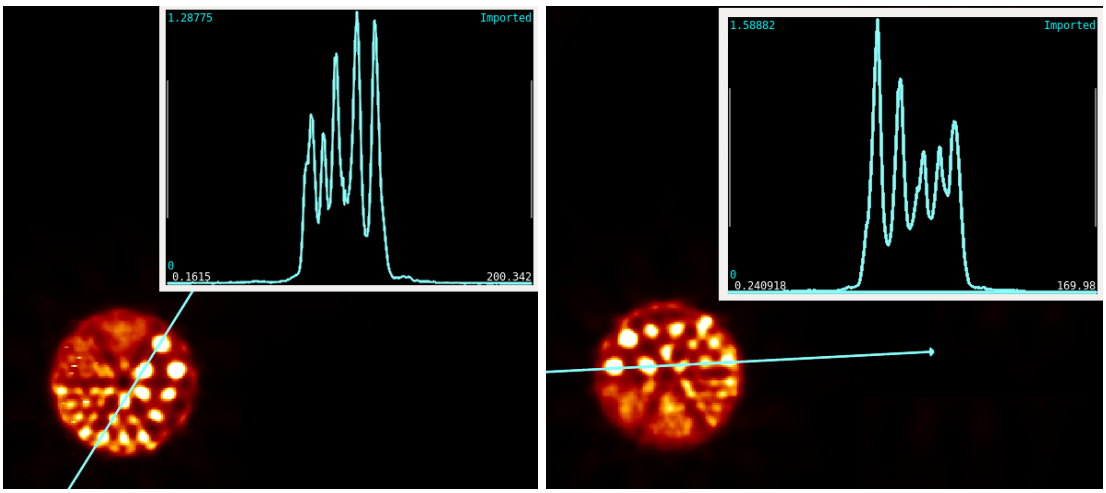


(a) (b)

Figure 5.17: Measurement of the Derenzo phantom, showing the image and the line-profile of the blue line, using: (a) the unpatterned ring, (b) the patterned ring.

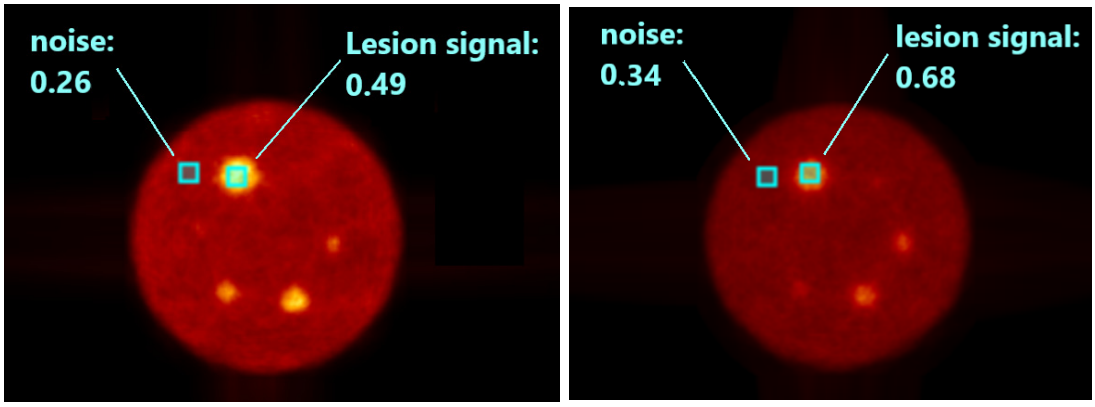


(a) (b)

Figure 5.18: Measurement of the Nema phantom used to simulate a body with a lesion, showing the produced image and the measured signal of the lesion and noise outside the lesion, using: (a) the unpatterned ring, (b) the patterned ring. Note that the difference in color intensity between the images does not necessarily represent the same difference in activity.

breast tissue. These values are indicated in figure 5.18. The lesion-to-noise ratio for the unpatterned ring (figure 5.18a) is $0.49/0.26 = 1.88$ and that for the patterned ring (figure 5.18b) $0.68/0.34 = 2.00$, a marginal advantage of the patterned ring of only 6% over the unpatterned ring.
As the values show, neither the 16% improvement in light output nor the 30% higher energy resolution of the patterned ring, seem to have a significant beneficial effect on the lesion-to-noise ratio, also combined with a slight deterioration in spatial resolution. A possible explanation for the unexpected deterioration in spatial resolution for this ring could be light scattering at the photonic layer being more pronounced there than at the polished crystal surface. It is assumed that this has a detrimental effect on the Anger logic to precisely reconstruct the interaction point in the crystal. On the other hand, the slight gain in lesion-to-noise ratio observed in the patterned ring, does not warrant a clinical study at this point.

## 5.7 Conclusion

In the course of this project, two different nano-imprint lithography methods were developed to produce stable $TiO_2$ nanostructures in the form of cones and pillars to be imprinted on the readout surfaces of large monolithic scintillators: (1) nano-imprint lithography combined with reactive ion etching and (2) sol-gel lithography.
From the nano-imprint lithography method combined with reactive ion etching, the best gain in light output obtained for black-painted MAMMI (or Albira) crystals was 1.34. This method, however, ensued a *loss* in energy resolution by 28%, probably attributed to inhomogeneities in the photonic crystal pattern across the crystal surface, resulting from irregular electrostatic charging during the reactive ion etching process. This is an aspect that is still to be improved, as well as the reproducibility of patterns with this method.
For sol-gel lithography, on the other hand, the maximum obtained gain in light output measured for black-painted MAMMI crystals was a factor of 1.24, slightly less than obtained with the nano-imprint process. However, contrary to the former process, this technology

resulted in an unexpected, at least to that extent, improvement in energy resolution by 30%. This could be associated with a more homogeneous photonic structure across the crystal surface, the extent of which still needs to be explained other than by photo statistics alone.
Another important outcome of this study was, next to the successful production of fully imprinted prototypes, to manufacture a set of 10 MAMMI crystals with the same imprint with high reproducibility.
In the end, a complete PET detector ring was assembled with these scintillating crystals and evaluated with phantoms. The outcome of the measurements with the patterned scanner ring, however, leads to the conclusion that an enhancement in the lesion-to-noise ratio by only a factor of 1.06 and even a deterioration, however lite, in spatial resolution, is too little to engage in a clinical study unless further improvements in this method can be made. Nonetheless, the results of this study show that there is indeed room for improvement at the single crystal level, to be incorporated eventually at the system level in a full scanner like TurboPET.

# Bibliography


[1] S. Zanettini, V. Gâté, E. Usureau, J. Ruscica, F. Hamouda, K. Nomenyo, L. L. Cunff, H. Kadiri, G. Lerondel, M. Salomini, R. Pots, E. Auffray, P. Lecoq, J. Alamo, J. Prior, A. Iltis, and D. Turover, "Improved light extraction efficiency on 2 inches lyso with nanopatterned tio2 photonic crystals." Poster presented at IEEE NSS/MIC, 29 October - 5 November 2016, Strasbourg.

[2] A. Knapitsch and P. Lecoq, "Review on photonic crystal coatings for scintillators," *International Journal of Modern Physics A*, vol. 29, no. 30, p. 1430070, 2014.

[3] M. Salomoni, R. Pots, E. Auffray, and P. Lecoq, "Enhancing light extraction of inorganic scintillators using photonic crystals," *Crystals*, vol. 8, p. 78, Feb 2018.

[4] M. Salomoni, *Boosting scintillation based detection*. PhD thesis, Università degli studi di Milano Bicocca, 2019.

[5] "Napa technologies homepage." `https://www.napa-technologies.com/`. Accessed: 2020-08-30.

[6] "Oncovision homepage." `https://www.oncovision.com/`. Accessed: 2020-08-30.

[7] "Mammi pet website from oncovision." `https://www.oncovision.com/mammi/`. Accessed: 2020-08-30.

[8] "Patient brochure of the mammi pet on the website of medical expo." `https://pdf.medicalexpo.fr/pdf-en/oncovision/mammi-dedicated-breast-pet/109898-153982.html`. Accessed: 2020-08-30.

[9] "Mammi pet information on the medical expo website." `https://www.medicalexpo.fr/prod/oncovision/product-109898-726353.html`. Accessed: 2020-08-30.

[10] "Mammi breast care website." `https://www.mammibreastcare.com/`. Accessed: 2020-08-30.

[11] L. Moliner, A. J. González, A. Soriano, F. Sánchez, C. Correcher, A. Orero, M. Carles, L. F. Vidal, J. Barberá, L. Caballero, M. Seimetz, C. Vázquez, and J. M. Benlloch, "Design and evaluation of the mammi dedicated breast pet," *Medical Physics*, vol. 39, no. 9, pp. 5393–5404, 2012.

[12] O. Kochebina, S. Jan, S. Stute, V. Sharyy, P. Verrecchia, X. Mancardi, and D. Yvon, "Performance estimation for the high resolution calipso brain pet scanner: A simulation study," *IEEE Transactions on Radiation and Plasma Medical Sciences*, vol. 3, no. 3, pp. 363–370, 2019.

# Chapter 6

# Photonic crystal slabs on cubes: evaluating timing

Results obtained from the research in this chapter have been published and presented in several meetings, conferences and journals:

- Results from sections 6.1 and 6.4.3 have been published in the scientific journal NIMA [1].
- Results from sections 6.2 and 6.4.1 have been presented at the 2017 SCINT school [2] and the SCINT conference in Chamonix [3], furthermore at the 2017 Crystal Clear Collaboration meeting at CERN [4] and on the occasion of the CERN Gentner Day 2017 [5]. They were published in an article in the scientific journal IEEE TNS [6].
- Results from sections 6.1 and 6.2 have been incorporated in a poster presentation at the CERN Doctoral Student Assembly 2018 [7] and in a presentation at the 2018 Luminescent Detectors and Transformers of Ionizing Radiation (LumDeTr) conference in Prague [8].

As discussed in chapter 2.5, there are several ways to improve the coincidence time resolution (CTR) of a crystal. One way is to improve the light transfer efficiency (LTE) of the scintillating crystal in conjunction with its photodetector. The goal of the work presented in here is to make a prototype nano-imprinted scintillating crystal, with a timing performance significantly improved due to the optimization of its LTE. Photonic crystals are designed to improve light extraction upon first photon incidence, an effect that might also be beneficial to fast timing. The figure of merit in this research is put on the coincidence time resolution that can be achieved with these prototypes.
To begin with, this chapter characterizes larger crystal sizes, i.e. 10x10x10 $mm^3$ LYSO cubes and 10x10x20 $mm^3$ LYSO parallelepipeds, with a photonic crystal slab produced on their readout face. The reduced surface of these crystals, much smaller than the monolithic types discussed in the previous chapter, though still larger than real pixel-sized crystals, aggravate edge effects near the border of the crystal resulting in a reduced light extraction from the crystal. On the other hand, the smaller crystal volume eases the reactive ion etching process, as used in one of the patterning methods.

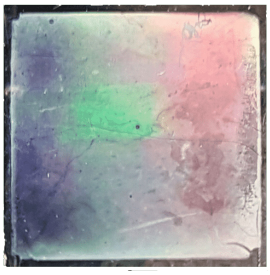

Figure 6.1: Image of the surface of the 10x10x10 $mm^3$ LYSO cube, after imprinting with nano-imprint lithography. [1]

This chapter presents a systematic study of prototypes with two different nano-pattering methods:

- **Nano-imprint lithography**; the prototypes produced with this method are discussed in section 6.1. This patterning process is the same as nano-imprint lithography addressed in the previous chapter. Section 4.4.1 gives a detailed explanation of the method.
- **UV-cured nano-imprint lithography**; prototypes produced with this process are evaluated in section 6.2 with a detailed explanation of the process given previously in section 4.4.3.

In the systematic study the crystals are coupled with an air gap to the photodetector, without any optical coupling agent.
Some additional measurements have been made and are presented in section 6.4, where some additional aspects such as wrapping and optical coupling grease are investigated.

## 6.1 Cubes Patterned with Nano-imprint Lithography

This section reports on the characterization of a 10x10x10 $mm^3$ LYSO cube imprinted via nano-imprint lithography, explained in detail in section 4.4.1. The pattern consists of pillars in a square lattice, etched into a $TiO_2$ layer with RI = 2.4 and with a long-range, i.e. over the entire surface, periodicity. It was produced by Silsef [9] and Napa Technologies. The stamp used for this pattern was an old stamp, where the pattern parameters were not optimized in a foregoing simulation.
The sample was visually inspected and imaged with SEM, thereafter the light output evaluated, with emphasis on what effect the nanopattern will have on the coincidence time resolution. Note, this section makes also reference to the article by Pots et al. [1].

### 6.1.1 Quality of the produced pattern

Figure 6.1 shows an image of the patterned crystal surface. The iridescent coloring extends over the whole surface, all the way up to the edges of the crystal, with however some "stains" and some lite inhomogineities. To examine more closely the fabricated pattern on the scintillator, the photonic crystal slab was scanned with an electron microscope. As in the previous chapter, the resulting images are not perfectly sharp due to electrostatic charging during the imaging process. The top-view images, figures 6.2a and 6.2b, indeed demonstrate the pillar-like structure in a square lattice. The pattern shows good periodicity over a long range, with hardly any defects. The diameter of the pillars is 390 nm,

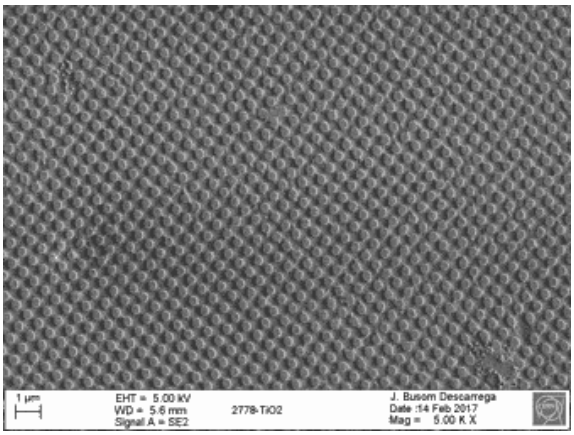


(a)

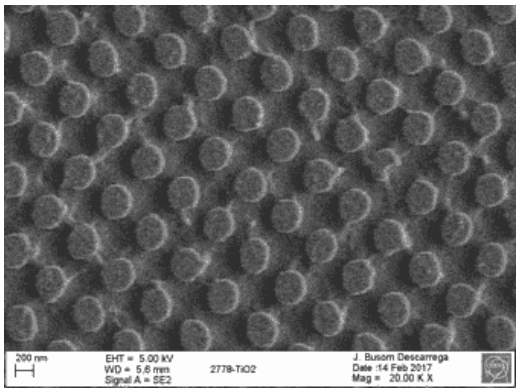


(b)

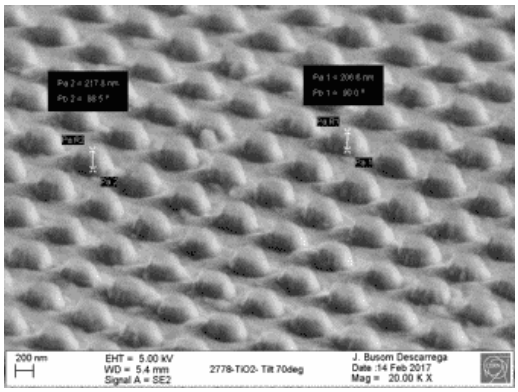


(c)

Figure 6.2: SEM images of the 10x10x10 $nm^3$ LYSO cube after imprinting with nano-imprint lithography. Imaged with (a) 4k magnification, (b) 20k magnification, (c) 20k magnification and this time the sample is tilted by 70 degrees. [1]

with a pitch of 580 nm.
From the tilted view (70 degrees) of the crystal in figure 6.2c one can deduce a pillar height of 180 nm.
The original thickness of the $TiO_2$ sputtered onto the LYSO cube was 300 nm. Therefore, the measured pillar height of 180 nm gives rise to the possibility that the $TiO_2$ layer between the pillars was not entirely etched away, i.e. all the way down to the bare scintillator surface. This could have been caused by too short an exposure to the reactive ion etching, leaving behind a residual layer of effectively up to 120 nm.

### 6.1.2 Simulations

The numbers drawn from the SEM images served as input parameters in the simulations of the pattern, in other words for a pattern with pillars of 300 nm height, 390 nm diameter and a pitch of 580 nm. At this stage no optimization of light output was performed. The simulated transmission of 420 nm light in this photonic crystal slab is shown in figure 6.3a. The red-shaded area in the graph indicates that a fraction of light from the extraction cone is reflected back by the photonic nano-pattern into the crystal. This light, on the other hand, would have been extracted from the crystal had there not been the photonic pattern. Furthermore, the green-shaded area denotes that part of the light that lies outside of the extraction cone, i.e. light that would have been reflected internally and hence lost without the photonic slab, now being extracted by this layer. Light still not being extracted by the photonic crystal is understood to be internally reflected by the photonic crystal in a diffracted manner and therefore under angles different from the incident angle. Since light from the outside of the extraction cone is reflected at different angles, a significant fraction of it is reflected inside the extraction cone and can therefore be extracted from the opposite side of the cube, which is not patterned.

The simulations were run for a cubic 10x10x10 $mm^3$ LYSO crystal *without* paint or wrapping and using air-coupling. The internal light distribution used for this study was furnished by [10]. Figure 6.3b shows this light distribution and the effect on light extraction. A light gain of 1.51 was found due to the presence of the photonic layer, calculated at first incidence.
Further simulations have been made to understand the effect of the suspected residual $TiO_2$ layer, estimated to be 120 nm thick, i.e. a remnant from an assumed incomplete etching process. This was observed in the SEM image in figure 6.2c and discussed above. Absorption by the residual $TiO_2$ floor, however, was deemed to be negligible, since it is highly transparent to 420 nm light. The simulations show that, in this case, the gain in light extraction increases by a factor of 1.59. Therefore, the presence of the residual $TiO_2$ layer does not necessarily lead to a degradation in light output as expected.

### 6.1.3 Characterization

#### 6.1.3.1 Light output

The light output measurements for this cube and a second one of the same dimension, which was used as a reference without nanopatterning, were made with a Hamamatsu R2059 PMT (datasheet in appendix I). The light output was measured only for scenarios where the crystals are *not* wrapped. Four different configuration were investigated:

1. Non-patterned reference crystal mounted to PMT;
2. Patterned crystal with patterned face mounted to PMT;

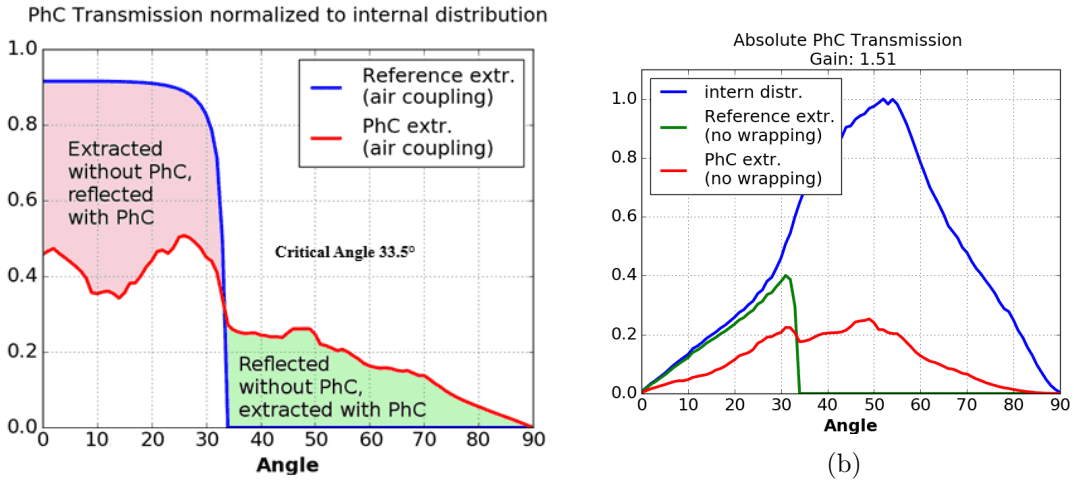


(a) (b)

Figure 6.3: Simulation of light transmission at 420 nm at the LYSO crystal-air interface, with and without a 300 nm thick photonic crystal layer as described above. (a) The red-shaded area indicates light from inside the extraction cone, internally reflected by the PhC. The green-shaded area indicates extracted light from outside of the extraction cone [1]. (b) Effect of the light transmission on the light output of a 10x10x10 $mm^3$ LYSO cube, air-coupled to the photodetector, equipped with and without a photonic layer [1][10].

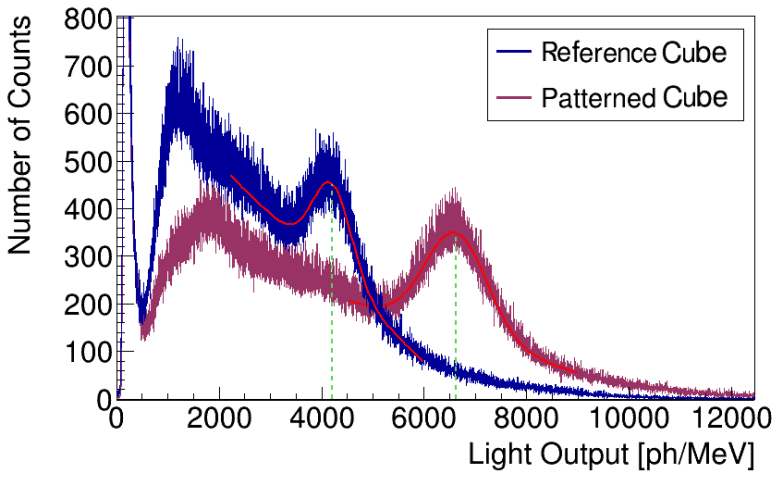


Figure 6.4: Example of a light output measurement with the the LYSO cube imprinted via nano-imprint lithography, compared to a measurement with the reference crystal.

3. Patterned crystal with opposite face mounted to PMT;

4. Patterned crystal with side face mounted to PMT.

The results of these measurements are shown in table 6.1. As the table shows, the patterned crystal improves light output and energy resolution by a factor of 1.5 and 1.1, respectively. The gain in LO is in perfect agreement with the simulations assuming a 0 nm residual $TiO_2$ layer, though also in good agreement with the value assuming a residual layer of 120 nm. It is interesting to see that a nearly identical gain in light yield is achieved when the crystal is read out from the untreated side, opposite to the patterned surface. This indeed is also expected from the simulations as explained in section 6.1. The gain in energy resolution is in line with what one would expect on purely statistical grounds, where $E_{res} = \frac{1}{\sqrt{LO}}$, taking into account the error on the measurement.

#### 6.1.3.2 Coincidence time resolution

Similar to the foregoing measurements, also the coincidence time resolution (CTR) was investigated and compared for the four different configurations as described above. The CTR was measured with the setup discussed in section 3.4 using the NINO readout. For all measurements the Hamamatsu S13360-6050 SiPM with an active surface of 6x6 $mm^2$ and a SPAD-size of 50x50 $\mu m^2$ was used. It should be noted that the 6x6 $mm^2$ area of the SiPM is not completely covering the 10x10 $mm^2$ surface of the LYSO cube. Therefore, one might expect a loss in light extraction owing to the part of the crystal surface not being covered by the photodetector and hence leading to a deterioration in coincidence time resolution. However, for the purpose of comparison, the CTR measurements of cubes with the same dimensions and read out by the same SiPM can be compared without problems, while the absolute CTR values themselves will be inferior because of the uncovered surface of the crystal.
The CTR is measured over a large threshold range, from 20-500 mV, the lowest value of which corresponds to a single photon trigger level. These results are shown in figure 6.5. Figure 6.5(a) shows the CTR plotted against the applied threshold, while figure 6.5(b) shows the calculated CTR ratios for each measurement point between the patterned and the reference cube. One can see, that the highest coincidence time resolution (i.e. lowest CTR value) is obtained for the photonic crystal with 426 ps FWHM, where the patterned surface is read out by the SiPM, or 406 ps FWHM when the opposite crystal face is read out. The CTR, however, deteriorates significantly, i.e. to 484 ps FWHM, when the crystal is read out from one of its side-faces. In contrast, the reference crystal only achieves a CTR

Table 6.1: Comparison of simulated and measured light output (LO) and energy resolution ($E_{res}$) and their gains induced by the nano-pattern. The measurements were performed with a Hamamatsu R2059 PMT. Both Lo and $E_{res}$ are measured with a 5% accuracy, leading to an accuracy of 7% for the measured gain.

| | Measured | | Simulated | | Measured | | Expected |
|---|---|---|---|---|---|---|---|
| | LO (kph/MeV) | gain LO | gain LO 0 nm residual | gain LO 120 nm residual | $E_{res}$ (%) | gain $E_{res}$ | gain $E_{res}$ from meas. LO |
| Reference crystal | 4.4 | - | - | - | 19 | - | - |
| PhC facing detector | 6.5 | 1.5 | 1.5 | 1.6 | 16 | 1.1 | 1.3 |
| PhC opposite side | 6.5 | 1.5 | - | - | 17 | 1.1 | 1.2 |

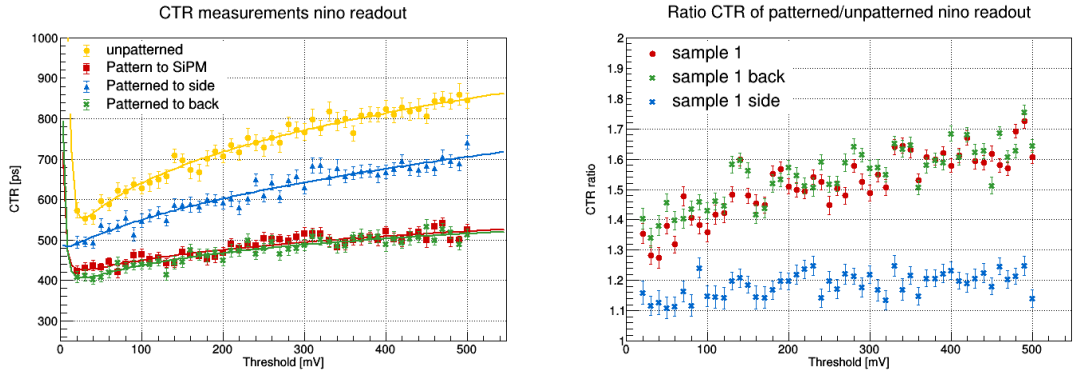


(a) (b)

Figure 6.5: Coincidence Time Resolution FWHM values of a nano-imprinted LYSO cube compared to a reference, unpatterned LYSO cube. The CTR is measured with a 3% accuracy. (a) CTR measurements are performed in three crystal orientations w.r.t. the SiPM window were used: patterned-face-to-SiPM (red squares), opposite-face-to-SiPM (green crosses) and side-face-to-SiPM (blue triangles). The yellow dots are measurements from the reference cube. (b) The ratio of the CTR values form the different configurations w.r.t. the reference crystal are calculated.

of 553 ps. Therefore, the CTR gain of the pattern-to-SiPM and opposite face-to-SiPM readout over the reference crystal is 1.3 and 1.4, respectively, both measured at the lowest possible threshold. It is interesting to note that the gain in CTR (not the absolute value of the CTR) for the patterned crystal increases towards higher thresholds, see also figure 6.5b, reaching ultimately a value of ∼1.6. For the side readout the CTR-gain starts at 1.1 at low thresholds and increases to ∼1.2 towards higher values. The benefit from running at higher thresholds, even at the expense of lower CTR values, becomes relevant when, at the system level, extremely low thresholds cannot be used.

In table 6.2 some threshold values were selected to demonstrate the gain in CTR of the patterned crystal over the reference crystal. The last column also shows what one would expect in CTR gain on photostatistical grounds from the previous light output measurements. As the result shows, the expected gain of 1.22 corresponds to that measured at the lowest possible thresholds, proving that the CTR can be measured close to the single photon level.

Table 6.2: List of CTR measurements and their gain compared to expected values derived from light output (LO) measurements. CTR values for the measurements with NINO (NI) readout are taken from the fits in figure 6.5a. The CTR is measured with a 3% accuracy, leading to an accuracy of 4% for the measured gain in CTR.

| Crystal readout face | Best Measured CTR (ps) | Gain in CTR @ best CTR | @ 40 mV | @ 400 mV | exp. from LO with PMT |
|---|---|---|---|---|---|
| Reference | 553 ± 17 | - | - | - | - |
| Side | 484 ± 15 | 1.1 | 1.1 | 1.2 | |
| Photonic | 426 ± 13 | 1.2 | 1.3 | 1.6 | 1.2 |
| Opposite | 406 ± 12 | 1.2 | 1.4 | 1.6 | 1.2 |

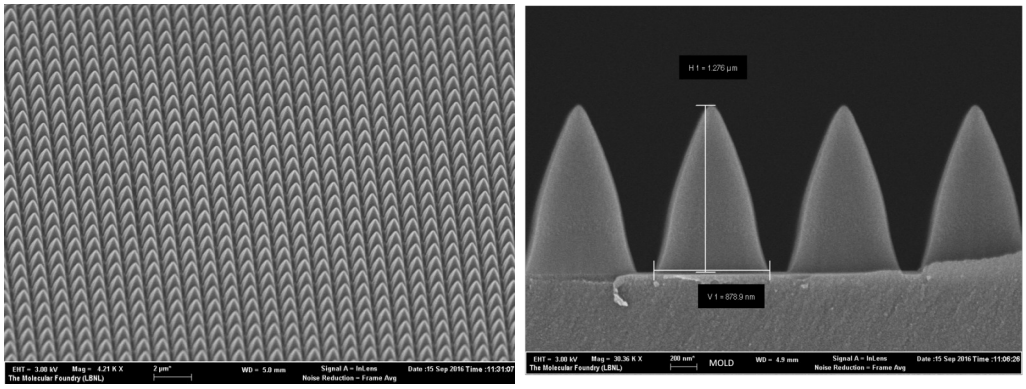

(a) (b)

Figure 6.6: SEM images of the silicon master stamp produced with interference lithography. This stamp is used to make UV-transparent replicas that in turn are used to imprint the UV-curable high refractive index polymer layer [6].

## 6.2 Cubes patterned with UV-cured nano-imprint lithography

This section presents a second photonic patterning process, called UV-cured nano-imprint lithography that was already explained in detail in section 4.4.3. As in the previous project, the goal was to develop a low-cost and scalable nano-imprint process to produce photonic crystal slabs on inorganic scintillators with the same goal, i.e. to enhance light output and coincidence time resolution.

### 6.2.1 Sample description

The crystal samples that were imprinted are two 10x10x10 $mm^3$ LYSO cubes, denoted here as sample 1 and sample 2. Unlike the measurement procedures described in section 6.1 both sample cubes, 1 and 2, served as their own reference *before* they were patterned. That made a third (reference) cube obsolete.

The mask used for the imprinting process contained a pattern that was designed approximately 6 years ago by A. Knapitsch [11] for imprinting a 10x10x10 $mm^3$ $SrI_2$:Eu cube, also to improve its light output. Since this crystal has about the same refractive index as LYSO (1.82 [12]) and a very similar peak emission, at 435 and 420 nm [12], this pattern was also deemed promising for LYSO crystals.
Figure 6.6 shows SEM images of the master stamp used for the samples in this project. As one can see, the pattern consists of highly regular cones, with a base diameter of 880 nm and a height of 1275 nm in a square lattice with a periodicity equal to the base diameter of the cones, i.e. the cones' bases touch each other. This mask is then used to imprint a layer of a high-refractive polymer, with an refractive index of 1.82.

### 6.2.2 Simulations

Simulations were made by [10], using as before the pattern parameters extracted from the SEM images. As such, unlike the *pillar*-shaped structure from the previous section, in this case the simulated configuration consisted of *cones* with a base diameter of 880 nm and a height of 1275 nm, in a square lattice with a 880 nm pitch. Also the refractive index is

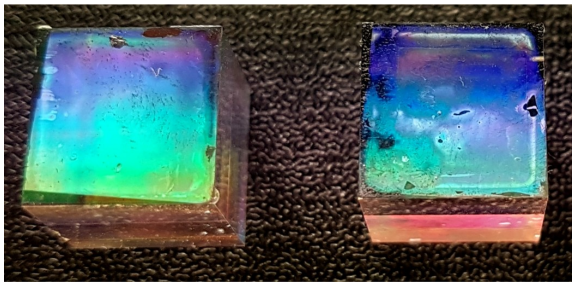

Figure 6.7: Pictures of the surfaces of sample 1 (left) and sample 2 (right) after imprinting with UV-nil [6].

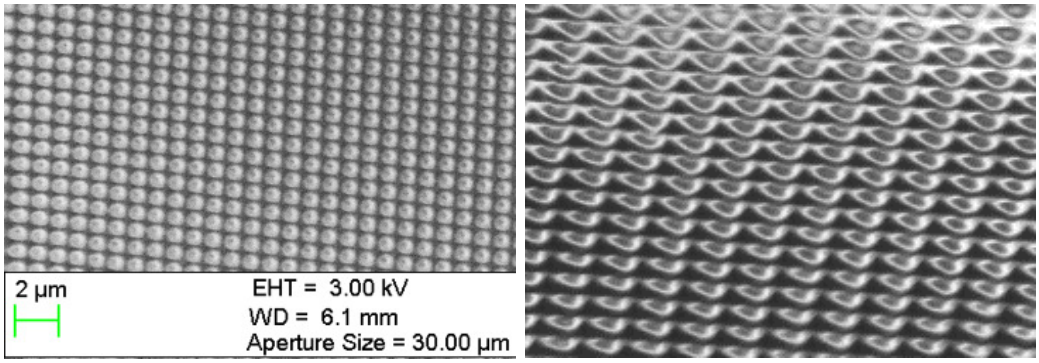


(a) (b)

Figure 6.8: SEM images of sample 1 after imprinting with UV-NIL, (a) from the top and (b) from a tilted perspective, upside-down.

only 1.82 (compared to 2.4 of the $TiO_2$ structure in the previous section).
The simulations show a light gain of 1.7 for a LYSO cube treated with this nanopattern.

### 6.2.3 Quality of the produced pattern

Figure 6.7 shows a photo of the imprinted crystal surfaces of the two samples. The iridescent coloring visible on the crystal surface is typical for the presence of a photonic layer on the crystal. One can see that the crystal edges are not 100% regular, an effect probably caused by a slight misalignment of the stamp, seen particularly on sample 1. Sample 2 on the other hand shows small defects inside the pattern, more pronounced near the crystal edges.
Figures 6.8 and 6.9 show SEM pictures of sample 1 and sample 2, respectively. Contrary to the photographic images, the microscopic scans show a strikingly clean, regular pattern in a square lattice with the expected long-range periodicity of ∼1280 nm. The SEM pictures are slightly blurred due to the known charging effects, making the structures in figure 6.8b difficult to visualize. The other side-view of sample 2 in figure 6.9b) shows the structures as an array of cones with rounded tops.

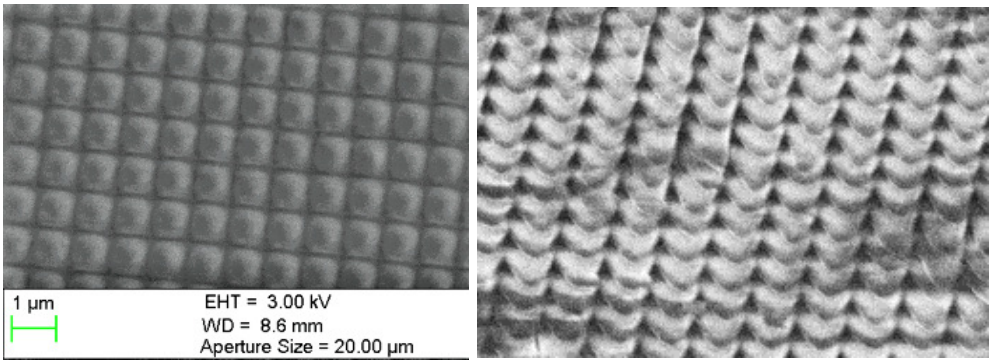


(a) (b)

Figure 6.9: SEM images of sample 1 after imprinting with UV-NIL, (a) from the top and (b) from a tilted perspective, upside-down.

Table 6.3: Results from light output (LO) measurements. The table shows pre- and post-patterning values, as well as the gain in light output. The LO is measured with an accuracy of $\sim 5\%$, leading to an accuracy of $\sim 7\%$ for the gain. The energy resolution is measured with an error of $\sim 10\%$.

| | **Pre-pattern** (reference) | | **Post-pattern** | | | |
|---|---|---|---|---|---|---|
| | LO (kph/MeV) | $E_{res}$ (%) | LO (kph/MeV) | $E_{res}$ (%) | gain LO | gain $E_{res}$ |
| sample 1 | 6.0 | 18 | 9.8 | 13 | 1.6 | 1.4 |
| sample 2 | 5.8 | 18 | 9.8 | 13 | 1.7 | 1.5 |

### 6.2.4 Characterization

#### 6.2.4.1 Light output

The light output measurements [6][10] followed the same protocol as in the previous section, however, this time a Hamamatsu R10755 PMT was used, again only with air-coupling to the photodetector. These results are summarized in table 6.3. Hence, as the table shows, there is a net light gain by a factor of 1.6 and 1.7 for sample 1 and sample 2, respectively. These values are in near-perfect agreement with the simulated gain of 1.67 for these crystals. The measured gain in energy resolution for the two samples, was found to be 1.4 and 1.5, respectively. It is interesting to observe that, similar to the previous observations, the measured improvement in energy resolution deviates from the predicted one as expected from photostatistics alone, i.e. $\approx 1.3$ for both.

#### 6.2.4.2 Coincidence time resolution

The coincidence time resolution measurements were made with the same CTR setup using as photodetector the Hamamatsu S13360-6050 SiPM and as readout the NINO chip, where again only the center of the 10x10x10 $mm^3$ was covered by the SiPM surface. Due to lack of time, the measurement series was reduced such that only sample 1 was investigated for both the patterned-face- and opposite-face readout with no side-readout measurement foreseen. The results are shown in figure 6.10, clearly demonstrating the improvement in CTR from nano-imprinting on both samples. Also the opposite face readout shows a

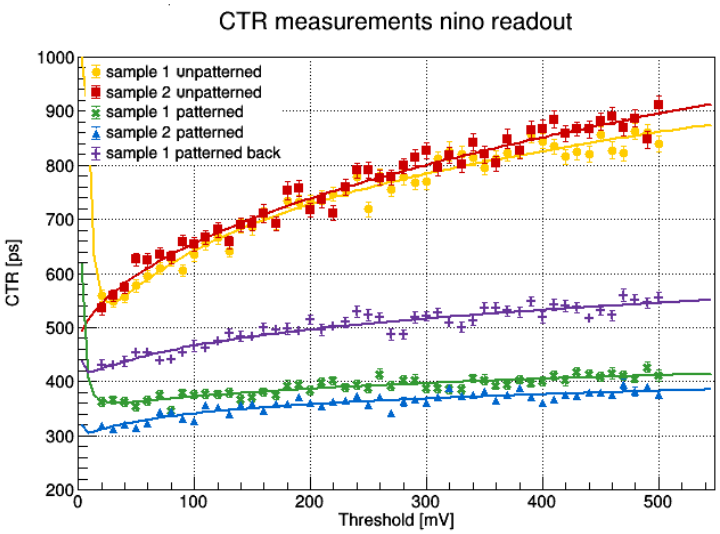


(a)

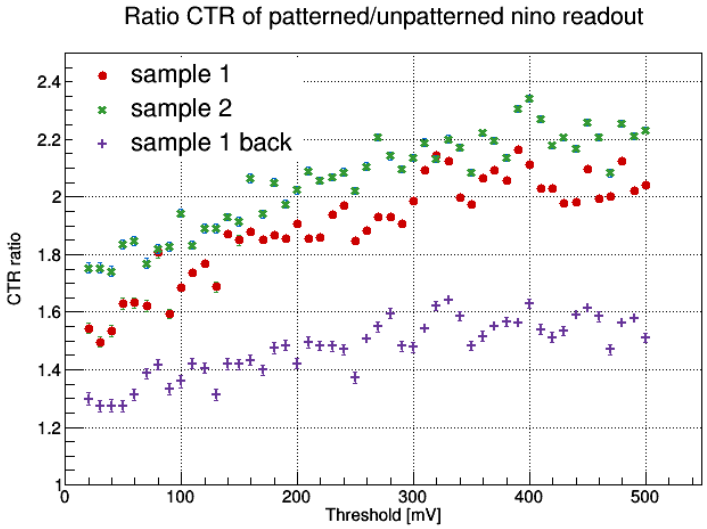


(b)

Figure 6.10: Coincidence time resolution measurements in FWHM of sample 1 and sample 2, before and after nano-imprinting, without wrapping and without optical coupling grease. Sample 1 has been measured with the photonic crystal pattern towards the SiPM and with the opposite surface towards the SiPM ("sample 1 patterned back") (a) absolute coincidence time resolution values, (b) ratio between coincidence time resolution before and after imprinting.

Table 6.4: List of CTR measurements and their gain compared to expected values derived from light output (LO) estimates from the amplitude of the analogue SiPM signal. All measurements were made with the NINO readout. The CTR is is measured with a 3% accuracy, leading to an accuracy of 4% for the measured gain in CTR.

| | **gain CTR** | | | **gain** | **exp. gain** |
|---|---|---|---|---|---|
| | @best | @40 mV | @400 mV | **LO (SiPM)** | **CTR** |
| Sample 1 | 1.5 | 1.6 | 2.1 | 2.4 | 1.5 |
| Sample 1 back | 1.3 | 1.3 | 1.6 | 1.8 | 1.3 |
| Sample 2 | 1.5 | 1.8 | 2.2 | 2.4 | 1.5 |

significant improvement in CTR, though somewhat smaller than for the patterned-face readout. This observation is in contrast to the same measurements made in section 6.1, where there was no difference in gain between the two configurations. Figure 6.10a shows that the CTR for this pattern is superior and less sensitive to threshold changes as compared to the nano-lithography imprint sample (see section 6.1). As a consequence of the fact that the CTR remains fairly flat over the chosen threshold range, the CTR gain between the patterned and unpatterned measurements becomes even more profound, i.e. 2.1 and even 2.2 for samples 1 and 2, respectively (figure 6.10b). The measurements are summarized in table 6.4. Interesting is that the gain in CTR, even at low thresholds, is larger than what one would expect from the measured increase in light output on grounds of photostatistics, i.e. for both samples $\approx 1.3$. This mismatch could be explained by the two different circumstances by which the crystal is read out, (a) for the light output measurements where the *entire* surface of the cube is read out by the PMT, and (b) by the only partial readout of the cube by the SiPM. Under the assumption that the PMT light output measurements underestimate the effective light gain, a similar light output measurement was made with the SiPM itself. This (analog) light output measurement is automatically made during the CTR measurements when selecting events from the photopeak. The imminent advantage of this method is that CTR and light output are measured under identical conditions. It turns out that, indeed, owing to this method, the gain in light output provided by the SiPM is significantly higher than that seen before with the PMT (see table 6.4). With these values, i.e. 2.4 for both samples, the expected CTR gain matches the measured one at lowest possible threshold. This corroborates our expectation that the CTR gain after nano-imprint is explained by photostatistics.

## 6.3 Summary

The previous sections introduced two photonic patterning methods, both based on nano-imprint lithography, where in the first case a multi-step process had been applied to produce *pillars* with a refractive index of 2.4 in a square lattice. The other process has the advantage of being simpler in the sense that the pattern is generated one step from a polymer layer subsequently UV-cured on the bare crystal. Unlike the first method, this resulted in *cones* of RI=1.82 arranged in a square lattice. Note, that the two technologies are described in full detail in section 4.4. To test the viability of these lithography methods and the resulting photonic structures, three prototypes of 10x10x10 $mm^3$ LYSO cubes with their photonic layers were used and tested for light output and coincidence time resolution with the aim to see if there was beneficial effect from the photonic layer. This meant that whatever gain was to be expected, it was always compared to a so-called

Table 6.5: Summary of LO and CTR measurements of 10x10x10 $mm^3$ LYSO prototypes nano-imprinted via NIL and UV-NIL.

| | sim. LO gain | LO gain | $E_{res}$ gain | CTR (ps) unpatterned | CTR (ps) patterned | CTR gain |
|---|---|---|---|---|---|---|
| NIL | 1.5 | 1.5 | 1.1 | 553 | 426 | 1.2 |
| UV-NIL sample 1 | 1.7 | 1.6 | 1.4 | 546 | 361 | 1.5 |
| UV-NIL sample 2 | 1.7 | 1.7 | 1.5 | 540 | 306 | 1.5 |

reference measurements, where no photonic layer was present.
Both photonic patterns show a net improvement in both light output and coincidence time resolution, with an even more substantial gain achieved with the UV-cured conical structure made with the second lithography method. These results apply to the configuration where the crystal is read out by the photodetector from the patterned side. The results are summarized in table 6.5.

An interesting fact is that in all cases an improvement in CTR was observed also when the crystals were read out from the opposite face of the patterned crystal. In this case however, the improvement is less pronounced when the second lithography method (UV-cured) was applied. This could be an indication that at least part of the light impinging on the photonic slab, that was originally outside the extraction cone, was back-reflected inside the extraction cone and therefore increased also the light output on the other side of the crystal. The fact that the UV-cured photonic pattern showed a weaker effect on the back side of the crystal, could be attributed to its higher light extraction efficiency of the patterned side.
It is also interesting to note that even a (unconventional) readout from the side face of the crystal yields an effective gain in CTR over a bare crystal, though smaller than the ones reported above.
Despite the encouraging results achieved with the two investigated nano-imprint lithography methods, more work needs to be invested to improve the quality, i.e. the homogeneity, of the photonic slabs, in particular near the crystal edges. This aspect becomes particularly important if scintillating pixels are imprinted rather than cubes.

## 6.4 Additional measurements

Further to the above-discussed measurements, some additional configurations have been evaluated.
To assess the performance of photonic crystal slabs on crystals also under commonly used wrapping- and optical coupling conditions, measurements on the UV-cured nano-imprint lithography samples have been made with scintillator cubes wrapped in Teflon, also both air- and grease-coupled to the photodetector. For further details see section 6.4.1.
Furthermore, a crystal geometry that resembles more closely, though at a larger scale, commonly used crystal pixels, of order 1-3 mm by 20 mm, was investigated with a 10x10x20 $mm^3$ parallelepiped. This is discussed in section 6.4.2.
Since photonic crystals, next to their capacity to extract *more* light from the scintillator, are also thought to be able to extract this light *faster* than from a bare crystal, a dedicated CTR run was made with the nano-imprint lithography cube introduced already in section 6.1, however applying a faster readout method, called the high frequency readout. For details of this readout, see section 3.4.2. The feature of this particular readout is that it is more sensitive to the detection of the photons right at the onset of the light cascade,

photons that would *not* have been detected by the NINO chip. These measurements are discussed in section 6.4.3.

### 6.4.1 Measurements with Teflon wrapping and glycerine coupling

The two cubes with their photonic pattern produced by UV-cure nano-imprint lithography (section 6.2) were dressed with Teflon and measured with air- and glycerine coupling. The idea was that standard methods of improving light output, like crystal wrapping and grease coupling, might further improve the results obtained above. As a coupling grease glycerine was chosen for the simple reason that it is water-soluble and therefore easily removable from the photonic surface without damaging the photonic slab after use. As in all cases before, LO and CTR were used as figures of merit in order to see improvements from measurements under these conditions, if any, with respect to the reference measurements. In this case, the expected effect of the photonic slab on the light extraction was simulated, for the case where Teflon wrapping *and* optical grease was used. This means that all the surrounding material of the nanopattern was assumed to be glycerine, i.e. with an refractive index 1.48 (instead of air, with RI=1.0 in the previous cases). The simulations showed a negligible expected improvement in light output, of a factor of 1.04.
Table 6.6 summarizes the measurements in terms of light output. As expected, the absolute light output in both configurations, pre-patterned and post-patterned, increases by 3 to 2 times for air-coupling, respectively. If, in addition, glycerine coupling is used, the light output increases by $\sim$3.6 for both configurations. This means that the classical methods applied to improve light output increase light transfer efficiency as expected. In comparison with that, the photonic crystal, despite its higher light extraction potential however, does not exceed the transfer efficiencies as achieved with the classical methods. Therefore, the net, i.e. "photonic" over "classical", gain is only between 1.0-1.1.

As to coincidence time resolution, figure 6.11 shows the results of the measurements with samples 1 and 2 when wrapped in Teflon and air-coupled, whereas figure 6.12 gives results when glycerine is used. Similar to the observations for the light output, also the absolute values of the pre- and post-patterned CTR are superior to those obtained in section 6.2. On the other hand, the differences in gain are not washed out to the same extent as those for light output, i.e. they are 20 and 30% for the two samples, respectively, as long as air coupling is used. If, instead of air coupling, glycerine is applied as agent, there is no measurable difference anymore between the pre- and post-patterned CTR. As was discussed in section 6.2.4.2 and from the arguments given therein, the light output measurement was again switched from PMT to the SiPM in order to check with this configuration what one would expect in terms of CTR on grounds of photostatistics. This is shown in the last two columns of table 6.7.

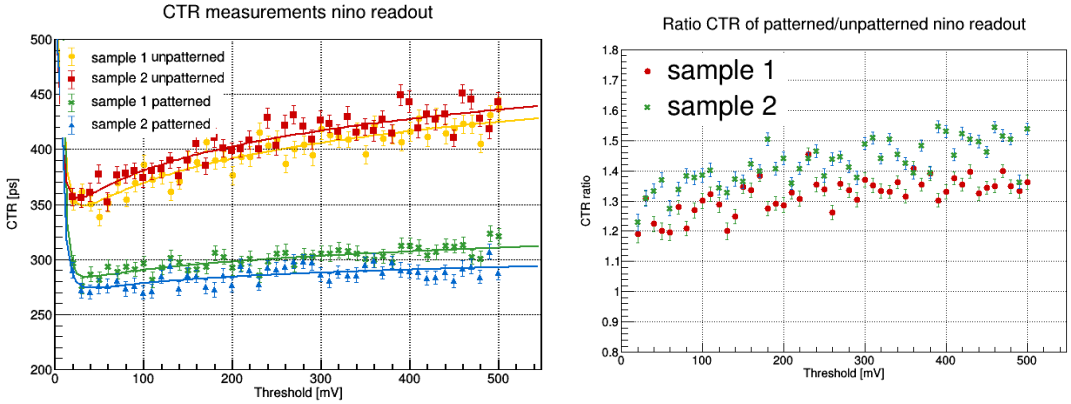


(a) (b)

Figure 6.11: Coincidence time resolution measurements in FWHM of sample 1 and sample 2, before and after nano-imprinting, with air coupling. (a) absolute coincidence time resolution values, (b) ratio between coincidence time resolution before and after imprinting.

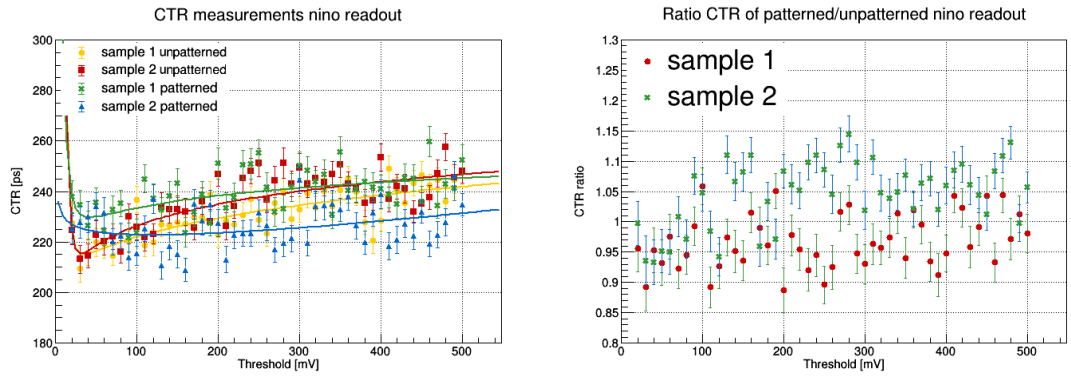


(a) (b)

Figure 6.12: Coincidence time resolution measurements of sample 1 and sample 2, before and after nano-imprinting, with Teflon wrapping and glycerine coupling. (a) absolute coincidence time resolution values, (b) ratio between coincidence time resolution before and after imprinting.

Table 6.6: Results from light output (LO) measurements with Teflon wrapping, with air- and grease coupling. The LO is measured with an accuracy of $\sim 5\%$, leading to an accuracy of $\sim 7\%$ for the gain. The energy resolution is measured with an error of $\sim 10\%$.

| | **Pre-pattern** | | **Post-pattern** | | | |
|---|---|---|---|---|---|---|
| | LO (kph/MeV) | $E_{res}$ (%) | LO (kph/MeV) | $E_{res}$ (%) | gain LO | gain $E_{res}$ |
| **sample 1** | | | | | | |
| Air coupling | 16.7 | 7 | 18.8 | 7 | 1.1 | 1.0 |
| Glycerine coupling | 21.0 | 6 | 21.7 | 6 | 1.0 | 1.0 |
| **sample 2** | | | | | | |
| Air coupling | 16.9 | 8 | 17.0 | 8 | 1.0 | 0.9 |
| Glycerine coupling | 21.0 | 6 | 20.4 | 6 | 1.0 | 1.0 |

Table 6.7: CTR gain measurements compared to expected values derived from light output (LO) estimates from the amplitude of the analogue SiPM signal. The CTR is is measured with a 3% accuracy, leading to an accuracy of 4% for the measured gain in CTR.

| | **gain CTR** | | | **gain** | **exp. gain** |
|---|---|---|---|---|---|
| Teflon wrapped | @best | @40 mV | @400 mV | **LO (SiPM)** | **CTR** |
| **air coupling** | | | | | |
| Sample 1 | 1.2 | 1.2 | 1.4 | 1.5 | 1.2 |
| Sample 2 | 1.3 | 1.3 | 1.5 | 1.4 | 1.2 |
| **glycerine coupling** | | | | | |
| Sample 1 | 1.0 | 1.0 | 1.0 | 1.0 | 1.0 |
| Sample 2 | 0.9 | 0.9 | 1.1 | 1.0 | 1.0 |

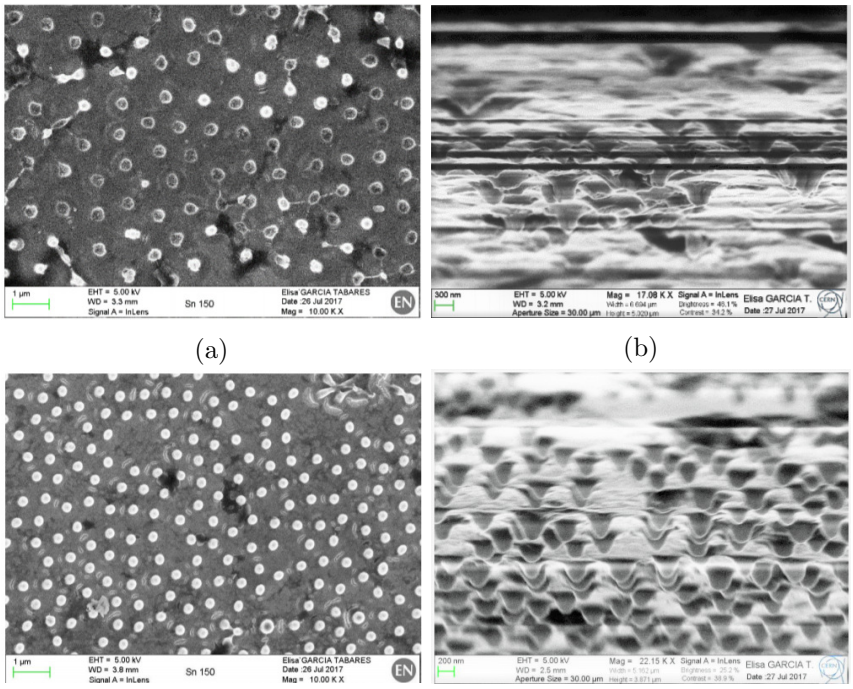


Figure 6.13: SEM images of two 10x10x20 $nm^3$ LYSO parallelepipeds after imprinting with sol-gel lithography. (a),(b) Sample P3, charging effects results into a bad image quality for the tilted image (b). (c),(d) Sample P5.

### 6.4.2 Evaluating parallelepipeds

This section reports on tests performed on two 10x10x20 $mm^3$ LYSO parallelepipeds, called P3 and P5, imprinted by yet another lithography process, the sol-gel lithography method as explained in section 4.4.2. Both samples have patterns of cones in a hexagonal lattice, produced with a self-assembly stamp with short-range periodicity. The cones are made of $TiO_2$ having a refractive index of 2.2. P3 and P5 have also been imaged using SEM, with the images shown in figure 6.13. Sample P3 exhibits a periodicity of ∼900 nm, an average cone height of ∼300 nm and an average cone diameter of ∼400 nm at the base. Sample P5 has the same pattern parameters, except for the periodicity, being ∼700 nm.

A Hamamatsu R10755 PMT was used to measure the light output for these two crystals, with no crystal wrapping and no coupling agent to the PMT. The results of these measurements are shown in table 6.8. They show that both patterned crystals improve LO by a factor of 1.5, with a corresponding measured gain in $E_{res}$ by a factor of 1.3 and 1.4, respectively; this being slightly higher than expected from photostatistics alone ($\sqrt{1.5} = 1.2$).

The same crystals, P3 and P5, were then investigated for coincidence time resolution with three different runs, i.e. (1) before patterning, (2) after patterning and with the patterned side read out, and (3) also after patterning but with the opposite side read out. Figures 6.14a and 6.14b show that the post-patterned CTR improvement with this crystal geometry is only marginal in the regime of the best CTR values obtained. This gain, however, shows again the typical behavior of a rapidly increasing CTR with increasing threshold. At a threshold of, e.g. 40 mV, the difference between patterned and unpatterned is already ∼10-20% for both crystals, irrespective of which side they are read out from.

Table 6.8: Light output (LO) and energy resolution ($R_{res}$) measurements of two 10x10x20 $mm^3$ LYSO crystals, P3 and P5. Measurements are performed in three conditions: no wrapping and no grease, Teflon wrapping and no grease and Teflon wrapping and glycerine coupling.

| | **Pre-patterning** | | **Post-patterning** | | | |
|---|---|---|---|---|---|---|
| **No wrapping No grease** | LO (kph/MeV) | $E_{res}$ (%) | LO (kph/MeV) | $E_{res}$ (%) | Gain LO | Gain $E_{res}$ |
| P3 | 5.0 | 22 | 7.4 | 17 | 1.5 | 1.3 |
| P5 | 4.9 | 23 | 7.4 | 16 | 1.5 | 1.4 |

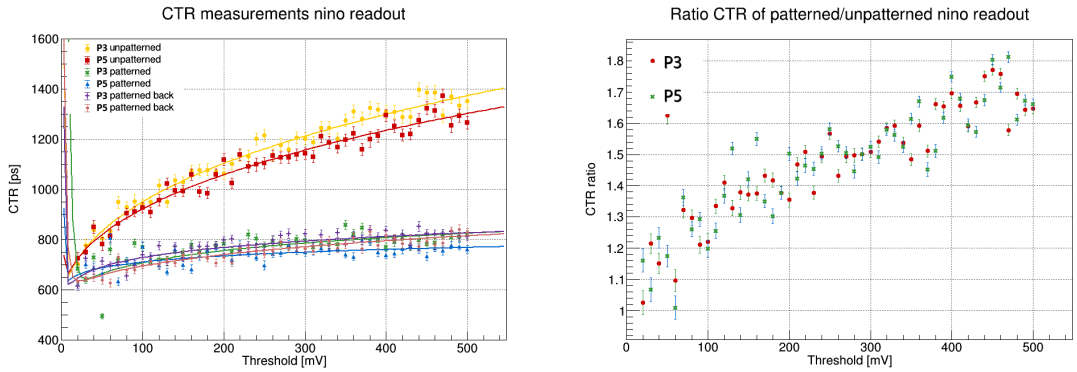


(a) (b)

Figure 6.14: Coincidence Time Resolution in FWHM obtained from two with sol-gel lithography nano-imprinted LYSO crystals, P3 and P5. The CTR is measured with a 3% accuracy. (a) Shows the CTR values against the applied threshold and (b) shows the ratio between the measurements of the patterned crystals and the pre-patterned measurements.

### 6.4.3 Measurements with high frequency readout

Part of the research done in this chapter was to see if the so-called high frequency (HF) readout [13], as explained in section 3.4.2, would yet show another improvement in CTR. As expected, the coincidence time resolution indeed proved superior with this readout than that with NINO as it samples the photon cascade closer to the noise than NINO. As table 6.10 shows, by looking at the *absolute* CTR values the improvements of HF over NINO are clearly visible, i.e. 10% for the reference crystal and ∼20% for the patterned one. By comparing the patterned CTRs measured with each readout type with their corresponding reference crystal's CTR, one can see that their relative *improvement* in CTR is the same for both readout methods.

Independent of the readout method used, it is an intriguing feature of the "patterned" CTR that its improvement over the reference CTR is not constant as a function of threshold, but that it rather shows a deterioration towards lower thresholds. This behavior is shown in figure 6.15 for three different configurations. This can be explained by the

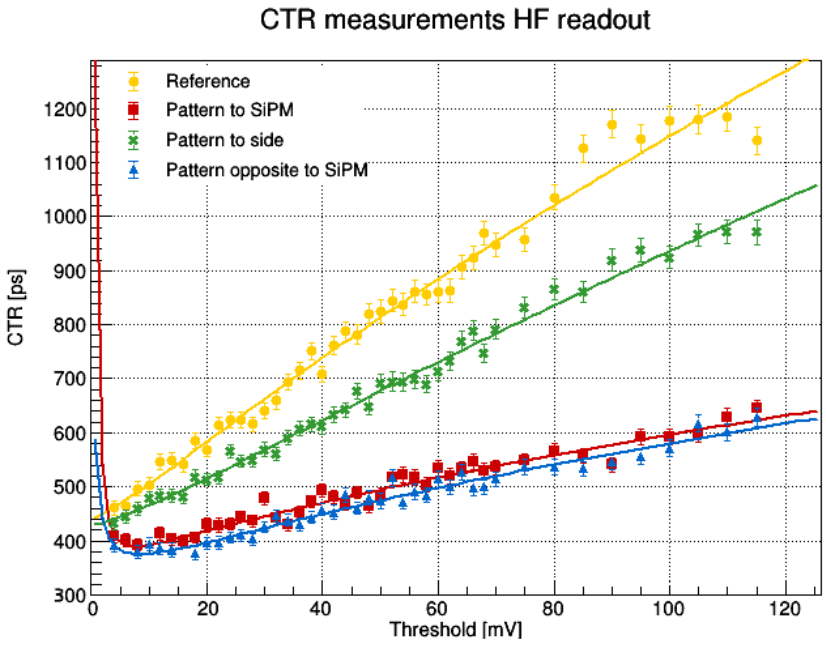


(a)

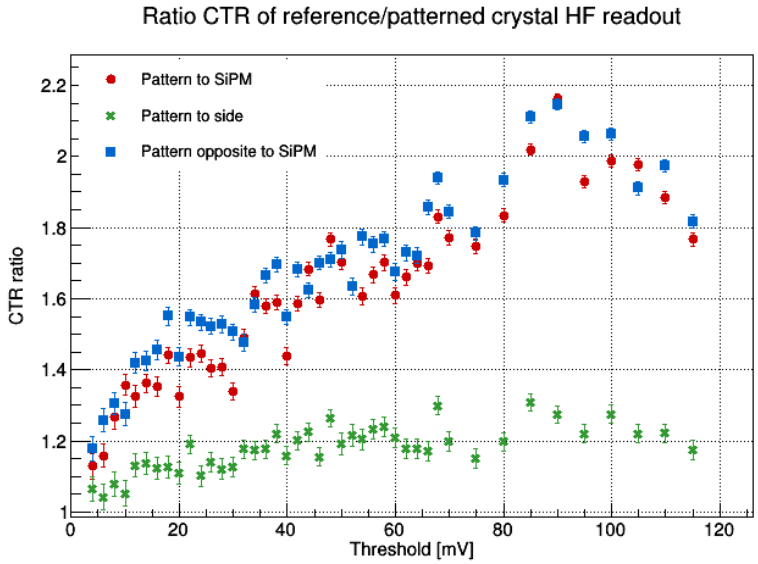


(b)

Figure 6.15: CTR from a nano-imprinted LYSO cube and reference crystal: three crystal orientations w.r.t. the SiPM window were used: patterned-face-to-SiPM (red squares), opposite-face-to-SiPM (blue triangles) and side-face-to-SiPM (green crosses). Measured with the HF-readout it a 3% accuracy. For all three configurations, the first data point at a threshold of 2 mV is in the electronic noise floor of the readout and thus leads to very high CTR values (not shown in the plot). (a) Shows the CTR values against the applied threshold and (b) shows the ratio between the measurements of the patterned cube and the reference. Measurements have been performed using the HF-readout.

Table 6.9: CTR and LO measurements. The CTR is measured with HF-readout with a 3% accuracy, leading to an accuracy of 4% for the measured gain in CTR. The expected gain in CTR also has an accuracy of about 4%.

| Crystal readout face | Best Measured CTR (ps) | Gain in CTR @ best CTR | @ 10 mV | @ 100 mV | exp. from LO with PMT |
|---|---|---|---|---|---|
| Reference | 450±14 | - | - | - | - |
| Side | 435±13 | 1.0 | 1.1 | 1.2 | |
| Photonic | 390±12 | 1.2 | 1.3 | 1.9 | 1.22 |
| Opposite | 375±11 | 1.2 | 1.3 | 2.0 | 1.22 |

Table 6.10: Comparison of CTR measurements with NINO readout and HF readout

| Crystal readout face | NINO readout CTR (ps) | NINO readout CTR gain | HF readout CTR (ps) | HF readout CTR gain |
|---|---|---|---|---|
| Reference | 553±17 | - | 450±14 | - |
| Side | 484±15 | 1.1 | 435±13 | 1.1 |
| Photonic | 426±13 | 1.2 | 390±12 | 1.2 |
| Opposite | 406±12 | 1.2 | 375±11 | 1.2 |

change of abundance of the light transfer modes between a patterned and a non-patterned crystal. In the case of a bare crystal, transfer modes are concentrated between incident angles of 0° and the critical angle of the crystal, as shown in figure 6.3a, whereas a patterned crystal accepts transfer modes over the entire incident angular range, though with lower small-angle abundance than in the non-patterned crystal, but significant abundance above the critical angle. Modes coming in at smaller angles correspond to short photon path lengths in the crystal, whereas modes at larger angles are due to photons with a longer path length. As such, a mix of these modes introduces an additional photon transfer time spread. To further substantiate this argument, S. Gundacker [14] introduced in his simulations [15] an additional photon transfer time spread due to the presence of the photonic layer. With this addition to the simulation it was found that the model more closely matches the results of the measurements made in this work. The additional time smearing in the photonic crystal arises from the fact that about 50% of the direct photons are reflected back into the crystal whereas delayed photons that normally are not collected by the photodetector can now, under the influence of the nano-pattern, reach the SiPM. In other words, photons exiting the crystal at larger angles imply a longer travel path in the crystal and therefore a larger delay time. Additional photons extracted at larger angles by the photonic layer thus come at a later time and do contribute to the signal formation now at higher thresholds and therefore improve the CTR at those thresholds. In other words, the investigated photonic pillar-like pattern transfers some of the early arriving photons to later times, nevertheless, increasing the total amount of photons extracted. Hence, also at earlier times the photon density is higher than in the non-patterned crystal and therefore improves the photostatistics leading to an overall improved CTR. In this sense the photonic pattern changes the weight of the diffraction modes. Depending on the application and the scintillator geometry this behavior varies, and it is even thinkable to use this feature of the photonic crystals to optimize the time structure of detected photons in special cases.

# Bibliography


[1] R. H. Pots, M. Salomoni, S. Gundacker, S. Zanettini, V. Gâté, E. Usureau, D. Turover, P. Lecoq, and E. Auffray, "Improving light output and coincidence time resolution of scintillating crystals using nanoimprinted photonic crystal slabs," *Nuclear Instruments and Methods in Physics Research Section A: Accelerators, Spectrometers, Detectors and Associated Equipment*, vol. 940, pp. 254 – 261, 2019.

[2] R. Pots and M. Salomoni, "Enhancing performance of scintillating crystals using nano-patterns." Poster presented at the SCINT School, 14-17 September 2017, Chamonix.

[3] M. Salomoni, R. Pots, P. Lecoq, E. Auffray, M. Paganoni, S. Gundacker, M. Pizzichemi, M. S. J. Marshall, S. Waterman, V. Nagarkar, and B. Singh, "Photonic crystals slabs applied to inorganic scintillators." Oral presentation at SCINT, 18-22 September 2017, Chamonix.

[4] R. Pots, M. Salomoni, P. Lecoq, E. Auffray, S. Gundacker, B. Singh, M. S. J. Marshall, S. Waterman, and V. Nagarkar, "Photonic crystals slabs applied to inorganic scintillators." Oral presentation at the CCC general meeting, 16 November 2017, CERN.

[5] R. Pots, "Improving light collection of scintillating crystals using photonic crystals." Oral presentation at bi-annual Gentner Day, 25 October 2017, CERN.

[6] M. Salomoni, R. Pots, P. Lecoq, E. Auffray, S. Gundacker, M. Paganoni, B. Singh, M. Marshall, and V. V. Nagarkar, "Photonic crystal slabs applied to inorganic scintillators," *IEEE Transactions on Nuclear Science*, vol. 65, pp. 2191–2195, Aug 2018.

[7] R. Pots and M. Salomoni, "Using photonic crystal slabs to improve light extraction from inorganic scintillators." Poster presented at the CERN Doctoral Student Assembly, 19 April 2018, CERN.

[8] R. Pots, M. Salomoni, S. Gundacker, P. Lecoq, and E. Auffray, "Photonic crystals slabs applied to inorganic scintillators." Oral presentation at LumDeTr, 9-14 September 2018, Prague.

[9] "Silsef homepage." `https://www.silsef.com/`. Accessed: 2018-12-01.

[10] M. Salomoni, *Boosting scintillation based detection*. PhD thesis, Università degli studi di Milano Bicocca, 2019.

[11] A. Knaptisch, *Photonic Crystals: Enhancing the Light Output of Scintillation Based Detectors*. PhD thesis, Technischen Universit¨at Wien, 2012.

[12] B. Singh, M. S. J. Marshall, S. Waterman, C. Pina-Hernandez, A. Koshelev, K. Munechika, A. Knapitsch, M. Salomoni, R. Pots, P. Lecoq, and V. V. Nagarkar, "Enhanced scintillation light extraction using nanoimprinted photonic crystals," *IEEE Transactions on Nuclear Science*, vol. 65, pp. 1059–1065, April 2018.

[13] S. Gundacker, R. M. Turtos, E. Auffray, M. Paganoni, and P. Lecoq, "High-frequency SiPM readout advances measured coincidence time resolution limits in TOF-PET," *Physics in Medicine & Biology*, vol. 64, p. 055012, feb 2019.

[14] "Private communication with s. gundacker from cern."

[15] S. Gundacker, F. Acerbi, E. Auffray, A. Ferri, A. Gola, M. Nemallapudi, G. Paternoster, C. Piemonte, and P. Lecoq, "State of the art timing in TOF-PET detectors with LuAG, GAGG and l(y)SO scintillators of various sizes coupled to FBK-SiPMs," *Journal of Instrumentation*, vol. 11, pp. P08008–P08008, aug 2016.

# Chapter 7

# Cross-luminescence in $BaF_2$: pushing the timing limits to new frontiers

**Remark**
The work that is presented in this chapter was reported on at three venues:

1. SCINT 2019 in Sendai, China, as a poster presentation [1];

2. IEEE NSS/MIC 2019 in Manchester, UK, as an oral presentation [2];

3. Crystal Clear Collaboration meeting 2019 at CERN, as an oral presentation [3].

The results were furthermore published at two scientific journals: (1.) Frontiers in Physics [4]; (2.) Physics in Medicine and Biology [5].

As discussed before, there are multiple approaches to improving timing performance in scintillating crystals. The last approach that will be examined in this thesis is choosing and investigation a scintillator that exhibits an intrinsically fast scintillation process.

There are many different scintillation processes of which some are relatively fast. One of the faster processes is a phenomenon called cross-luminescence, which usually has a decay time of the order of a nanosecond or less. This makes this scintillation process interesting for detectors requiring good timing performance. It is therefore no surprise that this phenomenon has been a center of interest since the early eighties of the last century [6][7][8][9][10].
The difficulty with cross-luminescence is that the emission is usually in the deep ultra-violet (UV). However, recent developments in photodetectors for experiments using liquid xenon as scintillator, led to the necessity of measuring light at the very short wavelength of 175 nm [11][12]. This recently made the exploitation of cross-luminescence feasible as well. In this Chapter, the timing properties of one of the brightest cross-luminescent scintillators known, $BaF_2$, has been investigated. At the end, an outline on the prospects of using $BaF_2$ in time-of-flight (TOF) detectors is given.

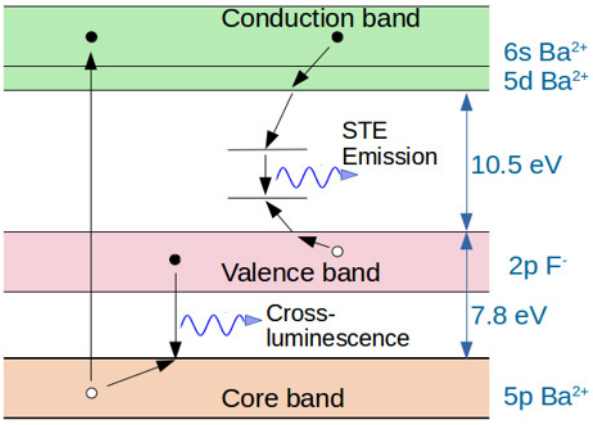


Figure 7.1: Schematic overview of the bandgap diagram of $BaF_2$ and corresponding emission mechanisms, based on [13].

## 7.1 Cross-Luminescence

Cross-luminescence is a scintillation process where an electron is excited from the core band to the conduction band. The resulting hole in the core band then recombines with an electron in the valence band. This process is illustrated in figure 7.1 [13]. Cross-luminescence is also referred to as core-valence luminescence [6][7], which is probably the most descriptive way for this type of luminescence, and Auger-free luminescence as well [14].

Cross-luminescence is only exhibited by crystals that have a sufficiently large bandgap between the valence band and the top of the core band, where the energy difference $E_{cv}$ is less than the energy difference $E_g$ between the conduction- and the valence band [6][7][13][14][15]. The latter forms the so-called forbidden bandgap that is usually involved in the scintillation process. So, one of the conditions for cross-luminescence in a crystal is that $E_{cv} < E_g$. If this is not the case, the emitted cross-luminescence light would be re-absorbed by the crystal, exciting electrons from the valence band to the conduction band, after which "normal" scintillation mechanisms between conduction- and valence band occur, either directly or via luminescence centers. Furthermore, in the case that $E_{cv} > E_g$, the non-radiative Auger recombination is allowed and would be competing with cross-luminescence. Since this Auger recombination is orders of magnitude faster, no remaining cross-luminescence would be observable.
As a consequence, possible candidates for cross-luminescence usually have a large forbidden bandgap, resulting in luminescence in the deep UV range. At the same time, the cross-luminescence process is very fast, with a typical decay time of the order of nanoseconds or less. This is due to the fact that, during cross-luminescence, holes in the core band recombine with electrons in the valence band, which is, unlike the conduction band, full of electrons. Electrons are readily available for the holes to recombine with, therefore increasing the recombination probability.

Since holes in the core band can recombine with electrons of any of the sub-bands of the valence band, the bandwidth of the emitted cross-luminescent light is determined by the bandwidth of the valence band. The different peaks in the cross-luminescence emis-

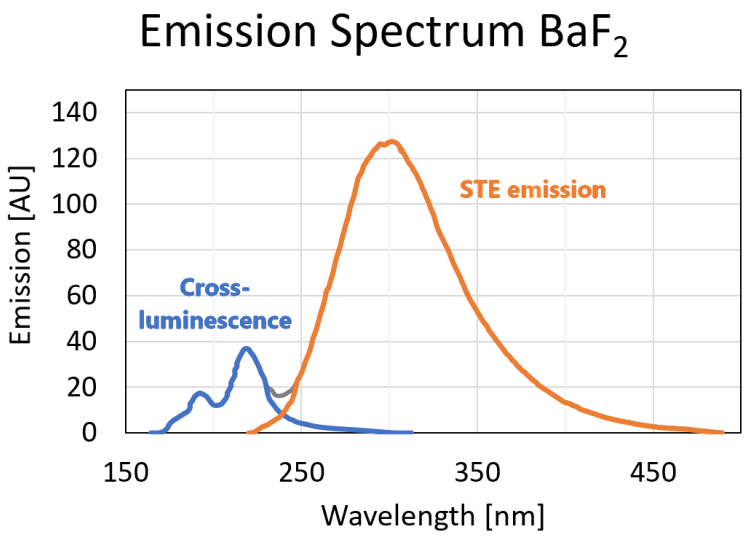


Figure 7.2: Emission spectrum of $BaF_2$, taken from [21]

sion spectrum follow the density of states inside the valence band [7]. Based on both the emission and excitation spectrum measured in photo-luminescence experiments, e.g. in the case of $BaF_2$, there is no emission peak above 7 eV [16]; it is assumed that the holes only recombine from the upper levels of the core band [6][9][17].
Scintillators exhibiting cross-luminescence also produce scintillation light from recombination of electrons and holes originating from the conduction band and valence band, respectively. These holes are generated in a twofold way, (1) directly by the ionizing particle in the valence band and (2) holes left behind by electrons from the valence band which had recombined with holes in the core band.

## 7.2 History of $BaF_2$ and motivation for investigating $BaF_2$ for time-of-flight detectors

Cross-luminescence was first seen in $BaF_2$. Already at the beginning of the '70s $BaF_2$ was known as a scintillator with an emission of 320 nm and a decay time of 630 ns [18]. This emission is self-trapped exciton emission between the conduction- and valence band. It would take approximately 10 years thereafter before another emission band, at 220 nm, was discovered [19]. Not long after, the decay-time of this emission had been determined to be only 0.6 ns [8], making $BaF_2$ the fastest inorganic scintillator at that time [13]. In the end, it was established that, on top of the normal scintillation with its emission peak at 320 nm caused by self-trapped exciton emission, $BaF_2$ has two more main emission peaks, namely at 220 nm and 195 nm, and a shoulder at around 175 nm [20], all attributed to cross-luminescence. The emission spectrum of $BaF_2$ is shown in figure 7.2.

$BaF_2$ is not the sole cross-luminescent material. To illustrate this, table 7.1 gives a non-exhaustive list of other cross-luminescent scintillators. However, $BaF_2$ belongs to one of the faster ones, and also with a reported light yield of 1400 ph/MeV (fast emission only) [21] to one of the brighter ones. Note for completeness, as to its slow emission the crystal exhibits a light yield of ∼10 kph/MeV. Furthermore, unlike e.g. CsF, $BaF_2$ is not

Table 7.1: Non-exhaustive list of cross-luminescent scintillators, taken from Rodnyi's book [6] table 3.3, except those marked by superscript. Values are only for the cross-luminescent emission. Given light yield values for $BaF_2$ are taken from Dorenbos et al. [21], the rest of the light yield values from van Eijk et al. [13].

| | Maxima of Emission Bands (eV) | Decay Time (ns) | Light Yield (ph/MeV) |
|---|---|---|---|
| $BaF_2$ | 5.6; 6.4 | 0.8 | 1400 |
| $BaLiF_3$ | 5.8; 6.7 | $\leq$1.0 | 1400 |
| $BaMgF_4$ | 5.6; 6.5 | - | 1000 |
| $BaYF_8$ | - | $\sim$3 | - |
| CsF | 3.2 | 2.9 | 2000 |
| CsCl | 4.4; 5.2 | 0.88 | 900 |
| $CsMgCl_3$ | 4.4; 5.1 | 2.1 | - |
| $CsCaCl_3$ | 4.0; 4.9 | 1.7 | 1400 |
| $CsSrCl_3$ | 4.1; 4.9 | 2.0 | - |
| CsBr | 5.0; 6.0 | 0.07 | 20 |
| $CsCaBr_3$ | 4.4; 5.4 | 0.8 | - |
| $CsSrBr_3$ | 4.4; $\sim$5.0 | 0.8 | - |
| RbCl [(1)] | 5.5-7.5 | - | 1 |
| RbF | 5.2 | 1.3 | 1700 |
| $RbMgF_3$ | 4.2 | 2.1 | - |
| $RbCaF_3$ | 4.3 | 2.82 | - |
| $KMgF_3$ | 7.2; 8.0 | 1.5 | 1400 |
| $KCaF_3$ | 7.3; 8.0 | $\leq$2 | 1400 |
| $KYF_4$ | 7.3 | 1.9 | 1000 |
| $K_2YF_5$ | 7.6 | 1.3 | 300 |
| $KLuF_4$ | 7.6; 6.7 | 1.3 | $\sim$200 |
| $KLu_2F_7$ | 7.5 | $\leq$2 | $\sim$200 |
| $K_2SiF_6$ [(2)] | 5.4; 7.3; 8.4 | - | - |
| $K_2LiGa_6$ [(2)] | 6.6; 7.5 | - | - |
| $K_2NaAlF_6$ [(2)] | 5.5; 6.5; 7.2; 8.0 | - | - |

[(1)] data from [13]
[(2)] estimates from data from [9]

Table 7.2: Overview of the general characteristics of $BaF_2$, LSO and BGO. Values are taken from the book *Inorganic Scintillators for Detector Systems* [26], unless otherwise indicated.

| | $BaF_2$ | LSO | BGO |
|---|---|---|---|
| Density $\rho$ (g/cm$^3$) | 4.88 | 7.4 | 7.13 |
| $Z_{eff}$ | 53 | 66 | 75.2 |
| photon absorption coefficient $\alpha$ @511 KeV (cm$^{-1}$) | 0.085 | 0.28 | 0.336 |
| radiation length $X_0$ (cm) | 2 | 1.1 | 1.12 |
| $LY_{intr}$ (ph/MeV) | $1400^{(a)}$ [21]<br>$9500^{(b)}$ [21] | 40000 | 10000 [27] |
| decay time $\tau$ (ns) | 0.6-0.8$^{(a)}$<br>$620^{(b)}$ | 40 | 300 |
| photon fraction @0.5MeV | 0.19 [28] | 0.34 [28] | 0.43 [28] |
| emission peak(s) $\lambda_{max}$ (nm) | $195^{(a)}$<br>$220^{(a)}$<br>$310^{(b)}$ | 420 [27] | 480 [27] |
| Refractive index (RI) @$\lambda_{mac}$ | 1.56 [29]<br>1.55 [29]<br>1.50 [29] | 1.82 [27] | 2.1 [27] |
| melting point (°C) | 1280 [30] | 2150 [31] | 1050 [31] |
| cost (\$/cm$^3$) | 15 [32] | 60 [32] | 35 [32] |

$^{(a)}$ cross-luminescence $^{(b)}$ STE emission

hygroscopic. Therefore, there has been an enormous interest in $BaF_2$ after its discovery, and numerous research groups started investigating the material [8][19][21][22][23][24][25], both to understand its characteristics and to use it in detectors requiring time-of-flight information. Table 7.2 gives an overview of the characteristics of $BaF_2$, as well of the commonly used scintillators LSO and BGO, for comparison.

At the time research on cross-luminescence was evolving, bismuth germanate (BGO) was the crystal that was predominantly used in medical PET scanners. BGO has an intrinsic light yield of about $10^4$ ph/MeV [27] and is very dense and also cheap to produce. However, its decay-time $\tau = 300$ ns makes it an unsuitable candidate for time-of-flight applications. Furthermore, at that time there were no other scintillating crystals fast enough to be suitable for time-of-flight PET.
The discovery of fast cross-luminescence in $BaF_2$ and also CsF finally opened the possibility for time-of-flight in PET. Following the discovery of these cross-luminescent materials several PET machines with $BaF_2$ [33][34][35][36] and also CsF [37][38] were developed. These were the first time-of-flight PET scanners with reasonable time resolutions between 450 ps and 750 ps FWHM. However, with the technical limitations imposed by relatively slow electronics, one could not make optimal use of the timing potential of the crystal. Furthermore, at that time monolithic crystals were coupled one-to-one to PMTs. However, also due to the fact that quartz windows were needed to pass the deep UV light into the PMTs, this apparatus became very expensive.
In addition, the density of $BaF_2$ and CsF is lower than that of BGO, an important aspect

that translates directly to the sensitivity of a PET scanner, this being one of the most important parameters in imaging. At the end, $BaF_2$, or any other cross-luminescent material for that matter, was not further developed for TOF-PET and has never been implemented in large scale PET scanners.

There has also been an effort to apply $BaF_2$ in high energy physics. At the Mainzer Mikrotron (MAMI) in Mainz the Two Arm Photon Spectrometer (TAPS) has been constructed, a calorimeter made of $BaF_2$ crystals read out by PMTs [39]. The detector has good timing performance with $\Delta t = 110\ ps$ for 43.5 MeV electrons and is excellent at measuring photons [40]. It has was installed at other accelerator facilities in Germany. Furthermore, research has been published on studies for the upgrade of TAPS at the Electron Stretcher and Accelerator (ELSA), to be able to continue using $BaF_2$ in detectors that need to deal with the high hit-rates without suffering from pile-up [41].
$BaF_2$ was also proposed as the crystal material for electromagnetic calorimetry at the proposed Superconductive Super Collider (SSC) [23], before the SSC project was cancelled by congress in 1993.

As a conclusion, it is safe to say that $BaF_2$ has already been successfully implemented in detectors for high energy physics. Nevertheless, earlier TOF-PET systems had only limited success, though $BaF_2$ is still a very promising material for time-of-flight applications in medical imaging. If used in conjunction with higher density materials, $BaF_2$, with the merits of its extraordinary timing performance, still is an excellent candidate for TOF-PET systems. This is discussed in more detail in section 7.6.2. Comparing the properties of $BaF_2$ with LYSO:Ce, this being the best performing scintillator (together with LSO) generally used in full PET systems, a rough estimate of its timing potential can be made using the following relation for the coincidence time resolution (CTR) as a function of decay time and light yield: $CTR \propto \sqrt{\frac{\tau_d}{LY}}$. Considering that LYSO:Ce has a light yield of 41 kph/MeV and a decay time of about $\tau = 39\ ns$ [27], and that $BaF_2$ has a reported light yield from fast emission of only 1.4 kph/MeV however associated with a decay time of 0.6-0.8 ns, this immediately translates to a CTR performance superior by a factor of 1.3-1.5 over that of LYSO:Ce. Taking the example of a $2 \times 2 \times 3\ mm^3$ pixel, the best measured CTR value for LYSO:Ce is 60±3 ps FWHM [27]. Based on the approximate assumption for the CTR given above, a $BaF_2$ pixel of the same size and used under the same conditions would even lead to a coincidence time resolution of 46-53 ps FWHM.
Already with available state-of-the-art high-speed and high-bandwidth electronics and using the most recent SiPMs with a $BaF_2$, we have measured in this work a coincidence time resolution of 51±4ps FWHM. This is discussed in more detail in section 7.5.5.
A last aspect of $BaF_2$ that has not been touched upon yet is its low production cost. Not withstanding its high attractiveness in photon applications, LSO is still relatively expensive, whereas $BaF_2$ is rather cheap to produce. Its production cost is even lower than that of BGO, still known as a popular and cheap scintillator. According to the Handbook of Particle Detection and Imaging [32], the prices/$cm^3$ of the most common scintillators compare as follows: LSO $\sim$ \$60, BGO$\sim$ \$35 and $BaF_2$ $\sim$ \$15. Note, the latter comes close to the price of cheap plastic scintillators with only $\sim$ \$11/$cm^3$. The low production cost of $BaF_2$ crystals is accounted to their low raw material cost and the relatively low temperature at which the they are grown.
All these characteristics make $BaF_2$ an excellent candidate for the pursuit of highest time resolution. This study aims at showing what potential lies ahead in $BaF_2$ judging from its current performance using state-of-the-art technology in electronics and photodetectors.

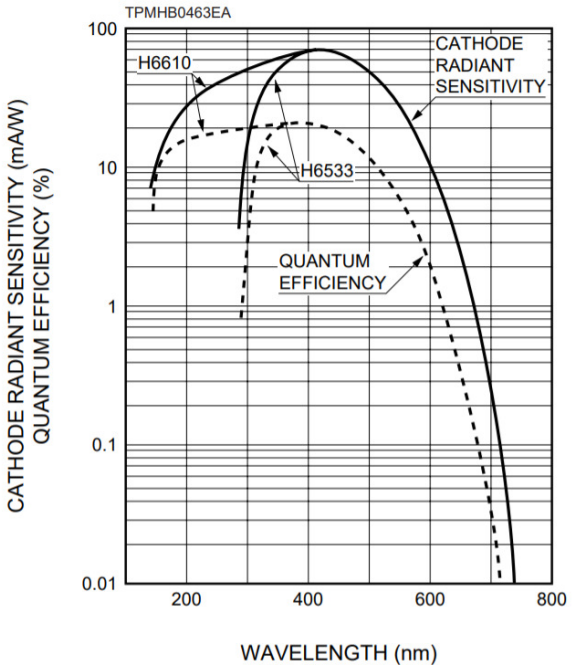


Figure 7.3: Quantum efficiency of the H6610 PMT from Hamamatsu, taken from its datasheet.

## 7.3 Material and methods used in this study

For the research performed in this chapter, $BaF_2$ samples from two different producers, Epic [42] and Proteus [43] were used. All samples are pure $BaF_2$ crystals without any doping.
Among the Epic crystals the following sizes were tested: $2 \times 2 \times 3\ mm^3$, $2 \times 2 \times 20\ mm^3$, $3 \times 3 \times 3\ mm^3$ and $3 \times 3 \times 20\ mm^3$. In the case of the Proteus crystals only $2 \times 2 \times 3\ mm^3$ and $2 \times 2 \times 20\ mm^3$ specimen were tested.

To characterize the crystals and eventually discover differences between the two producers, the following four different measurement series were followed up:

1. **Light transmission** measurements, with the setup described in section 3.1;
2. **Light output** measurements, with their specific setup described in section 3.2;
3. **Time correlated single photon counting** measurements, with the setup given in section 3.3, and finally
4. Measurements on **coincidence time resolution**, the setup of which is described in section 3.4.

In the light output setup, a Hamamatsu H6610 PMT (datasheet in appendix J) was used as photodetector. The quantum efficiency (QE) of this PMT, i.e. the probability of measuring an incoming photon as a function of wavelength, is shown in figure 7.3. Based on the reported emission curve of $BaF_2$ (see figure 7.2) and integrating the convolution of the quantum efficiency with the emission spectrum, the effective quantum efficiency

($QE_{eff}$) of this PMT was calculated to be 0.167 for the scintillation spectrum of $BaF_2$.

For the time-correlated single photon counting (TCSPC) measurements, a Hamamatsu hybrid PMT HPM-100-07 (datasheet in appendix K) was used. One should keep in mind that the QE of the hybrid PMT is only 7% at 220nm and dropping rapidly, as shown in figure 3.8 in section 3.3. Most probably, this leads to a significant underestimation of the abundance of the fast emission light, since it is emitted in a range where the QE is lower than in the regime of the slow emission light. Furthermore, it is not evident to compensate for the differences in QE at the different wavelengths.

For the measurement of the coincidence time resolution (CTR) two types of SiPMs from two different producers were used to extract the best possible performance. The chosen SiPMs are the HPK VUV S13370-3050CN from Hamamatsu [44] with $3 \times 3\ mm^2$ active surface and 50 $\mu$m SPAD pitch, and a VUV-HD device produced by the Fondazione Bruno Kessler (FKB), this SiPM with $4 \times 4\ mm^2$ active surface and 40 $\mu$m SPAD pitch. These SiPMs, unlike *common* commercial SiPMs, are specifically developed for light detection in the very deep UV [11] [12]. This feature is specifically discussed in the following section.

### 7.3.1 SiPMs for detection in the deep UV

Ordinary SiPMs on the market are in principle not compatible with light emitted in the deep UV. There are several reasons for this [45]. First of all, in order to protect the wire-bondings of the SiPM and the sensor itself, a protection layer is applied to the top surface of the SiPM, usually made of glass or epoxy resin. Both are principally not transparent to UV light. Underneath this protection layer there usually is an anti-reflective layer made of materials like $Si_3N_4$, which is not UV-transparent either.
Apart from absorption in materials outside the actual silicon sensor, UV-light only penetrates a few nanometers into the silicon layer. This is about 100 times shallower than for light above 400nm. This has the effect that the electron-hole pairs are effectively created at the surface of the SiPM. This is very disadvantageous for the quantum efficiency of the device and therefore leads to a low photon detection efficiency (PDE).
Relatively recently, there has been growing interest in developing SiPMs for liquid noble gas experiments, for instance for dark matter and neutrino experiments [45]. Typically, these detectors use liquid xenon that produces scintillation light at 175 nm or liquid argon emitting at 125 nm.
In this research, two types of SiPMs from the two different producers mentioned above were tested to asses the best possible coincidence time resolution. The specifications are given in section 7.3. One of the producers, Hamamatsu, claims a PDE of about 24 % for their VUV device [44]. An independent measurement, however, indicates a PDE of only 12-15% for the Hamamatsu device compared to a similarly measured PDE of 22-24% for the FBK device [12]. This difference in PDE would obviously have a significant effect on the CTR measured with these devices.
Furthermore, it is known that in FBK SiPMs the single photon time resolution (SPTR) is superior to that of the HPK devices [27]. This will also have an effect on the timing performance.
Measurements with these novel devices must be performed with caution. As explained before, they do not possess a conventional protection layer on top of their sensitive region, therefore making the surface of the SiPM more vulnerable to physical damage. Furthermore, the wire bonds are not protected either, as shown in figure 7.4 with the example of a HPK VUV S13370-3050CN SiPM. These bonds are prone to damage while handling

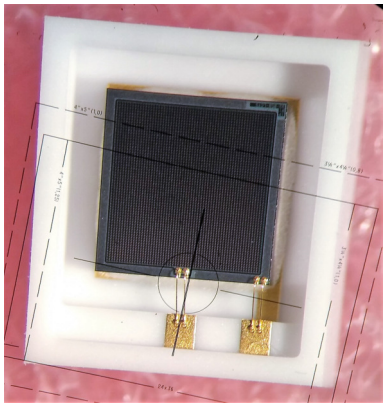

Figure 7.4: A magnified image of the HPK VUV S13370-3050CN SiPM. The structure of the SPADS in the 3x3mm$^2$ surface is visible, as well as the unprotected wire bonds

the crystals and/or during cleaning operations, and could easily render the SiPM non-operational.

## 7.4 Characterization of $BaF_2$

The first objective is to characterize the properties of $BaF_2$ and to determine its timing limits with state-of-the-art equipment.

### 7.4.1 Transmission

With the setup described in section 7.3, the transmission between 190 nm and 900 nm has been measured for the four different $BaF_2$ samples. Figure 7.5 shows the transmission of 3 mm long $BaF_2$ crystals from the different producers, and figure 7.6 that of the 20 mm long samples. Since there is no reliable data available on the refractive index of $BaF_2$ throughout its spectrum, the data is not corrected for Fresnel reflection that acts as a global absorption over the entire spectrum depending on the refractive index of the crystal at the given wavelength. This effect is further explained in annex E.
The measurements show that the crystals of both producers are very transparent down to 300 nm. Below 300 nm, the Proteus sample begins to gradually absorb light towards 190 nm. The absorption is more pronounced in the 20 mm long crystals with only 10% transmission left at 190 nm. On the other hand, the Epic crystal is transparent down to 270 nm from where on the transmission also decreases, however less steeply than in the Proteus sample. The Epic crystal still transmits more than 50% of its light at 190 nm. The difference in absorption between the samples is thus mainly in the domain of the cross-luminescent scintillation light.
Equation 7.1 shows the relation between the measured intensity $I$ after a certain length $z$, the initial intensity $I_0$ and the absorption coefficient $\alpha$.

$$I(z) = I_0 \cdot e^{-\alpha z} \tag{7.1}$$

The absorption length defined as $1/\alpha$ is given by equation 7.2. One should realize that the transmission $T(\lambda)$ in the equation is only the transmittance of the bulk material. The loss in transmission due to Fresnel reflection is not taken into account here.

$$Absorption\ Length(\lambda) = \frac{1}{\alpha(\lambda)} = -\frac{z}{ln[I/I_0]} = -\frac{z}{ln[T(nm)]} \tag{7.2}$$

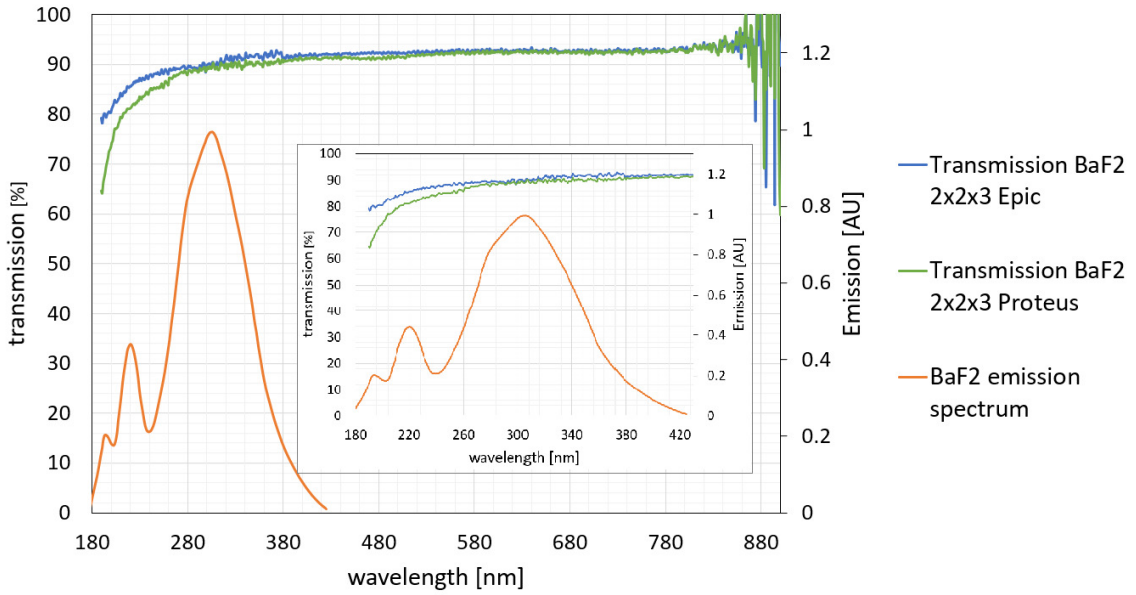


Figure 7.5: Transmission measurements of 3 mm $BaF_2$ pixels from Epic and Proteus, overlaying the emission spectrum of $BaF_2$. The inset shows a zoom over the range of emission of $BaF_2$.

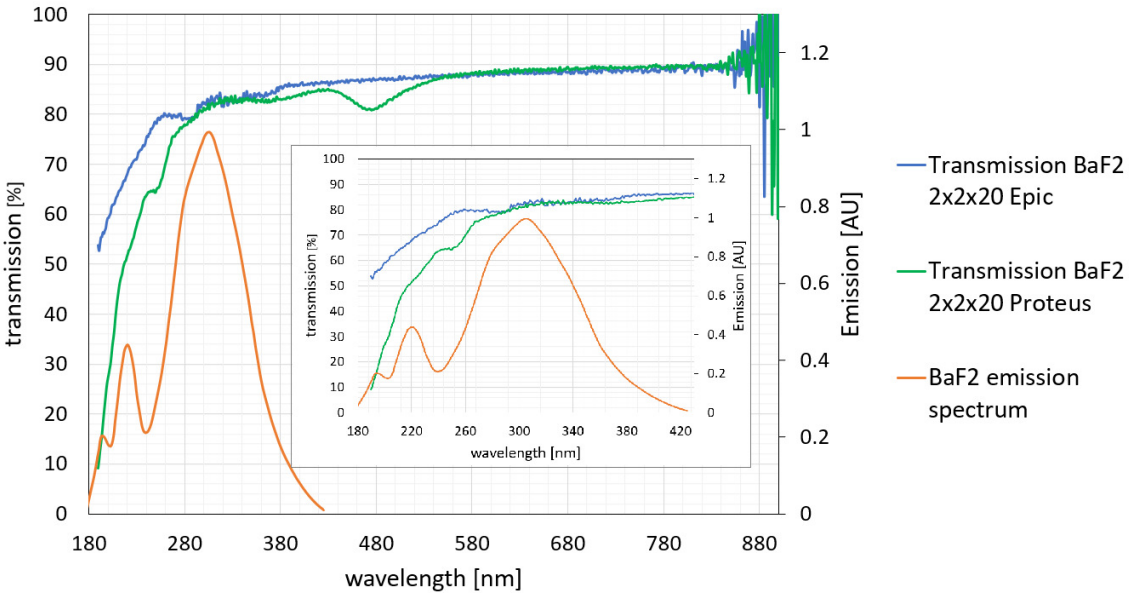


Figure 7.6: Transmission measurements of 20 mm $BaF_2$ pixels from Epic and Proteus, overlaying the emission spectrum of $BaF_2$. The inset shows a zoom over the range of emission of $BaF_2$.

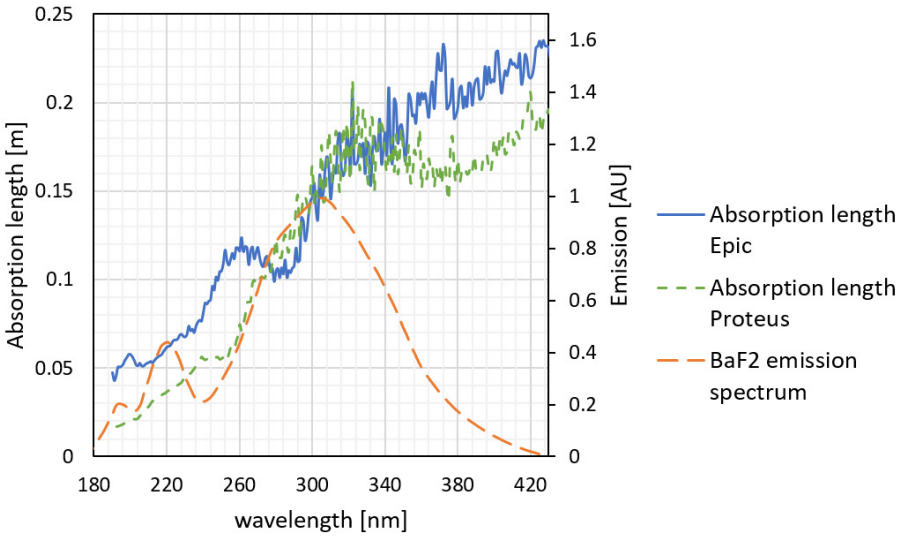


Figure 7.7: Absorption length of $BaF_2$, for pixels from Epic and Proteus and calculated from transmission measurements on 3 mm and 20 mm long crystals, overlaying the emission spectrum of $BaF_2$.

However, as shown in equation 7.3, the transmission obtained from measurements $T_{meas}(nm)$ does include the effect of Fresnel reflection $\mathcal{F}(\lambda)$. This expression is explained in more detail in appendix E, equation E.12.

$$T_{meas}(nm) = \frac{I_{meas}(z)}{I_0} = \cdot e^{-\alpha z} \cdot \mathcal{F}(\lambda) \tag{7.3}$$

With two transmission measurements of the same crystal material, but with different lengths, the effect of Fresnel reflection can be corrected for, as shown in equation 7.4. This leads to an expression for the absorption length in equation 7.5.

$$\frac{T_{meas,z_1}(nm)}{T_{meas,z_2}(nm)} = \frac{e^{-\alpha z_1} \cdot \mathcal{F}(\lambda)}{e^{-\alpha z_2} \cdot \mathcal{F}(\lambda)} = e^{-\alpha(z_1 - z_2)} \tag{7.4}$$

$$Absorption\ Length(nm) = -\frac{z_1 - z_2}{ln[T_{meas,z_1}/T_{meas,z_2}]} \tag{7.5}$$

In this study, the transmission measurements of both the 20 mm and 3 mm long $BaF_2$ crystals are used to determine the absorption lengths from equation 7.5. Figure 7.7 shows the obtained absorption length of the crystals from the two producers. There is a clear difference in absorption length between the two crystal producers, with Proteus having a shorter absorption length below approximately 270 nm than Epic.

From these measurements one can conclude that at least above 300 nm, the crystals from both producers are equally transparent and barely absorb. From that point onwards however, Proteus crystals are prone to absorption of more light than the ones from Epic. Since this absorption happens in the spectral range of their own emission, this will have an affect on the amount of detectable light and therefore on the light yield and CTR produced by the crystals. This effect is even more pronounced in the longer crystals as produced light follows a longer path to reach the readout surface and thus is being subject to more absorption along its way.

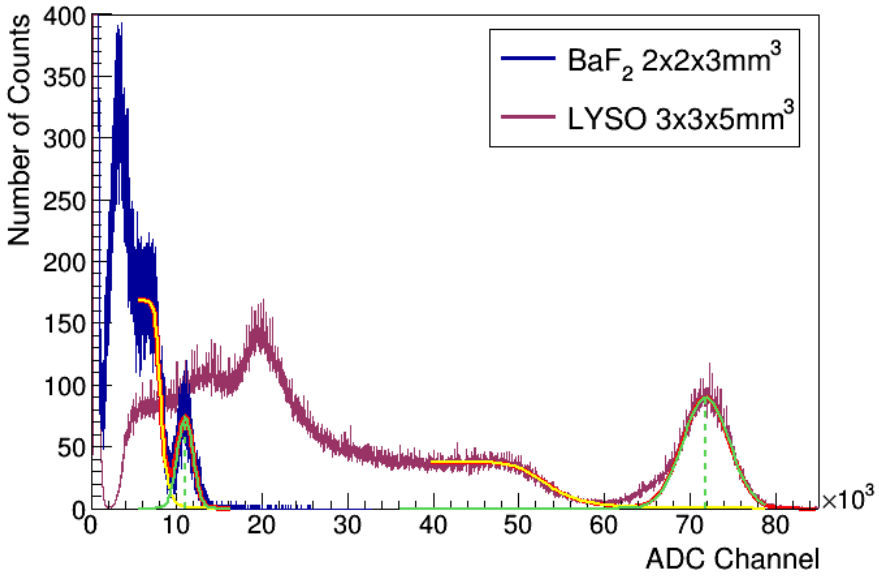


Figure 7.8: Light yield measurements of a $2 \times 2 \times 3$ $mm^3$ $BaF_2$ pixel of Proteus and a $3 \times 3 \times 5$ $mm^3$ LYSO pixel, air-coupled to the PMT. The red lines show the total fit, the green lines show only the contributions of the photopeak and the yellow lines the contributions of the compton edge.The fit does not take into account light produced due to the intrinsic radioactivity of LYSO.

### 7.4.2 Light output

As described in section 7.3, a setup with a special UV-sensitive PMT (Hamamatsu H6610) is used to measure the light output of $BaF_2$. This gives a spectrum with a compton shoulder and a photopeak, as shown in figure 7.8, where the position of the photopeak defines the light yield. Since the light yield is a priori given in terms of ADC channels, the amount of extracted light will then be calculated from the distance between the pedestal and the peak of the spectrum. A LYSO pixel was used as reference crystal for the measurements. Its light output ($LO_{ref}$) was measured both with the UV-sensitive and our standard (non-UV-sensitive) PMT with its known calibration curve converting ADC channel to extracted light. Then, taking into account the different effective quantum efficiencies of the PMTs, i.e. one for the sample under investigation ($QE_{sample}$) and one for the reference crystal ($QE_{ref}$), these values can be used to determine the effective light output ($LO$). This is shown in equation 7.6; $PPP_{sample}$ refers to the photopeak position of the sample and $PPP_{ref}$ to the photopeak position corresponding to the reference crystal:

$$LO = \frac{PPP_{sample}}{PPP_{ref}} * \frac{QE_{ref}}{QE_{sample}} * \frac{1}{LO_{ref}} \tag{7.6}$$

The results are shown in table 7.3; they are measured with an uncertainty of $\sim 10\%$. The measurements were made with an integration window of 5 $\mu$s, hence covering the full slow self-trapped exciton emission tail.

When comparing the results of the two different producers, the extracted amount of light from Proteus crystals is slightly higher, i.e. by about 15%, than that from Epic crystals. Irrespective of the measurement error, this is still a significant difference. It is to be seen in contrast with the transmission measurements where the Proteus crystal was found to absorb more light. Still, this absorption occurs only in the wavelength

Table 7.3: Light output measurements of crystals with different dimensions, from Epic and Proteus, air-coupled to a Hamamatsu H6610 PMT. The light transfer efficiency is calculated assuming 10900 ph/MeV as intrinsic light yield of $BaF_2$ [21].

| | Light Output (ph/MeV) | Light Transfer Efficiency |
|---|---|---|
| **Proteus** $2 \times 2 \times 3$ $mm^3$**:** | | |
| No wrapping | $1.5 \cdot 10^3$ | 0.13 |
| Teflon wrapping | $3.4 \cdot 10^3$ | 0.31 |
| **Epic** $2 \times 2 \times 3$ $mm^3$**:** | | |
| No wrapping | $1.2 \cdot 10^3$ | 0.11 |
| Teflon wrapping | $2.9 \cdot 10^3$ | 0.27 |
| **Epic** $3 \times 3 \times 3$ $mm^3$**:** | | |
| No wrapping | $1.7 \cdot 10^3$ | 0.15 |
| Teflon wrapping | $3.7 \cdot 10^3$ | 0.34 |
| **Epic** $3 \times 3 \times 20$ $mm^3$**:** | | |
| No wrapping | $1.0 \cdot 10^3$ | 0.09 |
| Teflon wrapping | $2.4 \cdot 10^3$ | 0.22 |

range of the fast emission. The light output measurements are dominated by the slow STE emission in the crystals, being about 7-8 times higher than that from the fast cross-luminescence. In the case of Proteus, it is therefore difficult to determine the exact origin of the higher light output. While the intrinsic light yield is the same for both crystals - a reasonable assumption because they are both made from the same material - the light transfer efficiency (LTE) of the Proteus crystal is slightly higher. This is probably due to a difference in cutting and/or polishing quality, which both significantly affect the LTE in crystals. This effect is not visible in the transmission measurements where the light beam enters the crystal in the middle of and perpendicular to its front face.
For both the short and long crystals, Teflon wrapping improves the light output by about a factor of 2. Furthermore, the 20 mm-long Epic crystal has a light output 1.6 times lower than the 3 mm long crystal, a well known effect from measurements with different crystals lengths.

The LTE is a useful measure to compare how well one can extract light from a crystal, and is basically the ratio between the intrinsic light yield ($LY_{intr}$) and the light output ($LO$). In his article, Dorenbos et al. [21] published comprehensive measurements of the intrinsic light yield of $BaF_2$. The measurements are made with large diameter crystals and two different PMTs. The authors furthermore explain their method of measurements and what corrections they made to obtain the intrinsic light yield. Their conclusion is that $BaF_2$ has a total intrinsic light yield of 10900 ph/MeV out of which 1400 ph/MeV originate from fast emission and 9500 ph/MeV from slow emission. Taking Dorenbos' 10900 ph/MeV as the total intrinsic light yield in $BaF_2$ and comparing that with the measured light output obtained with the Epic and Proteus crystals, one can calculate the respective LTE for each of the crystals. The results of this are also listed in table 7.3. Under the assumption that the refractive index and the geometry of the crystals, as well

as their wrapping and coupling conditions, are the driving factors for the estimate of the light transfer efficiency, a comparison was made between the LTE calculated by Gundacker et al. [27] for any crystal type and the LTE values obtained in this work. Considering that Gundacker calculated a LTE of ∼50% for a Teflon wrapped 3 mm long crystal, the LTE values of this work with with $BaF_2$ were found to be ∼30%. The discrepancy could be explained by specific absorption effects in the $BaF_2$ crystals due to imperfect surface states of the crystals, e.g. crystal edge defects. Furthermore, despite the well known effectiveness of Teflon wrapping on light extraction, its behaviour in the deep UV is still not completely understood and is therefore subject to further investigations.

### 7.4.3 Time correlated single photon counting (TCSPC)

Since the time correlated single photon counting (TCSPC) measurements cannot discriminate between wavelengths (see section 7.3), the contribution of light per wavelength to each scintillation component is not known. Therefore, the amount of detected light cannot be corrected for the QE of the hybrid-PMT in the different wavelength regimes. Since the QE is very low in the deep UV, this fact probably leads to an underestimation of the abundance of the emission at shorter wavelength, i.e. in the domain of the fast emission. The time window over which the data is taken is 9 $\mu$s such that it is sufficiently large to also properly measure the slow decay component.

The results obtained with the TCSPC setup, as shown in figures 7.9 and 7.10, are analyzed by fitting the data with an exponential fit. In addition to a single rise time component, this fit can vary according to the number of decay components taking as input the observed shape of the crystal scintillation decay. Furthermore, the exponential function is convoluted with the impulse response function (IRF) of the setup, as explained in section 3.3. The IRF is also shown in figures 7.9 and 7.10. In the case of $BaF_2$, literature reports only two decay components. In line with this, the exponential contains two decay time contributions. The fit covers a 2$\mu$s range, sufficient to adequately derive both the fast and slow decay components.
The rise times in all the $BaF_2$ measurements were found to be consistently less than 4 ps, far below the resolution of the system with its IRF of 162 ps FWHM (see section 3.3). As this value in the context of PET applications can be considered as practically zero, the rise time has been fixed to 0 ps during the final fits and in this way ensures a higher precision for the estimate of the decay times.
The fitted measurements of the Epic and Proteus crystals are shown in figures 7.9 and 7.10, respectively, where for both measurements the *double* exponential decay was used, shown on the left hand side of all plots. The fitted values are then summarized in table 7.4.
It can be seen that for both crystals the obtained decay times derived from the fit are consistent with those found in literature, i.e. 550 ns and 690 ns for the STE emission and 0.6 ns for the cross-luminescence. Even though the fit leads to a low $\chi^2$, it shows a deficiency in the first nanosecond of the emission, which leads to the assumption that there might be an additional, probably very fast, decay component hidden in the emission spectrum. To test this hypothesis, the data was consequently fitted with an exponent of *three* decay-constants. The results of these fits are shown in figures 7.9 and 7.10, on the right hand side. It is evident from these plots that the triple exponential decay function leads to a better fit then the double exponential decay function, although both $\chi^2$ are comparable. This confirms the assumption [46] of a third decay channel being present

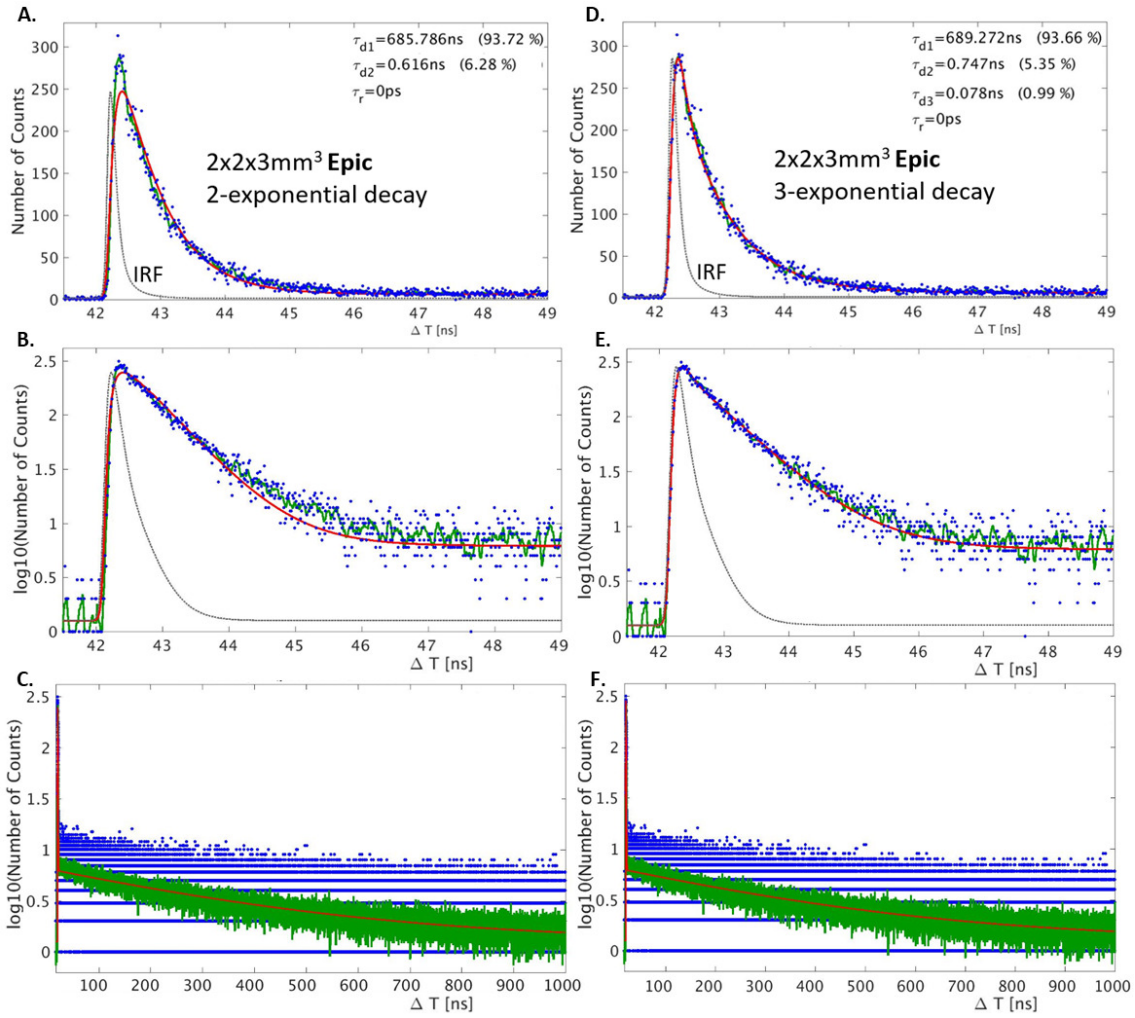


Figure 7.9: Time correlated single photon counting measurement, with 3 mm long $BaF_2$ crystals from Epic. The black dotted line gives the impulse response function (IRF) of the setup. The green line is a walking average and the red line a fit. All six plots are made with the same data. A.-C.: the data has been fitted with a double exponential decay. D.-F.: the data has been fitted with a triple exponential decay. A.,D.: Zoom of the first 7 ns of the measurement. B.,E.: Same zoom as before, of the first 7 ns, but with logarithmic y-axes. C.,F.: Partially zoomed out, showing the first 1$\mu$s of the measurement, also with logarithmic axes.

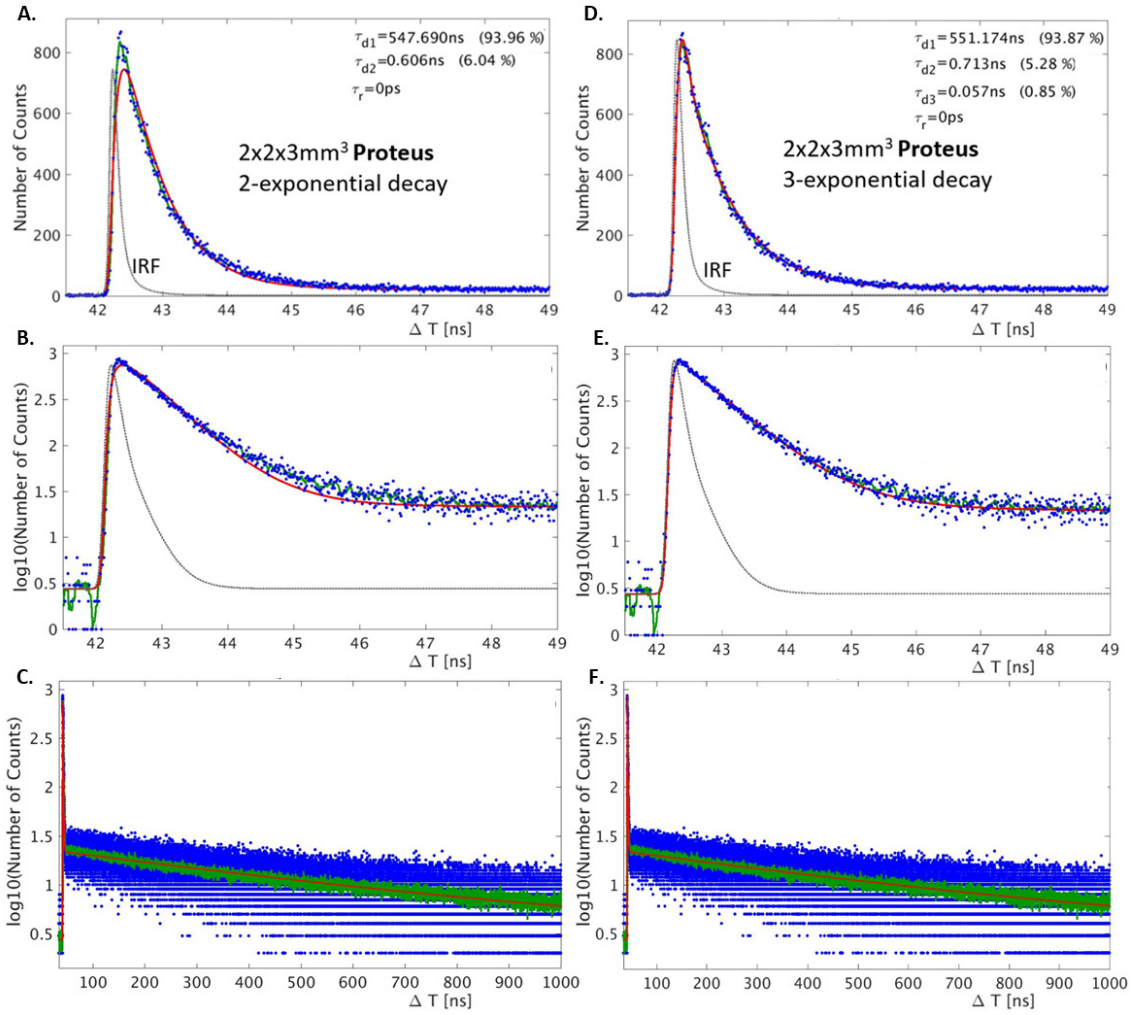


Figure 7.10: Time correlated single photon counting measurement with 3 mm long $BaF_2$ crystals from Proteus. The black dotted line gives the impulse response function (IRF) of the setup. The green line is a walking average and the red line a fit. All six plots are made with the same data. A.-C.: the data has been fitted with a double exponential decay. D.-F.: the data has been fitted with a triple exponential decay. A.,D.: Zoom of the first 7 ns of the measurement. B.,E.: Same zoom as before, of the first 7 ns, but with logarithmic y-axes. C.,F.: Partially zoomed out, showing the first 1$\mu$s of the measurement, also with logarithmic axes.

Table 7.4: Parameters of the double and triple exponential used to fit the the data from the TCSPC measurements with a $2 \times 2 \times 3\ mm^3$ $BaF_2$ pixels from Proteus and from Epic.The rise times were found to be consistently less than 4 ps, far below the resolution of the system, and were therefore set to 0 ps in the final fit as to ensures a higher precision for the fits of the decay times.

| | $\tau_r$ (ps) | $\tau_{d1}$ (ns) | $R_1$ (%) | $\tau_{d2}$ (ns) | $R_2$ (%) | $\tau_{d3}$ | $R_3$ (%) | $\chi^2 \pm 0.0036$ |
|---|---|---|---|---|---|---|---|---|
| **Double Exponential** | | | | | | | | |
| Proteus | 0 | - | - | 0.606 | 6.04 | 548 | 93.96 | 1.029 |
| Epic | 0 | - | - | 0.616 | 6.28 | 686 | 93.7 | 1.008 |
| Filter 240-395 nm + Proteus | 0 | - | - | 0.585 | 2.3 | 640 | 97.7 | 1.004 |
| **Triple Exponential** | | | | | | | | |
| Proteus | 0 | 0.057 | 0.85 | 0.713 | 5.28 | 551 | 93.87 | 1.016 |
| Epic | 0 | 0.078 | 0.99 | 0.747 | 5.35 | 689 | 93.7 | 1.005 |
| Filter 240-395 nm + Proteus | 0 | 0.170 | 0.50 | 0.786 | 1.89 | 641 | 97.61 | 1.002 |

with an abundance of only ∼1% and a presumed decay time of 0.1 $ns$. In view of its low abundance it is difficult to be more precise in determining its decay time and contribution to the emission spectrum. Furthermore, this decay time is at the limit of the intrinsic time resolution of the setup. Especially in view of high resolution timing measurements, this component could be of large interest in applications where even few photons with such a fast decay time could lead to significant improvements in time resolution. To see the effect of several prompt photons on the CTR, this work refers to an article by Gundacker et al. [47].
The results of the triple exponential fits are also shown in table 7.4. For the emission that has been identified as self-trapped exciton emission, a decay time of $\tau = 550 - 690$ $ns$ has been measured and similarly for the cross-luminescence a value of $\tau = 0.7$ $ns$. These values are in line with those found in literature.
As to the origin of the very fast decay, some groups [24] [25] have been contemplating about the existence of hot interband-luminescence in $BaF_2$. This type of luminescence is also very fast and could therefore explain the observed third decay component. On the other hand, hot interband-luminescence is emitted over all wavelengths and should therefore also be detectable at longer wavelengths. If 400 nm high-pass filter is placed in front of the photodetector, only a noise spectrum could be produced, which in fact proves that there is no significant emission above 400 nm. Therefore, it is concluded that the very fast decay is not caused by hot interband-luminescence. Measurements made within a wavelength window of 240-395 nm show that, within this spectral range, this third decay component drops by 50% in abundance. Therefore, at least the majority of this emission, the origin of which is still unknown, must be below 240 nm.
As to the decay channel clearly identified as cross-luminescence, the measurements with the same high band-pass filter show that cross-luminescence is reduced by a factor of ∼2.5, confirming that the majority of this emission type is below 240 nm, also consistent with literature.

### 7.4.4 Coincidence time resolution (CTR)

The coincidence time resolution (CTR) measurements are made with 3 mm long crystals only, found to be most suitable for comparing the timing performance of $BaF_2$ with other scintillators of same size. The aim of using shorter crystals is to minimize absorption effects and imperfections. Therefore, with these measurements one rather evaluates intrinsic properties of the scintillator material.

Figure 7.11 shows CTR measurements with Proteus and Epic crystals coupled to the HPK S13370-CN SiPM from Hamamatsu. The obtained results (FWHM) are 98±5 ps for the Epic and 94±5 ps for the Proteus crystal. It can be seen that, with the given SiPM, both crystals behave the same, irrespective of the Proteus' slightly higher light yield and higher absorption in the UV.

When coupled to the FBK VUV-HD SiPM the Proteus and Epic crystals yielded a CTR as shown in Figure 7.12. Here the CTR is significantly higher as compared to the one measured with the Hamamatsu SiPM. The Proteus crystal produces a CTR of 64±6 ps and the Epic of 54±6 ps. The 10 ps difference between the two is most likely attributed to the Epic crystals' higher transmission in the wavelength range of interest being crucial for good timing (refer to section 7.4.1). The subtle difference in CTR can be explained by the FBK's typically superior SPTR compared to that found in Hamamatsu devices. Furthermore, owing to its higher transmission in the deep UV, the Epic crystal delivers more fast photons to the photodetector than the Proteus crystal, which can only be detected by the FBK device.

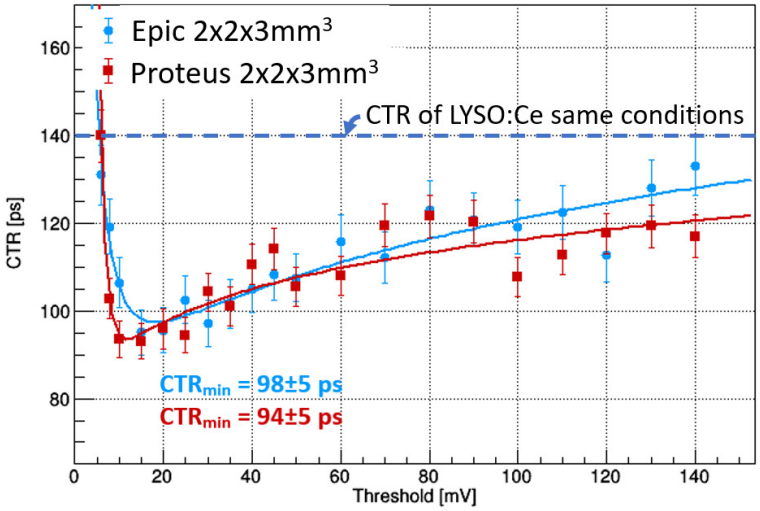


Figure 7.11: CTR measurements of $2 \times 2 \times 3$ $mm^3$ $BaF_2$ pixels from Epic and Proteus, air coupled to a S13370-CN SiPM from Hamamatsu at a bias of 61 V. Of both fits of the data, the minimum value is written (in the corresponding color).

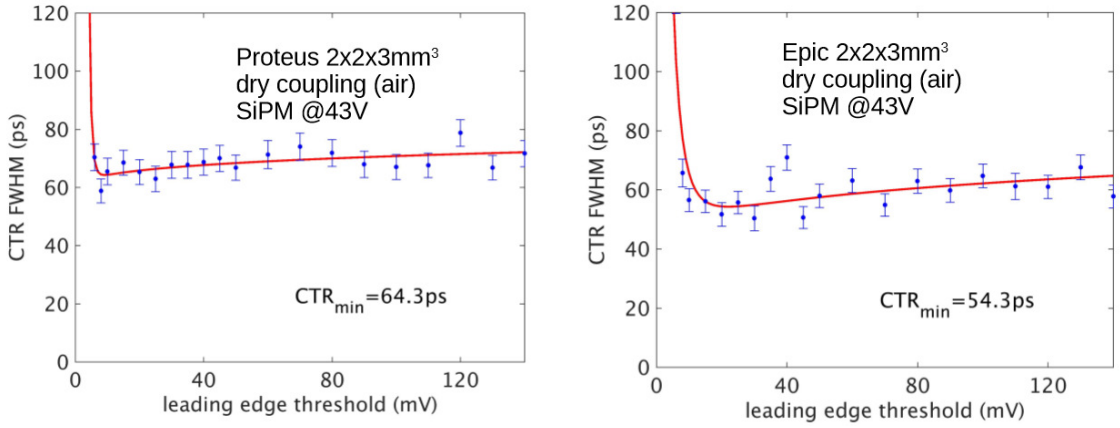


Figure 7.12: CTR measurements of $2 \times 2 \times 3$ $mm^3$ $BaF_2$ pixels from Epic and Proteus, air coupled to a VUV-HD SiPM from FBK at a bias of 43 V.

When comparing the two different SiPMs also the photon detection efficiency (PDE) of the devices from the the two different producers play an important role in assessing the CTR. Referring to the previous paragraph the FBK device, in terms of CTR, performs 1.5-1.8 times better than the HPK. The difference in PDE alone, 22% for the FBK compared to 15% for the HPK [12], already accounts for a factor of 1.2 in timing, or the equivalent of $\sim$ 20 ps in terms of CTR. As mentioned before, also the SPTR of the two devices is different. Gundacker et al. have shown [27] that the SPTR has a clear influence on the CTR. From their measurements and simulations with LSO:Ce:0.4%:Ca one can deduce a systematic difference in CTR between FBK and HPK of the order of 10-20 ps solely attributed to their different SPTRs. Then, the differences in PDE and SPTR fully account for the difference in the measured CTR of the two devices.

In summary, despite their significantly different CTRs both SiPMs in conjunction with $BaF_2$ still produce results competing with state-of-the-art scintillators commonly used in imaging. To give an example, an LYSO:Ce crystal of $2\times2\times3\ mm^3$ coupled with Meltmount to an FBK NUV-HD SiPM achieved a CTR of 69$\pm$3 ps FWHM [48]. In contrast to that, $BaF_2$ exceeds that value if it is coupled to a VUV-HD FBK SiPM with a CTR of 54$\pm$6 ps FWHM, even with no coupling grease used. When reading these results, one should also take into account that the PDE of the FBK device is only 22% at the emission wavelength of $BaF_2$, whereas the LYSO:Ce can profit from as high as 65% in PDE in its measurements.

## 7.5 Characterization of $BaF_2$ with grease-coupling

As the previous measurements show, the performance of the $BaF_2$ crystals when air-coupled is already very promising. This, however, gives rise to the question whether one could further improve the CTR when using optical coupling greases. The difficulty then is that there are not many compounds available that are transparent to UV-light with wavelengths shorter than 250-300 nm. There has been previous research on this subject by Klamra et al. [10] and Zhu [49]. However, Klamra et al. only measured the transmission of greases down to 240 nm.

### 7.5.1 Greases used in this study

Several optical coupling greases have been tested for this study. Rhodorsil 47V, normally used in our lab, is one of the first greases tested in conjunction with $BaF_2$. Meltmount, also frequently applied in our lab, was also added to the transmission measurements, although it was already suspected to be prone to absorption in the UV. Furthermore, Dow Corning 200 (500.000 cst) was part of the test series, for it was deemed by both Klamra et al. [10] and Zhu [49] to be very transparent in the deep UV. Further added to this test series was Viscasil, also claimed to be very transparent in the deep UV and tested by the above authors. Finally, also glycerine was taken as a promising candidate. Glycerine was previously previously in the experiments with photonic crystals. The difficulty, however, with it is that it behaves more like a liquid and therefore makes handling with it more difficult than with the other greases that are more viscous.

### 7.5.2 Transmission

In order to measure their transmission ability, the greases were applied in form of a thin layer between two quartz plates. Quartz was chosen because of its high transparency in

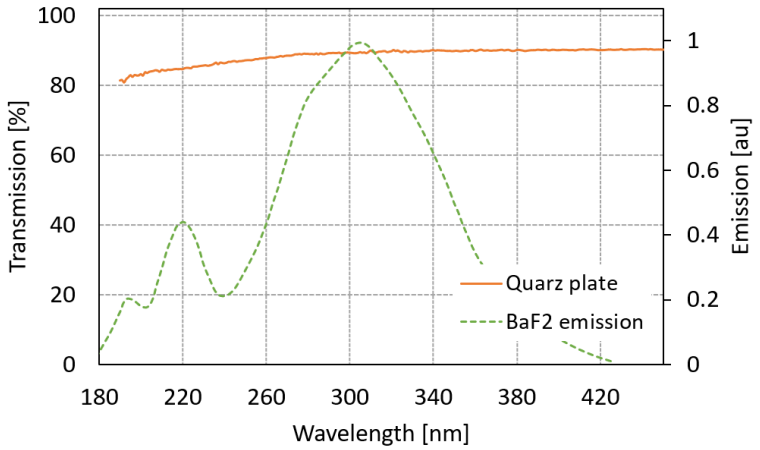


Figure 7.13: Zoom of transmission measurements of one quartz plate, which is performed between 190 nm and 900 nm. The majority of the absorption visible is actually caused by Fresnel reflection, changing with wavelength by the changing refractive index. Two of these plates are used for in the measurements of the investigated optical couplings in figure 7.14.

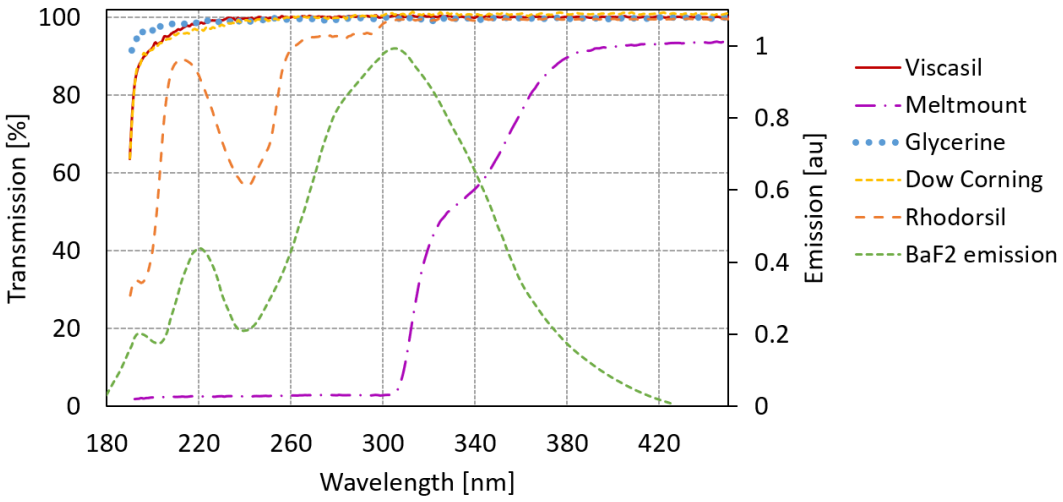


Figure 7.14: Zoom of transmission measurements of several optical couplings in between two quartz plates, performed between 190 nm and 900 nm, corrected for the absorption by one quartz plate and the Fresnel reflection between the quartz/air interface. The measurements used for the correction are shown in figure 7.13. Also the emission spectrum of $BaF_2$ has been plotted.

Table 7.5: Light output measurements on $2 \times 2 \times 3$ $mm^3$ crystals of $BaF_2$ from Epic and Proteus, coupled to a Hamamatsu H6610 PMT with several couplings. The error in the measurements is about 10%. The light transfer efficiencies (LTE) are calculated using 10900 ph/MeV as intrinsic light yield [21].

| | **Epic** | | | **Proteus** | | |
|---|---|---|---|---|---|---|
| | Light output (ph/MeV) | Light Transfer Efficiency (LTE) | Gain w.r.t. air-coupling | Light output (ph/MeV) | Light Transfer Efficiency (LTE) | Gain w.r.t. air-coupling |
| Air | $2.9{\cdot}10^3$ | 0.27 | | $3.7{\cdot}10^3$ | 0.34 | |
| Rhodorsil | $4.3{\cdot}10^3$ | 0.39 | 1.48 | $5.0{\cdot}10^3$ | 0.46 | 1.49 |
| Viscasil | $4.5{\cdot}10^3$ | 0.41 | 1.55 | $5.6{\cdot}10^3$ | 0.51 | 1.67 |
| Dow Corning | $5.1{\cdot}10^3$ | 0.46 | 1.75 | $5.7{\cdot}10^3$ | 0.52 | 1.70 |
| Glycerine | $5.1{\cdot}10^3$ | 0.46 | 1.75 | $6.0{\cdot}10^3$ | 0.55 | 1.77 |

the deep UV. Figure 7.13 shows the transmission measurement of one of the bare quartz plates. The main source of absorption visible in this measurement is Fresnel reflection at the air/quartz interfaces (see appendix E on Fresnel reflection). The transmission measurement of the quartz is used to correct the transmission measurements of the greases for the Fresnel effect and the absorption of the quartz plate. This means that the transmission measurements of the greases are still slightly offset by the absorption of one quartz plate. This contribution, however, is deemed negligible. The transmission measurements are shown in figure 7.14. They show that Meltmount is clearly not suitable as a glue for $BaF_2$ and was thus eliminated from further testing. Rhodorsil, reported by Klamra et al. [10] to be transparent down to 240 nm, shows a significant and broad absorption center at ∼250 nm and a cut-off at around ∼210 nm. Therefore, Rhodorsil was not deemed as a suitable optical coupling grease either. However, it remained included in the ensuing tests series serving only for comparison. As to Dow Corning 200 and Viscasil, there does not seem to be a significant difference between the two of them. Both are close to 100% transparent down to 220 nm, from where on they start to absorb gradually. They both seem to have a cut-off in transmission at 190 nm, an effect also observed by Zhu [49] and Dorenbos et al. [21]. All together, Dow Corning 200 and Viscasil look suitable as optical coupling compounds for $BaF_2$. In contrast to Dow Corning and Viscasil, glycerine extends its transparency even down to shorter wavelengths, i.e. 210 nm, before it also slowly starts absorbing light.
In sum up these observations, glycerine appears to be the most promising coupling candidate from the UV-transmission point of view. Still, Viscasil and Dow Corning 200 are almost equally suitable for being used with $BaF_2$.

### 7.5.3 Light output

Light output measurements were made with $2 \times 2 \times 3$ $mm^3$ $BaF_2$ pixels from both Proteus and Epic, coupled to a PMT with the selected greases.
An example of a measurement with a Proteus crystal coupled with Viscasil is shown in figure 7.15 as well as a measurement with the same crystal being air-coupled to the PMT. As expected, Viscasil significantly improved the light output. The results of the measurements are summarized in table 7.5. It shows that all greases, including Rhodorsil, clearly improve light extraction from the $BaF_2$ crystals. With Rhodorsil to a lesser extent, as expected from the transmission measurements.
Glycerine, Dow Corning and Viscasil show a gain in light output of as much as 1.6-1.8 over the entire wavelength spectrum as compared to air-coupling. To first order, this makes one

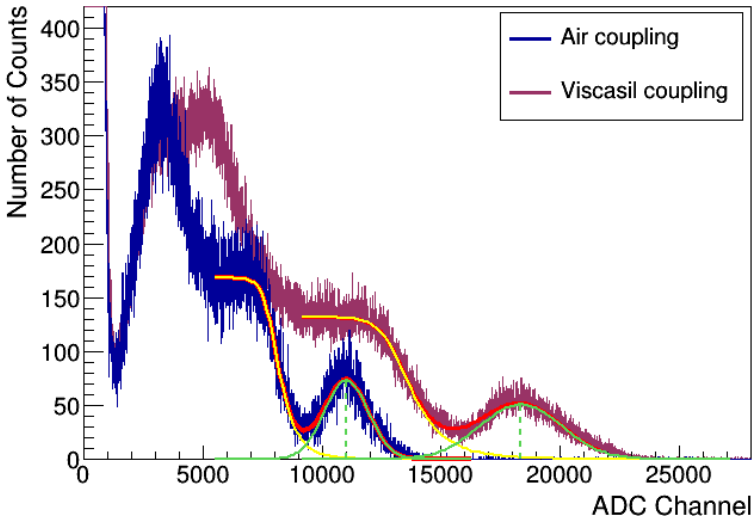


Figure 7.15: Light output measurements of a $2 \times 2 \times 3$ $mm^3$ $BaF_2$ pixel of Proteus, coupled to the PMT using air and using Viscasil. The red lines show the total fit, the green lines show only the contributions of the photopeak and the yellow lines the contributions of the Compton edge.

expect an improvement in CTR by a factor of ∼1.3 on photostatistical arguments only. On the other hand it is known that the CTR is mostly influenced by the *fast* emission modes of the crystal, which unfortunately has a much lower abundance than the *slow* emission mode. Furthermore, possible absorption effects of the greases at these *lower* wavelengths at that transmission mode would lower the CTR. All in all, the photostatistics alone do not give a complete picture of the CTR behaviour in $BaF_2$ tested with these coupling agents. Therefore, the 1.3 times improvement in CTR should be taken as an upper limit in CTR improvement. The CTR measurements are discussed in section 7.5.5.
Table 7.5 also shows the LTE values, calculated on the basis of 10900 ph/MeV as total light yield produced [21].

### 7.5.4 Time correlated single photon counting (TCSPC)

While optical coupling greases generally improve light extraction they are, at certain wavelengths, also subject to absorb light. As such, they will either increase or reduce the amount of light depending on that particular wavelength. Since different wavelength

Table 7.6: Parameters of the *triple* exponential used to fit the the data from the TCSPC measurements with a $2 \times 2 \times 3$ $mm^3$ $BaF_2$ pixels from Proteus, using various optical couplings and a filter in front of the hybrid PMT.

| | $\tau_r$ (ps) | $\tau_{d1}$ (ns) | $R_1$ (%) | $\tau_{d2}$ (ns) | $R_2$ (%) | $\tau_{d3}$ | $R_3$ (%) | $\chi^2 \pm 0.0036$ |
|---|---|---|---|---|---|---|---|---|
| Proteus Air | 0 | 0.057 | 0.85 | 0.713 | 5.28 | 551 | 93.87 | 1.016 |
| Proteus Viscasil | 0 | 0.040 | 0.82 | 0.720 | 4.86 | 617 | 94.32 | 1.038 |
| Proteus Glycerine | 0 | 0.043 | 0.75 | 0.710 | 4.86 | 626 | 94.41 | 1.014 |
| Proteus Dow Corning | 0 | 0.049 | 0.85 | 0.710 | 4.79 | 614 | 94.37 | 1.031 |
| Proteus Rhodorsil | 0 | 0.145 | 0.97 | 0.782 | 3.98 | 620 | 95.05 | 1.014 |

Table 7.7: Parameters of the *double* exponential used to fit the the data from the TCSPC measurements with a $2 \times 2 \times 3$ $mm^3$ $BaF_2$ pixels from Proteus, using various optical couplings and filters in front of the hybrid PMT.

| | $\tau_r$ (ps) | $\tau_{d1}$ (ns) | $R_1$ (%) | $\tau_{d2}$ (ns) | $R_2$ (%) | $\chi^2 \pm 0.0036$ |
|---|---|---|---|---|---|---|
| Proteus Air | 0 | 0.606 | 6.04 | 548 | 93.96 | 1.029 |
| Proteus Viscasil | 0 | 0.613 | 5.7 | 615 | 94.3 | 1.050 |
| Proteus Glycerine | 0 | 0.601 | 5.56 | 623 | 94.44 | 1.031 |
| Proteus Dow Corning | 0 | 0.596 | 5.52 | 612 | 94.48 | 1.039 |
| Proteus Rhodorsil | 0 | 0.613 | 4.78 | 617 | 95.22 | 1.017 |

regimes correspond to the different decay components of $BaF_2$, the use of optical greases can also influence the detected abundance of the different decay-components in the kinematics. As the grease-sample, applied between the two quartz plates, in the used TCSPC setup is not physically attached to the photodetector but rather placed in the scintillation light path, see figure 3.5, chapter 3.3, the grease only acts as a wavelength-dependent filter. First, measurements with air between the two plates are made to confirm that the quartz itself has no significant influence on the measurements. Then, in subsequent measurements a thin layer, order $\sim 100\mu$m and assumed to be similar as a layer between crystal and photodetector, of optical grease is applied between the two plates so as to see their influence on the measurements. Table 7.6 and 7.7 summarize these measurements. Based on the arguments made in section 7.4.3, a triple decay fit leads to better agreement with the data than a double-exponential fit. The goal of the TCSPC measurements is to investigate the coupling greases' effect on the abundancies of the decay components only. However, introducing the third, very fast, component into the fit lowers the data statistics, which gives rise to large fluctuations on the fitting. This necessarily complicates the precise determination of the parameters of the other decay components in the fit as well. Therefore, the double exponential fit was felt more suitable as it led to smaller uncertainties in the determination of the impact the greases have on the abundance of both the effective fast component and the slow STE component. Table 7.7 shows that the application of Viscasil, glycerine and Dow Corning only slightly decreases the abundance of the fast emission, i.e. by a factor of 0.94-0.92. Within the uncertainties these values are comparable to those measured with air between the quartz plates. This result is consistent with the prior transmission measurements of the greases, showing absorption mainly below 200 nm. Given the poor QE of the hybrid-PMT in this wavelength regime, the effect of absorption is probably not measurable with this TCSPC setup. It is also clearly seen that the application of Rhodorsil significantly reduces the abundance of the fast emission, namely by a factor 0.79. This again is in agreement with the earlier transmission measurements with this grease, showing its significant absorption below 260 nm. Weighting this loss against the overall gain in light extraction and its effects on the CTR will be discussed in section 7.5.6.

### 7.5.5 Coincidence time resolution (CTR)

Similar to the CTR measurements made with air-coupling to the photodetector, the two crystals of $2 \times 2 \times 3$ $mm^3$ were now coupled with grease to the photodetector for the next series of CTR measurements. This investigation was made with both the HPK and FBK SiPMs.

#### 7.5.5.1 Measurements with Hamamatsu S13370-CN SiPM

The outcome of the measurements made with the S13370-CN SiPM of Hamamatsu is shown in figures 7.16 and 7.17, with a summary of the results in table 7.8. Judging from this table the following conclusions can be drawn:

**1.** As to the Proteus crystal, within the statistical limits there seems to be no improvement at all no matter what grease is taken irrespective of the bias voltages chosen.

**2.** On the other hand, the Epic crystal shows improvement over air-coupling, but only significantly in conjunction with Viscasil. For the other compounds the improvement is within the confidence limits of the fit.

**3.** Rhodorsil shows no improvement, in fact slightly degrades the performance, and can be ruled out as a suitable coupling compound.

To illustrate the behavior of the CTR to the various applied greases, figure 7.18 gives a point chart showing the CTR of the two crystals for each of the greases, with respect to the two air-coupled measurements.
In summary, it is the Epic crystal coupled with Viscasil to the HPK SiPM at 61 V bias that yields the best CTR of $78 \pm 5$ *ps* FWHM.

#### 7.5.5.2 Measurements with FBK VUV-HD SiPM

Based on the positive results made with glycerine and Viscasil in the previous measurements, the following tests were made with these two coupling compounds only, together with the FBK VUV-HD SiPM. Note, unfortunately due to the fact that the FBK SiPM got damaged in this series of measurements, only the effect of glycerine over air could be tested with both crystals, whereas Viscasil was only investigated with the Proteus crystal. It was found from the outset, and similarly as observed with the Hamamatsu SiPM, that Viscasil in conjunction with the Proteus crystal showed no improvement over air-coupling. Figure 7.19 then shows the results obtained with glycerine only. Unlike the results obtained with the Hamamatsu SiPM, both crystals, Proteus and Epic, benefited from the use of glycerine. As before, it is the Epic crystal that after all leads to the best CTR, i.e. $51 \pm 6$ *ps* FWHM. This value, at his time, represents the best CTR measured with $BaF_2$ crystals, provided that a VUV-sensitive SiPM and a UV-transparent grease were used.
To put this result into context with latest published achievements, we compare this value with previous state-of-the-art CTR values obtained with lutetium-based crystals read out

Table 7.8: CTR measurements of $2 \times 2 \times 3$ $mm^3$ $BaF_2$ pixels from Epic and Proteus, coupled to a S13370-CN of Hamamatsu, using various optical couplings. All values given are in ps FWHM.

| | Bias voltage | Air | Rhodorsil | Dow Corning | Glycerine | Viscasil |
|---|---|---|---|---|---|---|
| Epic | at 60 V | 104±6 | 115±6 | 97±5 | 92±8 | 84±4 |
| Proteus | at 60 V | 102±4 | 104±5 | 99±4 | 106±6 | 100±5 |
| Epic | at 61 V | 98±5 | - | 94±5 | 93±8 [1] | 78±4 |
| Proteus | at 61 V | 94±4 | 117±6 | 94±4 | 106±6 [1] | 87±4 |

[1]Measurement at a bias voltage of 60.8 V, since 61 V was too high to be able to measure.

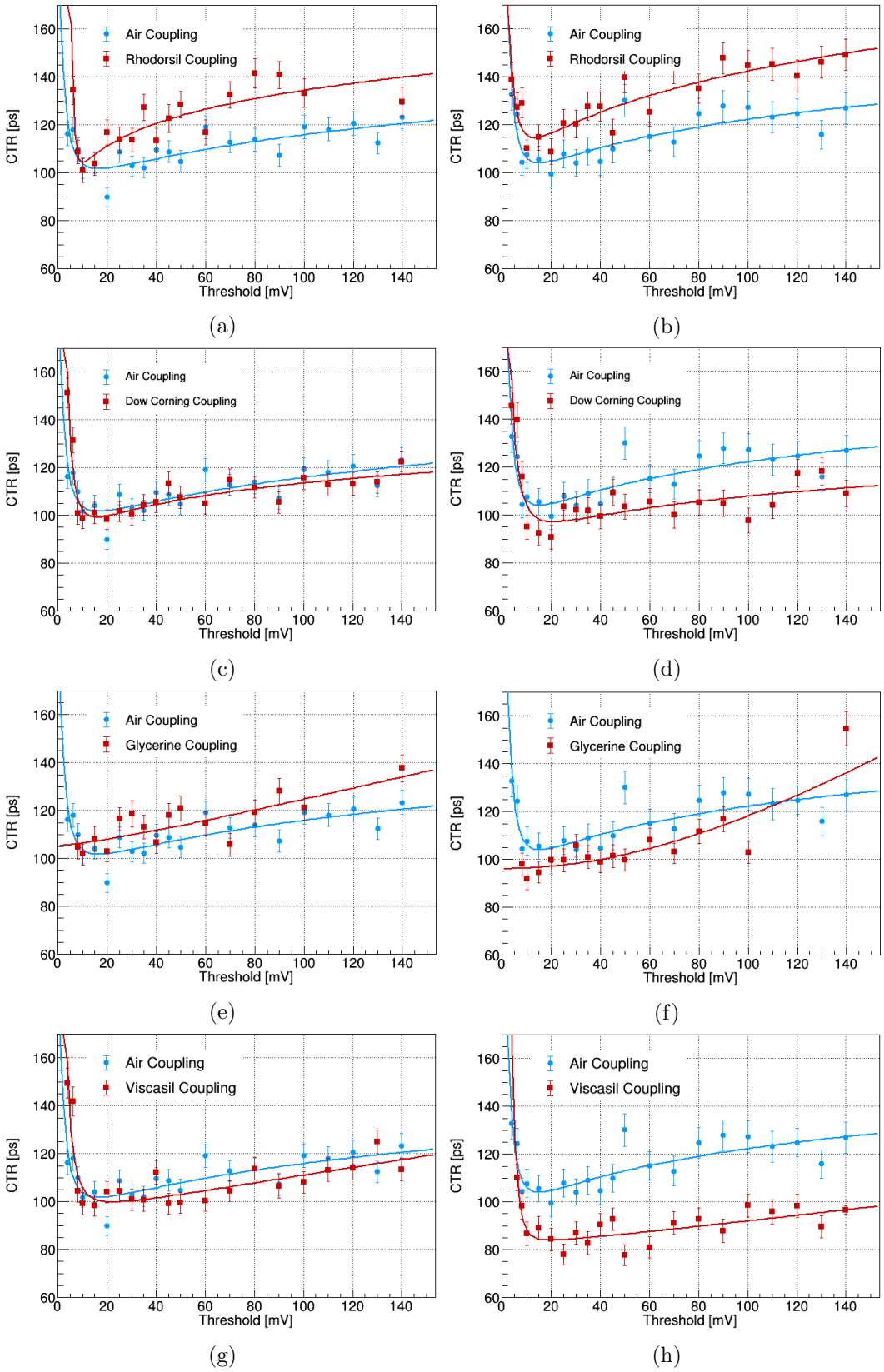


Figure 7.16: CTR measurements in FWHM of a 2x3x3 $mm^3$ $BaF_2$ pixel, produced by Proteus (left) and Epic (right), coupled to a S13370-CN of Hamamatsu with air and Rhodorsil (a),(b), Dow Corning (c),(d), glycerine (e),(f) and Viscasil (g),(h). Measured at a bias voltage of 60 V.

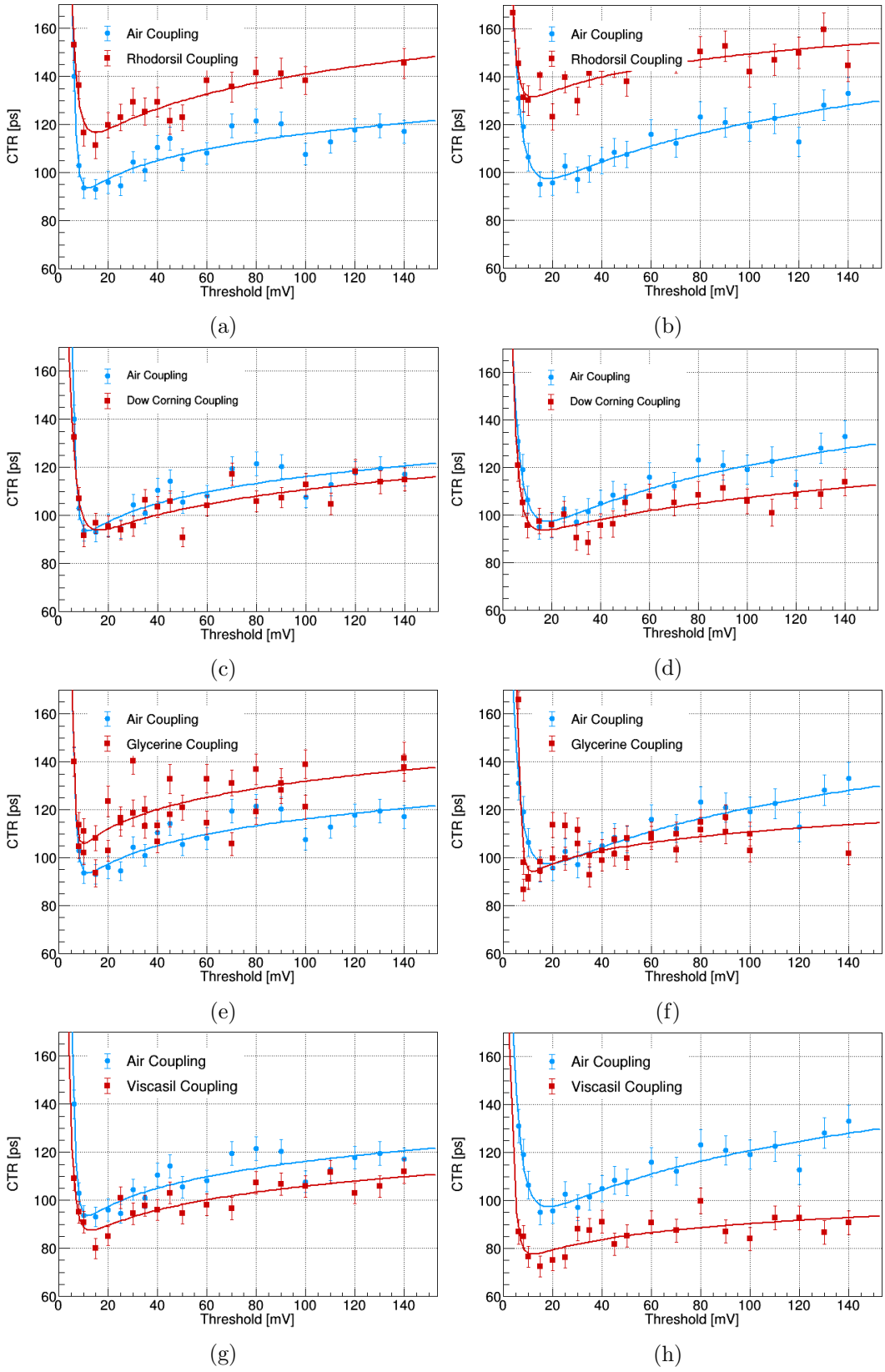


Figure 7.17: CTR measurements in FWHM of a 2x3x3 $mm^3$ $BaF_2$ pixel, produced by Proteus (left) and Epic (right), coupled to a S13370-CN of Hamamatsu with air and Rhodorsil (a),(b), Dow Corning (c),(d), glycerine (e),(f) and Viscasil (g),(h). Measured at a bias voltage of 61 V (glycerine at 60.8 V).

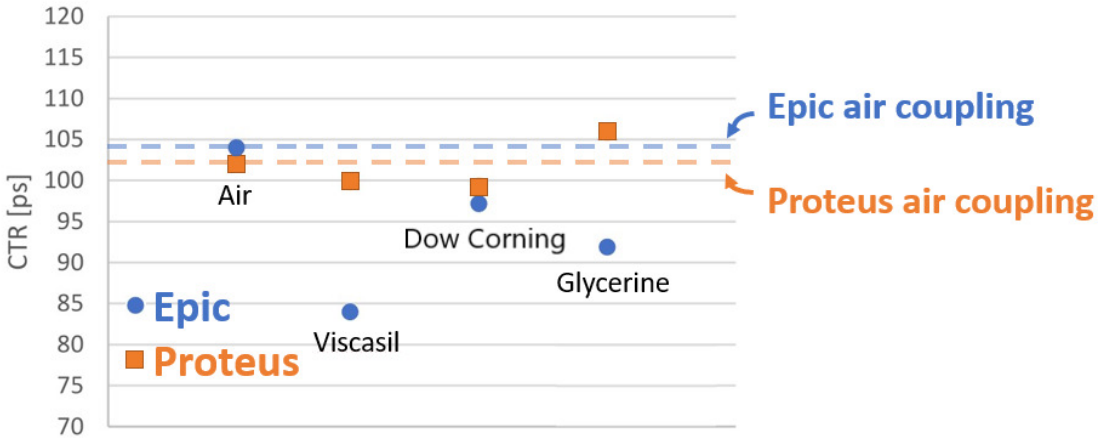


Figure 7.18: Minima of CTR measurements in FWHM of $2 \times 2 \times 3\ mm^3$ $BaF_2$ pixels from Epic and Proteus, coupled to a S13370-CN of Hamamatsu, using various optical couplings. Measurements are taking at a bias of 60V.

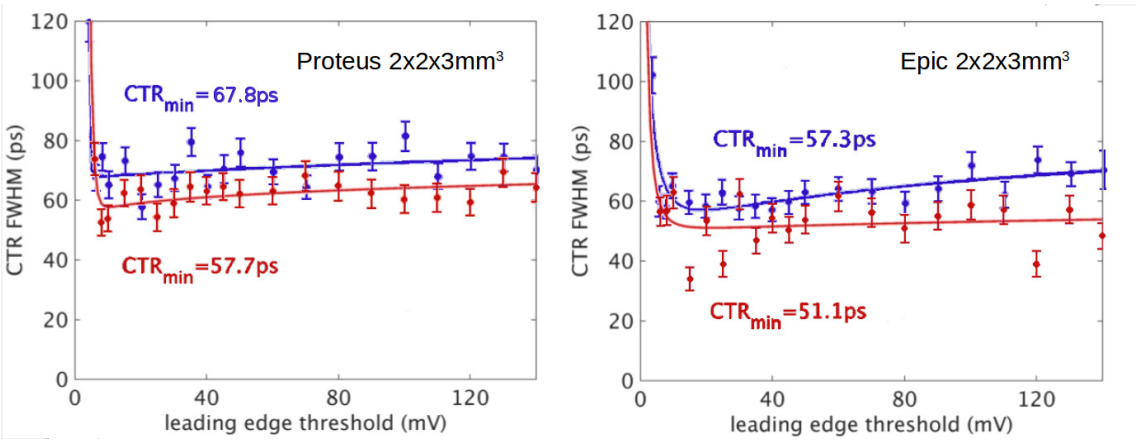


Figure 7.19: CTR measurements of $2 \times 2 \times 3\ mm^3$ $BaF_2$ pixels from Proteus (left) and Epic (right), air- (blue) and glycerine (red) coupled to a VUV-HD SiPM from FBK at a bias of 42 V.

with non-UV SiPMs and non-UV-transparent greases like Meltmount. In the case of commonly used LYSO:Ce the best CTR achieved is 69±3 ps FWHM [27]. Even if we compare the $BaF_2$ result with the current worldwide state-of-the-art CTR of 58±3 ps FWHM [50] measured with the more "exotic" calcium co-doped LSO:Ce:0.4%Ca crystals, the $BaF_2$ still outperforms this record. This result is ever more so encouraging by the fact that the PDE of the SiPM used with $BaF_2$ is only $\sim$ 22%, a significant "handicap" compared a PDE of $\sim$ 65% for the NUV-HD SiPM used in the measurement of LSO:Ce:0.4% and LYSO:Ce at their emission wavelength of 420 nm. Given the importance of the SiPM's PDE on the time resolution, then a projected similar value of 65% also for the deep UV would lead to an even further improvement in the $BaF_2$'s timing performance and as such to a projected CTR of $\sim$30 ps FWHM. This would constitute a significant milestone in the domain of timing in scintillation detectors using inorganic scintillators, spurring developments in time-of-flight imaging and high-speed calorimetry.

### 7.5.6 Discussion

The results obtained and reported in this chapter have proven $BaF_2$ as a viable candidate for very high-speed timing applications in, e.g., medical imaging and high energy physics, with a good understanding of the vital parameters responsible for its performance.
Since it was found that the Epic crystal consistently yields better results than its counterpart from Proteus, the following discussion focuses only on the grease measurements made with and the results obtained from the Epic crystal. Table 7.9 makes a comparison between the measured CTR gain and the expected gain in CTR ($CTR_{exptd}$), that is photostatistically expected from the number of fast photons deduced via the prior TCSPC measurements from the total light output. The discrepancy between the measured and expected CTR gain indicates that it is difficult, if not impossible at this time, to correctly estimate the number of fast extracted photons deemed to be mainly contributing to the CTR. There are several reasons for this:

1. The quantum efficiency of the hybrid PMT used in the TCSPC measurements in the very short wavelength range from 170-220 is unknown.

2. As figure 7.14 shows, also the behavior of the best greases at those wavelengths is uncertain. This necessarily leads to an underestimate of the fast photons being absorbed.

3. Also the absolute amount of fast photons seems to be underestimated, roughly by a factor of 2, as stated by Gundacker et al. [5] and Dorenbos. et al. [21], which would also account for a misjudgement on the amount of fast photons.

4. One cannot exclude whether the wavelength-dependence of the refractive index of the greases plays a role in the extraction of the fast photons.

5. The influence of the coupling agents in direct contact with the unprotected sensitive surface of the SiPM, specifically on the anti-reflective coating, are also unknown.

Given these uncertainties, table 7.9 cannot give a conclusive picture between the predicted CTR improvements and the corresponding CTR results from the measurements. One can see that, in case of Rhodorsil, there is no measured gain in CTR. On the other hand, in the case of Viscasil, the measured gain in CTR even exceeds the corresponding predicted gain. The results for glycerine are inconclusive due to another effect, attributed to the non-polar properties of glycerine suspected to increase the dark noise of the SiPM, especially of the Hamamatsu type.

#### Short summary

As to the usefulness of the various coupling compounds, Rhodorsil as coupling agent for $BaF_2$ should be ruled out from the outset due to its large absorption in the wavelength region of interest. This is clearly confirmed by the CTR measurements. The only remaining viable candidates applicable with $BaF_2$ are then Dow Corning, Viscasil and glycerine. Unlike Rhodorsil, all three of them show nearly 100% constant transmission all the way down to ∼220 nm, from when on Viscasil and Dow Corning begin to roll off, though slightly faster than glycerine. From the point of view of transmission, glycerine ought to be the best coupling agent in this game. All three of them, despite their common promising transmission characteristics, still show a different behavior when it comes to the CTR.

Table 7.9: Comparison of the measured CTR in terms of crystal used, SiPM used and coupling grease used, with the respective CTRs derived from the light output of the fast emission. All CTR figures are given in terms of gain relative to air-coupling. Note that no measurement of Epic and Viscasil was made with FBK because the SiPM was damaged.

| | $LO_{extr}$ [kph/MeV ] | $LO_{extr}$ Fast [kph/MeV ] | gain $CTR_{Exptd}$ | gain CTR HPK (@60 V) | gain CTR HPK (@61 V) | gain CTR FBK (@42 V) |
|---|---|---|---|---|---|---|
| Air | 2.9 | 0.18 | | | | |
| Rhodorsil | 4.3 | 0.21 | 1.08 | 0.9 | - | - |
| Viscasil | 4.5 | 0.26 | 1.21 | 1.24 | 1.25 | - |
| Dow Corning | 5.1 | 0.28 | 1.27 | 1.07 | 1.04 | - |
| glycerine | 5.1 | 0.28 | 1.28 | 1.13 | 1.05* | 1.12 |

* measured at 60.8 V bias voltage

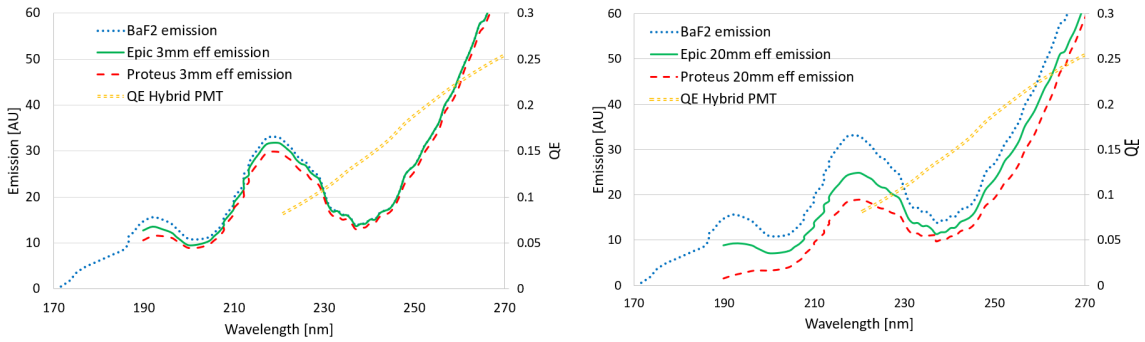


Figure 7.20: $BaF_2$ emission spectra [21] for Epic and Proteus in the low-wavelength region, taking into account the measured absorption spectra for two different photon path lengths (left for 3 mm, right for 20 mm). The right hand ordinate shows on its own scale the QE of the used hybrid-PMT indicating the zone where the Epic crystal pays the highest penalty for the poor QE.

It is interesting to note that in combination with the HPK SiPM and the Proteus crystal, the three compounds would not show any difference in CTR capability. This might indicate that the HPK-Proteus ensemble is not sensitive to the greases' subtle differences in transmission. Only when using the Epic crystal, it was possible to differentiate between the three different grease candidates:

1. Viscasil, when used with the HPK SiPM, showed improvement only with the Epic crystal (none with the Proteus crystal).

2. Glycerine, on the other hand, was beneficial with both Proteus and Epic when coupled to the FBK SiPM leading in general to the best CTR of order 50 ps FWHM.

3. Notwithstanding its excellent transmission characteristics, glycerine was found to give rise to an unforeseen increase in dark current with the HPK SiPM only, which rapidly degraded the CTR. This phenomenon could possibly be linked to its chemical characteristic. It is conjectured that, because of the bipolar nature of this polyol, polarization effects might occur on the surface of this SiPM.

4. As to the viability of Dow Corning and its inferior behavior compared to the others, no conclusive explanation can be given at this time unless its index of refraction, unknown in this wavelength range, is responsible for eventual reflective losses.

.

## 7.6 Conclusion and Prospects

Cross-luminescence is a very fast scintillation process and therefore very interesting for fast timing applications. Apart from the slow self-trapped exciton emission and the fast cross-luminescence emission, a second very fast decay component with $\tau_d \sim 100\ ps$ was observed in $BaF_2$ and with a very low abundance. This emission takes place predominantly below 240 nm, in a regime where the used hybrid PMT and other photodetectors in general suffer from very low detection efficiency. This will lead to a gross underestimation of the fast emissions' abundance. Further understanding of this new emission could give a handle to even further exploit $BaF_2$ in the future.
From standard light output measurements it is concluded that all the coupling greases tested, including Rhodorsil, brought an improvement in light output. However, in terms of highest CTR achievement the global light yield is not the one that is responsible for high time resolution but rather the fast emission component around 220 nm. The focus was therefore laid on the fast component in the test series with the different coupling greases to search for a possible improvement in CTR. From the TCSPC measurements we were able to fit a triple exponential decay function in order to derive the abundances of the fast decay, the very fast and the slow decay components. To overcome statistical limitations in the test series with the greases, only a double exponential fit was applied to estimate the potential gain in CTR from the use of the optical coupling greases. In the end, these results turned out to be inconclusive to make a reliable comparison between the expected CTR improvement and the one that was measured.

Table 7.10: Summary of the CTR performance (FWHM) of the different SiPM-crystal configurations using air coupling and the best greases found in our tests.

| | **Proteus** CTR (ps) | **Epic** CTR (ps) |
|---|---|---|
| **HPK** | | |
| Air | 94±4 | 98±5 |
| Viscasil | 87±4 | 78±4 |
| **FBK** | | |
| air | 64±7 | 54±6 |
| glycerine | 58±6 | 51±6 |

The CTR measurements show that the Epic crystal consistently yields better results than the Proteus crystal and that the FBK SiPM consistently works better than the Hamamatsu SiPM. The advantage of the Epic crystal over the Proteus is that it is more transparent to the fast emission of $BaF_2$, as this is the wavelength region of interest for the timing measurements in this work. As explained in detail in section 7.4.4, the differences in timing behavior between the FBK and Hamamatsu SiPM are fully explained by both their specific PDEs (22% for FBK against 15% for FBK [11][12]) and their particular SPTRs (order 90 ps FWHM for FBK against order 140 ps FWHM for HPK [27]). Table 7.10 summarizes the best CTR results from the different SiPM-crystal pairs using air-coupling and a selection of the best greases found in our tests.
In conclusion, this work has demonstrated that by exploiting the fast (and very fast) emission component(s) of $BaF_2$ and using state-of-the-art SiPMs and highly transmissive coupling compounds, a coincidence time resolution of 51±5 ps FWHM can be achieved. The timing capability of this crystal in this wavelength regime exceeds that of the currently fastest lutetium-based crystal, i.e. LSO:Ce:0.4%Ca, that benefits from a higher light yield in a non-UV wavelength regime, and is the current "reference" in high resolution timing with a CTR of 58±3 ps [50]. What makes $BaF_2$ even more competitive in this context, is the fact that the photodetectors coupled to it run at a PDE of only 22% compared to 65% for photodetectors reading out lutetium crystals. Therefore, it is reasonable to expect that, in view of the rapid progress in the development of fast photodetectors and driven by the large experiments with liquid xenon and liquid argon, new SiPMs with higher PDE in the deep ultra-violet may appear on the market, thus enabling them to truly exploit the full potential of $BaF_2$ and to provide coincidence time resolutions towards 30 ps FWHM.

### 7.6.1 Feasibility of photonic crystal slabs applied to $BaF_2$

In spite of their improvement on light extraction, optical greases do not always have the desired effect on the CTR as one would expect from the increased light extraction. As discussed in chapter 4 an alternative approach geared to increase light extraction is the application of photonic crystal slabs on the $BaF_2$ readout surface.
Although $BaF_2$, owing to its lower refractive index (RI) compared to LYSO, extracts a

larger fraction of its light to begin with than the latter, a properly designed and produced photonic crystal layer on the $BaF_2$ crystal would still be able to significantly improve the light extraction from the $BaF_2$ crystal. As such, the pattern would be specifically tailored to the extraction of the fast emission at short wavelengths. In other words, given the much shorter wavelength of deep UV light, the dimensions of the photonic pattern must be adapted to the smaller wavelength of this light as compared to LYSO with its emission at 420 nm, see chapter 4. Current patterning techniques are already well prepared for the application of structures of the order of 200-300 nm. However, on the other hand, highly refractive index materials suitable for nano-patterning and transparent in the deep UV are not available yet, an important prerequisite for the photonic crystals to function properly. In view of the side effects introduced by the greases, the photonic crystal lends itself as an attractive alternative to interface the scintillator with the photodetector as it couples via air. In that way one avoids the detrimental effects observed with greases, such as e.g. an increased dark current provoked by glycerine on Hamamatsu-type photodetectors and also reduces the potential of damage from physical contact with the photodetector surface.

### 7.6.2 Perspectives for using $BaF_2$ in time-of-flight PET

Although the promising timing potential of $BaF_2$ was discovered as early as 40 years ago, the interest for using it in time-of-flight (TOF) PET gradually diminished in view of its low photofraction and unfavorably long absorption length. However, given the recent encouraging results with respect to its fast timing and low production cost, the use of $BaF_2$ in PET, and other high-speed applications, should be reconsidered albeit its lower photo-sensitivity. One way to overcome this deficiency is to apply $BaF_2$ in a phoswich arrangement. As such, $BaF_2$ on one hand, with its very fast scintillation and high time resolution, could be combined with a highly sensitive crystal with short absorption length yet lower time resolution on the other hand, to build a highly sensitive *and* fast scintillation detector. In such an arrangement, the gamma entering the sandwich will either deposit its entire energy in one of the crystals or interact via Compton scattering in the first ($BaF_2$) crystal, with the rest of the energy deposited in the second (heavier) crystal. In the latter case, the recorded events can still be used for image reconstruction under the condition that the combined energy satisfies the 511 keV energy constraint. In all cases, the $BaF_2$ signal delivers the time stamp. Possible phoswich candidates for $BaF_2$ are first of all L(Y)SO crystals, currently and commonly used in modern PET scanners, or BGO used in an earlier generation of PET scanners because of its excellent stopping power and low production cost. Recently, BGO has regained in attractiveness as it emits prompt Cherenkov photons, another appealing handle to achieve highest time resolution [27] [51]. All things considered, including aspects of cost, one could imagine a TOF-PET scanner built out of a hybrid $BaF_2$-BGO scintillator, which could easily match if not exceed the current L(Y)SO scanners.
Phoswich arrangements are not a novelty in PET or imaging in general and have been applied already in ClearPET [52]. In any case, when using $BaF_2$ with another heavier scintillator, it ought to be placed such that the gammas always enter from the $BaF_2$ side. As to the readout of the hybrid scintillator, it should be noted that, since BGO is not transparent to the deep UV emission of the $BaF_2$, a single-sided readout at the back-side of the hybrid scintillator is not an option. With that constraint in mind, one could envisage the following 4 readout scenarios, with their respective pros and cons:

1. ***Single-sided front face readout:*** In this arrangement the SiPM is mounted onto the front face of the ensemble, and hence both the light from the BGO

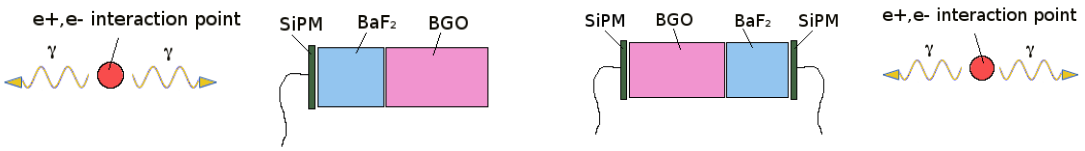


(a) (b)

Figure 7.21: Pixel made of 2 types of scintillator, one part $BaF_2$ and another part BGO, in phoswhich arrangement. (a) Readout on one side, with a VUV sensitive SiPM. Also the BGO light is detected with this SiPM. (b) Double sided readout on both pixel sides.

and $BaF_2$ are read out in a single-sided fashion, as shown in figure 7.21 (a). The advantage of this arrangement is a simple detector-crystal mount, but it would suffer from partial light losses at the $BaF_2$-BGO interface. Since the light produced in the BGO crystal, traversing the $BaF_2$ crystal, is captured by a VUV-sensitive SiPM attached to the $BaF_2$ crystal, part of the BGO light is therefore lost.

2. ***Double-sided (back-to-back) readout:*** Another readout scenario where each crystal is read out from its front/back face, is shown in figure 7.21 (b). This arrangement allows to have each crystal type being read out by its properly adapted SiPM, i.e. a VUV-sensitive photodetector on the $BaF_2$ side and a NUV-sensitive one on the BGO side. To further improve the light output, one could apply a reflective layer between the two crystals at their interface, the advantage of it being a reduction of light losses at the interface and hence an improvement in time resolution. On the other hand, this readout principle doubles the number of photodetectors and readout channels, hence increasing cost and complexity. A variant of this readout principle would be a double ring-arrangement, with two physically separated detector rings (the inner one made of $BaF_2$ and the outer one of BGO), with the same number of photodetector channels as before, yet with the photodetectors always mounted on the back side of the scintillators.

3. ***Side-readout:*** The side-readout, as shown in figure 7.22 (a), has the advantage of reducing time jitter due to a shorter light travel path and thus faster light extraction from the scintillator. To do that, one of the four side faces of the scintillator sandwich is fully covered with SiPMs, if necessary with more than two depending on the length of the sandwich, and with the other faces wrapped with a reflector. This would be the optimal scenario for best timing performance [53]. On the other though, this geometry has the disadvantage of increasing dead space between scintillators and increasing the number of photodetectors and readout channels.

4. ***Shashlik side-readout:*** A shashlik-type $BaF_2$-BGO hybrid crystal in the form of a so-called sampling metacrystal or metapixel as shown in the work of Turtos et al. [54] is made of thin layers, order $100\mu m$, of $BaF_2$ interchanged with similar layers of BGO. It was demonstrated [54] that not only "standard 511 keV events", i.e. those that have entirely converted in the heavier scintillator, but also "shared 511 keV events" resulting from energy deposition in

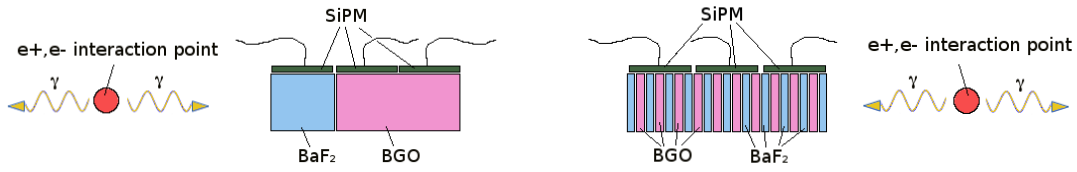


(a) (b)

Figure 7.22: Pixel made of 2 types of scintillator, one part $BaF_2$ and another part BGO. (a) Scintillators in phoswhich arrangement, with side readout. (b) Metapixel made of alternating $BaF_2$ and BGO layers, also with side readout.

both crystal materials, yield superior time resolution. This "combined" timing capacity is systematically better than that of the standard timing offered by the heavy scintillator alone [54]. In line with our previous arguments on complexity and cost, this method is clearly the most time- and cost intensive option.

It is without question that $BaF_2$ has become very attractive again for very fast timing applications, in particular for time-of-flight PET. To compensate for its insufficient conversion power, we have proposed four scenarios where the crystal could be combined with a denser "companion", like BGO, and where both would complement each other in performance. In the end, detector systems with such a hybrid scintillator might replace the current state-of-the-art and rather expensive L(Y)SO systems.

## Bibliography

[1] R. Pots, R. Turtos, M. Paganoni, P. Lecoq, E. Auffray, and S. Gundacker, "Investigation of cross-luminescence in $baf_2$ for ultrafast timing applications." Poster presented at SCINT, 29 September-04 October 2019, Sendai.

[2] R. Pots, R. Turtos, P. Lecoq, E. Auffray, and S. Gundacker, "Exploiting cross-luminescence of $baf_2$ for fast timing detectors." Oral presentation at IEEE NSS/MIC, 26 October-2 November 2019, Manchester.

[3] R. Pots, R. Turtos, P. Lecoq, E. Auffray, and S. Gundacker, "Exploiting cross-luminescence of baf2 for fast timing detectors." Oral presentation at the CCC general meeting, 14 November 2019, CERN.

[4] R. H. Pots, E. Auffray, and S. Gundacker, "Exploiting cross-luminescence in baf2 for ultrafast timing applications using deep-ultraviolet sensitive hpk silicon photomultipliers," *Frontiers in Physics*, vol. 8, p. 482, 2020.

[5] S. Gundacker, R. H. Pots, A. Nepomnyashchikh, E. Radzhabov, R. Shendrik, S. Omelkov, M. Kirm, F. Acerbi, M. Capasso, G. Paternoster, A. Mazzi, A. Gola, J. Chen, and E. Auffray, "Vuv-sipms applied to $baf_2$ cross-luminescence detection for high-rate ultrafast timing applications," *Physics in Medicine & Biology*, june 2021.

[6] P. A. Rodnyi, *Physical Processes in Inorganic Scintillators*. CRC Press LLC, 1997. Chapter 3.

[7] P. A. Rodnyi, "Core–valence luminescence in scintillators," *Radiation Measurements*, vol. 38, no. 4, pp. 343 – 352, 2004. Proceedings of the 5th European Conference on Luminescent Detectors and Transformers of Ionizing Radiation (LUMDETR 2003).

[8] M. Laval, M. Moszyński, R. Allemand, E. Cormoreche, P. Guinet, R. Odru, and J. Vacher, "Barium fluoride — inorganic scintillator for subnanosecond timing," *Nuclear Instruments and Methods in Physics Research*, vol. 206, no. 1, pp. 169 – 176, 1983.

[9] J. L. Jansons, V. J. Krumins, Z. A. Rachko, and J. A. Valbis, "Luminescence due to radiative transitions between valence band and upper core band in ionic crystals (crossluminescence)," *physica status solidi (b)*, vol. 144, no. 2, pp. 835–844, 1987.

[10] W. Klamra, T. Lindblad, M. Moszyński, and L. Norlin, "Properties of optical greases for baf2 scintillators," *Nuclear Instruments and Methods in Physics Research Section A: Accelerators, Spectrometers, Detectors and Associated Equipment*, vol. 254, no. 1, pp. 85 – 87, 1987.

[11] A. Jamil, T. Ziegler, P. Hufschmidt, G. Li, L. Lupin-Jimenez, T. Michel, I. Ostrovskiy, F. Retière, J. Schneider, M. Wagenpfeil, A. Alamre, J. B. Albert, *et al.*, "Vuv-sensitive silicon photomultipliers for xenon scintillation light detection in nexo," *IEEE Transactions on Nuclear Science*, vol. 65, pp. 2823–2833, Nov 2018.

[12] G. Gallina, P. Giampa, F. Retière, J. Kroeger, G. Zhang, M. Ward, P. Margetak, G. Li, T. Tsang, L. Doria, *et al.*, "Characterization of the hamamatsu vuv4 mppcs for nexo," *Nuclear Instruments and Methods in Physics Research Section A: Accelerators, Spectrometers, Detectors and Associated Equipment*, vol. 940, p. 371–379, Oct 2019.

[13] C. van Eijk, "Cross-luminescence," *Journal of Luminescence*, vol. 60-61, pp. 936 – 941, 1994.

[14] T. Ikeda, H. Kobayashi, Y. Ohmura, H. Nakamatsu, and T. Mukoyama, "Electronic structure of alkaline-earth fluorides studied by model clusters. ii. auger-free luminescence," *Journal of the Physical Society of Japan*, vol. 66, no. 4, pp. 1079–1087, 1997.

[15] P. Lecoq, A. Gektin, and M. Korzhik, *Addressing the increased demand for fast timing*, pp. 103–124. Particle Acceleration and Detection, 2017.

[16] Y. A. Valbis, Z. A. Rachko, and Y. L. Yansons, "Short-wave UV luminescence of $BaF_2$ crystals caused by crossover transitions," *Soviet Journal of Experimental and Theoretical Physics Letters*, vol. 42, p. 172, Aug 1985.

[17] M. Itoh, S. Hashimoto, S. Sakuragi, and S. Kubota, "Auger-free luminescence due to interatomic transitions of valence electrons into core holes in baf2," *Solid State Communications*, vol. 65, no. 6, pp. 523 – 526, 1988.

[18] M. R. Farukhi and C. F. Swinehart, "Barium fluoride as a gamma ray and charged particle detector," *IEEE Transactions on Nuclear Science*, vol. 18, pp. 200–204, Feb 1971.

[19] N. N. Ershov, N. G. Zakharov, and P. A. Rodnyi, "Spectral-kinetic study of the intrinsic-luminescence characteristics of a fluorite-type crystal," *Optics and Spectroscopy*, vol. 53, pp. 51–54, Jul 1982.

[20] J. Andriessen, P. Dorenbos, and C. V. Eijk, "Electronic structure and transition probabilities in pure and ce3+ doped baf2, an explorative study," *Molecular Physics*, vol. 74, no. 3, pp. 535–546, 1991.

[21] P. Dorenbos, J. de Haas, R. Visser, C. W. V. Eijk, and R. Hollander, "Absolute light yield measurements on baf/sub 2/ crystals and the quantum efficiency of several photomultiplier tubes," *IEEE Transaction on Nuclear Science*, vol. 40, no. 4, pp. 424–430, 1992.

[22] R. Novotny, R. Riess, R. Hingmann, H. Ströher, R. Fischer, G. Koch, W. Kühn, V. Metag, R. Mühlhans, U. Kneissl, W. Wilke, B. Haas, J. Vivien, R. Beck, B. Schoch, and Y. Schutz, "Detection of hard photons with baf2 scintillators," *Nuclear Instruments and Methods in Physics Research Section A: Accelerators, Spectrometers, Detectors and Associated Equipment*, vol. 262, no. 2, pp. 340 – 346, 1987.

[23] R.-y. Zhu, *A Barium Fluoride Crystal Calorimeter for the SSC*, pp. 437–455. Boston, MA: Springer US, 1991.

[24] M. Kirm, A. Lushchik, C. Lushchik, A. Nepomnyashikh, and F. Savikhin, "Dependence of the efficiency of various emissions on excitation density in baf2 crystals," *Radiation Measurements*, vol. 33, no. 5, pp. 515 – 519, 2001. Proceedings of the International Symposium on Luminescent Detectors and Transformers of Ionizing Radiation.

[25] S. Omelkov, V. Nagirnyi, A. Vasilev, and M. Kirm, "New features of hot intraband luminescence for fast timing," *Journal of Luminescence*, vol. 176, pp. 309 – 317, 2016.

[26] P. Lecoq, A. Gektin, and M. Korzhik, *Scintillation and Inorganic Scintillators*, pp. 1–42. Particle Acceleration and Detection, 2017.

[27] S. Gundacker, R. M. Turtos, N. Kratochwil, R. H. Pots, M. Paganoni, P. Lecoq, and E. Auffray, "Experimental time resolution limits of modern SiPMs and TOF-PET detectors exploring different scintillators and cherenkov emission," *Physics in Medicine & Biology*, dec 2019.

[28] S. Derenzo, "The quest for new radiation detector materials," March 2008.

[29] H. H. Li, "Refractive index of alkaline earth halides and its wavelength and temperature derivatives," *Journal of Physical and Chemical Reference Data*, vol. 9, no. 1, pp. 161–290, 1980.

[30] R.-Y. Zhu, "The next generation of crystal detectors," *Journal of Physics: Conference Series*, vol. 587, p. 012055, feb 2015.

[31] N. Sarukura, T. Nawata, H. Ishibashi, M. Ishii, and T. Fukuda, "4 - czochralski growth of oxides and fluorides," in *Handbook of Crystal Growth (Second Edition)* (P. Rudolph, ed.), Handbook of Crystal Growth, pp. 131 – 168, Boston: Elsevier, second edition ed., 2015.

[32] Z. Bell, *Handbook of particle detection and Imaging, Chapter 15: Scintillation Counters*. Springer-Verlag Berlin Heidelberg, 2012.

[33] R.Gariod, R. Allemand, E. Carmoreche, M. Laval, and M. Moszynski, "The leti posistron tomograph architecture and time of flight improvements," *Proceeding of*

*the Workshop on Time-of-Flight tomography, Washington University, St. Louis, Mo*, pp. 25–29, May 1982.

[34] K. Ishii, H. Orihara, T. Matsuzawa, D. M. Binkley, and R. Nutt, "High resolution time-of-flight positron emission tomograph," *Review of Scientific Instruments*, vol. 61, no. 12, pp. 3755–3762, 1990.

[35] T. K. Lewellen, A. N. Bice, R. L. Harrison, M. D. Pencke, and J. M. Link, "Performance measurements of the sp3000/uw time-of-flight positron emission tomograph," *IEEE Transactions on Nuclear Science*, vol. 35, pp. 665–669, Feb 1988.

[36] P. Bruyndonckx, X. Liu, S. Tavernier, and S. Zhang, "Performance study of a 3d small animal pet scanner based on baf2 crystals and a photo sensitive wire chamber," *Nuclear Instruments and Methods in Physics Research Section A: Accelerators, Spectrometers, Detectors and Associated Equipment*, vol. 392, no. 1, pp. 407 – 413, 1997. Position-Sensitive Detectors Conference 1996.

[37] M. M. Ter-Pogossian, D. C. Ficke, M. Yamamoto, and J. T. Hood, "Super pett i: A positron emission tomograph utilizing photon time-of-flight information," *IEEE Transactions on Medical Imaging*, vol. 1, pp. 179–187, Nov 1982.

[38] W. Wong, N. Mullani, E. Philippe, R. Hartz, D. Bristow, K. Yerian, J. Gaeta, and N. Ketharnavaz, "Performance characteristics of the university of texas tofpet-i pet camera," *J. Nucl. Med.; (United States)*, vol. 25:5, 1 1986.

[39] R. Novotny, "The baf/sub 2/ photon spectrometer taps," *IEEE Transactions on Nuclear Science*, vol. 38, pp. 379–385, April 1991.

[40] R. Novotny, "The baf2 spectrometer taps: A system for high energy photon and neutral meson detection," *Nuclear Tracks and Radiation Measurements*, vol. 21, no. 1, pp. 23 – 26, 1993.

[41] S. Diehl, R. W. Novotny, B. Wohlfahrt, and R. Beck, "Readout concepts for the suppression of the slow component of BaF2for the upgrade of the TAPS spectrometer at ELSA," *Journal of Physics: Conference Series*, vol. 587, p. 012044, feb 2015.

[42] "Homepage epic crystals." `http://www.epic-crystal.com/`, Accessed: 13-07-2020.

[43] "Homepage proteus crystals." `https://proteus-pp.com/`, Accessed: 13-07-2020.

[44] "Hpk s13370-cn." `https://www.hamamatsu.com/jp/en/product/optical-sensors/mppc/mppc_mppc-array/index.html`. accessed: 28/01/2019.

[45] A. Gola, F. Acerbi, M. Capasso, M. Marcante, A. Mazzi, G. Paternoster, C. Piemonte, V. Regazzoni, and N. Zorzi, "Nuv-sensitive silicon photomultiplier technologies developed at fondazione bruno kessler," *Sensors*, vol. 19, p. 308, Jan 2019.

[46] S. E. Derenzo, M. J. Weber, W. W. Moses, and C. Dujardin, "Measurements of the intrinsic rise times of common inorganic scintillators," *IEEE Transactions on Nuclear Science*, vol. 47, no. 3, pp. 860–864, 2000.

[47] S. Gundacker, E. Auffray, K. Pauwels, and P. Lecoq, "Measurement of intrinsic rise times for various l(y)so and luag scintillators with a general study of prompt photons to achieve 10 ps in tof-pet," *Physics in medicine and biology*, vol. 61, p. 2802—2837, April 2016.

[48] S. Gundacker and A. Heering, "The silicon-photomultiplier: fundamentals and applications of a modern solid-state photon detector," *Physics in Medicine & Biology*, 2020.

[49] R. yuan Zhu, "On quality requirements to the barium fluoride crystals," *Nuclear Instruments and Methods in Physics Research Section A: Accelerators, Spectrometers, Detectors and Associated Equipment*, vol. 340, no. 3, pp. 442 – 457, 1994.

[50] S. Gundacker, R. M. Turtos, E. Auffray, M. Paganoni, and P. Lecoq, "High-frequency SiPM readout advances measured coincidence time resolution limits in TOF-PET," *Physics in Medicine & Biology*, vol. 64, p. 055012, feb 2019.

[51] N. Kratochwil, S. Gundacker, P. Lecoq, and E. Auffray, "Pushing cherenkov PET with BGO via coincidence time resolution classification and correction," *Physics in Medicine & Biology*, vol. 65, p. 115004, jun 2020.

[52] K. Ziemons, R. Achten, E. Auffray, A. Bauer, G. Brandenburg, P. Bruyndonckx, Y. Choi, J. Daemen, M. Dehnhardt, O. Devroede, M. Fleischer, L. Fuss, U. Heinrichs, A. Hollendung, M. Holschbach, M. Khodaverdi, P. Kirchner, H. Kleines, M. Krieguer, H. Larue, P. Lecoq, M. Leyendecker, R. Moeller, C. Morel, J. . Mosset, C. Parl, U. Pietrzyk, J. Schmitz, M. Streun, S. Tavernier, M. Veggian, E. Zimmermann, H. H. Coenen, H. Halling, R. Sievering, and K. Zilles, "The clearpet/spl trade/ neuro scanner: a dedicated lso/luyap phoswich small animal pet scanner," in *IEEE Symposium Conference Record Nuclear Science 2004.*, vol. 4, pp. 2430–2433 Vol. 4, 2004.

[53] M. S. Lee, J. W. Cates, M. Kapusta, M. Schmand, and C. S. Levin, "Study of lutetium-based scintillators for pet system design with 100-ps coincidence time resolution," in *2019 IEEE Nuclear Science Symposium and Medical Imaging Conference (NSS/MIC)*, pp. 1–2, 2019.

[54] R. M. Turtos, S. Gundacker, E. Auffray, and P. Lecoq, "Towards a metamaterial approach for fast timing in PET: experimental proof-of-concept," *Physics in Medicine & Biology*, vol. 64, p. 185018, sep 2019.

# Chapter 8

# Conclusions and Prospects

This thesis has shown an investigation on improving several aspects of a scintillation-based detector. Photonic crystals have been investigated as a novel technology to improve light transport from the scintillator to the photodetector in order to enhance light output and ultimately time resolution. $BaF_2$, with its intrinsically fast cross-luminescence, has been investigated for its potential of pushing the timing limits beyond the current state-of-the-art time resolution in lutetium-based scintillators, even with non-standard calcium co-doping. For this cause, also state-of-the-art UV-sensitive photodetectors and several UV-transparent optical coupling greases were explored. This chapter gives an overview of the conclusions to be drawn from the ensemble of this work and an outlook of their impact on domains such as TOF-PET and high luminosity-high energy physics.

## 8.1 Photonic crystals

As to photonic crystals, this work has shown that it is possible to produce photonic crystal slabs on the readout surface of large monolithic LYSO crystals and smaller 10 mm LYSO cubes. In total, three different lithography methods were developed for the succesfull production of these photonic crystal slabs:

1. Nano-imprint lithography, for the production of $TiO_2$ pillars in a square lattice with RI=2.4;

2. Sol-gel lithography, for the production of $TiO_2$ cones in a hexagonal lattice with RI=2.1 and

3. UV-cured nano-imprint lithography, for the production of polymer cones in a square lattice with RI=1.82.

### 8.1.1 Influence on light output

In the case where *no* reflective wrapping and *no* optical coupling are used, the photonic crystal slabs fabricated with these methods improved the light output of large trapezoidal monolithic LYSO crystals by $\lesssim$20%. For smaller LYSO cubes the improvement could reach 50-70%. It is interesting to note that even a readout from the crystal face opposite to the patterned face leads to a similar increase in light output, a phenomenon that is well understood from the simulations.

### 8.1.2 Influence on energy resolution

It was observed that for photonic crystals with a cone-like structure the measured gain in energy resolution was consistently higher than what one would expect from photostatistics alone. The discrepancy and origin of this effect are not understood at this time. If, on the other hand, the photonic structure is made of pillars the opposite effect is observed. This, however, is attributed to inhomogeneities across the structured surface caused by charging effects during the reactive ion etching as part of the production process.

### 8.1.3 Influence on coincidence time resolution

When it comes to coincidence time resolution, one could achieve with photonic crystals on LYSO cubes an improvement in CTR by 20-50%, where the 50% corresponds to a nano-pattern produced via UV-cured nano-imprint lithography. In line with an increase in light output observed on the opposite crystal face, coincidence time resolution also an improvement on that side.

### 8.1.4 Influence of wrapping and optical coupling

In this test, the LYSO cubes treated with UV-cured nano-imprint lithography were checked for their timing behavior when wrapped with Teflon and/or coupling them with optical grease. In the case of Teflon wrapping and air-coupling (no grease), the CTR was found to be enhanced by 20% over the same untreated crystal. This improvement, however, disappeared when both Teflon wrapping and glycerine as coupling grease were used in the test. This brings us to the conclusion that apparently no benefit can be gained from using wrapping and grease coupling with photonic crystals. It should be noted that in case of untreated scintillators, the effects of both wrapping and optical coupling are very dramatic. This then leads to the question whether further improvements in light transfer efficiency, particularly to the benefit of higher coincidence time resolution, can be made, if photonic crystals were specifically tailored to grease coupling. There are, however, applications prohibiting grease coupling when detectors operated in vacuum and/or high temperature. All things considered, at this time, photonic crystals only deliver positive results, i.e. in terms of light extraction and coincidence time resolution, if they are solely used in conjunction with air-coupling to the photodetector.

### 8.1.5 Photonic crystals at the system level

The TurboPET project served as a test bench for 10 large monolithic LYSO scintillators treated with a photonic layer produced via sol-gel lithography. Also this scenario showed a marginal improvement in light output and energy resolution by only 10-20% and 20-30%, respectively. With these figures one could only achieve a gain of 6% in signal-to-noise ratio when imaging a Nema phantom in the TurboPET ring.

## 8.2 $BaF_2$

Unlike the previous work that had concentrated on light extraction improvements from standard scintillators, the experiments with $BaF_2$ focused on exploiting the intrinsically fast and very fast light decay components in its emission spectrum. The results from measurements with $BaF_2$ crystals from two different producers, Epic and Proteus, read out by state-of-the-art photodetectors are truly encouraging.

Furthermore, in this work with $BaF_2$ we also investigated the so-called standard methods of increasing light output and improving coincidence time resolution by using Teflon wrapping and four different coupling agents, i.e. Rhodorsil, Viscasil, Dow Corning and glycerine with $BaF_2$ crystals. In the long run, only Viscasil and glycerine emerged as viable coupling agents that could significantly improve coincidence time resolution, which was taken as one of the figures of merit to judge the capabilities of the various agents.
Among the two tested $BaF_2$ candidates, Epic and Proteus, the Epic crystal delivered consistently better results owing to its higher transparency at the cross-luminescence wavelengths.
It is common practice to compare the results achieved with $BaF_2$ in this thesis with those obtained and published in earlier works, being considered the current bench marks in this domain of research. In all cases, comparisons were made with 3 mm long crystals so as to rely only on the intrinsic material properties. Comparing $BaF_2$ with LYSO:Ce mounted to commercially available photodetectors, one comes to the following result:

- $BaF_2$: CTR=78±4 ps FWHM with Hamamatsu S13370-3050 SiPM and Viscasil as optical coupling agent;

- LYSO:Ce: CTR=86±2 ps FWHM [1] with Hamamatsu S13360-3050 SiPM and Meltmount as optical coupling agent.

To further improve the above values one would have to resort to non-commercial scintillator- and photodetector prototypes developed only dedicated research objects. The current state-of-the-art scintillator in terms of time resolution is the LSO:Ce:0.4%Ca crystal and a prototype SiPM produced by Fundazione Bruno Kessler (FBK). On the $BaF_2$ side, FBK also produced a prototype research SiPM sensitive to deep UV light and with a comparatively high PDE of 22%. With these state-of-the-art components, one gets:

- $BaF_2$: CTR=51±6 ps FWHM with FBK VUV-HD SiPM and glycerine as optical coupling agent;

- LSO:Ce0.4%Ca: CTR=58±3 ps FWHM [2] with FBK NUV-HD SiPM and Meltmount as optical coupling agent.

Knowing that the FBK VUV-HD SiPM suffers from a PDE three times lower than that of the NUV FBK device used in conjunction with the lutetium-based crystal, leaves room for further developments in this sector of photodetectors, also in terms of single photon time resolution. With these future improvements in mind, the potential of $BaF_2$ could be fully exploited to the extent that coincidence time resolutions of $<$30 ps FWHM could be eventually reached. To break even through that barrier, innovative research is needed in the domain of crystal growth so as to produce scintillators with yet higher transparency in the 200 nm wavelength regime. There is also room for further dedicated developments of reflectors optimized for that wavelength.
In applications like medical imaging, in particular TOF-PET, the above results are of imminent interest when the very high speed of $BaF_2$, notwithstanding its lower density, is explored to its full potential when combined with a heavier scintillator such as BGO. Such a hybrid scintillator could lead to a very fast and yet highly sensitive detector of low cost to enter the frontier of sub-100 ps TOF-PET. In future high energy physics experiments, where high luminosity plays an increasing role for the detection of rare events, fast scintillators such as $BaF_2$, and perhaps also plastic scintillators, could play a dominant role in the tagging of collision vertices and mitigating pile-up effects in e.g. calorimetry.

# Bibliography

[1] Stefan Gundacker and Arjan Heering. The silicon-photomultiplier: fundamentals and applications of a modern solid-state photon detector. *Physics in Medicine & Biology*, 2020.

[2] Stefan Gundacker, Rosana Martinez Turtos, Etiennette Auffray, Marco Paganoni, and Paul Lecoq. High-frequency SiPM readout advances measured coincidence time resolution limits in TOF-PET. *Physics in Medicine & Biology*, 64(5):055012, feb 2019.

# Appendix A

# Illustration of the TCSPC method

Time-correlated single photon counting measurements use a method that allows precise determination of (rise- and) decay times of light pulses produced by, e.g., a scintillator. The method relies on the registration of the arrival times of a large amount of single photons, each from a different scintillation event. At every event, the time delay between a start signal and the detection of a photon from the scintillation pulse, as such measuring its arrival time. By repeating this procedure many times, scintillation pulse is basically sampled one photon at a time. This is illustrated in figure A.1.

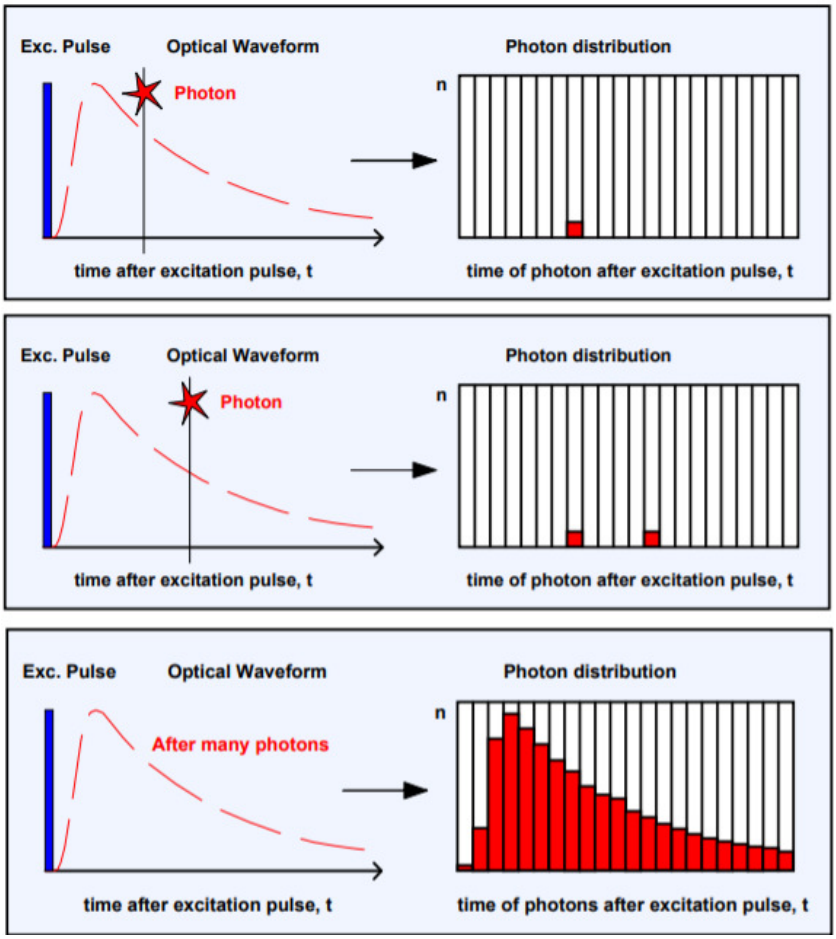


Figure A.1: Illustration of the principle behind TCSPC measurements, the scintillation pulse produced by the scintillator is basically sampled one photon at a time. [1]

# Appendix B

# Relaxation and thermalization of electrons and holes

The ability of scintillating crystals to produce light stems from the band-structure with only certain energy levels being allowed in the crystal. Due to its crystalline structure, the scintillator has a core band, a valence band and a conduction band, each with corresponding sub-bands. Between the conduction- and valence band there is a bandgap with energy $E_g$, the so-called forbidden gap. Recombination of an electron above and a hole below this bandgap can result in the emission of scintillation light. The hot electrons are created in the conduction band, the "holes" that they leave behind are created in the core- and the valence band. The top image of figure B.1 shows the case where rare earths are present. In this case the rare earth introduces an extra set of bands within the bandgap of the crystal, i.e. (usually) a 4f just below the conduction band and the 5d level just above the valence band. The extra set of bands induces two additional effects. The first is that it is possible for the hot electrons in the crystal to not only scatter with electrons, but also with the rare earth atoms, until the energy of the electrons is below the corresponding scattering threshold. Since this threshold generally lays below the electron-electron scattering threshold, the multiplication process in these type of scintillators continues longer and therefore a larger amount of excitations and finally scintillation light *can* be produced. A second effect is that the electrons and holes can thermalize into the band corresponding to the rare earth atoms, which facilitates a fast recombination.
The bottom image of figure B.1 shows the case of cross-luminescence, present in crystals with an energy difference between the top core band and the bottom of the valence band that is less than the forbidden bandgap. In this case, Auger processes in the core band are energetically forbidden for the holes. As such, core holes can relax towards the top of the core band instead and recombine with electrons from the valence band, leading to the emission of scintillation light called cross-luminescence. Since the valence band is full of electrons, holes easily localize near an electron. As such, cross-luminescence is a very fast, sub-nanosecond, scintillation process. One should note that every recombination of a core hole and valence electron leads to a new valence hole. This hole can again take part in the "normal" scintillation process between the conduction- and valence band.

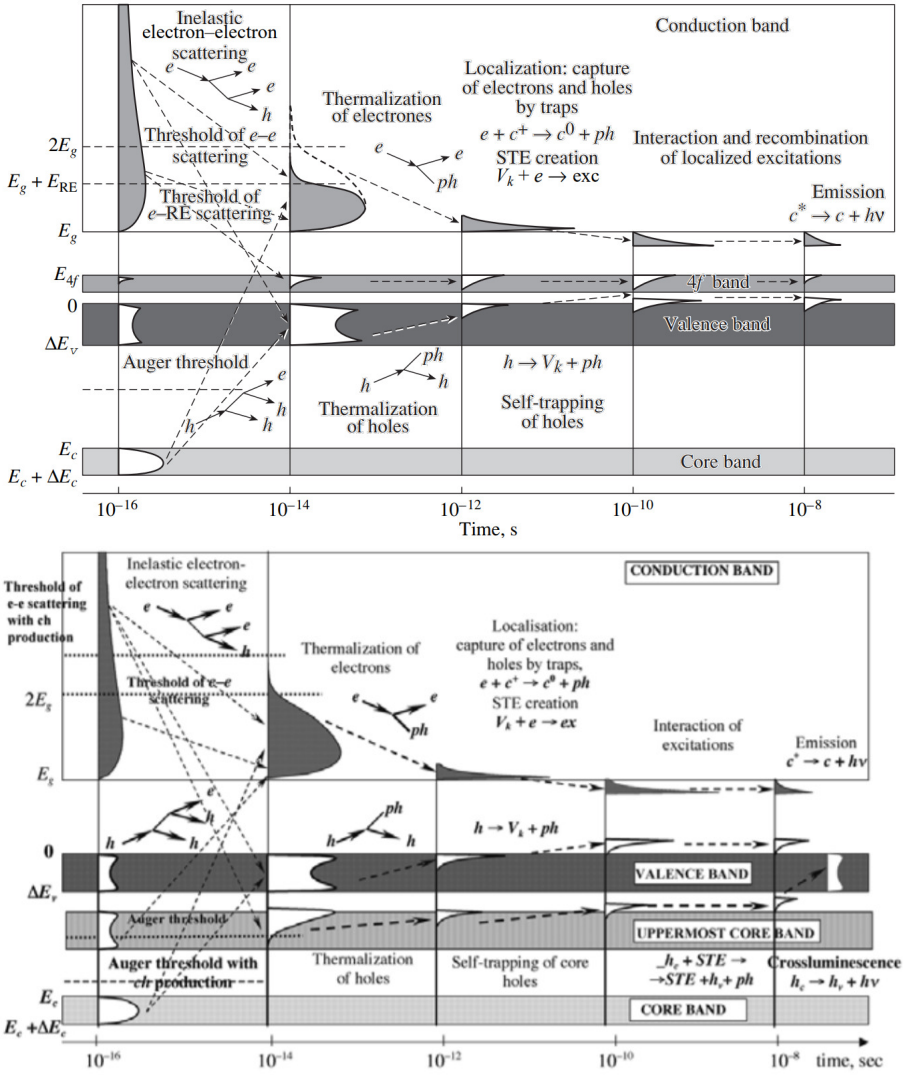


Figure B.1: Schematics of the relaxation and thermalization of electrons and holes in a scintillating crystal in the case where (top) rare earths are present, either in the crystal matrix or due to doping, and where (bottom) the crystal exhibits cross-luminescence. Images taken from [2]

# Appendix C

# Derivation of the Helmholtz Equation

To understand the behavior of light, i.e. electromagnetic waves in photonic crystals one must start with the general description of electromagnetic dynamics. They are described by the Maxwell equations:

$$\nabla \times \mathbf{E} + \frac{\partial \mathbf{B}}{\partial t} = 0 \qquad \text{(C.1)} \qquad\qquad \nabla \cdot \mathbf{B} = 0 \qquad \text{(C.3)}$$

$$\nabla \times \mathbf{H} - \frac{\partial \mathbf{D}}{\partial t} = \mathbf{J} \qquad \text{(C.2)} \qquad\qquad \nabla \cdot \mathbf{D} = \rho \qquad \text{(C.4)}$$

where $\mathbf{E}$ and $\mathbf{D}$ are the electric and the displacement field, respectively, $\mathbf{H}$ and $\mathbf{B}$ the magnetic- and magnetic induction field, $\rho$ the free charge density and $\mathbf{J}$ the free current density. These four equations form the base of electrodynamics and are applicable in almost any situation.
In vacuum $\mathbf{E}$ and $\mathbf{D}$ are equal, however inside a dielectric material the situation changes. The electric field in vacuum $\mathbf{E}$ can partly polarize dielectric materials by the effect it has on the bound and the free charges in the material. The displacement field $\mathbf{D}$ takes this effect into account. Analogously, the magnetic induction field in vacuum $\mathbf{H}$ can magnetize magnetic materials and the magnetic field $\mathbf{B}$ takes this effect into account.
Assuming that the dielectric constant is linear and not dependent on the frequency and that the dielectric material is isotropic, $\mathbf{E}$ and $\mathbf{D}$, and the $\mathbf{H}$ and the $\mathbf{B}$ can then be related in the following way:

$$\mathbf{D}(\mathbf{r}) = \epsilon_0 \epsilon(\mathbf{r}) \mathbf{E}(\mathbf{r}) \qquad \text{(C.5)}$$

$$\mathbf{B}(\mathbf{r}) = \mu_0 \mu(\mathbf{r}) \mathbf{E}(\mathbf{r}) \qquad \text{(C.6)}$$

where $\epsilon_0$ is the dielectric constant, $\epsilon(\mathbf{r})$ the relative dielectric constant of the material, $\mu_0$ the permeability of free space and $\mu(\mathbf{r})$ the relative permeability of the material. Furthermore, $\epsilon_0$ and $\mu_0$ can be related to the speed of light by $c = \frac{1}{\sqrt{\epsilon_0 \mu_0}}$. Assuming then that the considered material not to be magnetic, which is the case for the materials used in this thesis work, $\mu(\mathbf{r}) \approx 1$. Assuming additionally the use of non-conductive material, i.e. no free charges and no free currents, $\rho = \mathbf{J} = 0$. Considering that the fields have a time dependency and a position dependency, and inserting the above assumption in equations C.5 and C.6, equations C.1-C.4 can be rewritten as:

$$\nabla \times \mathbf{E}(\mathbf{r}, t) + \mu_0 \frac{\partial \mathbf{H}(\mathbf{r}, t)}{\partial t} = 0 \qquad \text{(C.7)}$$

$$\nabla \times \mathbf{H}(\mathbf{r},t) - \epsilon_0 \epsilon(\mathbf{r}) \frac{\partial \mathbf{E}(\mathbf{r},t)}{\partial t} = 0 \tag{C.8}$$

$$\nabla \cdot \mathbf{H}(\mathbf{r},t) = 0 \tag{C.9}$$

$$\nabla \cdot [\epsilon(\mathbf{r}) \mathbf{E}(\mathbf{r},t)] = 0 \tag{C.10}$$

$\epsilon(\mathbf{r})$ can be a complex number, the imaginary component then represents the absorption of electromagnetic waves in the material. However, by considering only fully transparent materials, $\epsilon(\mathbf{r})$ is assumed to only have a real component. Also, $\epsilon(\mathbf{r})$ is assumed to be positive (a negative value would be used for e.g. metals). Since $\mu$ is assumed to be unity, the refractive index can be related to the dielectric constant by $n = \sqrt{\epsilon\mu} = \sqrt{\epsilon}$, indicating the refractive index to be real valued and positive.
As the Maxwell equations are linear equations, the fields can be expressed in a form where the time- and spatial dependencies are separated and expressed as harmonic modes:

$$\mathbf{E}(\mathbf{r},t) = \mathbf{E}(\mathbf{r}) e^{-\imath\omega t} \tag{C.11}$$

$$\mathbf{H}(\mathbf{r},t) = \mathbf{H}(\mathbf{r}) e^{-\imath\omega t} \tag{C.12}$$

where $\omega$ is the frequency. These fields are complex fields, of which the real part represents the physical fields. Fourier theory dictates that any function can be built from a sum of harmonic modes. As such imposing the above fields to be harmonic in time does not limit the systems that can be described by these expressions. Inserting these fields into equations C.7-C.10 gives a new set of four relations:

$$\nabla \times \mathbf{E}(\mathbf{r}) - \imath\omega\mu_0 \mathbf{H}(\mathbf{r}) = 0 \tag{C.13}$$

$$\nabla \times \mathbf{H}(\mathbf{r}) + \imath\omega\epsilon_0 \epsilon(\mathbf{r}) \mathbf{E}(\mathbf{r}) = 0 \tag{C.14}$$

$$\nabla \cdot \mathbf{H}(\mathbf{r}) = 0 \tag{C.15}$$

$$\nabla \cdot [\epsilon(\mathbf{r}) \mathbf{E}(\mathbf{r})] = 0 \tag{C.16}$$

Now the objective is to obtain a differential equation containing only $\mathbf{H}(\mathbf{r})$. This can be effectuated by dividing equation C.14 by $\epsilon(\mathbf{r})$:

$$\frac{1}{\epsilon(\mathbf{r})} \nabla \times \mathbf{H}(\mathbf{r}) + \imath\omega\epsilon_0 \mathbf{E}(\mathbf{r}) = 0 \tag{C.17}$$

and subsequently taking the curl:

$$\nabla \times \left( \frac{1}{\epsilon(\mathbf{r})} \nabla \times \mathbf{H}(\mathbf{r}) \right) + \imath\omega\epsilon_0 \nabla \times \mathbf{E}(\mathbf{r}) = 0 \tag{C.18}$$

Then, inserting equation C.13 in the resulting equation C.18, eliminates the electric field from the equation.

$$\nabla \times \left( \frac{1}{\epsilon(\mathbf{r})} \nabla \times \mathbf{H}(\mathbf{r}) \right) + \epsilon_0\mu_0\omega^2 \mathbf{H}(\mathbf{r}) = 0 \tag{C.19}$$

This expression can be rewritten as follows:

$$\nabla \times \left( \frac{1}{\epsilon(\mathbf{r})} \nabla \times \mathbf{H}(\mathbf{r}) \right) = -\left(\frac{\omega}{c}\right)^2 \mathbf{H}(\mathbf{r}) \tag{C.20}$$

A similar expression can be derived for the electric field $\mathbf{E}(\mathbf{r})$, starting from equation C.13 instead of C.14. However, equation C.20 already contains the information about both field $\mathbf{H}(\mathbf{r})$ and $\mathbf{E}(\mathbf{r})$. When a solution for one of the fields is found, the other can be easily derived by inserting the first in the corresponding reformulation of equations C.13 and C.14:

$$\mathbf{E}(\mathbf{r}) = \frac{\imath}{\omega\epsilon_0\epsilon(\mathbf{r})}\nabla \times \mathbf{H}(\mathbf{r}) \tag{C.21}$$

$$\mathbf{H}(\mathbf{r}) = \frac{\imath}{\omega\mu_0}\nabla \times \mathbf{E}(\mathbf{r}) \tag{C.22}$$

Equation C.20 is called the Helmholtz equation and describes the system as an eigenvalue problem to be solved for a given dielectric constant $\epsilon(\mathbf{r})$:

$$\hat{\Theta}\mathbf{H}(\mathbf{r}) = \left(\frac{\omega}{c}\right)^2 \mathbf{H}(\mathbf{r}) \tag{C.23}$$

with $\hat{\Theta}F = \nabla \times \left(\frac{1}{\epsilon(\mathbf{r})}\nabla \times F\right)$, where $F$ is an arbitrary function and $\hat{\Theta}$ a Hermitian operator. The solutions to this eigenvalue problem are the eigenmodes of the system.

# Appendix D

# Calculating the effective refractive index

The effective refractive index of a periodic structure of cones at their base or of pillars depends on their periodicity (p), their diameter (d) (at the base) and the refractive indices of the structures ($n_{phc}$) and their surroundings ($n_{am}$). In order to calculate the effective refractive index, one only needs to consider a surface of $p \times p$. The most comprehensive way to make this calculation is by taking this surface such that it contains exactly *one* cone or pillar. In this way the cone (at its base) or pillar (at any height) has a intersection or surface of $\frac{\pi}{4}d^2$. As the total surface is $p^2$, the surface of the ambient material is $p^2 - \left(\frac{\pi}{4}d^2\right)$. Therefore, the effective refractive index $n_{eff}$ is given by the following expression:

$$n_{eff} = \frac{\left(\frac{\pi}{4}d^2\right) n_{phc} + \left(p^2 - \frac{\pi}{4}d^2\right) n_{am}}{p^2} = \frac{\pi}{4}\frac{d^2}{p^2}\left(n_{phc} - n_{amb}\right) + 1 \tag{D.1}$$

To calculate $n_{phc}$ when a certain $n_{eff}$ is required, equation D.1 can be rewritten into:

$$n_{phc} = \frac{n_{eff} - 1}{\frac{\pi}{4}\frac{d^2}{p^2}} + n_{amb} \tag{D.2}$$

As an example, in the case where one requires an $n_{eff} = 1.8$ and where $d = p$ and $n_{amb} = 1$, the required $n_phc$ is:

$$n_{phc} = \frac{1.8 - 1}{\frac{\pi}{4} \times 1} + 1 = 2.0 \tag{D.3}$$

# Appendix E

# Effect of Fresnel Reflection on Transmission Measurements

When a light beam enters an interface of two materials with different refractive indices, the angle of the transmitted beam changes according to Snell's law. This is shown in figure E.1 (a). The angle $\theta_t$ of the transmitted beam is thus given by [3]:

$$\theta_t = \frac{n_1}{n_2} \arcsin(\theta_i) \tag{E.1}$$

where $n_1$ is the refractive index of the material before the interface, $n_2$ the refractive index of the material after the interface and $\theta_i$ the angle of the incoming beam, as in figure E.1. However, due this interface, not the entire intensity of the beam is transmitted: part of it will be reflected at the interface, as also shown in figure E.1 (a). This reflection is called Fresnel reflection, a classic reflection where the reflection angle $\theta_r$ equals the incoming angle $\theta_i$. Since the refractive index of materials changes with wavelength, also the amount of reflected light depends on the wavelength. It further depends on the impinging angle of the light on the interface and on the transmitted angle. Looking at figure E.1(a), the following can be said about the amount of reflected light $I_r$:

$$I_r = I_i \cdot \mathscr{R}(\lambda, \theta_i) \tag{E.2}$$

where $\mathscr{R}(\lambda, \theta_i)$ is the reflection coëfficient due to Fresnel reflection. As per this equation, the amount of light $I_c$ that is transmitted into the second medium equals:

$$I_c = I_i \cdot [1 - \mathscr{R}(\lambda, \theta_i)] \tag{E.3}$$

However, when the second material is absorbing, equation E.3 changes into:

$$I_c = I_i \cdot [1 - \mathscr{R}(\lambda, \theta_i)] \cdot e^{-\mu \cdot x} \tag{E.4}$$

where $\mu$ is the absorption coëfficient of the second material, blue in the figure, and $x$ the length of the path through that material. Therefore, $e^{-\mu \cdot x}$ is the absorption of the light by the material it travels through.
Figure E.1 (b) illustrates the situation where a finite second material is placed inside another medium, thus introducing two interfaces between the materials with different refractive indices. Since Fresnel reflection does not discriminate between going from the lower refractive index material to the higher refractive index material or going from the higher refractive index material to the lower index material, the reflection at the two interfaces is the same. In the figure, only the first time the light reflects at an interface

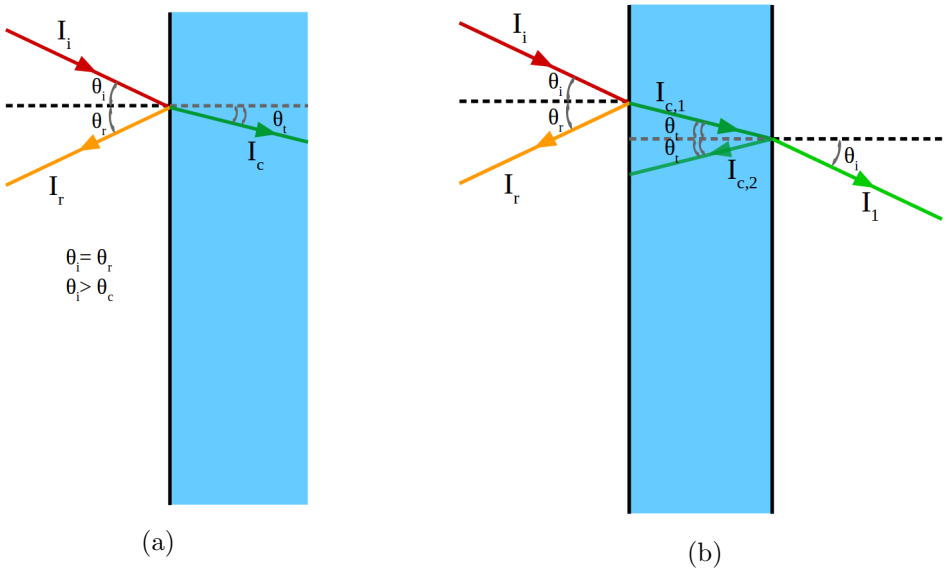


Figure E.1: Reflection and refraction of light on an interface of materials with different indices of refraction. (a) One interface between two materials. (b) A finite material in another material, thus introducing two interfaces. The reflection at the two interfaces is the same, since Fresnel reflection does not discriminate between going from the lower refractive index material to the higher refractive index material, or going from the higher refractive index material to the lower. Here only the first Fresnel reflection on each interface is drawn.

is shown. In the finite material, that is assumed to absorb light, there is a constant absorption when light travels between the two interfaces. For geometrical reasons, this amount depends on the transmitted angle $\theta_t$ of the light as this changes the traveled path of the light. However, since this transmitted angle depends on the given materials and the impinging angle, see equation E.1, one could say that for a given set of interfaces between two materials the Fresnel reflection on every surface depends only on the impinging angle (or only the transmitted angle), the wavelength of light and the refractive indices of the materials. Therefore, equation E.4 changes into:

$$\begin{aligned} I_c &= I_i \cdot [1 - \mathscr{R}(\lambda, \theta_i)] \cdot \mathscr{T}(\theta_t) \\ &= I_i \cdot [1 - \mathscr{R}(\lambda, \theta_i)] \cdot \mathscr{T}(\theta_i) \end{aligned} \tag{E.5}$$

where $\mathscr{T}(\theta_i) = 1 - e^{-\mu \cdot x}$ is the transmission if the light traveling at an angle $\theta_t$ through the medium. The amount of light $I_1$ extracted at the other end of the medium, see figure E.1(b), is the following:

$$\begin{aligned} I_1 &= I_c \cdot [1 - \mathscr{R}(\lambda, \theta_i)] \\ &= I_i \cdot \mathscr{R}(\lambda, \theta_i) \cdot \mathscr{T}(\theta_i) \cdot [1 - \mathscr{R}(\lambda, \theta_i)] \\ &= I_i \cdot [1 - \mathscr{R}(\lambda, \theta_i))]^2 \cdot \mathscr{T}(\theta_i) \end{aligned} \tag{E.6}$$

In reality, there are many reflection in the medium, every time reflecting part of the light and transmitting part of it as shown in figure E.2. As the figure also shows, the total amount of light exiting the medium is the sum of all the partial transmissions:

$$I_t = I_1 + I_2 + I_3 + ... + I_n = \sum_{n=1}^{\infty} I_n \tag{E.7}$$

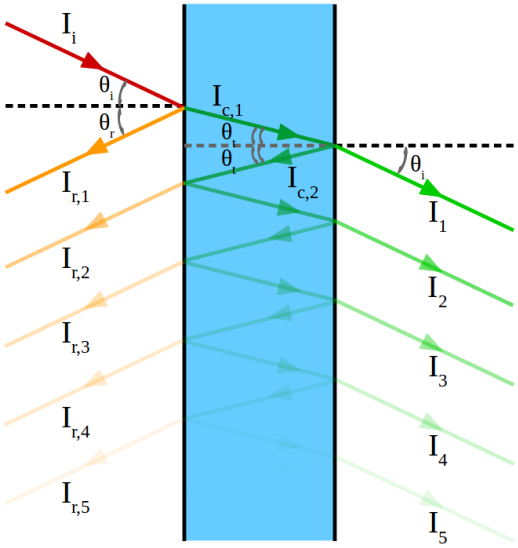


Figure E.2: Reflection and refraction of light traveling from a material with a certain refractive index into a finite material with a different refractive index at an angle $\theta_i$. The reflection at the two interfaces is the same, since Fresnel reflection does not discriminate between going from the lower refractive index material to the higher refractive index material, or going from the higher refractive index material to the lower. The light reflects many times inside the medium, every time a transmitting part of the light is transmitted outside the medium. The medium might also absorb part of the light.

Continuing in the same line of thinking as during the derivation of equations E.4-E.6, the following holds for $I_2$, $I_3$ and $I_n$:

$$\begin{aligned} I_2 &= I_c \cdot \mathscr{R}(\lambda,\theta_i) \cdot \mathscr{T}(\theta_i) \cdot \mathscr{R}(\lambda,\theta_i) \cdot \mathscr{T}(\theta_i) \cdot [1-\mathscr{R}(\lambda,\theta_i)] \\ &= I_c \cdot \mathscr{R}(\lambda,\theta_i)^2 \cdot \mathscr{T}(\theta_i)^2 \cdot [1-\mathscr{R}(\lambda,\theta_i)] \\ &= I_i \cdot [1-\mathscr{R}(\lambda,\theta_i)] \cdot \mathscr{T}(\theta_i) \cdot \mathscr{R}(\lambda,\theta_i)^2 \cdot \mathscr{T}(\theta_i)^2 \cdot [1-\mathscr{R}(\lambda,\theta_i)] \\ &= I_i \cdot [1-\mathscr{R}(\lambda,\theta_i)]^2 \cdot \mathscr{R}(\lambda,\theta_i)^2 \cdot \mathscr{T}(\theta_i)^3 \end{aligned} \tag{E.8}$$

$$\begin{aligned} I_3 &= I_c \cdot \mathscr{R}(\lambda,\theta_i)^4 \cdot \mathscr{T}(\theta_i)^4 \cdot [1-\mathscr{R}(\lambda,\theta_i)] \\ &= I_i \cdot [1-\mathscr{R}(\lambda,\theta_i)] \cdot \mathscr{T}(\theta_i) \cdot \mathscr{R}(\lambda,\theta_i)^4 \cdot \mathscr{T}(\theta_i)^4 \cdot [1-\mathscr{R}(\lambda,\theta_i)] \\ &= I_i \cdot [1-\mathscr{R}(\lambda,\theta_i)]^2 \cdot \mathscr{R}(\lambda,\theta_i)^4 \cdot \mathscr{T}(\theta_i)^5 \end{aligned} \tag{E.9}$$

$$\begin{aligned} I_n &= I_i \cdot [1-\mathscr{R}(\lambda,\theta_i)]^2 \cdot \mathscr{R}(\lambda,\theta_i)^{2(n-1)} \cdot \mathscr{T}(\theta_i)^{2(n-1)+1} \\ &= I_i \cdot [1-\mathscr{R}(\lambda,\theta_i)]^2 \cdot \mathscr{T}(\theta_i) \cdot [\mathscr{R}(\lambda,\theta_i) \cdot \mathscr{T}(\theta_i)]^{2(n-1)} \end{aligned} \tag{E.10}$$

Therefore, the total amount of extracted light $I_t$ is given by the following expression:

$$\begin{aligned} I_t &= \sum_{n=1}^{\infty} I_i \cdot [1 - \mathscr{R}(\lambda, \theta_i)]^2 \cdot \mathscr{T}(\theta_i) \cdot [\mathscr{R}(\lambda, \theta_i) \cdot \mathscr{T}(\theta_i)]^{2(n-1)} \\ &= I_i \cdot [1 - \mathscr{R}(\lambda, \theta_i)]^2 \cdot \mathscr{T}(\theta_i) \cdot \sum_{n=1}^{\infty} [\mathscr{R}(\lambda, \theta_i) \cdot \mathscr{T}(\theta_i)]^{2(n-1)} \\ &= I_i \cdot [1 - \mathscr{R}(\lambda, \theta_i)]^2 \cdot \mathscr{T}(\theta_i) \cdot \sum_{k=0}^{\infty} [\mathscr{R}(\lambda, \theta_i) \cdot \mathscr{T}(\theta_i)]^{2k} \end{aligned} \tag{E.11}$$

As both $\mathscr{R}(\lambda, \theta_i) < 1$ and $\mathscr{T}(\theta_i) \leq 1$, also $[\mathscr{R}(\lambda, \theta_i) \cdot \mathscr{T}(\theta_t)]^2 < 1$. Therefore, the sum in expression E.11 is a geometric series with the common ratio smaller than 1. This means that equation E.11 can be rewritten as follows:

$$\begin{aligned} I_n &= I_i \cdot [1 - \mathscr{R}(\lambda, \theta_i)]^2 \cdot \mathscr{T}(\theta_i) \cdot \frac{1}{1 - [\mathscr{R}(\lambda, \theta_i) \cdot \mathscr{T}(\theta_i)]^2} \\ &= I_i \cdot \mathscr{T}(\theta_i) \cdot \frac{[1 - \mathscr{R}(\lambda, \theta_i)]^2}{1 - [\mathscr{R}(\lambda, \theta_i) \cdot \mathscr{T}(\theta_i)]^2} \\ &= I_i \cdot \mathscr{T}(\theta_i) \cdot \mathscr{F}(\lambda, \theta_i) \end{aligned} \tag{E.12}$$

where the total Fresnel reflection $\mathscr{F}(\lambda, \theta_i)$ is given by $\frac{[1-\mathscr{R}(\lambda,\theta_i)]^2}{1-[\mathscr{R}(\lambda,\theta_i)\cdot\mathscr{T}(\theta_i)]^2}$.

In the case where the light is impinging under an angle of $\theta_i = 90°$, the Fresnel equation simplifies to [3]:

$$\mathscr{R}(\lambda, \theta_i = 90°) = (\frac{n_1 - n_2}{n_1 + n_2})^2 \tag{E.13}$$

with $n_1$ and $n_2$ the refractive indices of the two media. In this case, equation E.12 can be written as:

$$I_n = I_i \cdot \mathscr{T}(l) \cdot \frac{[1 - (\frac{n_1-n_2}{n_1+n_2})^2]^2}{1 - \mathscr{T}(l)^2 \cdot (\frac{n_1-n_2}{n_1+n_2})^4} \tag{E.14}$$

where $\mathscr{T}(l)$ is the transmission of light after traveling a distance of the thickness $l$ of the finite medium.

# Appendix F

# Crystal surfaces of 9 MAMMI crystals for the TurboPET scanner

## F.1 Photos of the crystal surfaces

Figures F.1a-F.1i show pictures of 9 of the MAMMI crystals, selected for the TurboPET ring, after imprinting with sol-gel lithography. The crystal samples are presented in 5.5.

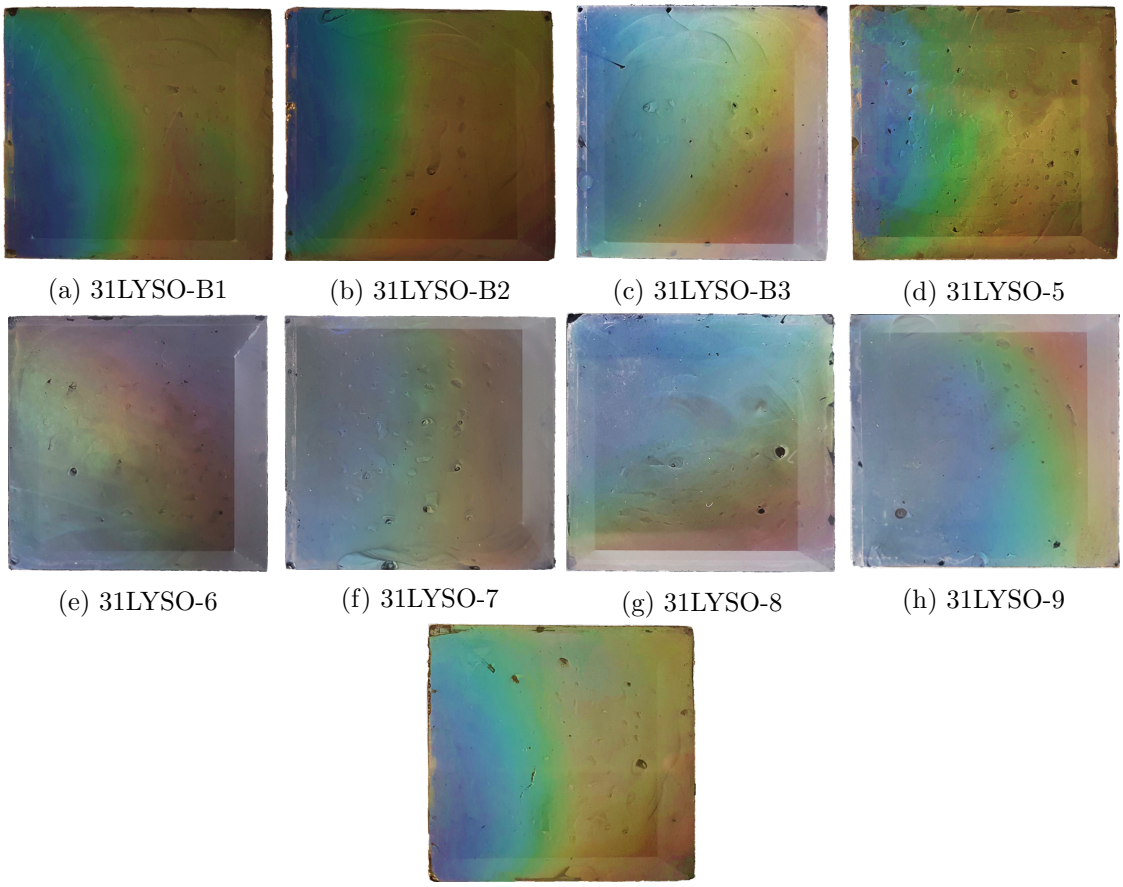

(a) 31LYSO-B1 (b) 31LYSO-B2 (c) 31LYSO-B3 (d) 31LYSO-5

(e) 31LYSO-6 (f) 31LYSO-7 (g) 31LYSO-8 (h) 31LYSO-9

(i) 31LYSO-12

Figure F.1: Surface of nine MAMMI crystals for the final TurboPET ring after undergoing nano-imprinting with sol-gel lithography.

## F.2 SEM images of the crystal surfaces

Figures F.2a-F.4d show SEM images of 6 of the MAMMI crystals for the TurboPET ring after imprinting with sol-gel lithography. The crystals are discussed in 5.5. All crystals show a photonic crystal structure with cones in a hexagonal lattice with a periodicity of 1000 nm. All the patterns show only local periodicity, for crystals 31LYSO-5, 31LYSO-6 and 31LYSO-7 (figures F.3c-f) even only a weak local periodicity. Furthermore, crystal 31LYSO-5 in figure F.3c shows voids in the nanopattern. All the crystals show regions with , such as clustering of cones, in the pattern. All the crystals show some regions with broken cones. The cones all have a base diameter of 400 nm and are sitting on a pedestal-like base above the crystal surface. The height of the cones fluctuate slightly throughout the surface. The average height of the cones for each crystal are summarized in table 5.3 in chapter 5.5.

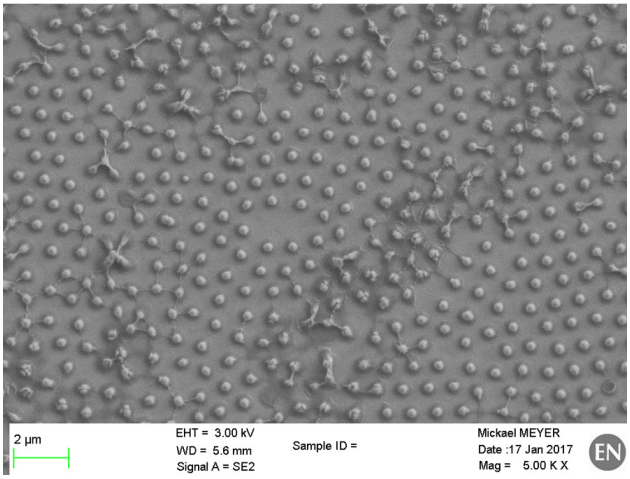


(a) 31LYSO-B1

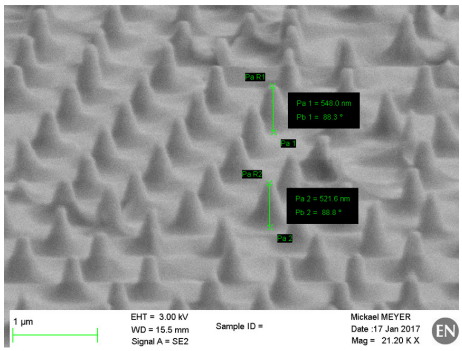


(b) 31LYSO-B1

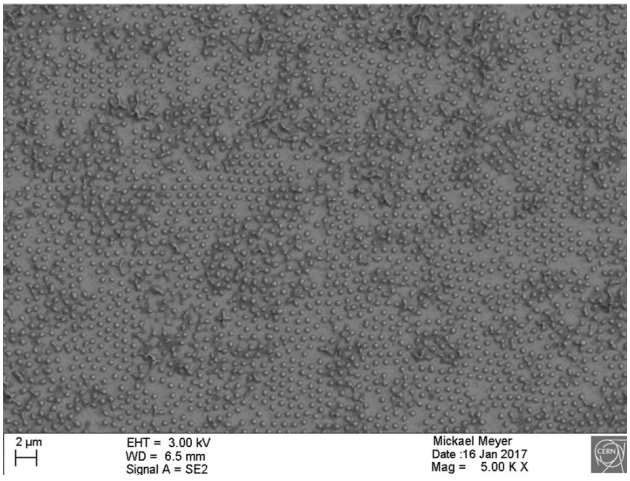


(c) 31LYSO-B2

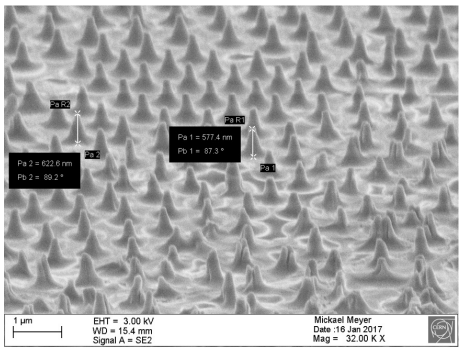


(d) 31LYSO-B2

Figure F.2: SEM images of two of the MAMMI crystals for the final TurboPET ring after undergoing nano-imprinting with sol-gel lithography.

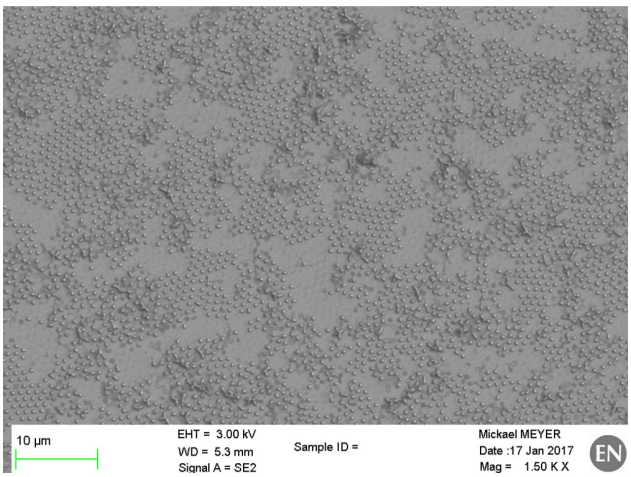


(a) 31LYSO-5

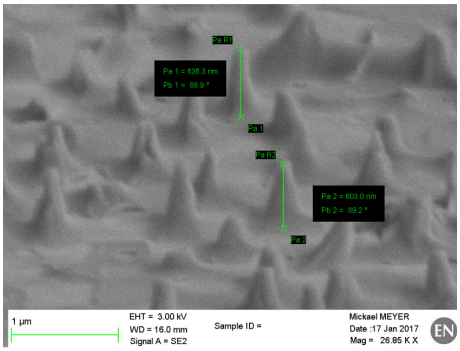


(b) 31LYSO-5

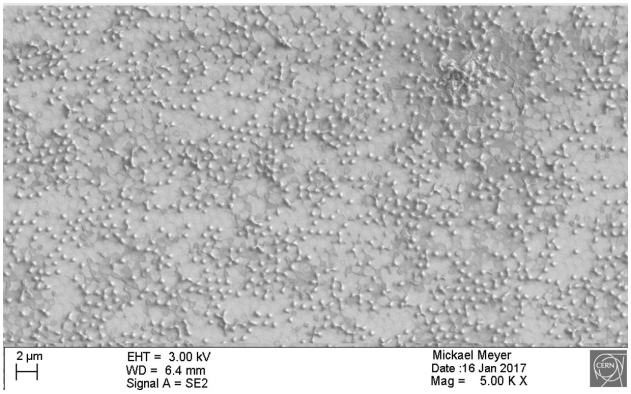


(c) 31LYSO-6

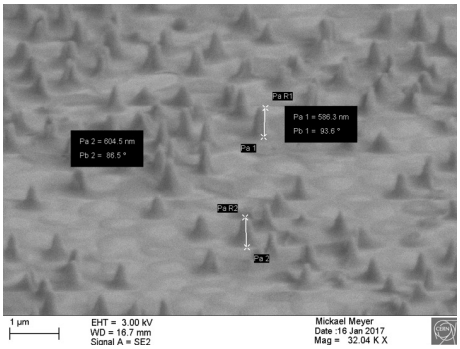


(d) 31LYSO-6

Figure F.3: SEM images of two of the MAMMI crystals for the final TurboPET ring after undergoing nano-imprinting with sol-gel lithography.

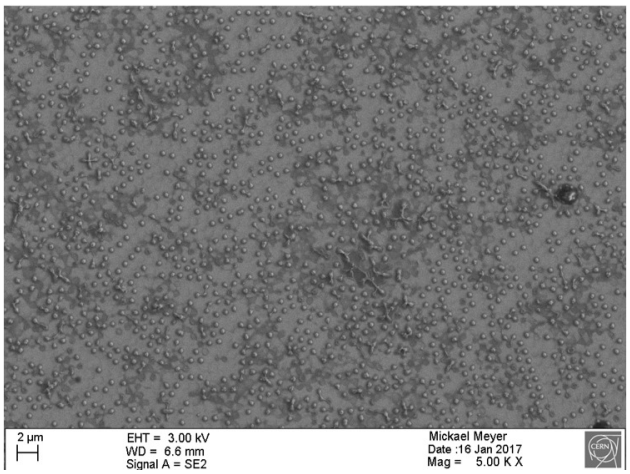


(a) 31LYSO-7

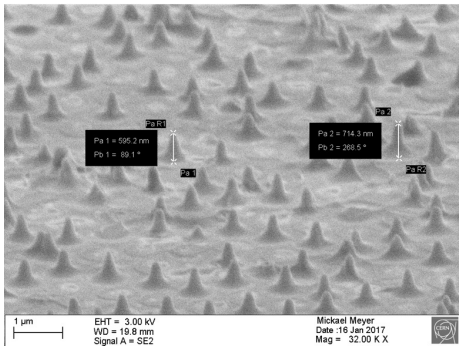


(b) 31LYSO-7

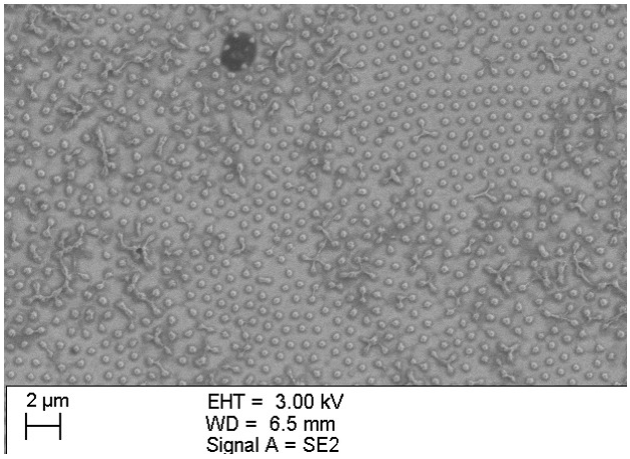


(c) 31LYSO-12

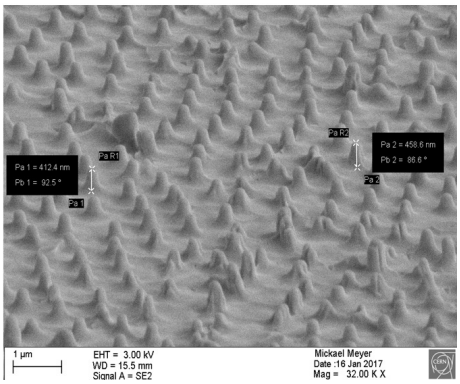


(d) 31LYSO-12

Figure F.4: SEM images of two of the MAMMI crystals for the final TurboPET ring after undergoing nano-imprinting with sol-gel lithography.

# Appendix G

# Schematics Perkin Elmer LAMBDA 650 UV/VIS spectrophotometer

Figure G.1 shows the schematics of the Perkin Elmer LAMBDA 650 UV/VIS spectrophotometer.

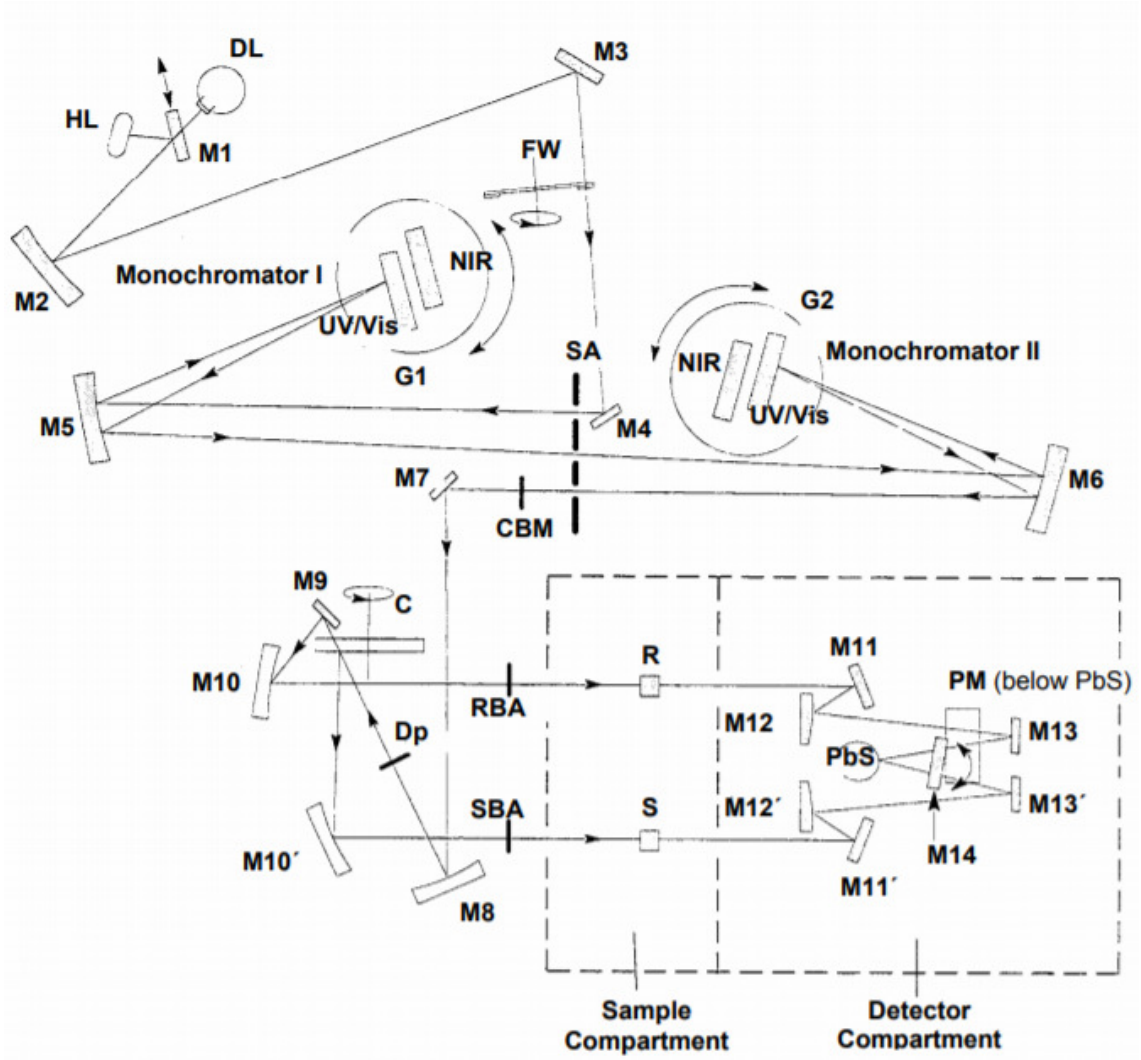


Figure G.1: Schematics of the Perkin Elmer LAMBDA 650 UV/VIS spectrophotometer. [4]

# Appendix H

# Datasheet Hamamatsu R10755 PMT

Datasheet of the Hamamatsu R10755 PMT, used for the measurements in chapter 5 and on the next page a measurements on the wavelength-dependent quantum efficiency.

HAMAMATSU

PHOTOMULTIPLIER TUBE

Apr. 2014

# R10755

For Scintillation Counting, Bialkali
90 mm (3.5 inch) Diameter, 10-stage, Head-on Type

GENERAL

| Parameter | | Description / Value | Unit |
|---|---|---|---|
| Spectral Response | | 300 to 650 | nm |
| Wavelength of Maximum Response | | 420 | nm |
| Photocathode | Material | Bialkali | - |
| | Minimum Effective Area | 85 | mm dia. |
| Windows Material | | Borosilicate glass | - |
| Dynode | Structure | Box & Grid | - |
| | Number of Stage | 10 | - |
| Weight | | 210 | g |

MAXIMUM RATINGS (Absolute Maximum Values)

| Parameter | | Value | Unit |
|---|---|---|---|
| Supply Voltage | Between Anode to Cathode | 1500 | V |
| | Between Anode to Last Dynode | 250 | V |
| Average Anode Current | | 0.1 | mA |
| Operating Temperature | | -30 to +50 | °C |
| Storage Temperature | | -30 to +50 | °C |

CHARACTERISTICS (at 25°C)

| Parameter | | Min. | Typ. | Max. | Unit |
|---|---|---|---|---|---|
| Cathode Sensitivity | Luminous (2856K) | 80 | 110 | - | uA/lm |
| | Blue Sensitivity Index (CS 5-58 filter) | 10 | 11.5 | - | - |
| | Quantum Efficiency at Peak Wavelength | - | 28 | - | % |
| Anode Sensitivity | Luminous (2856K) | 10 | 90 | - | A/lm |
| Gain | | - | $8.2X10^5$ | - | - |
| Anode Dark Current (after 30min. Storage in Darkness) | | - | 5 | 30 | nA |
| Time Response | Anode Pulse Rise Time | - | 19 | - | ns |
| | Electron Transit Time | - | 90 | - | ns |
| Pulse Hight Resolution(NaI(Tl)3"Dia.X3"Thick.+Cs137) | | - | 6.5 | - | % |
| Pulse Linearity at +/- 2 % deviation | | - | 1 | - | mA |
| Pulse Linearity at +/- 5 % deviation | | - | 5 | - | mA |

(For anode characteristics, its applied voltage is 1000V.)

VOLTAGE DISTRIBUTION (K : Cathode, G : Grid, Dy : Dynode, P : Anode)

| K | G | Dy1 | Dy2 | Dy3 | Dy4 | Dy5 | Dy6 | Dy7 | Dy8 | Dy9 | Dy10 | P |
|---|---|---|---|---|---|---|---|---|---|---|---|---|
| 1 | 1 | 1 | 1 | 1 | 1 | 1 | 1 | 1 | 1 | 1 | 1 | |

<Attached Data>
Cathode Luminous Sensitivity , Cathode Blue Sensitivity , Anode Luminous sensitivity , Anode Dark Current

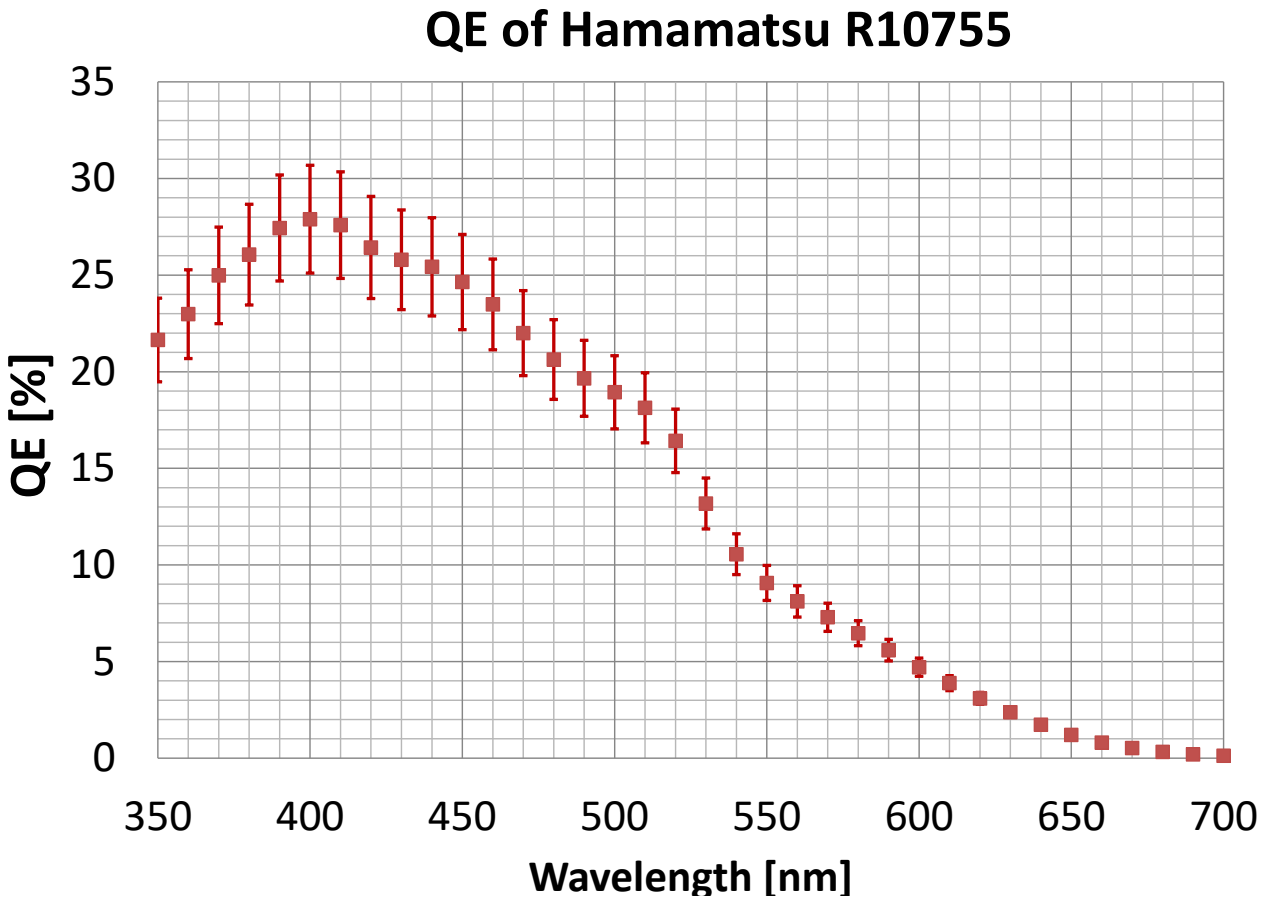
QE of Hamamatsu R10755
QE [%]
35
30
25
20
15
10
5
0
350
400
450
500
550
600
650
700
Wavelength [nm]

# Appendix I

# Datasheet Hamamatsu R2059 PMT

Datasheet of the Hamamatsu R10755 PMT, used for the measurements in chapter 6.

HAMAMATSU

PHOTON IS OUR BUSINESS

# PHOTOMULTIPLIER TUBE
# R1828-01, R2059

## FEATURES

- **Fast time response**
- **51 mm (2 inch) diameter**
- **Bialkali photocathode**

## SPECIFICATIONS

### GENERAL

| Parameter | | Description / Value | Unit |
|---|---|---|---|
| Spectral response | R1828-01 | 300 to 650 | nm |
| | R2059 | 160 to 650 | nm |
| Wavelength of maximum response | | 420 | nm |
| Photocathode | Material | Bialkali | — |
| | Minimum effective area | $\phi$46 | mm |
| Window material | R1828-01 | Borosilicate glass | — |
| | R2059 | Silica glass | — |
| Dynode | Structure | Linear focused | — |
| | Number of stages | 12 | — |
| Operating ambient temperature | | -30 to +50 | °C |
| Storage temperature | | -30 to +50 | °C |
| Base | | JEDEC No. B20-102 | — |
| Suitable socket | | E678-20B (supplied) | — |

### MAXIMUM RATINGS (Absolute maximum values)

| Parameter | | Value | Unit |
|---|---|---|---|
| Supply voltage | Between anode and cathode | 3000 | V |
| | Between anode and last dynode | 400 | V |
| Average anode current | | 0.2 | mA |

### CHARACTERISTICS (at 25 °C)

| Parameter | | Min. | Typ. | Max. | Unit |
|---|---|---|---|---|---|
| Cathode sensitivity | Luminous (2856 K) | 60 | 90 | — | μA/lm |
| | Radiant at 420 nm | — | 85 | — | mA/W |
| | Blue sensitivity index (CS 5-58) | — | 10.5 | — | — |
| Anode sensitivity | Luminous (2856 K) | 200 | 1800 | — | A/lm |
| | Radiant at 420 nm | — | $1.7 \times 10^6$ | — | A/W |
| Gain | | — | $2.0 \times 10^7$ | — | — |
| Anode dark current (after 30 min storage in darkness) | | — | 50 | 400 | nA |
| Time response | Anode pulse rise time | — | 1.3 | — | ns |
| | Electron transit time | — | 28 | — | ns |
| | Transit time spread (FWHM) | — | 550 | — | ps |
| Pulse linearity * | at 2 % deviation | — | 250 | — | mA |
| | at 5 % deviation | — | 500 | — | mA |

**NOTE:** Anode characteristics are measured with the voltage distribution ratio shown below.
* Measured with the special voltage distribution ratio show below.

### VOLTAGE DISTRIBUTION RATIO AND SUPPLY VOLTAGE

| Electrodes | K | G | Dy1 | Dy2 | Dy3 | Dy4 | Dy5 | Dy6 | Dy7 | Dy8 | Dy9 | Dy10 | Dy11 | Dy12 | P |
|---|---|---|---|---|---|---|---|---|---|---|---|---|---|---|---|
| Ratio | 1.2 | 2.8 | 1.2 | 1.8 | 1 | 1 | 1 | 1 | 1 | 1 | 1.5 | 1.5 | 3 | 2.5 | |

Supply voltage: 2500 V, K: Cathode, Dy: Dynode, P: Anode, G: Grid

### SPECIAL VOLTAGE DISTRIBUTION RATIO FOR PULSE LINEARITY MEASUREMENTS

| Electrodes | K | G | Dy1 | Dy2 | Dy3 | Dy4 | Dy5 | Dy6 | Dy7 | Dy8 | Dy9 | Dy10 | Dy11 | Dy12 | P |
|---|---|---|---|---|---|---|---|---|---|---|---|---|---|---|---|
| Ratio | 1.2 | 2.8 | 1.2 | 1.8 | 1 | 1 | 1.2 | 1.5 | 2 | 2.8 | 4 | 5.7 | 8 | 5 | |

Supply voltage: 2500 V, K: Cathode, Dy: Dynode, P: Anode, G: Grid

# PHOTOMULTIPLIER TUBE R1828-01, R2059

Figure 1: Typical spectral response

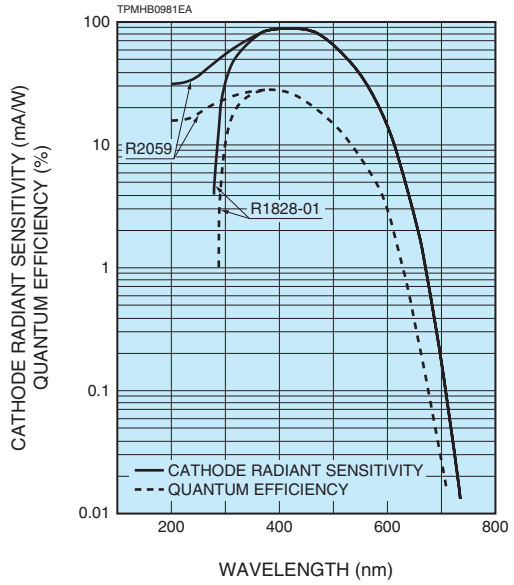


Figure 2: Typical gain characteristics

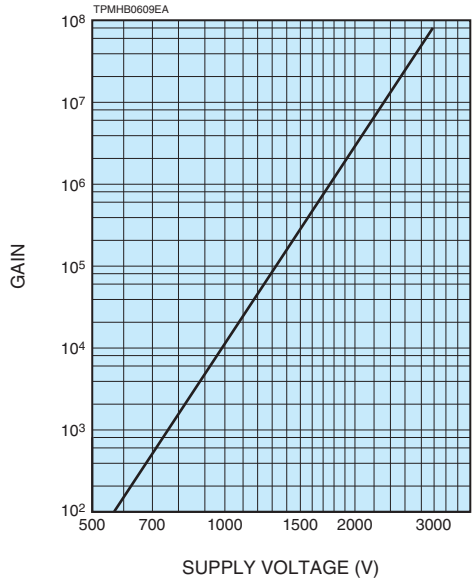


Figure 3: Dimensional outline and basing diagram (Unit: mm)

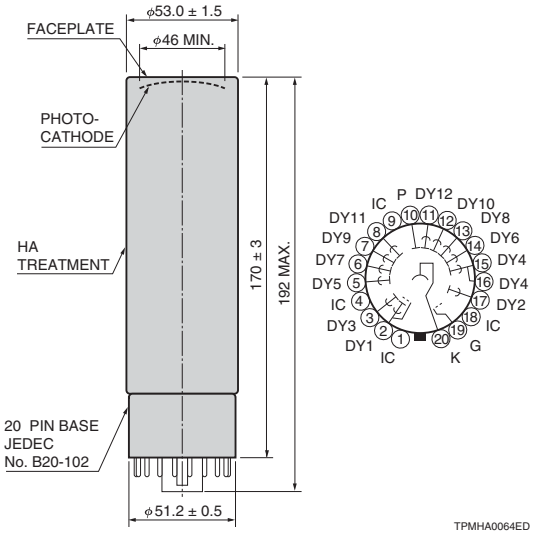





**Socket E678-20B (Supplied)**

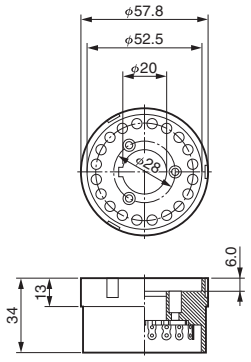


## RELATED PRODUCTS

### PHOTOMULTIPLIER TUBE ASSEMBLY H1949-51/ H3177-51

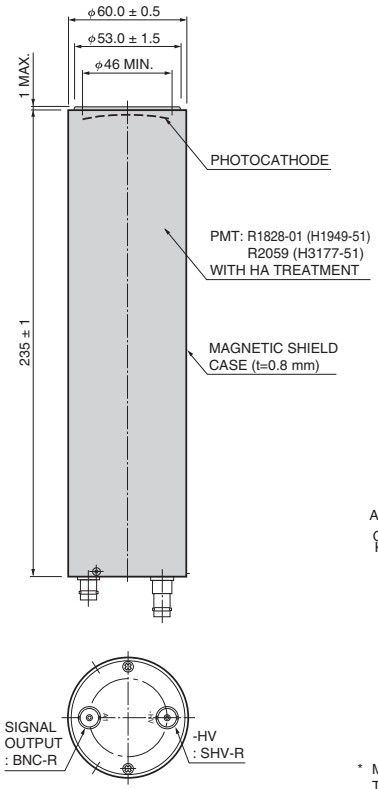


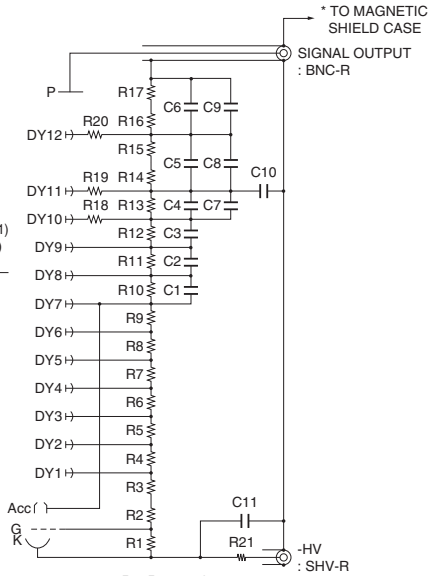


R1, R4: 240 kΩ
R2, R5: 360 kΩ
R3, R6 to R11, R17: 200 kΩ
R12 to R16: 300 kΩ
R18 to R20: 51 Ω
R21: 10 kΩ
C1 to C7: 0.01 μF
C8: 0.022 μF
C9: 0.033 μF
C10: 0.01 μF
C11: 470 pF

* MAGNETIC SHIELD IS CONNECTED TO GND INSIDE OF THIS PRODUCT.

TPMHA0637EA


## HAMAMATSU PHOTONICS K.K. www.hamamatsu.com

**HAMAMATSU PHOTONICS K.K., Electron Tube Division**
**314-5, Shimokanzo, Iwata City, Shizuoka Pref., 438-0193, Japan, Telephone: (81)539/62-5248, Fax: (81)539/62-2205**

**U.S.A.:** Hamamatsu Corporation: 360 Foothill Road, Bridgewater, NJ 08807, U.S.A., Telephone: (1)908-231-0960, Fax: (1)908-231-1218 E-mail: usa@hamamatsu.com
**Germany:** Hamamatsu Photonics Deutschland GmbH.: Arzbergerstr. 10, D-82211 Herrsching am Ammersee, Germany, Telephone: (49)8152-375-0, Fax: (49)8152-265-8 E-mail: info@hamamatsu.de
**France:** Hamamatsu Photonics France S.A.R.L.: 19, Rue du Saule Trapu, Parc du Moulin de Massy, 91882 Massy Cedex, France, Telephone: (33)1 69 53 71 00, Fax: (33)1 69 53 71 10 E-mail: infos@hamamatsu.fr
**United Kingdom:** Hamamatsu Photonics UK Limited: 2 Howard Court,10 Tewin Road, Welwyn Garden City, Hertfordshire AL7 1BW, UK, Telephone: (44)1707-294888, Fax: (44)1707-325777 E-mail: info@hamamatsu.co.uk
**North Europe:** Hamamatsu Photonics Norden AB: Torshamnsgatan 35 16440 Kista, Sweden, Telephone: (46)8-509 031 00, Fax: (46)8-509 031 01 E-mail: info@hamamatsu.se
**Italy:** Hamamatsu Photonics Italia S.r.l.: Strada della Moia, 1 int. 6, 20020 Arese (Milano), Italy, Telephone: (39)02-93 58 17 33, Fax: (39)02-93 58 17 41 E-mail: info@hamamatsu.it
**China:** Hamamatsu Photonics (China) Co., Ltd.: 1201 Tower B, Jiaming Center, 27 Dongsanhuan Beilu, Chaoyang District, 100020 Beijing, P.R.China, Telephone: (86)10-6586-6006, Fax: (86)10-6586-2866 E-mail: hpc@hamamatsu.com.cn
**Taiwan:** Hamamatsu Photonics Taiwan Co., Ltd.: 8F-3, No.158, Section2, Gongdao 5th Road, East District, Hsinchu, 300, Taiwan R.O.C. Telephone: (886)3-659-0080, Fax: (886)3-659-0081 E-mail: info@hamamatsu.com.tw



TPMH1259E05
FEB. 2019 IP

# Appendix J

# Datasheet Hamamatsu H6610 PMT

Datasheet of the Hamamatsu R10755 PMT, used for the measurements in chapter 7.

HAMAMATSU

# PHOTOMULTIPLIER TUBE ASSEMBLIES H6533/H6610

## High Speed Response (Rise Time = 0.7ns, TTS = 0.16ns FWHM)
## 25mm (1 Inch) Diameter, 10 - stage, Bialkali Photocathode, Head - On Type

### GENERAL

| Parameter | | H6533 | H6610 | Unit |
|---|---|---|---|---|
| Assembled Photomultiplier Tube | | R4998 | R5320 | — |
| Spectral Response | | 300 to 650 | 160 to 650 | nm |
| Wavelength of Maximum Response | | 420 | | nm |
| Photocathode | Material | Bialkali | | — |
| | Minimum Effective Area | 20 | | mm dia. |
| Window Material | | Borosilicate glass | Synthetic silica | — |
| Dynode | Structure | Linear focused | | — |
| | Number of Stages | 10 | | — |
| Case | | Magnetic shield case | | — |

### MAXIMUM RATINGS (Absolute Maximum Values)

| Parameter | | Description/Value | Unit |
|---|---|---|---|
| Supply Voltage | Between Anode and Cathode | -2500 | Vdc |
| Voltage Divider Current | | 0.36 | mA |
| Average Anode Current | | 0.016 | mA |
| Ambient Temperature | | -30 to +50 | °C |

### CHARACTERISTICS (at 25 °C)

| Parameter | | Min. | Typ. | Max. | Unit |
|---|---|---|---|---|---|
| Cathode Sensitivity | Luminous (2856 K) | 60 | 70 | — | μA/lm |
| | Blue (CS 5 - 58 filter) | 6 | 9 | — | μA/lm-b |
| Anode Sensitivity | Luminous (2856 K) | 100 | 400 | — | A/lm |
| Gain | | — | $5.7 \times 10^6$ | — | — |
| Anode Dark Current (after 30 min. storage in darkness) | | — | 100 | 800 | nA |
| Time Response | Anode Pulse Rise Time | — | 0.7 | — | ns |
| | Electron Transit Time | — | 10 | — | ns |
| | Transit Time Spread (T.T.S.) | — | 0.16 | — | ns |

***NOTE:*** Anode characteristics are measured with the voltage distribution ratio shown below.

### VOLTAGE DISTRIBUTION RATIO AND SUPPLY VOLTAGE

| Electrodes | K | G | Dy1 | Dy2 | Dy3 | Dy4 | Dy5 | Dy6 | Dy7 | Dy8 | Dy9 | Dy10 | P |
|---|---|---|---|---|---|---|---|---|---|---|---|---|---|
| Ratio | 1.3 | 4.8 | 1.2 | 1.8 | 1 | 1 | 1 | 1 | 1 | 1.5 | 3 | 2.5 | |

Supply Voltage: -2250 Vdc, K: Cathode, Dy: Dynode, P: Anode, G: Grid
Acc to be connected to Dy7

# PHOTOMULTIPLIER TUBE ASSEMBLIES H6533/H6610

### Figure 1: Typical Spectral Response

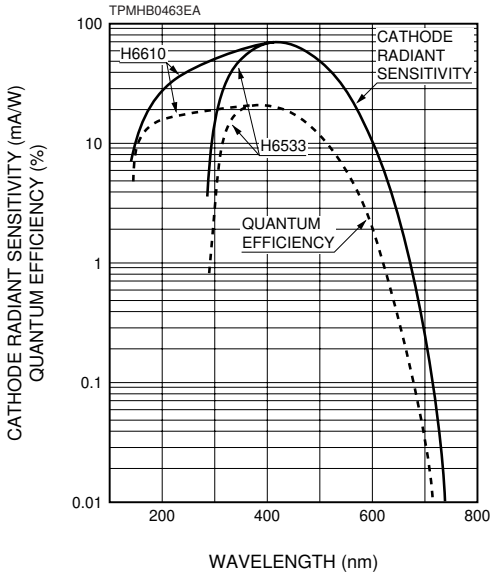


### Figure 2: Typical Gain and Anode Dark Current

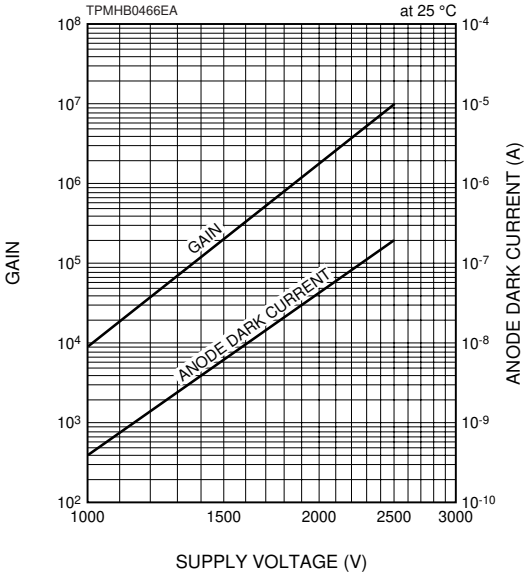


### Figure 3: Dimensional Outline and Circuit Diagram (Unit: mm)

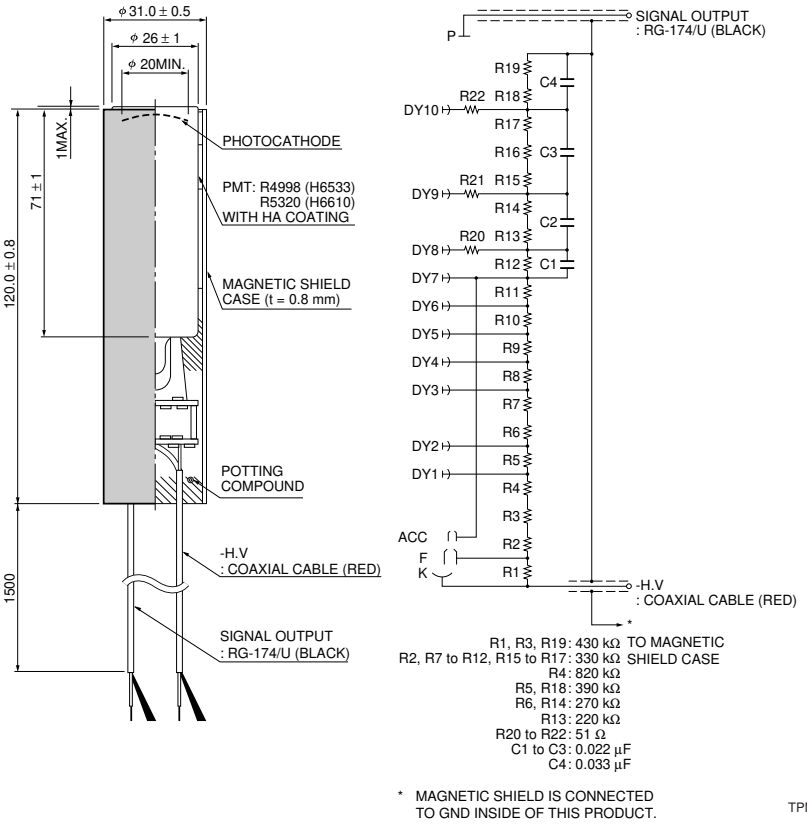



HAMAMATSU

HAMAMATSU PHOTONICS K.K., Electron Tube Center
314-5, Shimokanzo, Toyooka-village, Iwata-gun, Shizuoka-ken, 438-0193 Japan, Telephone:(81)539/62-5248, Fax:(81)539/62-2205

*U.S.A.*: Hamamatsu Corporation: 360 Foothill Road, P.O.Box 6910, Bridgewater, N.J. 08807-0910, U.S.A., Telephone:(1)908-231-0960, Fax:(1)908-231-1218
*Germany*: Hamamatsu Photonics Deutschland GmbH: Arzbergerstr. 10, D-82211 Herrsching am Ammersee, Germany, Telephone:(49)8152-375-0, Fax:(49)8152-2658
*France*: Hamamatsu Photonics France: S.A.R.L.: 8, Rue du Saule Trapu, Parc du Moulin de Massy, 91882 Massy Cedex, France, Telephone:(33)1 69 53 71 00, Fax:(33)1 69 53 71 10
*United Kingdom*: Hamamatsu Photonics UK Limited: Lough Point, 2 Gladbeck Way, Windmill Hill, Enfield, Middlesex EN2 7JA, United Kingdom, Telephone:(44)181-367-3560, Fax:(44)181-367-6384
*North Europe*: Hamamatsu Photonics Norden AB: Färögatan 7, S-164 40 Kista, Sweden, Telephone:(46)8-703-29-50, Fax:(46)8-750-58-95
*Italy*: Hamamatsu Photonics Italia S.R.L.: Via della Moia, 1/E 20020 Arese, (Milano), Italy ,Telephone: (39)2 935 81 733 Fax: (39)2 935 81 741



TPMH1199E01
FEB. 1998 SI
Printed in Japan (500)

# Appendix K

# Datasheet HPM-100-07

Datasheet of the HPM-100-07 hybrid PMT, used for the measurements in chapter 7.

# HPM-100-06/07

## Ultra-High Speed Hybrid Detectors for TCSPC

**Ultra fast instrument response function: <20 ps FWHM with SPC-150NX**

**HPM-100-06: 290 to 600 nm (Bialkali)**

**HPM-100-07: 220 to 850 nm (Multialkali)**

**No afterpulsing background**

**Excellent dynamic range of TCSPC measurements**

**Internal generators for PMT operating voltages**

**Power supply and control via bh DCC-100 card**

**Overload shutdown**

**Direct interfacing to all bh TCSPC systems**

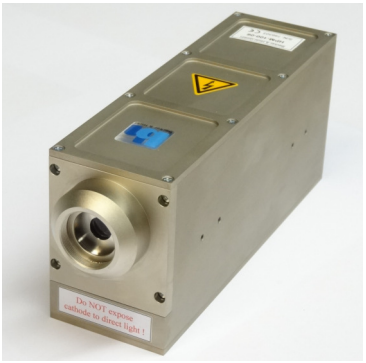


**The HPM-100 module combines a Hamamatsu R10467 hybrid detector tube with a preamplifier and the generators for the tube operating voltages in one compact housing. The principle of the hybrid detector yields excellent timing resolution, a clean TCSPC instrument response function, high detection quantum efficiency, and extremely low afterpulsing probability. The absence of afterpulsing results in a substantially increased dynamic range of TCSPC measurements.**

**The HPM-100 module is operated via the bh DCC-100 detector controller of the bh TCSPC systems. The DCC-100 provides for power supply, gain control, and overload shutdown. The HPM-100 interfaces directly to all bh SPC or Simple Tau TCSPC systems. It is available with standard C-mount adapters, adapters for the bh DCS-120 confocal scanning FLIM system, and adapters for the NDD and BIG ports of the Zeiss LSM 710/780/880 NLO multiphoton laser scanning microscopes.**

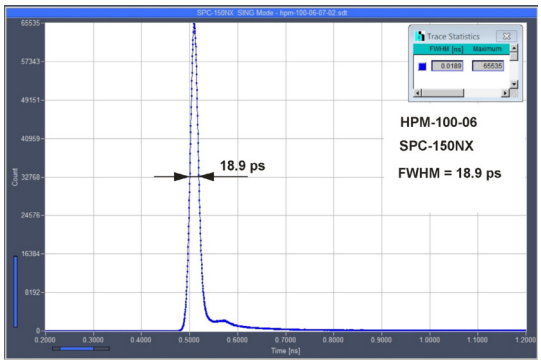


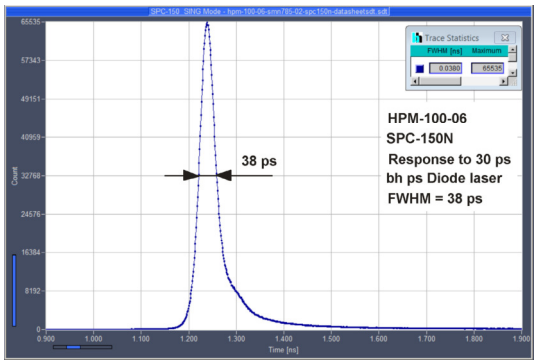


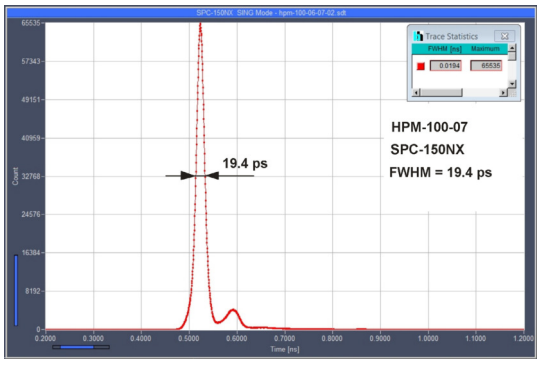


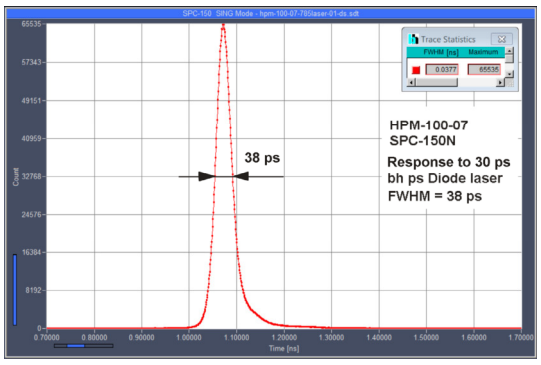


Left: Intrument response function, measured with 100-fs fibre laser. Recorded with SPC-150NX TCSPC module. Right: Response to pulses from bh picosecond diode laser, 30 ps pulse width. Recorded with SPC-150N TCSPC module.

**Technology Leader in TCSPC**

# HPM-100-06/07

## Detection quantum efficiency vs. wavelength

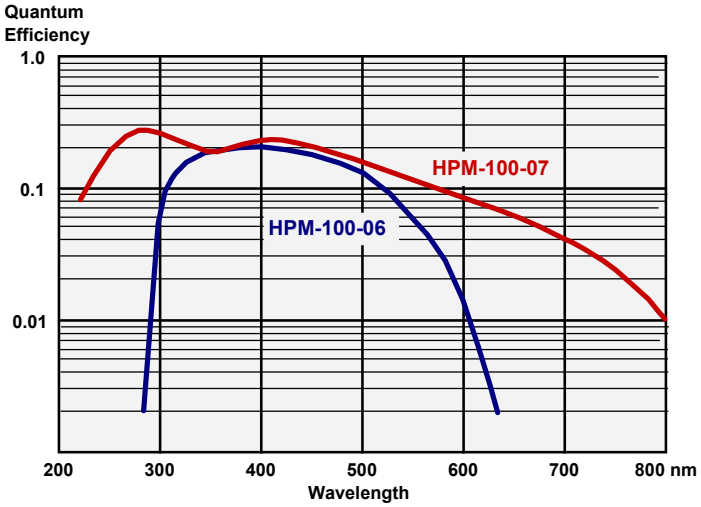


(after Hamamatsu Specifications)

## Specifications, typical values

| | -06 version | -07 version |
|---|---|---|
| Wavelength Range | 290 nm to 600 nm | 220 to 850 nm [1] |
| Peak detection Quantum efficiency | 20 % (at 400nm) | 26% at 290 nm, 22% at 400nm [1] |
| Dark Count rate, Tcase = 22°C, 3mm version | 100 to 400 $s^{-1}$ | 100 to 1000 $s^{-1}$ |
| Cathode Diameter | 3 mm | |
| TCSPC IRF width (Transit Time Spread, with SPC-150NX) | <20 ps, FWHM | |
| Single Electron Response Width | 850 ps, FWHM | |
| Single Electron Response Amplitude | 50 to 150 mV, -8000 V, $V_{apd}$ 95% of $V_{breakdown}$ | |
| Output Polarity | negative | |
| Output Impedance | 50 Ω | |
| Max. Count Rate (Continuous) | 10 MHz | |
| Overload shutdown at | >15 MHz | |
| Detector Signal Output Connector | SMA | |
| Power Supply (from DCC-100 Card) | + 12 V, +5 V, -12V | |
| Dimensions (width x height x depth) | 60 mm x 90 mm x 170 mm | |
| Optical Adapters | C-Mount, DCS-120, LSM 710/780/880 NDD and BIG ports | |

1) according to Hamamatsu specifications

**Related products:** HPM-100-40/42 GaAsP and HPM-100-50 GaAs hybrid detector modules
**Literature:** The bh TCSPC Handbook, 6th edition, Becker & Hickl GmbH. Printed copies or electronic version on www.becker-hickl.com
Sub-20ps IRF Width from Hybrid Detectors and MCP-PMTs. Application note, available from www.becker-hickl.com


**Becker & Hickl GmbH**
Nahmitzer Damm 30
12277 Berlin, Berlin
Tel. +49 / 30 / 787 56 32
Fax. +49 / 30 / 787 57 34
email: info@becker-hickl.com
www.becker-hickl.com


## International Sales Representatives

US:
**Boston Electronics Corp**
tcspc@boselec.com
www.boselec.com

UK:
**Photonic Solutions PLC**
sales@psplc.com
www.psplc.com

Japan:
**Tokyo Instruments Inc.**
sales@tokyoinst.co. jp
www.tokyoinst.co.jp

China:
**DynaSense Photonics Co. Ltd.**
info@dyna-sense.com
www.dyna-sense.com

# Appendix L

# Bibliography of appendix

## Bibliography

[1] W. Bekker, *Advanced Time-Correlated Single Photon Counting Applications*. Springer International Publishing, Cham, 2005. Chapter 1.

[2] A. Vasile'ev, "Relaxation of hot electronic excitations in scintillators: account for scattering, track effects, complicated electronic structure," *Proceedings of the fifth conference on Inorganic Scintillators and Their Applications*, pp. 43–52, August 1999.

[3] M. Born and E. Wolf, *Principles of Optics*. Eddington Hill Hall, Oxford OX3 OBW, England: Oxford: Pergamon Press, 4 ed., 1970.

[4] "Hardware guide of the perkin elmer lambda 650 uv/vis spectrometer." `https://cmdis.rpi.edu/sites/default/files/UVVis-PerkinElmer-Lambda950-HardwareGuide.pdf`. Accessed: 2020-07-21.

# List of Publications


[1] R. H. Pots, E. Auffray, and S. Gundacker, "Exploiting cross-luminescence in baf2 for ultrafast timing applications using deep-ultraviolet sensitive hpk silicon photomultipliers," *Frontiers in Physics*, vol. 8, p. 482, 2020.

[2] R. H. Pots, M. Salomoni, S. Gundacker, S. Zanettini, V. Gâté, E. Usureau, D. Turover, P. Lecoq, and E. Auffray, "Improving light output and coincidence time resolution of scintillating crystals using nanoimprinted photonic crystal slabs," *Nuclear Instruments and Methods in Physics Research Section A: Accelerators, Spectrometers, Detectors and Associated Equipment*, vol. 940, pp. 254 – 261, 2019.

[3] S. Gundacker, R. H. Pots, A. Nepomnyashchikh, E. Radzhabov, R. Shendrik, S. Omelkov, M. Kirm, F. Acerbi, M. Capasso, G. Paternoster, A. Mazzi, A. Gola, J. Chen, and E. Auffray, "Vuv-sipms applied to $baf_2$ cross-luminescence detection for high-rate ultrafast timing applications," *Physics in Medicine & Biology*, jun 2021.

[4] M. Salomoni, R. Pots, E. Auffray, and P. Lecoq, "Enhancing light extraction of inorganic scintillators using photonic crystals," *Crystals*, vol. 8, p. 78, Feb 2018.

[5] M. Salomoni, R. Pots, P. Lecoq, E. Auffray, S. Gundacker, M. Paganoni, B. Singh, M. Marshall, and V. V. Nagarkar, "Photonic crystal slabs applied to inorganic scintillators," *IEEE Transactions on Nuclear Science*, vol. 65, pp. 2191–2195, Aug 2018.

[6] S. Gundacker, R. Martinez Turtos, N. Kratochwil, R. H. Pots, M. Paganoni, P. Lecoq, and E. Auffray, "Experimental time resolution limits of modern SiPMs and TOF-PET detectors exploring different scintillators and cherenkov emission," *Physics in Medicine & Biology*, vol. 65, p. 025001, jan 2020.

[7] B. Singh, M. S. J. Marshall, S. Waterman, C. Pina-Hernandez, A. Koshelev, K. Munechika, A. Knapitsch, M. Salomoni, R. Pots, P. Lecoq, and V. V. Nagarkar, "Enhanced scintillation light extraction using nanoimprinted photonic crystals," *IEEE Transactions on Nuclear Science*, vol. 65, pp. 1059–1065, April 2018.

[8] F. Ferrulli, M. Caresana, F. Cova, S. Gundacker, N. Kratochwil, R. Pots, M. Silari, A. Vedda, I. Veronese, and G. Zorloni *Sensors and Actuators A: Physical*, vol. 332, p. 113151, 2021.

**Eidesstattliche Erklärung**

**Declaration of Authorship**

I, Rosalinde Hendrika Pots

declare that this thesis and the work presented in it are my own and has been generated by me as the result of my own original research.

Hiermit erkläre ich an Eides statt / I do solemnely swear that:

1. This work was done wholly or mainly while in candidature for the doctoral degree at this faculty and university;

2. Where any part of this thesis has previously been submitted for a degree or any other qualification at this university or any other institution, this has been clearly stated;

3. Where I have consulted the published work of others or myself, this is always clearly attributed;

4. Where I have quoted from the work of others or myself, the source is always given. This thesis is entirely my own work, with the exception of such quotations;

5. I have acknowledged all major sources of assistance;

6. Where the thesis is based on work done by myself jointly with others, I have made clear exactly what was done by others and what I have contributed myself;

7. Parts of this work have been published before as:

    - R. H. Pots, E. Auffray, and S. Gundacker, "Exploiting cross-luminescence in baf2 for ultrafast timing applications using deep-ultraviolet sensitive hpk silicon photomultipliers," Frontiers in Physics, vol. 8, p. 482, 2020.
    - R. H. Pots, M. Salomoni, S. Gundacker, S. Zanettini, V. Gâté, E. Usureau, D. Turover, P. Lecoq, and E. Auffray, "Improving light output and coincidence time resolution of scintillating crystals using nanoimprinted photonic crystal slabs," Nuclear Instruments and Methods in Physics Research Section A: Accelerators, Spectrometers, Detectors and Associated Equipment, vol. 940, pp. 254 – 261, 2019.
    - S. Gundacker, R. H. Pots, A. Nepomnyashchikh, E. Radzhabov, R. Shendrik, S. Omelkov, M. Kirm, F. Acerbi, M. Capasso, G. Paternoster, A. Mazzi, A. Gola, J. Chen, and E. Auffray, "Vuv-sipms applied to baf2 cross-luminescence detection for high-rate ultrafast timing applications," Physics in Medicine & Biology, June 2021.
    - M. Salomoni, R. Pots, E. Auffray, and P. Lecoq, "Enhancing light extraction of inorganic scintillators using photonic crystals," Crystals, vol. 8, p. 78, Feb 2018.

- M. Salomoni, R. Pots, P. Lecoq, E. Auffray, S. Gundacker, M. Paganoni, B. Singh, M. Marshall, and V. V. Nagarkar, "Photonic crystal slabs applied to inorganic scintillators," IEEE Transactions on Nuclear Science, vol. 65, pp. 2191–2195, Aug 2018.
- S. Gundacker, R. Martinez Turtos, N. Kratochwil, R. H. Pots, M. Paganoni, P. Lecoq, and E. Auffray, "Experimental time resolution limits of modern SiPMs and TOF-PET detectors exploring different scintillators and cherenkov emission," Physics in Medicine & Biology, vol. 65, p. 025001, Jan 2020.

11.05.2022

Rosalinde Hendrika Pots